

# Thermomechanical behavior of underground energy infrastructures

Présentée le 6 août 2020

à la Faculté de l'environnement naturel, architectural et construit  
Laboratoire de mécanique des sols - Chaire gaz naturel Petrosvibri  
Programme doctoral en mécanique

pour l'obtention du grade de Docteur ès Sciences

par

**Jacopo ZANNIN**

Acceptée sur proposition du jury

Prof. I. Smith, président du jury  
Prof. L. Laloui, Dr A. Ferrari, directeurs de thèse  
Prof. J.-M. Pereira, rapporteur  
Prof. A. Di Donna, rapporteuse  
Prof. D. Khovalyg, rapporteuse

*Alla mia famiglia*



# Acknowledgements

I would like to gratefully thank my thesis directors, Prof. Lyesse Laloui and Prof. Alessio Ferrari for their supervision during my doctoral studies. Your guidance, support, attention to details have decisively contributed to improving my professional skills. You gave me the opportunity to develop projects and to propose ideas that go deeply towards my main research interests. I have always found your support, your availability to discuss my ideas and to challenge myself in a very constructive way.

I would like to thank as well Profs. Ian Smith, Dolaana Khovalyg, Alice Di Donna and Jean-Michel Pereira, for having accepted to take part in the Jury, for the time they've spent revising my work and for the very interesting discussions arisen during my PhD exam.

I would like to acknowledge the financial support of the European Commission via the Marie Skłodowska-Curie Innovative Training Networks (ITN-ETN) project TERRE 'Training Engineers and Researchers to Re-think Geotechnical Engineering for a low carbon future' (H2020-MSCA-ITN-2015-675762). A special thank goes to Dr. Pyrène Larrey-Lassalle and Maxime Pousse of Nobatek, for their support and industrial collaboration during this project. I would like to warmly thank also Prof. Alessandro Tarantino, the project coordinator, for his leadership and confidence in our work especially during the school competition organization. I thank also Prof. Simon Wheeler and Prof. Charles Augarde for the very interesting discussions arisen during the project meetings. A warm thank goes to Katharine Houston, for her neverending administrative support.

I would like to acknowledge the financial support of Services Industriels de Genève (SIG) during the in-situ project on energy walls at the Lancy-Bachet CEVA train station, and thank the project leader, Sandra Mamboundou. The collaboration with Dr. Azad Koliji, Dr. Tohid Kazerani and Emmanuel Rigaud of BG Consulting Engineers is gratefully acknowledged. The support of Luc Burnier of LESO-PB laboratory of EPFL with the thermal camera equipment is gratefully acknowledged.

A huge thank you goes to the whole team of the Laboratory of Soil Mechanics (LMS) of EPFL. I was very lucky for joining this great group and participating in the everyday campus life with all of you. A huge thanks goes to all my (former and current) colleagues for your continuous support: Dr. Barnaby, Angelica, Cristiano, Jose, Etienne, Elena, Benoit, Margaux, Lorenzo, Jinu, Tae, Ariadni, Ray, Matteo, Erica. Thank you also to some (former) colleagues: Dr. Aldo Madaschi, Dr. Dimitrios Terzis, Dr. Patrycia Baryla for the very interesting scientific discussions; Prof. Melis Sutman for the discussions on energy geostructures. A special thanks goes to Rosana and Barbara for their administrative support; and to Patrick, Luc and Erwan for their help with the TRT equipment and the onsite installation works.

I would like to thank Prof. Alessandro F. Rotta Loria, Dr. Alberto Minardi and Dr. Eleonora Crisci for their support throughout the difficult steps of the PhD, for their guidance as experienced colleagues and for their friendship.



In spite of the daily arguments about football, I would like to particularly thank the support and friendship of my officemate Dr. Gianluca Speranza. During the last four years we shared many adventures together at EPFL and touring around Europe for meetings and conferences. I think I am lucky because I have found not only an extremely competent colleague with whom I have shared lots of scientific discussions, but mostly a great friend. Merci, Jeanluc!

I would like to thank also the support of my colleagues and friends of LEMR, Chiara, Corentin, Dr. Mateo, Prof. Felipe.

A special thanks goes to some students with whom I have collaborated during their semester and master projects. Such experiences have been extremely enriching for me, showing me once again the importance of teamworking for developing successful research activities. Thank you to Qazim Llabjani, Nicolas Delessert, Héloïse Fuselier, Richard Wyss, Gaetan Gindrat.

A warm acknowledgement goes to my colleagues of Terre project. We shared many discussions and ideas, and also many beers together. This has been an incredible journey, and I would like to thank all of you for having been such a great inspiration for me: Abhi, Alessandro, Roberta, Riccardo, Sravan, Emmy, Gianluca, Sofia, Raniero, Alessia, Lorenzo, Pavlina, Elodie, Javi, Slimane.

A special thanks goes to Prof. Shideh Dashti, Dr. Juan Olarte, Dr. Balaji Paramasivam and Dr. Jenny Ramirez, which are the people that, for the first time, asked me the question ‘why don’t you do a PhD?’. I strongly believe that, without them, I would have never thought about doing a PhD...but in the end, here we are. They instilled in me the passion for research, and for this reason I gratefully thank them.

I would like to thank all the new friends that I’ve made since I moved to Lausanne. Thank you very much for all the great times we shared together cooking and touring around Switzerland: Messié, Cristina, Ele, Nico. Je voudrais remercier en particulier mes amis du groupe CBMD avec lesquels on amène du funk et de musique des films dans les rues de Lausanne. Un ringraziamento speciale al Maestro Matteo Frigo, per il Balelec, la matematica da bar, la grinta, il Syrah dei Pays d’Oc e “daghe Charles”.

Grazie ai miei amici di sempre Pippo, Filo e Cristian per le risate, i concerti, e per esserci sempre nonostante la distanza, anche nei momenti difficili. A Enrico, Lisa e Luca. Alla mia amica Dott.ssa Giulia, per la sua amicizia di quasi trent’anni. A Batto e Silvia, che ci sono sempre. Ai Radiatori ed ai Chobez, amici veri.

A mia mamma, mio papà, e mia sorella, per farmi sempre sentire a casa nonostante la distanza e le difficoltà.

A Chiara, per aver accettato la sfida di raggiungermi in un Paese dove si parla una lingua nuova, e per essere al mio fianco tutti i giorni. Grazie.

# Abstract

The employment of geostructures as structural supports and as heat exchangers represent an effective, renewable and sustainable way to satisfy thermal needs of the built environment. The structural support of conventional geotechnical structures is coupled with the heat exchanger role by inserting heat exchangers attached to the reinforcing cage of concrete geostructures. Hence, geostructures act as multifunctional elements, called energy geostructures. The concurrent dual role involves thermal and mechanical aspects to be considered during analysis and design, causing novel challenges for engineers. This doctoral thesis focuses on the thermomechanical behavior of underground energy infrastructures (e.g., vertical retaining walls, diaphragm walls, cut-and-cover tunnels, base slabs, multi-floored underground basements, etc...). Prior to this work, limited knowledge on this topic was available and the main challenges were: (i) to thoroughly understand the thermal and hydrothermal aspects linked to the heat transfer within and around the energy geostructure; (ii) to detect fundamental aspects on the thermomechanical behavior; (iii) to provide feedback from real installations. To address such challenges, this doctoral thesis employed experimental, numerical and analytical techniques. Firstly, fundamental aspects on thermomechanical behavior and on hydrothermal aspects linked to the thermal performance are presented. Secondly, aspects related to the early-stage thermal performance design are tackled, presenting a methodology for thermal performance design based on a flowchart. Thirdly, the only analytical model able of considering combinations of axial and flexural thermal and mechanical loads is presented and used to tackle several examples in the field of energy geostructures. Finally, an experimental, in-situ, campaign on an energy wall of an underground energy infrastructure in Geneva (CH) is presented focusing on: the execution of (i) a thermal response test (TRT) and (ii) heating/cooling tests, including aspects linked to test execution, thermomechanical monitoring, data interpretation, and (iii) the determination of the thermal potential of the entire underground energy infrastructure installation. The main results provided by this thesis are: (a) thermal behavior of underground energy infrastructures involves strong interactions with the surrounding environments (e.g., air interfaces); (b) the temperature variation distributions induced by thermal operations are nonuniform, inducing axial and flexural mechanical actions; (c) a modified TRT execution procedure is proposed, allowing for the consideration of non-negligible hydrothermal aspects occurring within the energy geostructure and its surroundings; (d) the in-situ testing campaign undertaken at the site in Geneva revealed a very strong thermal storage potential and a slightly lower extraction potential due to the influence of thermal boundary conditions.

## Keywords

Renewable energy; Sustainability; Underground energy infrastructures; Thermal performance; Hydrothermal behavior; Thermomechanical behavior; Analytical modelling; Soil-structure interaction; Numerical modelling; Non-isothermal analysis; In-situ testing; Thermal Response Test;

# Resumé

L'utilisation des géostructures comme supports structuraux et comme échangeurs de chaleur représente un moyen efficace, renouvelable et durable de satisfaire les besoins thermiques de l'environnement bâti. Le support structural des structures géotechniques conventionnelles est couplé au rôle d'échangeur de chaleur par l'insertion d'échangeurs de chaleur fixés à la cage d'armature des géostructures en béton. Ainsi, les géostructures agissent comme des éléments multifonctionnels, appelés géostructures énergétiques. Ce double rôle simultané implique des aspects thermiques et mécaniques à prendre en compte lors de l'analyse et de la conception, ce qui pose de nouveaux défis aux ingénieurs. Cette thèse se concentre sur le comportement thermomécanique des infrastructures énergétiques souterraines (par exemple, les murs de soutènement verticaux, les tranchées couvertes, les dalles de base, les sous-sols souterrains à plusieurs étages, etc...). Avant cette thèse, les connaissances sur ce sujet étaient limitées et les principaux défis étaient les suivants : (i) comprendre en profondeur les aspects thermiques et hydrothermaux liés au transfert de chaleur à l'intérieur et autour de la géostructure énergétique ; (ii) détecter les aspects fondamentaux du comportement thermomécanique ; (iii) étudier le comportement in-situ et fournir un retour d'expérience concernant les installations réelles. Pour relever ces défis, cette thèse de doctorat a utilisé des techniques expérimentales, numériques et analytiques. Tout d'abord, des aspects fondamentaux sur le comportement thermomécanique et sur les aspects hydrothermiques liés à la performance thermique sont présentés. Ensuite, les aspects liés à la conception de la performance thermique dans les phases initiales du projet sont abordés, en présentant une méthodologie pour la conception de la performance thermique basée sur un organigramme. Troisièmement, le seul modèle analytique capable de prendre en compte les combinaisons de charges thermiques et mécaniques axiales et de flexion est présenté et utilisé pour aborder plusieurs exemples dans le domaine des géostructures énergétiques. Enfin, une campagne expérimentale in-situ sur une paroi énergétique d'une infrastructure souterraine à Genève (CH) est présentée. Cette étude se concentre sur : l'exécution de (i) un essai de réponse thermique (TRT) et (ii) des essais de chauffage/refroidissement, y compris les aspects liés à l'exécution des essais, le monitoring thermomécanique, l'interprétation des données, et (iii) la détermination du potentiel thermique de toute l'installation de l'infrastructure énergétique souterraine. Les principaux résultats fournis par cette thèse sont les suivants (a) le comportement thermique des infrastructures énergétiques souterraines implique de fortes interactions avec les environnements environnants (par exemple interfaces air); (b) les distributions des variations de température induites par les opérations thermiques sont non uniformes, induisant des actions mécaniques axiales et de flexion; (c) une procédure d'exécution modifiée du TRT est proposée, permettant de prendre en compte les aspects hydrothermaux non négligeables se produisant au sein de la géostructure énergétique et de ses environs; (d) la campagne d'essais in-situ entreprise sur le site de Genève a révélé un très fort potentiel de stockage thermique et un potentiel d'extraction légèrement plus faible en raison de l'influence des conditions thermiques aux bords.

## Mots-clé

Énergie renouvelable; Développement durable; Infrastructures énergétiques souterraines; Performance thermique; Comportement hydrothermal; Comportement thermomécanique; Modélisation analytique; Interaction sol-structure; Modélisation numérique; Analyse non isothermique; Essais in situ; Test de réponse thermique;

# Riassunto

L'utilizzo delle geostrutture come supporto strutturale e come scambiatori di calore rappresenta un modo efficace per soddisfare il fabbisogno termico degli edifici, in modo sostenibile e rinnovabile. Inserendo degli scambiatori di calore agganciati alle barre d'armatura, il ruolo di supporto strutturale delle geostrutture convenzionali è accoppiato con il ruolo di scambiatore geotermico. Le geostrutture, quindi, diventano degli elementi multifunzionali, chiamati geostrutture energetiche. Il simultaneo, duplice ruolo coinvolge aspetti termici e meccanici da considerare durante l'analisi e la progettazione, causando nuove sfide per gli ingegneri. Questa tesi di dottorato si focalizza sul comportamento termomeccanico delle infrastrutture sotterranee termoadattive (e.g., muri di sostegno verticali, diaframmi, gallerie scatolari, solai di base, costruzioni sotterranee a più piani, ecc...). Prima di questo lavoro, la conoscenza scientifica relativa alle infrastrutture sotterranee energetiche era limitata. Le principali sfide scientifiche erano relative a: (i) la comprensione dei dettagli riguardanti il funzionamento termico e gli aspetti idrotermici legati ai meccanismi di trasferimento del calore all'interno ed attorno alla geostruttura energetica; (ii) l'individuazione degli aspetti fondamentali del comportamento termomeccanico e lo sviluppo di modelli semplificati che consentano di considerare la simultaneità di azioni termiche e meccaniche sulla geostruttura; (iii) la comprensione del comportamento della geostruttura su scala reale, includendo aspetti legati all'esecuzione dei test in-situ ed il monitoraggio termomeccanico. Per affrontare tali sfide, questa tesi di dottorato si è avvalsa di tecniche sperimentali, numeriche ed analitiche. In primo luogo, sono presentati gli aspetti fondamentali caratterizzanti il comportamento termomeccanico e quello idrotermico legato alla prestazione termica. In secondo luogo, viene sviluppato il tema della progettazione termica preliminare, presentando una metodologia di progetto basata su un diagramma di flusso. In terzo luogo, viene proposto l'unico modello analitico disponibile, capace di considerare combinazioni di carichi termomeccanici assiali e flettenti. Tale modello viene applicato a vari esempi riguardanti le geostrutture energetiche. Infine, vengono presentati i dettagli di una campagna sperimentale, in-situ, legata al comportamento di un muro energetico facente parte di una stazione ferroviaria sotterranea ubicata a Ginevra (CH). Sono trattati i seguenti aspetti: l'esecuzione di (i) un test di risposta termica (TRT) e successivi (ii) test di riscaldamento/raffrescamento, includendo dettagli relativi all'esecuzione pratica, il monitoraggio termomeccanico e l'interpretazione dei dati; (iii) la determinazione del potenziale termico dell'intera installazione geotermica. I risultati principali di questo lavoro sono i seguenti: (a) il comportamento termico dell'infrastruttura energetica sotterranea è caratterizzato da importanti interazioni termiche con gli ambienti circostanti (e.g., interfacce struttura-aria); (b) la distribuzione di variazione di temperatura nella geostruttura indotta dal funzionamento geotermico è non uniforme. Gli effetti meccanici indotti nella geostruttura includono, quindi, effetti meccanici assiali e flessionali; (c) viene proposta una procedura modificata per l'esecuzione di TRT nei muri, rispetto alle linee guida esistenti. Tale procedura consente di considerare gli aspetti idrotermici non trascurabili che si verificano all'interno e nelle vicinanze della geostruttura energetica; (d) la campagna sperimentale effettuata al sito di Ginevra

ha rivelato un ottimo potenziale per lo stoccaggio di energia termica ed un potenziale di estrazione leggermente inferiore, a causa dell'influenza delle condizioni al contorno termiche.

## Parole chiave

Energia rinnovabile; Sostenibilità; Infrastrutture energetiche sotterranee; Prestazione termica; Comportamento idrotermico; Comportamento termomeccanico; Modellazione analitica; Interazione terreno-struttura; Modellazione numerica; Analisi non-isotermica; Test in-situ; Test di risposta termica;

# Contents

<b>Acknowledgements .....</b>	<b>iii</b>
<b>Abstract .....</b>	<b>v</b>
<b>Keywords.....</b>	<b>vi</b>
<b>Resumé.....</b>	<b>vii</b>
<b>Mots-clé.....</b>	<b>viii</b>
<b>Riassunto .....</b>	<b>ix</b>
<b>Parole chiave .....</b>	<b>x</b>
<b>List of Figures .....</b>	<b>xvi</b>
<b>List of Tables .....</b>	<b>xxiii</b>
<b>List of Symbols.....</b>	<b>xxv</b>
<b>Chapter 1 Introduction .....</b>	<b>29</b>
1.1 General context of the thesis .....	29
1.2 Scientific challenges.....	29
1.3 Contributions and structure of the thesis .....	31
<b>Part 1 : Thermal behavior.....</b>	<b>33</b>
<b>Chapter 2 Fundamentals on thermal efficiency and mechanical behaviour of an energy wall and slab.....</b>	<b>35</b>
2.1 Foreword .....	35
2.2 Introduction .....	35
2.3 Finite Element Modelling of Energy Wall and Slab .....	37
2.3.1 Features of the 3D Finite Element models .....	38
2.3.2 Boundary and initial conditions .....	40
2.3.3 Description of the materials .....	40
2.4 Thermal behavior of different design solutions.....	41
2.4.1 Effect of fluid velocity in the pipes .....	41
2.4.2 Comparing pipe spacing and layout effects .....	44
2.4.3 Activation of the base slab .....	48



2.5	Thermally Induced Mechanical Effects.....	50
2.6	Conclusions.....	57
<b>Chapter 3</b>	<b>Hydrothermal interactions in energy walls.....</b>	<b>59</b>
3.1	Foreword.....	59
3.2	Introduction.....	59
3.3	Numerical modelling of hydrothermal behaviour of EWs .....	61
3.3.1	Mathematical formulation.....	62
3.3.2	Material characterisation.....	65
3.3.3	3D model; boundary and initial conditions .....	66
3.4	Results.....	67
3.4.1	Groundwater flow perpendicular to the infrastructure .....	69
3.4.2	Groundwater flow parallel to the infrastructure .....	71
3.5	Conclusions.....	73
<b>Chapter 4</b>	<b>Early-stage thermal performance design of thermo-active walls implemented in underground energy infrastructures.....</b>	<b>77</b>
4.1	Foreword.....	77
4.2	Introduction.....	78
4.3	Materials and methods .....	79
4.3.1	Hydro-thermal phenomena involved with thermo-active walls .....	79
4.3.2	Features of the numerical analyses .....	79
4.3.3	Material properties of the involved materials .....	84
4.3.4	Definition and choice of the thermal input .....	85
4.4	Results and discussion.....	86
4.4.1	Thermal behaviour of the energy geostructure in different environmental conditions .....	88
4.4.2	Effect of the thermal characteristics of the structure.....	91
4.5	A flowchart for the early-stage thermal performance design .....	92
4.5.1	Analytical solution and Péclet number for steady flux calculations .....	93
4.5.2	Proposition of a flowchart for early-stage thermal performance design .....	95
4.6	Conclusions.....	96
<b>Part 2</b>	<b>Thermomechanical behavior .....</b>	<b>99</b>
<b>Chapter 5</b>	<b>Extension of Winkler’s solution to non-isothermal conditions for capturing the behaviour of plane geostructures subjected to thermal and mechanical actions.....</b>	<b>101</b>
5.1	Foreword.....	101
5.2	Introduction.....	101
5.3	Analytical model for plane geostructures subjected to thermal and mechanical actions.....	103

5.3.1	Fundamentals .....	103
5.3.2	Influence of thermal and mechanical actions on plane geostructures .....	104
5.3.3	Degree of freedom: definition for axial and flexural actions .....	105
5.3.4	The analytical model.....	107
5.3.5	Analysis of simple plane geometries.....	109
5.3.6	Analysis of complex plane geometries .....	111
5.3.7	Boundary conditions .....	111
5.3.8	Modulus of subgrade reaction.....	112
5.4	Application and validation of the analytical model – simple plane geometries .....	113
5.4.1	General.....	113
5.4.2	The problem.....	113
5.4.3	Comparison between analytical and numerical modelling results .....	114
5.4.4	Considerations about axial and flexural effects caused by thermal actions .....	118
5.5	Application and validation of the analytical model – complex plane geometries .....	118
5.5.1	General.....	118
5.5.2	The problem.....	118
5.5.3	Analysis approach.....	119
5.5.4	Calibration of boundary conditions.....	120
5.5.5	Comparison between analytical and numerical modelling results .....	126
5.6	Concluding remarks .....	130
<b>Chapter 6</b>	<b>Analytical modelling of energy geostructures: applications and advanced analytical models</b>	<b>133</b>
6.1	Introduction.....	133
6.2	Applications of the Winkler model in non-isothermal conditions to energy geostructures.....	133
6.2.1	Laterally loaded energy pile.....	133
6.2.2	Application to a complex plane geometry: the three-span continuous beam .....	144
6.2.3	Partly embedded energy wall.....	152
6.3	Extension of the two-parameters soil model to non-isothermal conditions.....	156
6.3.1	General.....	156
6.3.2	The problem.....	158
6.3.3	Results and discussions.....	159
6.3.4	Concluding remarks .....	161
6.4	Extension of the linearly varying reaction modulus model to non-isothermal conditions .....	162
6.4.1	General.....	162
6.4.2	The problem.....	163

6.4.3	Validation.....	165
6.4.4	Results and discussions .....	166
6.4.5	Concluding remarks .....	170
<b>Part 3 : In-situ testing.....</b>		<b>173</b>
<b>Chapter 7</b>	<b>Thermal Response Testing on an underground thermo-active train station in Switzerland</b>	<b>175</b>
7.1	Foreword .....	175
7.2	Introduction .....	175
7.2.1	Energy geostructures implemented at the CEVA Lancy-Bachet underground train station (Geneva, Switzerland) .....	177
7.3	Materials and methods .....	179
7.3.1	Details on the experimental setup .....	179
7.3.2	Features of the numerical analyses .....	181
7.4	Results and discussion.....	183
7.4.1	Experimental results.....	183
7.4.2	Numerical modelling: calibration, validation and interpretation of the experimental results	186
7.5	Is TRT suitable for underground energy infrastructures?.....	191
7.6	Concluding remarks .....	192
<b>Chapter 8</b>	<b>On the determination of the thermo-hydro-mechanical behavior and the quantification of thermal potential of an underground energy infrastructure .....</b>	<b>195</b>
8.1	Foreword .....	195
8.2	Introduction .....	195
8.3	Hydrothermal behavior .....	197
8.3.1	Tunnel behavior .....	197
8.3.2	Definition of the yearly temperature profiles at the environments in the vicinity of the underground energy infrastructure .....	201
8.3.3	Thermal activation tests .....	202
8.3.4	Wall intrados temperature and wall-tunnel interactions.....	209
8.3.5	Numerical modelling: validation against experimental results and interpretation of the results	212
8.4	Thermomechanical behavior .....	220
8.4.1	Determination of the temperature distribution in the wall .....	220
8.4.2	Thermomechanical behavior of the energy wall .....	227
8.5	Main observations and outcomes from the in-situ activities .....	236
8.6	Determination of the thermal potential of the underground energy infrastructure .....	237
8.6.1	Definition of the design parameters and of the analysis tools.....	237
8.6.2	Definition of the elementary unit and upscaling to the entire installation's behavior .....	238
8.6.3	Determination of the thermal potential .....	240

8.6.4	Comments on the thermal behavior for the four scenarios .....	249
8.7	Concluding remarks .....	255
<b>Chapter 9</b>	<b>Conclusions and perspectives .....</b>	<b>257</b>
9.1	Main conclusions .....	257
9.2	Perspectives.....	260
<b>References.....</b>		<b>261</b>
<b>Appendix A</b>	<b>Mathematical formulation of the numerical models.....</b>	<b>273</b>
<b>Appendix B</b>	<b>Method of initial conditions .....</b>	<b>275</b>
<b>Appendix C</b>	<b>Determination of the modulus of subgrade reaction for horizontal foundations .....</b>	<b>277</b>
<b>Appendix D</b>	<b>Description of the numerical model employed in Chapter 5 .....</b>	<b>278</b>
<b>Appendix E</b>	<b>Additional features for the numerical model employed in Chapter 8 .....</b>	<b>281</b>
<b>Curriculum Vitae.....</b>		<b>283</b>

## List of Figures

Figure 2.1. Sketch of the considered geometry at a vertical cross section in correspondence of the heat exchangers .....	38
Figure 2.2. Finite element model and boundary conditions .....	39
Figure 2.3. Pipe layouts analyzed, from left to right: W, Slinky 1, Slinky 2 with indication of the pipe spacing, $a$ . ....	39
Figure 2.4. Temperature ( $^{\circ}\text{C}$ ) profile contour map of the EG and the soil around it at steady flux conditions.....	42
Figure 2.5. Variations in the thermal power extracted from different fluid velocities over different time spans .....	43
Figure 2.6. Embedded pipe length per square meter of wall for each situation analyzed	45
Figure 2.7. Axial temperature distribution inside the wall in steady-state conditions	45
Figure 2.8. Thermal power extracted over time for different design configurations	46
Figure 2.9. Comparison of thermal power extracted at selected time points for different design configurations .....	47
Figure 2.10. (a) Axial temperature distribution in the slab, and (b) fluid temperature distribution in the pipes in the slab and the wall at selected time points .....	49
Figure 2.11. Thermal power extracted from the wall and the slab.....	50
Figure 2.12 Thermally induced vertical displacements in the EW. (a) results for the pipe layout comparison. Results for the pipe spacing comparison: (b) $a = 0.2\text{ m}$ ; (c) $a = 0.3\text{ m}$ ; (d) $a = 0.4\text{ m}$ ; (e) $a = 0.5\text{ m}$ ; (f) $a = 0.75\text{ m}$ .....	53
Figure 2.13. Thermally induced (a) horizontal and (b) vertical displacements: top row relates to the wall and bottom row to the slab.....	54
Figure 2.14. Thermally induced internal actions: (a) axial force, (b) shear force and (c) bending moment. Top row relates to the wall and bottom row to the slab .....	55
Figure 2.15. Axial stresses developed in the wall at different depths, at steady flux	56
Figure 3.1 3D model, indicators of groundwater flow directions and boundary conditions: 1- Left; 2- Rear; 3- Right; 4- Front; 5- Bottom; 6- Top .....	61
Figure 3.2 Cross section of the infrastructure (Note: the figure is not scaled, dimensions in metres).....	62
Figure 3.3 Temperature-dependent water properties: (a) Density, (b) Dynamic viscosity, (c) Thermal conductivity, (d) Heat capacity .....	65
Figure 3.4 Pipe loop configuration and numbering (Note: zoom-in as indicated in Figure 3.4) .....	66
Figure 3.5 2D model of a fully saturated porous medium heated from the side (adapted from Nield & Bejan, 2006) .....	68
Figure 3.6 (a) Contour plot of the vertical component of the groundwater velocity ( $v_{w,z}$ ) zoomed in the vicinity of the geostructure; (b) Zoomed-in image of selected zones with arrows indicating the groundwater velocity vector for wall heating (left) and cooling (right) .....	69
Figure 3.7 Temperature contour plot for groundwater flow perpendicular to the infrastructure with flownet: streamlines (light blue) and equipotential lines of the hydraulic head ( $H$ , grayscale) .....	70

Figure 3.8 Temperature contour plot for groundwater flow parallel to the infrastructure with flownet: streamlines (light blue) and equipotential lines of the hydraulic head [m] (greyscale). (a) winter operation, (b) summer operation, (c) zoom-in image of selected zones. ....	71
Figure 3.9 Variation in the y (a) and z (b) components of the groundwater velocity vector evaluated at the wall–soil interface with the average temperature difference. ....	72
Figure 3.10 Evolution of the power extraction/injection of adjoining pipe loops with time for different values of groundwater velocity. The pipe loops are numbered as in Figure 3.4. ....	73
Figure 4.1 View of the 3D model with indications of the boundaries: 1-left; 2-rear; 3-right; 4-front; 5-bottom; 6-top .....	80
Figure 4.2 Model performance test: simulation of the Shanghai test (Xia et al., 2012) including a comparison among the experimental data and the numerical results ...	81
Figure 4.3 Cross section view with indication of the boundaries (NOTE: the figure is not scaled) .....	82
Figure 4.4 Thermal response of a heat exchange loop at steady flux varying the inflow temperature input. ....	86
Figure 4.5 Applied thermal input with indication of the heat transfer conditions ..	87
Figure 4.6 Power extraction/injection rate of adjoining pipe loops in the case of groundwater flow parallel to the wall .....	89
Figure 4.7 Charts for groundwater flow parallel to the wall .....	90
Figure 4.8 Charts for groundwater flow perpendicular to the wall .....	90
Figure 4.9 Charts with dependency on concrete thermal conductivity for groundwater flow parallel to the wall.....	92
Figure 4.10 Charts with dependency on concrete thermal conductivity for groundwater flow perpendicular to the wall.....	92
Figure 4.11 Porous medium heated from the side, 3D case (a) and 2D sketch (b). ..	93
Figure 4.12 Evaluation of Péclet number with groundwater flow velocity for (a) parallel and (b) perpendicular groundwater flow with respect to the wall.....	95
Figure 4.13 Flowchart for early-stage thermal performance design of energy walls	96
Figure 5.1 Idealised schematic of the temperature variation within the cross-section of a plane geostructure interfacing, from one side, the air, and from the other side, the ground. The considered schematic can refer to a slab resting on the ground or to the exposed portion of a retaining wall. $\Delta T_1$ and $\Delta T_2$ refer to the temperature variations at the geostructure-air and geostructure-soil interfaces, respectively. ....	105
Figure 5.2 Qualitative development of deformations and internal actions caused by (a) constant and (b) linear distribution of temperature variations in a geostructure: (A) free case, (B) completely restrained case, (C) partly restrained case with significant prevention of deformations, and (D) less restrained case with less significant prevention of deformations.....	107
Figure 5.3 Schematic of (a) the equilibrium of a beam element of length $dx$ and (b) the geometric decomposition of shear actions. ....	108
Figure 5.4 Examples of simple plane geometries characterised by different boundary conditions: (a) hinged, (b) fixed and (c) partly restrained.....	110
Figure 5.5 Example of (a) a complex plane geometry (i.e., a cut-and-cover tunnel) and (b) a related geometrical decomposition approach into four simple plane geometries	111

Figure 5.6 Thermo-mechanical response of a geostructure resting on different soil conditions and subjected to a linear distribution of temperature variation: comparison between analytical and numerical models.....	115
Figure 5.7 Determination of structural rotational stiffness: (a) fixed case, (b) hinged case, (c) partly restrained case. Determination of the soil-structure interaction rotational stiffness: (d) first estimation and (e) final estimation.....	122
Figure 5.8 Relationship between the dimensionless rotational boundary stiffness and the beam geometry that can be used to calibrate the rotational boundary condition ..	123
Figure 5.9 (a) Components to be considered for the evaluation of the transversal stiffness boundary condition. Determination of the structural transversal stiffness at the connections: (b) fixed case, (c) hinged case, (d) partly restrained case. Determination of the soil-structure interaction transversal stiffness: (e) first estimation and (f) final estimation.....	125
Figure 5.10 Relationship between the dimensionless transversal boundary stiffness and the beam geometry that can be used to calibrate the transversal boundary condition	126
Figure 5.11 Response of a cut-and-cover structure with $L/H=1$ subjected to thermal and mechanical loading to the bottom beam only: deflection .....	127
Figure 5.12 Response of a cut-and-cover structure with $L/H=1$ subjected to thermal and mechanical loading to the bottom beam only: rotation .....	128
Figure 5.13 Response of a cut-and-cover structure with $L/H=1$ subjected to thermal and mechanical loading to the bottom beam only: bending moment.....	129
Figure 5.14 Response of a cut-and-cover structure with $L/H=1$ subjected to thermal and mechanical loading to the bottom beam only: shear force.....	130
Figure 6.1 Scheme of the modelled problem: the transversally loaded EP.....	135
Figure 6.2 Comparison between the analytical results presented in this study with the ones proposed by Wood, 2004 .....	137
Figure 6.3 Thermomechanical behaviour of an energy pile subjected to unitary thermal and mechanical loads, the selected static scheme is fixed (i.e., $k_{head} = k_{base}$ ).....	140
Figure 6.4 Differences between the mechanical only case and the thermomechanical one presented in Figure 6.3.....	140
Figure 6.5 Thermomechanical behaviour of an energy pile subjected to unitary thermal and mechanical loads, the selected static scheme is intermediate (i.e., $k_{head} \ll k_{base}$ ).....	141
Figure 6.6 Differences between the mechanical only case and the thermomechanical one presented in Figure 6.5 .....	141
Figure 6.7 Thermomechanical behaviour of an energy pile subjected to thermal and mechanical loads, the selected static scheme is fixed (i.e., $k_{head} = k_{base}$ ).....	143
Figure 6.8 Differences between the mechanical only case and the thermomechanical one presented in Figure 6.7 .....	143
Figure 6.9 Thermomechanical behaviour of an energy pile subjected to thermal and mechanical loads, the selected static scheme is intermediate (i.e., $k_{head} \ll k_{base}$ ).....	143
Figure 6.10 Differences between the mechanical only case and the thermomechanical one presented in Figure 6.9.....	144
Figure 6.11 Schematic view of a beam composed by three consecutive spans resting on a spring foundation and bounded by rotational and transversal springs. ....	145
Figure 6.12 Results for the parametric analysis on $ks$ .....	148
Figure 6.13 Results for the parametric analysis on $ks_2$ and $L_2$ for (a) low $L_2$ length and (b) high $L_2$ length .....	149

Figure 6.14 Results for the parametric analysis on $EI$ : (a) parametric study on $s$ ; (b) highlight for the case $s \rightarrow +\infty$ .....	150
Figure 6.15 Results for the parametric analysis on $EI2$ and $L2$ for (a) low $L2$ length and (b) high $L2$ length .....	151
Figure 6.16 Geometry of the partly embedded wall.....	153
Figure 6.17 Results for the partly embedded wall: analytical results compared with numerical ones .....	155
Figure 6.18 Sketch of a beam lying on a two parameters soil model.....	157
Figure 6.19 Sketch of the elementary unit employed for the two parameters soil model analysis.....	158
Figure 6.20 Results for the analysis employing the two-parameters soil model: the dotted lines represent the results employing the two-parameters soil model for the cases described in Table 6.6, the continuous line represents the results for the case $Gp \rightarrow 0$ which corresponds to the Winkler model .....	161
Figure 6.21 Sketch of the problem: a vertical beam laying on a linearly varying subgrade reaction modulus subjected to a linear distribution of temperature variation along the beam axis and to concentrated shear and bending actions at his head.....	163
Figure 6.22 Comparison among the analytical, numerical results and the ones available in the literature. The results for the application of a concentrated shear force are denoted with $F$ , while the results for the application of a concentrated bending moment are denoted with $W$ .....	166
Figure 6.23 Results for the parametric analysis for the beam on a linearly varying subgrade reaction modulus .....	167
Figure 6.24 Particular over the results for the free static scheme .....	169
Figure 6.25 Particular over the results for the partly constrained static scheme ...	170
Figure 7.1 Plan view of the new railway line with location of the UEI at Lancy-Bachet (source: <a href="http://www.ceva.ch/">www.ceva.ch/</a> ).....	177
Figure 7.2 Cross section of the Lancy-Bachet underground train station with indication of the heat exchanger locations .....	178
Figure 7.3 Details of the equipment at: (a) level -1; (b) level -2; (c) temperature sensor and anemometer at position -2A; (d) temperature sensor and anemometer at position -2B; (e) partial view of the strain gauges.....	181
Figure 7.4 Geometry of the numerical model with indication of the boundary conditions .....	182
Figure 7.5 Experimental data from the TRT Module (fluid temperature and thermal power) with fitting of the numerical results .....	184
Figure 7.6 Experimental data for temperature and wind velocity during the test execution .....	185
Figure 7.7 Comparison among temperature recorded by the strain gauges and by the temperature sensors.....	186
Figure 7.8 Temperatures of the air boundary conditions used for the numerical model initialization .....	187
Figure 7.9 Temperature contour plot (a-d) with indication of the heat flux at the EW intrados and extrados (b,c,d only) for the following time steps: (a) before the test, (b) after 1 day of test, (c) at the end of the transient phase and (d) at the end of the test....	190
Figure 7.10 Magnitude of the heat flux at the wall intrados and extrados .....	190



Figure 7.11 Comparison among numerical (a,b) and experimental (c,d) results related to the wall intrados temperature: (a) numerical temperature contour plot at the wall intrados on date 21/08/2019, (b) numerical contour plot at the wall intrados on date 29/08/2019, (c) thermal photo taken on date 21/08/2019, at level -2B, (d) thermal photo taken on date 29/08/2019, at level -2B.....	191
Figure 8.1 Tunnel air temperature profile and wind velocity from summer to winter behavior.....	198
Figure 8.2 Tunnel air temperature profile and wind velocity: zoom-in to analyze the winter behavior.....	199
Figure 8.3 Analysis of the wind speed: (a) behavior before and after the beginning of train circulation; (b) behavior during few days after train circulation, definition of the differences between day and night behaviors; (c) zoom-in at three different times during a typical day and correlations between the measurements and the train passages .....	200
Figure 8.4 Temperature profile with wall height during winter.....	201
Figure 8.5 Cross section with indication of the location of the heat pump.....	203
Figure 8.6 HP behavior zoomed during some cycle type (data related to the test performed in December 2019).....	205
Figure 8.7 HP behavior during the test performed in December 2019 .....	205
Figure 8.8 HP behavior zoomed during some cycle type (data related to the test performed in February 2020).....	206
Figure 8.9 HP behavior during the test performed in February 2020 .....	207
Figure 8.10 HP behavior zoomed during some cycle type (data related to the test performed in March 2020).....	208
Figure 8.11 HP behavior during the test performed in March 2020 .....	209
Figure 8.12 Analysis of the thermal camera photos taken at the end of the heating test performed in December 2019: (a) thermal camera photo taken at level -2B, (b) thermal camera photo taken at level -2B (zoomed image), (c) intrados temperature profile from numerical analysis. NOTE: the red coloured vertical bars at (a) are neon lights which are impossible to shut down, as they represent the only lighting system of the underground train station.....	210
Figure 8.13 Analysis of the thermal camera photos taken at the end of the heating test performed in February 2020: (a) thermal camera photo taken at level -2B, (b) thermal camera photo taken at level -2A, (c) zoomed-in image taken at level -2B, (d) intrados temperature profile from numerical analysis. NOTE: the red coloured vertical bars at (a) and (b) are neon lights which are impossible to shut down, as they represent the only lighting system of the underground train station.....	211
Figure 8.14 Analysis of the thermal camera photos taken at the end of the cooling test performed in March 2020: (a) thermal camera photo taken at the bottom part of level -2B, (b) thermal camera photo taken at the top part of level -2B, (c) intrados temperature profile from numerical analysis. NOTE: the red coloured vertical bars at (a) and (b) are neon lights which are impossible to shut down, as they represent the only lighting system of the underground train station .....	212
Figure 8.15 Temperature profile (from numerical analyses) within and around the UEI determined by the application of the tunnel, technical room and external boundary conditions: (a) summer; (b) winter.....	214
Figure 8.16 Contour plot of the temperature profile of the cross section in correspondence of the heat exchangers with indication (i.e., arrows) of the heat flux vectors at the intrados and extrados for the December 2019 heating test: (a) before the start of the test; (b) after 1 day of test; (c) after one week of test; (d) at the end of the test .....	216

Figure 8.17 Magnitude of the heat flux at the intrados and extrados during the December 2019 heating test .....	216
Figure 8.18 Contour plot of the temperature profile of the cross section in correspondence of the heat exchangers with indication (i.e., arrows) of the heat flux vectors at the intrados and extrados for the February 2020 heating test: (a) before the start of the test; (b) after 1 day of test; (c) after one week of test; (d) at the end of the test .....	217
Figure 8.19 Magnitude of the heat flux at the intrados and extrados during the February 2020 heating test .....	217
Figure 8.20 Contour plot of the temperature profile of the cross section in correspondence of the heat exchangers with indication (i.e., arrows) of the heat flux vectors at the intrados and extrados for the March 2020 cooling test: (a) at the extrados, before the start of the test; (b) at the extrados, after 1 day of test; (c) at the extrados, at the end of the test; (d) at the intrados, before the start of the test; (e) at the intrados, after one day of test; (f) at the intrados, at the end of the test.....	219
Figure 8.21 Magnitude of the heat flux at the intrados and extrados during the March 2020 cooling test .....	220
Figure 8.22 Determination of the temperature distribution (values in °C) in the EW. For the December 2019 heating test: (a) portion exposed to air; (b) fully embedded portion. For the February 2020 heating test: (c) portion exposed to air; (d) fully embedded portion. For the March 2020 cooling test: (e) portion exposed to air; (f) fully embedded portion. NOTE: figures are not scaled.....	222
Figure 8.23 Schematic view of the model geometry.....	224
Figure 8.24 Results for the modelling of wall temperature through FD model, and comparison with numerical and experimental results: simulation of the December 2019 heating test .....	225
Figure 8.25 Results for the modelling of wall temperature through FD model, and comparison with numerical and experimental results: simulation of the February 2020 heating test .....	226
Figure 8.26 Results for the modelling of wall temperature through FD model, and comparison with numerical and experimental results: simulation of the March 2020 cooling test .....	226
Figure 8.27 Mechanical behavior of the wall intrados facing the tunnel: experimental results. The figure includes results from the following in-situ tests: TRT (August 2019, details at section 7.4.1, indicated as $\Delta T = +20^{\circ}\text{C}$ ), heating tests (December 2019, indicated as $\Delta T = +40^{\circ}\text{C}$ , and February 2020, indicated as $\Delta T = +30^{\circ}\text{C}$ ), cooling test (March 2020, indicated as $\Delta T = -10^{\circ}\text{C}$ ) .....	228
Figure 8.28 Sketch of the longitudinal deformed shape: plan view of the -2 level. NOTE: the figure is not scaled .....	229
Figure 8.29 Sketch of the vertical deformed shape at a vertical cross section. NOTE: the figure is not scaled .....	229
Figure 8.30 Evaluation of deflection and internal actions through the analytical model proposed at section 6.2.3 featuring for thermal loads only (positive signs of rotation and internal actions refer to Figure 6.16).....	230
Figure 8.31 Comparison among the experimental and numerical results for the heating (December 2019) and cooling (March 2020) tests.....	231
Figure 8.32 Sketch of the geostructural geometry over a vertical cross section in correspondence of the heat exchangers with indications of the mechanical loads detailed in Table 8.3.....	232

Figure 8.33 Wall axis vertical and horizontal displacement at SLS: results from 3D numerical thermomechanical model .....	234
Figure 8.34 Internal actions in the wall at ULS: results from 3D numerical thermomechanical model .....	235
Figure 8.35 Sketch of one elementary unit featuring 8 wall U-loops and one slinky-shaped slab loop, connected in parallel.....	239
Figure 8.36 Yearly dimensionless thermal demand curves.....	241
Figure 8.37 Temperature evaluated at the points A to F indicated in Figure 8.5 for case 1 .....	242
Figure 8.38 Heat carrier fluid temperature for case 1 .....	243
Figure 8.39 Details of the thermal demand curve for offices and apartments after a dedicated literature review .....	244
Figure 8.40 Temperature evaluated at the points A to F indicated in Figure 5 for case 2 .....	245
Figure 8.41 Heat carrier fluid temperature for case 2 .....	245
Figure 8.42 Temperature evaluated at the points A to F indicated in Figure 8.5 for case 3 .....	246
Figure 8.43 Heat carrier fluid temperature for case 3 .....	247
Figure 8.44 Temperature evaluated at the points A to F indicated in Figure 5 for case 4 .....	248
Figure 8.45 Heat carrier fluid temperature for case 4 .....	248
Figure 8.46 Comparison of the monthly energy delivered among the four scenarios	250
Figure 8.47 Summary of the annual energy delivered for the four scenarios .....	250

## List of Tables

Table 2.1. Material properties .....	41
Table 2.2. Parametric analysis of the fluid flow velocity in the pipes .....	41
Table 2.3. Thermal performance of different pipe configuration at steady state ....	48
Table 3.1 Material properties .....	65
Table 3.2 Boundary conditions for groundwater flow perpendicular to the wall, where $H$ represents the total hydraulic head, $n$ is the unitary outflow normal vector to the selected surface, and $q$ is the heat flux (Note: “b.c.” stands for boundary condition).....	67
Table 4.1 - Thermal and hydraulic boundary conditions (the numbered boundaries refer to Figure 4.1, Figure 4.3 and Table 4.2).....	81
Table 4.2 Boundary conditions at the wall-air interfaces (the boundary conditions names refer to Figure 4.3) .....	83
Table 4.3 Configurations used for the boundary conditions comparison.....	84
Table 4.4 Material properties .....	85
Table 4.5 Ranges of values for the studied parameters.....	87
Table 5.1 Boundary conditions for selected cases .....	112
Table 5.2 Determination of $k_s$ from empirical formulations .....	113
Table 5.3 Input parameters for the modelling of the considered problem .....	114
Table 5.4 Steps for resolving the cut-and-cover structure employing the proposed analytical model.....	120
Table 6.1 Input parameters for the comparison with the analytical solution available in Wood, 2004.....	136
Table 6.2 Input parameters for the evaluation of the pile behavior under unitary loads .....	139
Table 6.3 Input parameters for the evaluation of the pile behavior subjected to a worst-case scenario loading condition .....	142
Table 6.4 Input parameters for the parametric analyses.....	147
Table 6.5 Input parameters for the study of the partly embedded wall.....	154
Table 6.6 Input material properties for the analyses reported in this section.....	159
Table 6.7 Input parameters for the analyses of a beam on a two-parameters soil model .....	160
Table 6.8 Input parameters for the analyses of a beam on a linearly-varying subgrade reaction soil model for the validation against literature and numerical results.....	165
Table 6.9 Input parameters for the parametric analyses of a beam on a linearly varying subgrade reaction soil model.....	167
Table 7.1 Details of the sensors employed in the experimental setup for monitorin level -2 .....	180
Table 7.2 Evaluation of thermal conductivity for concrete and soil: determination of soil thermal conductivity to best match the experimental results for a given concrete thermal conductivity.....	188
Table 8.1 Determination of the temperature yearly profiles for each boundary condition .....	202
Table 8.2 Input parameters used for the FD model.....	225

Table 8.3 Description of the mechanical loads considered for the thermomechanical analysis.....	233
Table 8.4 Summary of the thermal behavior for the first scenario: Case 1.....	252
Table 8.5 Summary of the thermal behavior for the first scenario: Case 2.....	252
Table 8.6 Summary of the thermal behavior for the first scenario: Case 3.....	253
Table 8.7 Summary of the thermal behavior for the first scenario: Case 4.....	253

# List of Symbols

Symbol	Name	Unit
<b>Roman symbols</b>		
$a$	Pipe spacing	m
$A$	Surface area	m <sup>2</sup>
$A_{PIPE}$	Cross section of the pipe	m <sup>2</sup>
$A_w$	Surface area of the wall	m <sup>2</sup>
$b$	Width of the beam	m
$Bi$	Biot number	
$c_f$	Concrete cover	m
$COP$	Coefficient of performance	
$C_p$	Heat capacity at constant pressure	$\frac{J}{kg\ K}$
$d_{h,th}$	Thermally induced horizontal displacement	m
$d_{v,th}$	Thermally induced vertical displacement	m
$DOF$	Degree of freedom	
$DOF_a$	Axial degree of freedom	
$DOF_c$	Curvature degree of freedom	
$E$	Young Modulus	Pa
$E_{he}$	Effectiveness of the heat exchangers	
$E_{th}$	Thermal energy	kWh
$f_D$	Friction factor	
$Fo$	Fourier number	
$f_{th}$	Dimensionless thermal power demand	
$g$	Gravity acceleration	m/s <sup>2</sup>
$G_p$	Modulus of the virtual shear layer	N/m
$h$	Height of the beam	m
$H$	Hydraulic head	m
$h_{c,i}$	Convective coefficient	$\frac{W}{m^2\ K}$
$h_{raft}$	Raft height	m
$H_{wall}$	Wall height	m
$I$	Moment of inertia	m <sup>4</sup>
$k^*$	Geometric permeability	m <sup>2</sup>

$k_{base}$	Base restraint stiffness	N/m
$k_{head}$	Head restraint stiffness	N/m
$k_{r,i}$	Rotational spring stiffness	N/m
$k_s$	Subgrade reaction modulus	N/m <sup>3</sup>
$k_{v,i}$	Vertical spring stiffness	N/m
$L$	Length	m
$L_{PIPE}$	Pipe length	m
$L_{raft}$	Raft length	m
$L_{tunnel}$	Tunnel length	m
$M_b^{th}$	Blocked thermally induced bending moment	kNm
$M_o^{th}$	Observed thermally induced bending moment	kNm
$M^{th}$	Thermally induced bending moment	kNm
$M(x)$	Bending moment	kNm
$n$	Porosity	
$\mathbf{n}$	Outflow unitary normal vector	
$N_b^{th}$	Blocked thermally induced axial force	kN
$n_{EU}$	Number of elementary units	
$N_o^{th}$	Observed thermally induced axial force	kN
$N^{th}$	Thermally induced axial force	kN
$Nu$	Nusselt number	
$P$	Transversal concentrated load	kN
$Pe$	Péclet number	
$Pr$	Prandtl number	
$p_s$	Phase shift	
$P_{th}$	Delivered thermal power	W
$P_{th,S}$	Thermal power of the primary circuit	W
$p_w$	Pore water pressure	Pa
$q$	External distributed load	kN/m
$\dot{q}$	Heat flux	W/m <sup>2</sup>
$\dot{q}_{bc,i}$	Heat flux boundary condition	W/m <sup>2</sup>
$\dot{q}_p$	Heat flux per unit length through the pipe wall	W/m
$Q_{th}$	Thermal power	W
$Q_{th,f}$	Thermal power from the heat exchangers	W
$Re$	Reynolds number	

$t$	Time	s
$T$	Temperature	°C
$T_{amb}$	Solid temperature at convective boundary	°C
$T_c$	Concrete temperature	°C
$T_{EG}$	Energy geostructure temperature	°C
$T_{f,in}$	Fluid inflow temperature	°C
$T_{f,out}$	Fluid outflow temperature	°C
$T_{ref}$	Reference temperature	°C
$T_s$	Soil temperature	°C
$T_{S-W}$	Wall-soil interface temperature	°C
$t_{wall}$	Wall thickness	m
$\dot{u}_x$	Velocity of fluid moving in the x direction	m/s
$V(x)$	Shear force	kN
$v_f$	Fluid velocity	m/s
$\dot{V}_f$	Flowrate	l/min
$V_n$	Component of the shear force normal to the neutral axis	kN
$\mathbf{v}_{rw}$	Groundwater velocity vector	m/d
$V^{th}$	Thermally induced shear force	kN
$V_v$	Vertical component of the shear force at undeformed conditions	kN
$v_w$	Wind velocity	m/s
$W$	Concentrated bending moment	kNm
$x$	x-xoordinate	m
$y$	y-coordinate	m
$y_n$	Distance from neutral axis	m
$y(x)$	Deflection	m
$z$	Depth, vertical z-coordinate	m

---

#### Greek symbols

$\alpha$	Thermal expansion coefficient	1/K
$\alpha_{th}$	Thermal diffusivity	m <sup>2</sup> /s
$\gamma_w$	Water unit weight	N/m <sup>2</sup>
$\Delta T_a$	Uniform distribution of temperature variation	°C
$\Delta T_c$	Linear distribution of temperature variation	°C
$\Delta T_f$	Temperature difference of the fluid between the inflow and the outflow	°C



$\varepsilon_f^{th}$	Free thermally induced deformation	
$\varepsilon_h$	Longitudinal deformation	
$\varepsilon_o^{th}$	Observed thermally induced deformation	
$\boldsymbol{\varepsilon}_{kl}$	Deformation tensor	
$\varepsilon_v$	Vertical deformation	
$\theta$	Rotation	rad
$\lambda$	Thermal conductivity	$\frac{\text{W}}{\text{m K}}$
$\lambda L$	Characteristic length	m
$\mu_{PIPE}$	Density of installed pipes	m/m <sup>2</sup>
$\mu_w$	Dynamic viscosity of water	Pa s
$\nu$	Poisson's ratio	
$\rho_f$	Density of the fluid phase	kg/m <sup>3</sup>
$\rho_s$	Density of the solid phase	kg/m <sup>3</sup>
$\rho_w$	Density of water	kg/m <sup>3</sup>
$\boldsymbol{\sigma}_{ij}$	Total stress tensor	Pa
$\sigma_n$	Stress normal to the neutral axis	Pa
$\sigma_{v,th}$	Thermally induced vertical stress	Pa
$\Phi_i$	Inner diameter	m
$\Phi_{out}$	Outer diameter	m
$\chi_f^{th}$	Free thermally induced curvature	
$\chi_o^{th}$	Observed thermally induced curvature	

# Chapter 1 Introduction

## 1.1 General context of the thesis

This doctoral thesis focuses on the thermomechanical behavior of underground energy infrastructures, representing an innovative technology for thermal energy harvest and production in a renewable and sustainable way. Energy and environmental implications are nowadays paramount aspects for ensuring to respect the long-term objectives linked to the greenhouse gas emissions in the coming decades. Actions towards a sustainable development must be undertaken by everyone on their daily life. With this view, this study focuses on proposing further developments on a sustainable and renewable technology linked to the energy supply of the built environment.

This research was partly developed in the context of the European Project Terre (Training Engineers and Researchers to Rethink geotechnical engineering for a low carbon future), funded in the framework of the Marie Skłodowska-Curie Innovative Training Networks (ITN-ETN) of the European Commission. Within this project, the work of the PhD candidate (i.e., the author of this thesis) was to study thermal-hydraulic-mechanical aspects linked to the geothermal activation of underground infrastructures, used for a dual purpose: as structural elements and as heat exchangers. This project aimed for a strong academic-industrial partnership. For this reason, intra-European secondments with the industrial partner Nobatek (Bordeaux, France) were carried out.

This research was also partly developed in the context of the “Projet pilote en géothermie sur parois moulées”, funded by the Services Industrielles de Genève (SIG). This project envisaged the development of in-situ testing activities at the underground energy infrastructures installed at the Lancy-Bachet underground train station in Geneva (CH).

## 1.2 Scientific challenges

In recent years, innovative technologies on the renewable energy agenda were developed and represent attractive alternatives to the employment of fossil-based resources. Geothermal energy, the second most abundant energy source on earth (Lee et al., 2007), may represent a tremendous potential for energy exploitation thanks to its different employments. The capabilities of the ground to harvest,

store and release heat make possible the geothermal exploitation even at very shallow depths (i.e., few meters into the soil). Soil temperature is quasi-constant, and equal to  $13 \div 20$  °C, between depths ranging from  $5 \div 100$  m and then it increases following an approximate geothermal gradient of around  $\frac{3}{100} \frac{^\circ\text{C}}{\text{m}}$  (Barbier, 2002). Taking advantage from this fact, heat can be injected and extracted into/from the soil and used to satisfy the human thermal energy requirements, in a renewable and sustainable way. In this context, underground civil geostructures and infrastructures may serve as geothermal heat exchangers in addition to their structural roles (i.e., energy geostructures, EG). The thermal activation of underground infrastructures (i.e., underground energy infrastructures, UEI) such as singly- and multi-floored basements, traffic, service and railway tunnels, and underground train stations may represent a great thermal potential because of (i) the large surface areas available for thermal exploitations and of (ii) the proximity to the built environment.

Prior to this research, the main challenges related to underground energy infrastructures were related to the following three topics:

- **Determining the thermal performance:** the thermal performance is intended as the heat exchangers' response during seasonal operations of the UEI. Particularly, it is affected by all the heat exchange modes occurring within and around the UEI. In underground energy infrastructures, several conductive and convective heat exchanges are simultaneously occurring during geothermal operation, affecting thermal exploitation. A correct assessment of each heat transfer component is paramount to detail thermal performance, to optimize heat exchangers' installation layout and to propose thermal performance design guidelines.
- **Thermomechanical modelling:** geothermal operation induces temperature variations within the UEI, that affect the thermomechanical behavior by means of the development of structural deformations and stresses. A correct assessment of the temperature profile within the UEI during geothermal operation is needed to correctly clarify which and how deformations and internal actions affect the geostructure. This is a key aspect to develop models for thermomechanical analysis. Moreover, the thermomechanical behavior is usually assessed through the employment of costly, computationally speaking, numerical model. At the same time, various simplified and/or approximated analytical solutions are frequently employed for the mechanical analysis because of their attractive nature. Yet, no contributions allowing for the thermomechanical analysis in non-isothermal conditions are available.
- **In-situ testing and monitoring:** a scarce amount of data coming from real installations is available in the literature. Such data are needed and will be key for understanding the real behavior of underground energy infrastructures as well as for validating numerical and analytical models. Moreover, no standards nor guidelines are available for the execution of in-situ tests, and for ensuring a successful monitoring of the geothermal operations. Full-scale in-situ testing activity

will also be useful for investigating what are the best thermal exploitation modes for this innovative type of EG.

### 1.3 Contributions and structure of the thesis

To address the aforementioned challenges, this doctoral thesis is divided in three parts, aiming to reply to each of the challenges.

*Part 1* is devoted to tackling the first challenge, on thermal performance. This part is composed of three chapters.

Chapter 2 investigates the optimization of the heat exchangers' layout by studying fundamental thermo-hydraulic aspects linked to the thermal exploitation on different heat exchangers layout scenarios and detailing the thermal activation of energy walls and slabs. A comparison among different types of heat exchangers layouts is presented. A methodology that allows for selecting the optimal heat exchangers layout design depending on the desired thermal exploitation mode is proposed. Moreover, this chapter tackles fundamental concepts on thermomechanical aspects. Geothermal activation of walls and slabs involves nonuniform temperature variations within the UEI, giving rise to axial and bending deformations and internal actions. These aspects are tackled together with the detailed assessment of the thermomechanical interactions among adjoining thermo-active elements, such as energy walls and energy slabs.

Chapter 3 investigates thermal aspects linked to geothermal activation by tackling the problem at the infrastructure scale, detecting possible hydrothermal interactions between the energy infrastructure and the surrounding environments and their impact on thermal exploitation. Conductive and convective heat exchanges within the UEI and its surroundings (i.e., concrete elements, soil, air interfaces) are analyzed with emphasis on thermally induced effects of the presence of groundwater flow in soils.

Chapter 4 investigates thermal aspects devoted to understanding how environmental conditions affect geothermal operation. Various numerical and analytical tools are employed to analyze the results and to define a thermal performance design methodology that can be employed at early-stage design phases. The results presented in this chapter define a very practical tool, that can be employed by engineers to define the thermal potential of sites that can be equipped with underground energy infrastructures.

*Part 2* is devoted to tackling the second challenge, on thermomechanical behavior. This part is composed of two chapters.

Chapter 5 investigates thermomechanical aspects linked to thermal activation of plane geostructures. After extending the degree of freedom concept for structures subjected to axial thermal actions to the flexural case, an analytical model that extends the classical Winkler's subgrade reaction's theory to the

non-isothermal case is presented. This model is able to capture the thermomechanical behavior in terms of deflection, rotation and internal actions for geostructures subjected to axial and bending thermomechanical actions. The model performance is compared with more rigorous yet time consuming numerical techniques showing closed agreement. Applications to simple and complex plane geometries (i.e., single beams and cut-and-cover structures) are reported. This model represents the first available analytical model able to capture thermomechanical behavior of geostructures in both axial and bending, paving the road for further developments in this scope.

Chapter 6 investigates again thermomechanical aspects starting from the knowledge acquired in Chapter 5 and extending it to various geotechnical structures. Applications to various EGs are proposed with focus on: (i) energy piles, (ii) three-span continuous beam and (iii) partly embedded energy wall. Moreover, variations of the proposed analytical model including the extension to non-isothermal conditions are reported, featuring examples applied to vertical and horizontal footings: (i) the two-parameters soil model and (ii) the linearly varying subgrade reaction modulus model.

*Part III* is devoted to tackling the third challenge, on in-situ testing and monitoring. This part is composed of two chapters.

Chapter 7 investigates hydrothermal aspects linked to the execution of a Thermal Response Test (TRT) on a portion of the energy walls of the underground train station Lancy-Bachet in Geneva (CH). A full-scale in situ test and dedicated monitoring are performed. Highlights on the wall-tunnel hydrothermal interactions, the thermal behavior of the energy wall are monitored on-site. With the help of numerical simulations, validated against the experimental data, results are interpreted giving a global view of the hydrothermal aspects characterizing the studied underground energy infrastructure. Additionally, in view of the absence of guidelines for the TRT execution on walls (and, more generally, on any geostructure in contact with an air interface), feedback and preliminary prescriptions for a successful TRT execution on this type of EG are proposed.

Chapter 8 investigates thermo-hydro-mechanical aspects by continuing the in-situ testing campaign at the same site reported at Chapter 7. Heating and cooling tests simulating realistic summer/winter operations are performed. Details on the seasonal wall-tunnel hydrothermal interactions as well as implications on thermomechanical behavior are studied employing numerical and analytical modelling in conjunction with the experimental, in-situ, results. Finally, by means of numerical modelling validated against experimental results, the thermal potential of the entire underground energy infrastructure is evaluated and four different scenarios for thermal exploitation are proposed highlighting main strong/weak points of this installation.

# Part 1 : Thermal behavior



# Chapter 2 Fundamentals on thermal efficiency and mechanical behaviour of an energy wall and slab

## 2.1 Foreword

Energy walls and slabs have a potential for renewable energy exploitation and storage. The structural support to the sides and base of excavations is coupled with the structure's heating/cooling role. The goals of this study are to propose a heat exchangers layout optimization ensuring the best thermal efficiency and to thoroughly analyze thermally induced mechanical actions on an energy wall and slab. The energy optimization of pipe layout design using 3D numerical sensitivity analyses is presented, by means of full-scale simulations of an energy wall and slab operating in winter. Emphasis is put on the following parameters: *(i)* water flow regimes and pressure drops in the heat exchangers, *(ii)* heat exchangers' layout, *(iii)* pipe spacing. Thermally induced mechanical effects in the wall and slab are analyzed with reference to: *(i)* axial and transversal displacements and, *(ii)* internal actions. Pipe spacing has a predominant effect on energy exploitation. Pipe layout can be optimized by finding the best trade-off solution between the installed pipe length and power extraction. Wall and slab activations induce thermal interactions among the two adjoining elements. Thermally induced mechanical effects are the result of two components: an axial and a bending effect, in view of the geometry definition, interactions with air interfaces and of the non-constant temperature distribution across the thermo-active elements. Wall-slab mutual mechanical interactions due to different geothermal operations are highlighted.

## 2.2 Introduction

The use of renewable energies, designed using a holistic approach, contributes to target the needed heating and cooling supply of the built environment. In this context, geothermal energy represents one of the most important sources of renewable energy, one which may help the transition from fossil fuels to widespread green-energy use (E.P.B.D.r., 2010; Lund & Boyd, 2016; Rees, 2016). Among various types of geothermal installations, energy geostructures (EG) are shallow geothermal structures that use the ground itself as a heat exchanger and as a heat storage medium (Laloui & Di Donna, 2013; Laloui & Rotta Loria, 2019). Heat-exchange pipe loops are attached to the reinforcing cage of concrete geostructures with a heat-carrier fluid circulating inside the pipes. The structural role of the geostructure is coupled with the heating-cooling role of the heat exchangers. EGs are usually



coupled with heat pumps to increase the overall system's performance and to better meet the energy needs of its users (Kavanaugh & Rafferty, 2014). This technology is growing and developing in recent years thanks to applications on piles (Batini et al., 2015; Dupray et al., 2014; Rotta Loria & Laloui, 2017a), vertical retaining walls (Bourne-Webb & da Costa Goncalves, 2016; Dong et al., 2019; Makasis et al., 2019; Shafagh et al., 2020; Sterpi et al., 2020; Zannin et al., 2020), tunnels (M. Barla et al., 2019; Bidarmaghz & Narsilio, 2018; Cousin et al., 2019; Peltier et al., 2019), anchors (Mimouni et al., 2014), and sewers (Adam & Markiewicz, 2009).

The present study deals with energy walls (EWs) and slabs (ESs), which are plane geotechnical structures, such as retaining walls and base slabs built for excavation works, made using reinforced concrete. They are partly fully embedded in the soil, and partly exposed to air. Depending on the depth of the excavation, props or anchors may be needed to meet structural and geotechnical safety requirements. Typical civil engineering structures that can be built employing EWs include multi-level basements (Amis et al., 2010), subway lines and stations (Zannin et al., 2020), and underground car parks (Di Donna, 2016). Applications of EW may involve also thermal activation of other structural elements in contact with the EW, such as ESs. ESs involve horizontal heat exchanger loops installed in the concrete geostructure. The thermal activation of such structures usually involves heat exchangers installed at the soil side of the geostructure to avoid any possible damage to the pipes during works on the air side. EWs and ESs may have great potential for energy exploitation because of their large surface areas exposed to soil and air.

Main challenges related to EWs and ESs refer to hydrothermal aspects (e.g., thermal performance, identification of heat exchange modes) and to thermomechanical implications on the structural stability (e.g., identification of thermally induced mechanical effects). Some of such challenges were tackled in recent years. The hydrothermal behavior has been tackled at the laboratory (Kürten et al., 2015b) and at the field scale (Sterpi et al., 2018; Xia et al., 2012) identifying the main heat exchange mechanisms and reporting insights on the thermal behavior of selected case studies (Brandl, 2006; Di Donna et al., 2016; Kürten et al., 2015a; Sun et al., 2013). The thermomechanical behavior was mainly reported through numerical investigations (Barla et al., 2020; Bourne-Webb et al., 2016; Rui & Yin, 2017; Sailer et al., 2019), laboratory scaled models (Dong et al., 2019), highlighting the involvement of various internal actions. Thermomechanical behavior through real, full-scale, in-situ investigations was rarely reported (Brandl, 2016), highlighting the low magnitude of thermally induced mechanical actions when compared with mechanical ones detected during construction phases, on a piled wall of the Vienna subway. Extensive literature has been published about horizontal ground-loop heat exchangers, evaluating the thermal performance (Kupiec et al., 2015) of various layouts (Benazza et al., 2011; Chong et al., 2013; Congedo et al., 2012) either numerically or experimentally (Wu et al., 2010). Little evidence (Sterpi et al., 2018) is available on ES.

Despite the knowledge revealed in the literature review, researchers and practitioners still face several challenges in their search for the optimal design, both in terms of thermal performance and hydraulic

behavior of the heat exchangers, and of mechanical behavior of the EW and ES systems. When it comes to energy design, the optimization of heat exchangers is of primary importance. Additionally, a detailed description of thermo-mechanical implications on EW and ES remain still to be assessed. This study aims at bringing a generic knowledge related to (i) the choice of the heat exchangers layout design based on the expected thermal operation modes and (ii) the impact of slab thermal activation. Additionally, a theoretical background for understanding (iii) the details of thermally induced mechanical effects on the geostructure is presented.

To reach such goals, the EG composed by an EW and an ES is numerically modelled by employing a 3D thermomechanical finite element (FE) model. Winter operation mode (*e.g.*, the soil is cooled in order to heat the superstructure) is simulated. The numerical model features are firstly described (section 2.3). Secondly, thermal aspects on the layout optimization are tackled, with emphasis on the heat exchangers behavior, regarding: (i) fluid flow regimes, (ii) pipe spacing, and (iii) pipe layouts. A dedicated analysis also considered the possibility of thermally activating the EW and the connected ES (section 2.4). Then, the EW and ES's thermally induced mechanical behavior is discussed (section 2.5) with reference to the different proposed design solutions and their effects: (i) axial and transversal displacements and (ii) internal actions. Concluding remarks are reported.

## 2.3 Finite Element Modelling of Energy Wall and Slab

This study models a cast-in-place EW built in a sandy-gravelly moraine soil deposit which sustains the underground levels of a station and its subway line. All the modelled materials behave elastically. Construction stages are not considered here as the objective is to consider only thermally induced mechanical effects on the geostructure. Concurrent occurring of thermal and mechanical actions induced by the construction process is very unlikely as thermal activation takes place after construction (Brandl, 2016). In the considered case, the retaining wall must retain a 20.5-m deep excavation with the groundwater table located at the top of the soil deposit. The geometries of the vertical and horizontal structural elements were designed to satisfy Eurocode 7 requirements (*EN 1997 Eurocode 7: Geotechnical Design*, 2004). The structure's geometry consists of a  $H_{wall} = 40$  m high wall whose top 18 m are exposed to air and whose bottom 22 m are embedded in the soil. The wall's thickness is  $w = 1.20$  m. Three horizontal slabs are connected to the wall at different depths (Figure 2.1), presenting a length of  $L_{slab} = 15.0$  m. The pipes are buried in the concrete and the wall top 4 m are thermally insulated to limit the influence of external climatic conditions. Convective heat transfer occurs inside the heat exchangers and at the geostructure-air interfaces (*e.g.*, wall-tunnel, wall-station, in Figure 2.1), while conduction is predominant within the pipe wall, concrete and soil. Heat carrier fluid circulation inside the heat exchangers accounts for water as circulating medium and the detailed heat exchangers' shape must be fully modelled accounting for an inflow fluid velocity and temperature. Additionally, the heat exchangers' layout should best use the space given at the geostructure-soil surface: ideally, the

most performant design is the one that minimizes the installed pipe length and maximizes the heat exchanges with the surroundings.

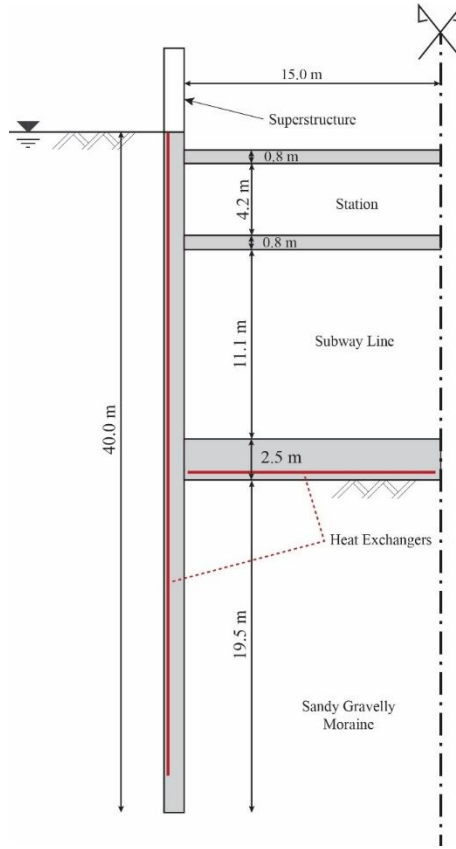


Figure 2.1. Sketch of the considered geometry at a vertical cross section in correspondence of the heat exchangers

Several assumptions are made: (i) the soil is considered isotropic and fully saturated; (ii) drained conditions are considered during the whole duration of the process, neglecting pore pressure variations due to thermal loads; and (iii) there is no consideration of interface degradation due to thermal loads between the soil and the concrete (Di Donna et al., 2015). The mathematical formulation of the model is reported in Appendix A.

### 2.3.1 Features of the 3D Finite Element models

The present study describes various sets of analyses conducted using the Finite Elements COMSOL Multiphysics® software (COMSOL Inc., 2018). We simulate a 3-m long panel of the EW model whose overall dimensions are  $L_{x,tot} = 10 H_{wall}$ ,  $L_{y,tot} = 3$  m,  $L_{z,tot} = 3 H_{wall}$  (Figure 2.2). In all the sets of analyses, after a dedicated mesh sensitivity analysis, the mesh size in the EG goes from 0.05 m in the vicinity of the pipes, to 1.0 m. As the distance from the EG increases, the mesh refinement becomes coarser. Tetrahedral elements are employed. The first set of analyses studies the fluid flow velocity inside the pipes using a *W*-shaped layout and a pipe spacing of  $a = 0.50$  m. The next set of

analyses is conducted using three pipe layouts named *W*, *Slinky 1*, and *Slinky 2* (Figure 2.3). The heat exchanger layouts are chosen as different ways (i.e., vertical/horizontal curves) to optimize the space given by the lateral surface of each wall panel. The third set of analyses includes an EW and an ES. The parametric analyses is based on sixteen different combination accounting for these pipe configurations.

The pipes are defined as linear entities, placed at a distance  $c_f = 0.15$  m from the concrete–soil interface. The fluid flow and associated convective heat transfer inside the pipes are simulated using linear elements that account for cylindrical pipes containing a fluid (i.e., water) in motion.

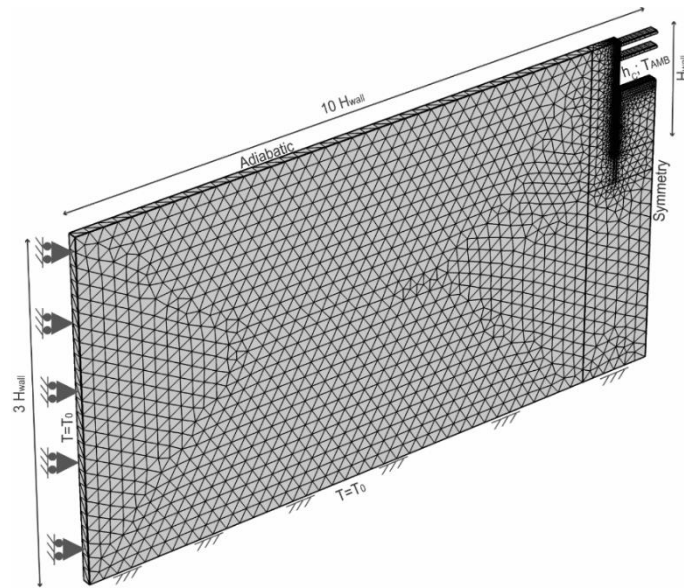


Figure 2.2. Finite element model and boundary conditions

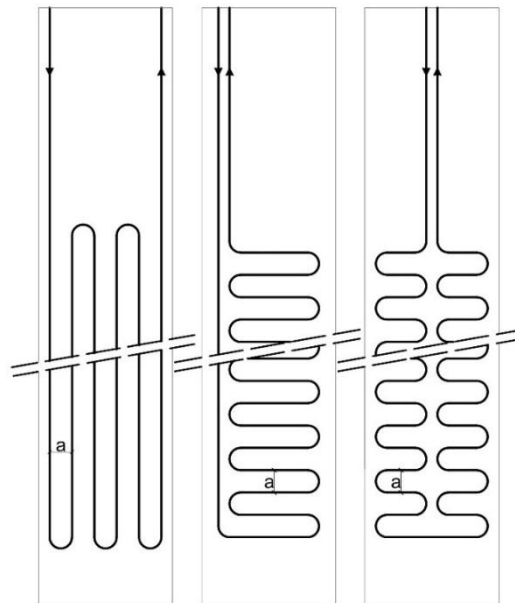


Figure 2.3. Pipe layouts analyzed, from left to right: *W*, *Slinky 1*, *Slinky 2* with indication of the pipe spacing,  $a$ .

### 2.3.2 Boundary and initial conditions

The FE model mesh and boundary conditions are described in Figure 2.2. The model simulates the geothermal system operating in winter. The model is symmetrical with respect to the plane that cuts the slab in half. The two planes orthogonal to the tunnel's longitudinal direction are adiabatic and with null normal displacement: this is chosen with the intent to represent only a portion of an infinitely long thermo-active underground infrastructure. A fixed boundary condition is applied to the bottom boundary, whereas a roller boundary condition is applied to the left boundary. The thermal boundary conditions are defined with reference to the potential construction of a tunnel in the Swiss Alpine region: (i) the bottom and the left vertical side of the model have a fixed temperature of  $T_0 = 13.2\text{ °C}$ ; (ii) the ground surface, the top level of the superstructure and the station are considered as adiabatic; (iii) the subway line is modelled with a convective boundary condition (Figure 2.2) which accounts for an ambient temperature,  $T_{AMB} = 13.2\text{ °C} = T_0$ , set as an average winter temperature of a shallow tunnel in an urban environment (Bourne-Webb & da Costa Goncalves, 2016; Brandl, 2006), and a convective heat transfer coefficient,  $h_c = 10\text{ W/m}^2/\text{K}$ , which relates to a wind speed velocity,  $v_{AIR} = 1 \div 1.5\text{ m/s}$  (Peltier et al., 2019).

Null stresses and displacements are set as initial conditions, together with a uniform temperature,  $T_0$ , across the entire geometry. The inner and outer diameters of the pipes are set at  $\Phi_i = 25\text{ mm}$  and  $\Phi_{out} = 30\text{ mm}$ , respectively (Batini et al., 2015; Xia et al., 2012). The constant inflow temperature is set at  $T_{f,in} = 5\text{ °C}$ , simulating winter operation. Such thermal input was chosen to detail the thermal behavior at transient and steady flux conditions (Li & Lai, 2015; Xia et al., 2012; Zannin et al., 2020). The shallowest 4 m of pipes are considered to be thermally insulated to limit the effect of ground surface climatic conditions. Their thermal conductivity is set as  $\lambda_{p,shallow} = 0\text{ W/(m K)}$ .

### 2.3.3 Description of the materials

The soil, concrete, and pipe characterizations were chosen based on the literature review. In particular, the soil deposit characterization simulates the sandy-gravelly moraine layer of the energy piles test located at the SwissTech Convention Centre at the Swiss Federal Institute of Technology in Lausanne (EPFL) (Batini et al., 2015; Mimouni & Laloui, 2015). Material properties are summarized in Table 2.1, where  $E$  is the Young modulus,  $\nu$  is the Poisson ratio,  $n$  the porosity,  $\rho_s$  the density of the solid,  $C_p$  thermal capacity,  $\lambda$  the thermal conductivity and  $\alpha$  the thermal expansion coefficient.

Table 2.1. Material properties

	Material	$E$ (MPa)	$\nu$ (-)	$n$ (-)	$\rho_s$ (kg/m <sup>3</sup> )	$C_p$ (J/(kg K))	$\lambda$ (W/(m K))	$\alpha$ (1/K)
<i>Soil</i>	Sandy-gravelly moraine	84	0.40	0.35	2735	890	1.80	$1 \times 10^{-5}$
<i>Wall</i>	Concrete	28000	0.25	0.10	2722	837	1.63	$1 \times 10^{-5}$
<i>Pipes</i>	HDPE	-	-	-	-	-	0.42	-

## 2.4 Thermal behavior of different design solutions

### 2.4.1 Effect of fluid velocity in the pipes

The first series of analyses equips the EW with a W-shaped pipe layout, with a pipe spacing of  $a = 0.50$  m. The geothermal system is activated by imposing a constant time inflow temperature,  $T_{f,in} = 5$  °C, the simulation lasts until steady flux is reached (Figure 2.4). The fluid flow velocity,  $v_f$ , varies from 0.005 m/s to 1.0 m/s (see Table 2.2). Some preliminary knowledge on the role of fluid flow velocity in EW geothermal operation is known (A. Di Donna et al., 2016), but a detailed description of the fluid flow regime that best enhances geothermal activation remains to be assessed. Additionally, no evidences on the quantification of the pressure drops ( $\Delta p_f$ ) along the heat exchangers are made available.

Table 2.2. Parametric analysis of the fluid flow velocity in the pipes

Velocity (m/s)	Reynolds number (-)	Fluid flow regime	$\Delta T_f$ (°C)	$Q_{th,f}$ (kW)	$\Delta p_f$ (bar)
$v_A = 0.005$	89	Highly laminar	7.95	0.07	$65 \cdot 10^{-6}$
$v_B = 0.05$	900	Laminar	5.72	0.50	0.0008
$v_C = 0.1$	1785	Laminar/Turbulent transition	3.92	0.68	0.0029
$v_D = 0.2$	3570	Turbulent	2.30	0.80	0.0104
$v_E = 0.5$	8930		1.01	0.88	0.0885
$v_F = 1.0$	17587	Fully turbulent	0.54	0.94	0.2184

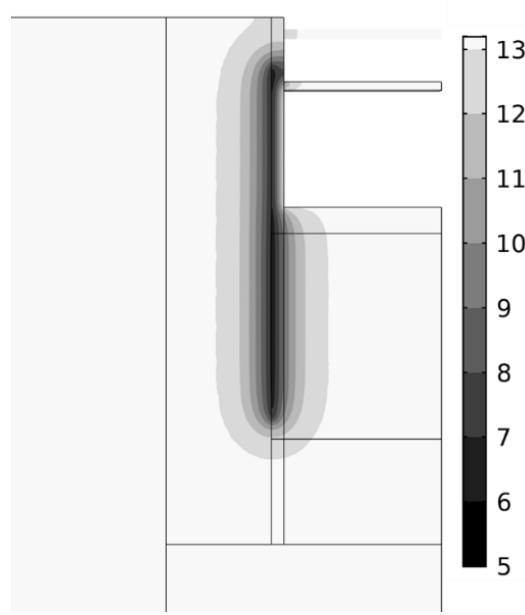


Figure 2.4. Temperature (°C) profile contour map of the EG and the soil around it at steady flux conditions

Convective heat transfer occurs in the pipes, such that the thermal power extracted from the ground ( $Q_{th,f}$ ) can be defined as:

$$Q_{th,f} = A_{PIPE} \rho_f C_{p,f} v_f \Delta T_f \quad (2.1)$$

where  $A_{PIPE}$  is the pipe cross-section,  $\rho_f = 1000 \text{ kg/m}^3$ , and  $C_{p,f} = 4186 \text{ J/(kg K)}$  are the density and specific heat at constant pressure of the heat carrier fluid, respectively.  $\Delta T_f = T_{f,out} - T_{f,in}$  is the difference between the outflow ( $T_{f,out}$ ) and the inflow heat carrier fluid temperature.

Thermal power extraction can be divided by the surface area of the equipped EW,  $A_w$ , to obtain the power extraction per square meter of thermo-active wall surface:

$$\dot{q} = \frac{Q_{th,f}}{A_w} \text{ (W/m}^2\text{)} \quad (2.2)$$

Once the fluid and pipe types are fixed, power extraction is mainly governed by  $v_f$  and  $\Delta T_f$ . It is worth noting that although  $v_f$  can vary by three orders of magnitude, the measured outflow temperature increases by less than one order of magnitude. Moreover, for highly laminar to laminar/turbulent transition flows, the decrease in the output temperature is slower over time. The steady state is reached at the end of the first seasonal thermal activation. For turbulent to fully turbulent flows, the outflow temperature decreases abruptly during the first days of thermal activation and the steady state is reached after 50 days. Highly laminar velocity ( $v_A$ ), as would be expected, gives a very low value of power extraction, whereas the steady-state response from laminar to highly turbulent flow is similar.

The transient response is strongly affected by the fluid velocity, as shown in Figure 2.5 (“Transient” defined after 3 days of geothermal activation). Taking the power extraction of the case  $v_f = 0.5$  m/s, as a reference value ( $\dot{q}_{v=0.5 \text{ m/s}}$ ), we see that during transient conditions an increase of the fluid velocity leads to a considerable increase in the power extracted. Moving towards steady flux condition in laminar flow (e.g.,  $v_A$ ,  $v_B$ ,  $v_C$ ), the dependency between the power extracted and fluid velocity does not change with respect to the first days of activation. However, an increase in the velocity of a turbulent flow corresponds to a very low increase of power extraction. Hence, for long-term constant operational design, it would be preferable to use a slightly turbulent to turbulent fluid regime.

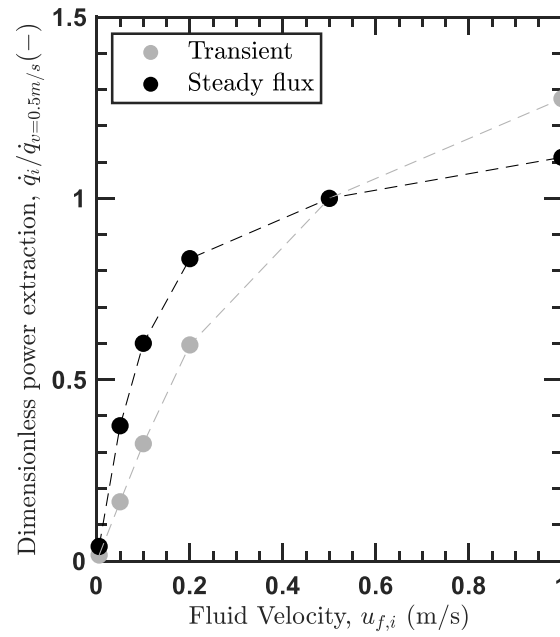


Figure 2.5. Variations in the thermal power extracted from different fluid velocities over different time spans

From Bernoulli’s principle for incompressible fluid flow, the variation of heat carrier fluid pressure,  $\Delta p_f$ , is representative of the charge losses between the inflow and the outflow pipe sections if the hypothesis of null variation of heat carrier fluid velocity throughout the pipe holds, as it is in the presented case. Table 2.2 shows that, at steady state conditions, turbulent conditions ensure a maximization of the thermal behavior of the heat exchangers while keeping relatively low charge losses along the heat exchanger loop (i.e. pressure drops lower than 0.1 bar). Increasing values of heat carrier fluid velocity to fully turbulent conditions induce an increase of the charge losses by a factor 2.5. A lowering of the heat carrier fluid velocity below the laminar/turbulent transition considerably minimizes the charge losses (i.e.,  $\Delta p_f < 0.01$  bar) but the thermal behavior decreases by  $> 40\%$  with respect to turbulent conditions (Table 2.2, Figure 2.5). It follows that a range of fluid velocity  $v_f = 0.2 \div 0.5$  m/s (i.e., turbulent conditions) allows to maximize the thermal behavior of the heat exchangers while keeping the pressure drops relatively low (i.e.,  $\Delta p_f < 0.1$  bar). In the following, attention is devoted to the heat



exchangers' thermal behavior, hence the fluid velocity is kept at the upper range within the turbulent regime (i.e.,  $v_f = 0.5$  m/s).

## 2.4.2 Comparing pipe spacing and layout effects

Some preliminary knowledge on the role of pipe spacing on geothermal exploitation is known (i.e., it is one of the top three most important parameters when assessing thermal aspects) (Di Donna et al., 2016). However, no evidences on its application in conjunction with different pipe layouts is available. This further set of analyses presents the 40-m-high, 3-m-wide, 1.2-m thick EW described in the previous sections, equipped with either a W, Slinky 1, or Slinky 2-shaped pipe layout, and with pipe spacing,  $a$ , taking the following values: 0.20 m, 0.30 m, 0.40 m, 0.50 m, or 0.75 m. The geothermal system is activated by imposing a constant with time inflow temperature  $T_{f,in} = 5$  °C. The fluid-flow velocity is fixed at  $v_f = 0.5$  m/s (turbulent flow). The model simulates 50 days of activation, which have been proven to be sufficient to reach the steady flux within the EW. The thermal power exchanged between the EW and the surrounding materials is represented by the enthalpy drop of the fluid from the pipe's inflow to its outflow sections. At steady state, the heat capacity effects,  $\rho C_p$ , are negligible and heat exchange is governed by the thermal conductivity of the materials involved. The classic effectiveness method for heat exchangers (Bergman et al., 2011) can be used to compare various pipe configurations. It gives results that are independent to the choice of the thermal input: in other words, even a unitary thermal load could be used to determine the effectiveness of the heat exchangers,  $E_{he}$ .

$$E_{he} = \frac{T_{f,out} - T_{f,in}}{T_{S-W} - T_{f,in}} \quad (2.3)$$

where  $T_{S-W}$  is the average temperature at the soil–wall interface at steady state.

$$\mu_{PIPE} = \frac{L_{PIPE}}{A_w} \quad (2.4)$$

The parameter  $\mu_{PIPE}$  is defined by the ratio between the length of the installed pipes,  $L_{PIPE}$ , and  $A_w$ .  $L_{PIPE}$  varies with pipe spacing and layout, whereas  $A_w$  is fixed: the panel width is 3 m and its equipped height is 34.5 m because the pipes are insulated in the shallowest 4 m, and the bottom 1.5 m are not equipped with geothermal pipes.

Figure 2.6 shows the overall length of piping installed per square meter of EW when varying pipe-spacing widths for the three pipe layouts. For small pipe spacings, Slinky 1 presents shorter pipes ( $-2 \div -31\%$  with respect to W, and  $-5 \div -10\%$  with respect to Slinky 2). For higher pipe spacings, Slinky 2 needs less installed pipes (up to  $-12\%$  with respect to Slinky 1 and  $-30\%$  with respect to W). It should be remembered that the longer the installed pipe, the greater pumping power required to overcome charge losses along it.

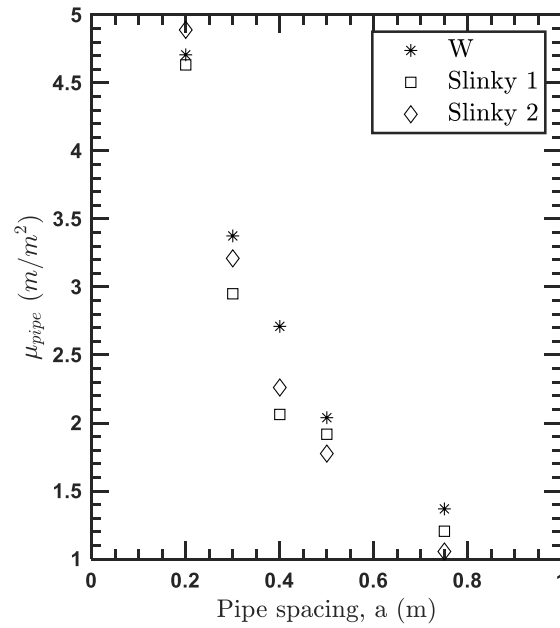


Figure 2.6. Embedded pipe length per square meter of wall for each situation analyzed

The axial temperature distributions at the central cross-section of the concrete wall, at steady state, present only minor variations with regard to pipe spacing and with the longitudinal sections of the EW (see Figure 2.7). For *W* configuration, the maximum difference is 1.19 °C, for *Slinky 1* it is 1.48 °C and for *Slinky 2* it is 1.76 °C.

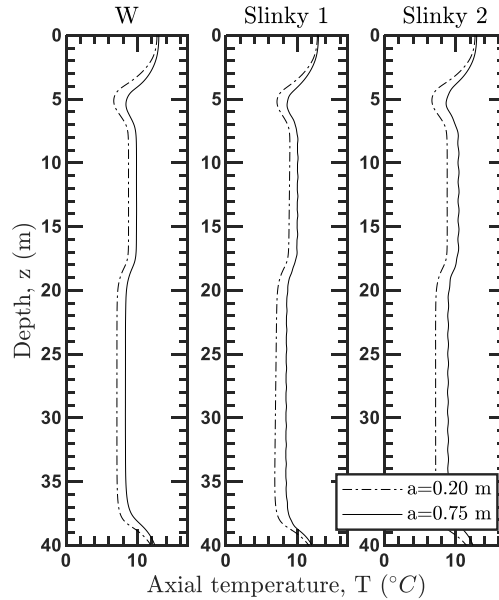


Figure 2.7. Axial temperature distribution inside the wall in steady-state conditions

The bulk temperature's evolution inside the pipe over space and time shows an increase that depends on the location of the pipe's curves along its overall length. The spatial increase in the fluid's

temperature depends on the progressive decrease in the thermal exchange with the soil and the consequent decrease in the temperature difference between the fluid and the surrounding materials. The main part of the bulk temperature decrease takes place during the initial 10 days of activation. The temperature difference between the outflow and inflow at steady state ranges between  $+1.12\text{ }^{\circ}\text{C}$  and  $+1.14\text{ }^{\circ}\text{C}$  (spacing  $a = 0.20\text{ m}$ ) and  $+0.85\text{ }^{\circ}\text{C}$  and  $+0.92\text{ }^{\circ}\text{C}$  (spacing  $a = 0.75\text{ m}$ ). The dependency on the pipe layout is not evident.

Thermal power extraction decreases with time, consistently with the temperature drop in the soil. An abrupt decrease occurs during the initial days of heat extraction, but after 25 days the rate of decrease is lower and steady-state is reached within 50 days (Figure 2.8). For closer pipe-spacing, *i.e.*,  $a \leq 0.5\text{ m}$ , a sharper decrease occurs during the first 25 days of thermal activation; for wider pipe spacing, steady-state is reached earlier (after 10 to 15 days).

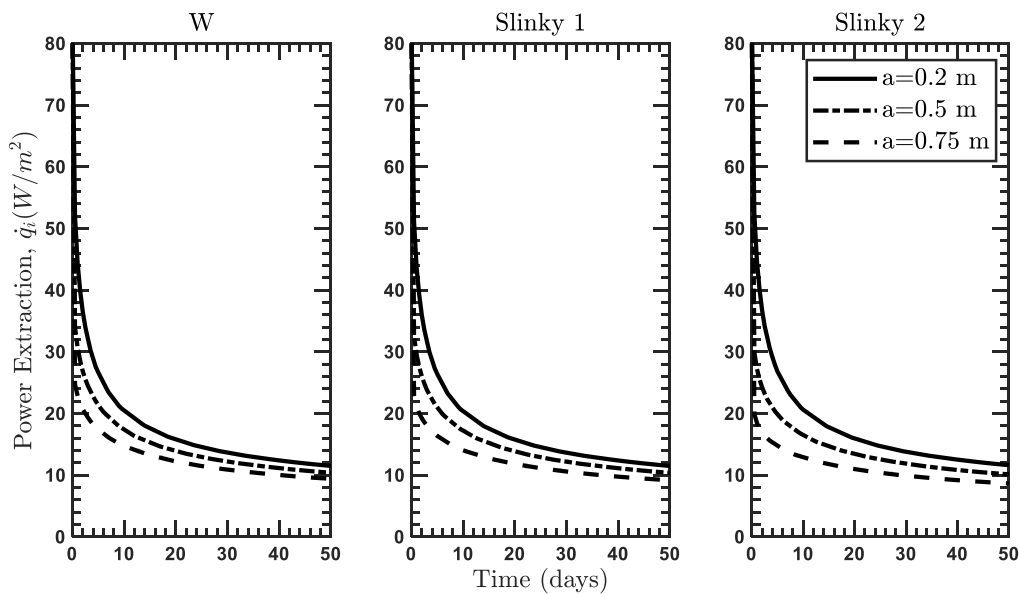


Figure 2.8. Thermal power extracted over time for different design configurations

In transient conditions, the system's thermal response is strongly dependent on pipe spacing (Figure 2.9), with the three different pipe layouts delivering similar power extraction: the closer the pipe spacing, the greater the power extraction. The decrease in power extraction as pipe spacing increases is approximately linear, with the slope decreasing with time. During the initial days of activation, thermal power extraction decreases considerably. In this time range, the power extraction varies between  $50 \div 30\text{ W/m}^2$ . On average, after 5 days of thermal activation, the decay in power extraction will be 40%; after 50 days of continuous operation it will be around 80%. During a longer, continuous thermal operation, the thermal interaction between adjoining pipe sections leads to a stabilization in the level of thermal power extracted, hence, the dependency on the pipe spacing vanishes. The energy performance of the three pipe layouts analyzed is similar: at steady state, all the pipe layouts present an average power extraction of  $10\text{ W/m}^2$ . The W layout generally shows higher performances, up to  $+7.87\%$  with

respect to the other layouts. For small pipe spacing, *Slinky 1* shows similar performances with respect to  $W$  (−1.5% up to −4%) but needing considerably less pipe length. For larger pipe spacings, *Slinky 2* performs −8% with respect to  $W$  while needing up to −30% of installed pipe length.

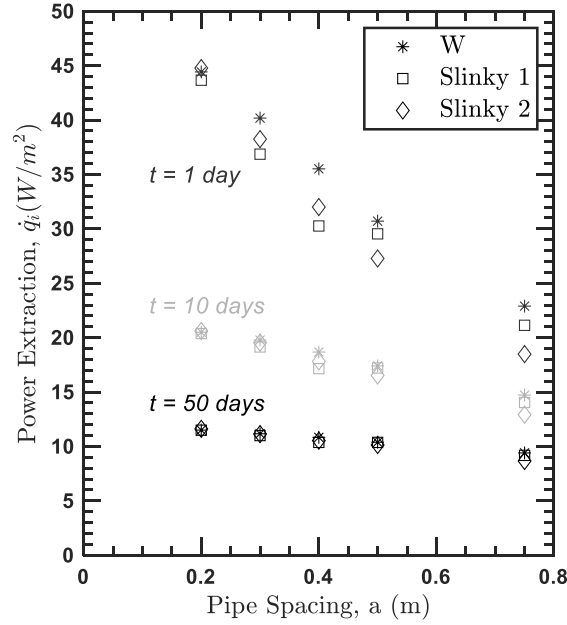


Figure 2.9. Comparison of thermal power extracted at selected time points for different design configurations

The effectiveness of the heat exchangers ( $E_{he}$ , Table 2.3) decreases with wider pipe spacing, with higher values for the  $W$  pipe layout. *Slinky 1* and *Slinky 2* perform similarly, with an average effectiveness of −33.6% with respect to the  $W$  layout. The best trade-off solution must be found by considering all the aforementioned parameters. Finally, temperature distribution into the soil is unaffected by the pipe layout.

Hydraulic aspects are also affecting the thermal behavior of the heat exchangers. Employing different layouts as well as different pipe spacings have consequences on the hydraulic aspects (e.g., heat carrier fluid pressure). The longer the pipe circuit, the greater the pressure drops among the inflow and return sections. For such reason, for narrower pipe spacings, higher pressure drops are recorded. Reducing the pipe spacing from  $a = 0.75$  m to  $a = 0.20$  m, the pressure drops triplicate (Table 2.3). With equal spacing, the performance of the three layouts is very similar. For  $a > 0.3$  m *Slinky 2* minimizes the pressure drops, while for  $a \leq 0.3$  m it is *Slinky 1*.

Table 2.3. Thermal performance of different pipe configuration at steady state

Pipe layout	Pipe spacing (m)	$T_{f,out}$ (°C)	$\Delta T_f$ (°C)	$T_{S-W}$ (°C)	$E_{he}$ (—)	$L_{PIPE}$ (m)	$\mu_{PIPE}$ (m/m <sup>2</sup> )	$\Delta p_f$ (bar)	$\dot{q}$ (W/m <sup>2</sup> )
W	0.2	6.12	1.12	6.13	0.99	473.08	4.71	0.14	11.50
	0.3	6.09	1.09	6.17	0.93	339.24	3.38	0.12	11.17
	0.4	6.06	1.06	6.40	0.76	272.40	2.71	0.09	10.83
	0.5	6.02	1.02	6.71	0.60	204.93	2.04	0.09	10.39
	0.75	5.92	0.92	7.26	0.41	137.53	1.37	0.04	9.40
Slinky 1	0.2	6.12	1.12	6.20	0.93	465.62	4.63	0.14	11.49
	0.3	6.08	1.08	6.55	0.70	296.49	2.95	0.09	11.00
	0.4	6.01	1.01	6.87	0.54	207.31	2.06	0.09	10.37
	0.5	6.01	1.01	7.09	0.48	192.69	1.92	0.07	10.37
	0.75	5.90	0.90	7.97	0.30	121.01	1.20	0.05	9.18
Slinky 2	0.2	6.14	1.14	6.37	0.83	491.50	4.89	0.15	11.62
	0.3	6.09	1.09	6.65	0.66	322.67	3.21	0.09	11.14
	0.4	6.03	1.03	7.05	0.50	227.21	2.26	0.07	10.53
	0.5	5.99	0.99	7.16	0.46	178.38	1.77	0.05	10.13
	0.75	5.85	0.85	8.28	0.26	106.03	1.06	0.05	8.66

### 2.4.3 Activation of the base slab

In this simulated analysis, the slab and EW are equipped with W-shaped pipe layouts with a pipe spacing  $a = 0.30$  m. The 40-m-high, 3-m long, 1.2-m thick EW and the 2.5-m-thick, 3-m-long, 15-m wide base slab are both equipped with geothermal pipes installed at a distance  $c_f = 0.15$  m from the concrete–soil interface at the bottom part of the horizontal slab and towards the soil side of the vertical plane of the EW, respectively. The geothermal system is activated by imposing a constant inflow temperature  $T_{f,in} = 5$  °C. The outflow temperature is monitored throughout the simulation. The fluid flow velocity is fixed to a value  $v_f = 0.5$  m/s (turbulent flow). The model simulates 50 days, which has been proven to be sufficient to reach a steady state temperature within both the wall and base slab.

The axial temperature inside the base slab drops with time but remains uniform along the axial surface. The left part of the base slab (Figure 2.10a) is influenced by the presence of the EW. Hence the temperature drop is emphasized throughout the thermal activation. Over 50 days of thermal activation the average temperature change is  $\Delta T = -3.8$  °C.

Figure 2.10b highlights the fluid temperature after 1 and 50 days of geothermal activation. The total lengths of installed pipes are 134.13 m in the base slab and 351.83 m in the EW. Due to this shorter pipe length, the slab undergoes a smaller temperature rise.

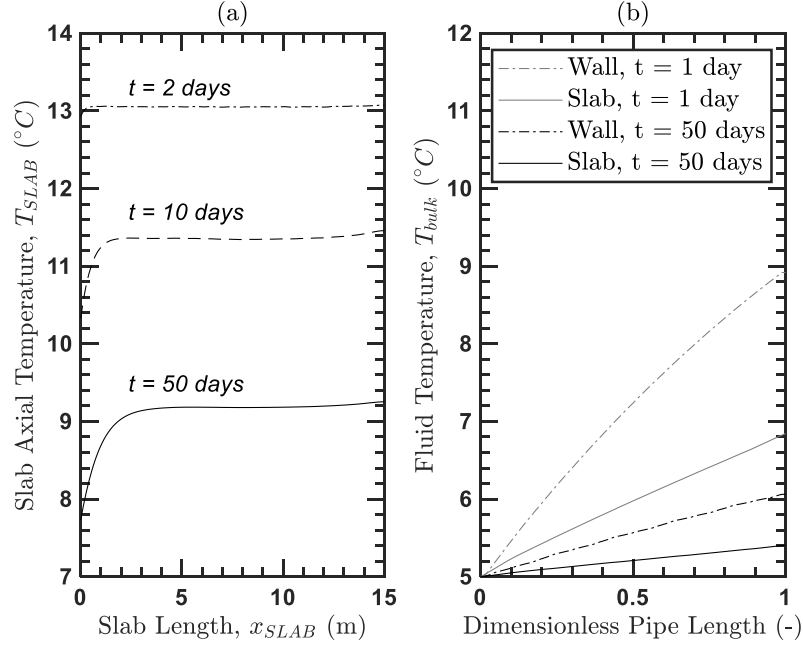


Figure 2.10. (a) Axial temperature distribution in the slab, and (b) fluid temperature distribution in the pipes in the slab and the wall at selected time points

As previously described, thermal power extraction decreases with time. An initial, abrupt decrease takes place within the first 2 days of thermal activation, and afterwards, the thermal extraction decay slows down over time, with a steady state reached within 50 days of continuous thermal activation. Thermal extraction is governed by the temperature difference between the inflow and outflow pipes. The heat exchanging surfaces are different:  $100 \text{ m}^2$  for the EW and  $45 \text{ m}^2$  for the base slab. Consequently, the power extracted per square meter of thermo-active surface is similar for the EW and the base slab, as highlighted in Figure 2.11, with the wall showing 13.6% higher performance. The results showed in this study report a thermal power for both the slab and wall that range between  $10 \div 20 \text{ W/m}^2$  when approaching steady-flux conditions (Figure 2.11). The pressure drop in the heat carrier fluid between the inflow and outflow of the pipe circuit is of  $\Delta p_f = 0.04 \text{ bar}$ , which is in line with the results for the wall for a similar pipe length.

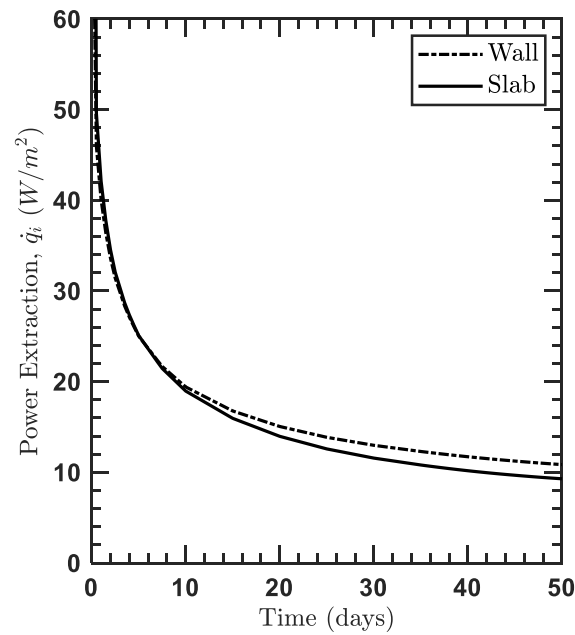


Figure 2.11. Thermal power extracted from the wall and the slab

## 2.5 Thermally Induced Mechanical Effects

This study analyzes the thermally induced mechanical effects on an EW and an ES by comparing different pipe design layouts and geothermal operations. Tensile stresses are considered to be positive, as are downward displacements. Positive bending moment is located at the intrados (i.e., intrados concrete fibers undergo tension). In the following, “thermally-induced” effects are defined as the internal actions and displacements that the EG undergoes only because of geothermal operation.

The goals of this section are: (i) to give a theoretical background for understanding thermally induced mechanical effects in an EW and ES or, more generally, within any geostructure partly in contact with an air interface, (ii) to understand how stresses and strains redistribute within the geostructure consequently to thermal activation of one (or more) of its geostructural elements.

Geothermal activation induces mechanical actions in the concrete structure because of the temperature variation distribution across the EG’s thickness. The shape of the temperature variation profile can generally be nonuniform because (i) of the non-symmetrical location of the heat exchangers and (ii) the concurrent effects of different heat exchange modes at the structure-air interfaces. This situation leads to two concurrent thermally induced mechanical effects: axial deformation and bending. In the present study, the EG is equipped with heat exchangers located closed to the wall-soil interface; hence, during winter operation, the side of the wall closest to the pipes shows a lower temperature distribution than the wall–tunnel interface. From the theory of thermo-elasticity, at steady flux, a non-uniform temperature variation distribution along the wall/slab thickness can be analyzed as a sum of two components: a

uniform and a linear distribution. The uniform component leads to a partial axial deformation whereas the linear one partly generates a thermal curvature (i.e., bending). The deformation of the EG upon temperature variations is partly blocked because of the presence of constraints such as the structural elements (e.g., slabs) and the soil. The blocked portion of the thermal deformation gives rise to variations in the solicitations within the geostructure (i.e., internal actions). As a result of such two mechanisms, axial and transversal displacements, axial force, bending moment, and shear force will all affect the structure. The same applies to the thermal activation of any other geostructural element (e.g., the slab).

In this section, the mechanical behavior is initially compared for the different design solutions, then three additional cases are defined and described.

Design solutions present local differences in thermally induced effects because the peaks of vertical stresses are recorded near the pipes (i.e., the closer the pipes, the closer the locations of peak stresses). Thermally induced vertical displacements ( $d_{v,th}$ ) represent the biggest differences in the design solutions comparison (Figure 2.12). In the evaluation of the thermally induced vertical displacements of the wall, no external vertical loads are applied to the EW. Because of the EW cooling, maximum (absolute) values are recorded at the EW's head (settlement) and base (heave).  $d_{v,th}$  are the result of a time-dependent process, increasing with time but independently of the pipe layout (Figure 2.12 (a)). Studying the pipe spacing,  $d_{v,th}$  are 16.7% higher for narrower pipe spacing, the maximum difference between narrow and large pipe spacing being  $\Delta d_{v,th} = 0.2$  mm, respectively (Figure 2.12 (b-f)). In every analyzed condition, the null point (i.e., the location that shows null thermally induced vertical displacement) lies in the fully embedded part of the EW. Following the EW displacement, also the ground at its sides displaces: vertical displacements (i.e., settlement) of the ground surface present a peak located at the wall-soil interface, with maximum value of 1.8 mm. At steady-flux, ground settlement is uniform along the longitudinal direction of the subway line. Settlement due to geothermal activation affects the soil's top surface up to a distance  $d_{x,th} \cong H_{wall}$  on the side of the EW. The recorded settlement halves with respect to the peak value at a location  $d_{x,0.5 th} \cong \frac{H_{wall}}{4}$  away from the wall. At steady flux, vertical and horizontal displacements are uniform all along the longitudinal direction of the subway line because of the bending stiffness offered by the nearby cross-sections of the EW.

A further set of analyses is performed to allow for a detailed description of the thermomechanical behavior of the EG. Three geothermally activated cases are studied: (a) ES only, (b) EW only and (c) the simultaneous activation of the two (EW+ES). The EG is here equipped with a W pipe layout with pipe spacing  $a = 0.30$  m both in the wall and in the slab. This was chosen to have the same pipe layout in both elements.



Axial force,  $N_{th}$ , is evaluated by integrating the thermally induced axial stress ( $\sigma_{a,th}$ , i.e. vertical for the wall and horizontal for the slab) on a linear cross section of length  $w_s$ , which represents the thickness of the structural element:

$$N_{th} = \int_{-w_s/2}^{w_s/2} \sigma_{a,th} ds \quad (2.5)$$

where  $s$  is the infinitesimal change over  $w_s$ .

Thermally induced shear force,  $V_{th}$ , is obtained as follows:

$$V_{th} = \int_{-w_s/2}^{w_s/2} \sigma_{xz,th} ds \quad (2.6)$$

Thermally induced bending moment,  $M_{th}$ , is derived by integrating  $\sigma_{a,th}$ , multiplied by the distance to the centerline,  $d_{cw}$ , along the cross-section of the structure:

$$M_{th} = \int_{-w_s/2}^{w_s/2} \sigma_{a,th} d_{cw} ds \quad (2.7)$$

In Figure 2.13 and Figure 2.14, thermally induced vertical and horizontal displacements and internal actions are presented. The top row relates to the wall while the bottom one to the slab.

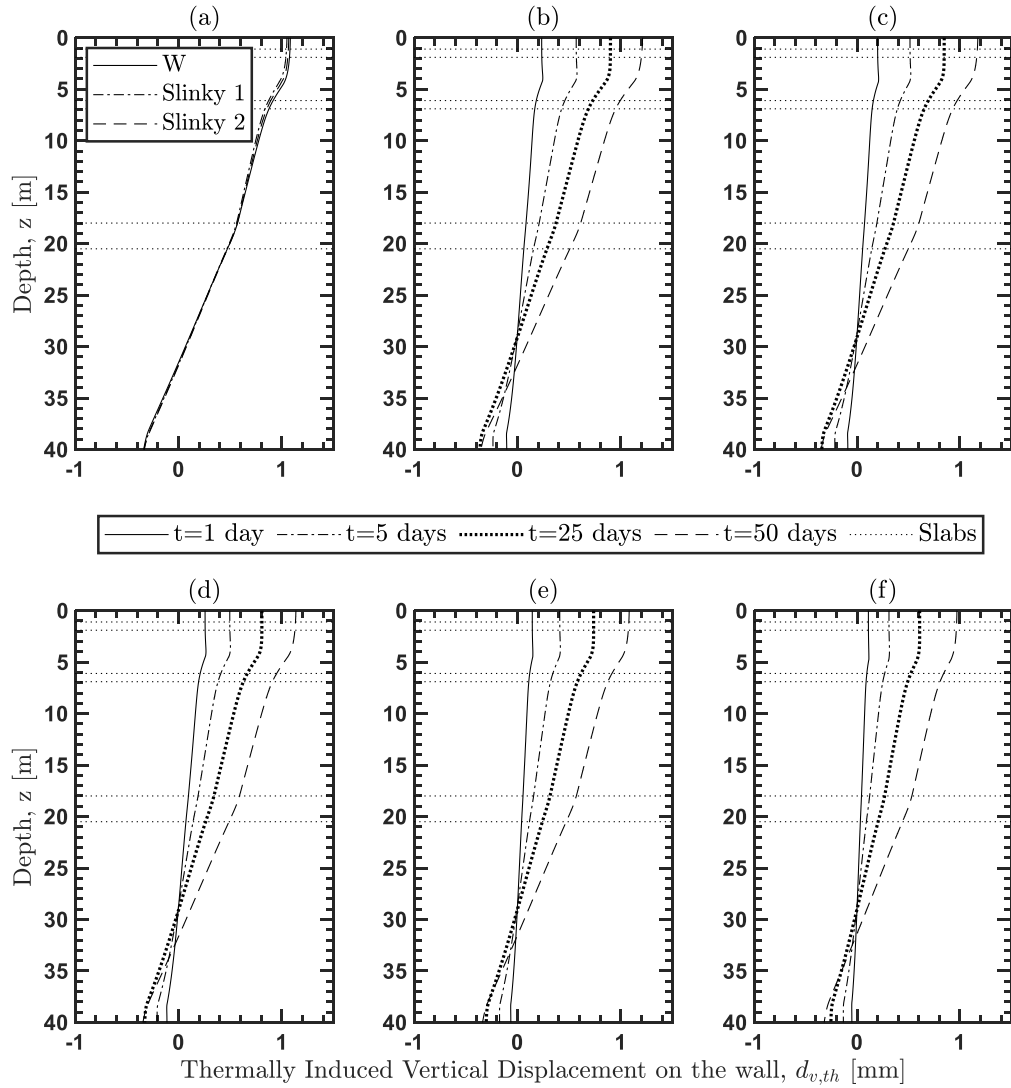


Figure 2.12 Thermally induced vertical displacements in the EW. (a) results for the pipe layout comparison. Results for the pipe spacing comparison: (b)  $a = 0.2$  m; (c)  $a = 0.3$  m; (d)  $a = 0.4$  m; (e)  $a = 0.5$  m; (f)  $a = 0.75$  m

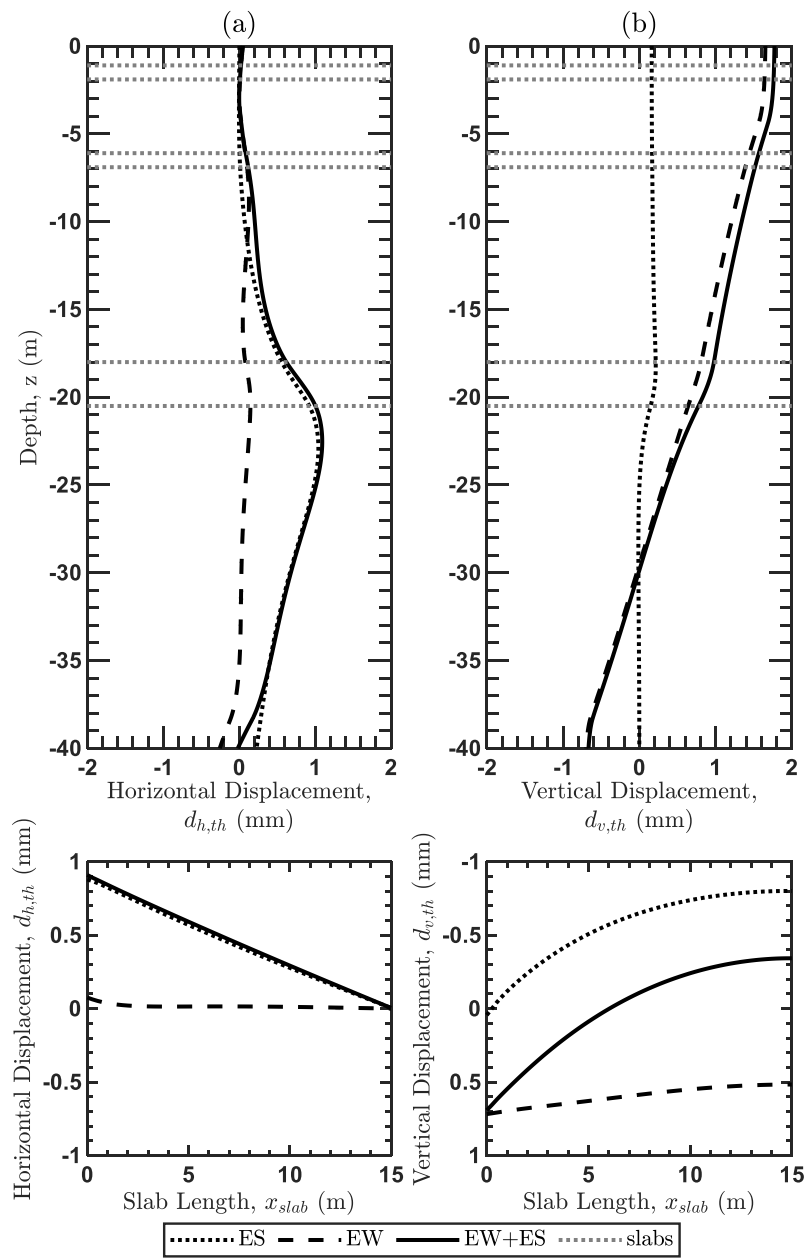


Figure 2.13. Thermally induced (a) horizontal and (b) vertical displacements: top row relates to the wall and bottom row to the slab

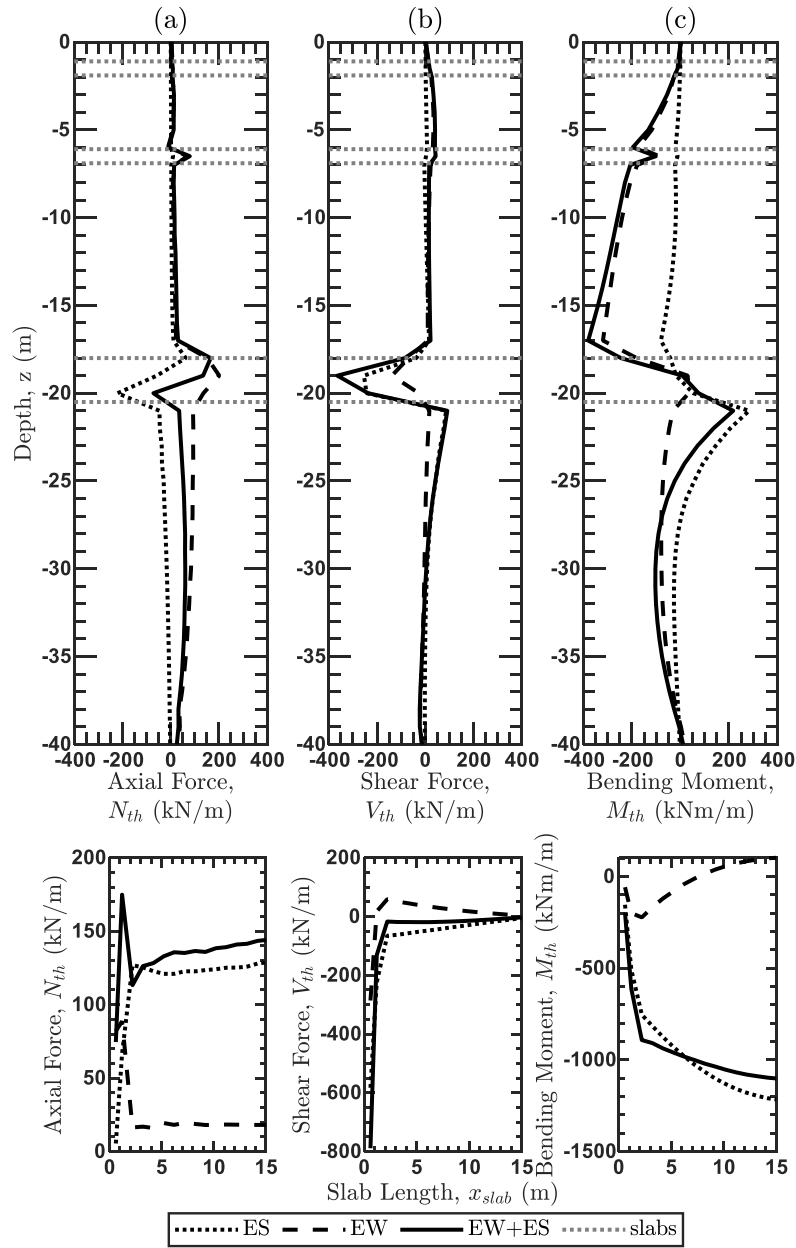


Figure 2.14. Thermally induced internal actions: (a) axial force, (b) shear force and (c) bending moment. Top row relates to the wall and bottom row to the slab

For ES, a tensile action is developed in the slab as a consequence of slab cooling due to geothermal operation, curvature is partially dissipated by vertical displacement and partially is blocked giving rise to internal actions. An upwards curvature and bending moment at the extrados (tensile stresses developed in the vicinity of the pipes) is shown. The slab displaces upwards (Figure 2.13) and the bending moment is negative (Figure 2.14), meaning that lower fibers undergo tensile actions. This behavior is expected and it is peculiar to thermal actions, similarly to what happens with energy piles (Knellwolf

et al., 2011; Moreni et al., 2003), but in flexural case. The lower fibers are not completely free to contract upon cooling, hence tension and bending is developed there. Slab geothermal activation has also an effect on the wall because it is inducing a localized shear action and bending moment at the wall-slab connection. Slab axial behavior results in a distribution of tensile axial force throughout the slab, displacing horizontally at the slab-wall connection and inducing a localized shear action in the wall. Slab bending moment is particularly high because of the high thickness of the structural element.

In the EW case, the axial behavior is similar to what shown before: the wall undergoes an axial shrinkage with top part that moves downwards and heaving at the bottom. The null point is located in the fully embedded zone, with the location of it that doesn't change among the three considered cases (Figure 2.13). The axial force is quasi constant and very closed to zero because of the distribution of axial stresses along the wall thickness: tensile stresses develop in the vicinity of the heat exchangers while compressive stresses develop moving towards the intrados (convective boundary condition) at the excavated side. The same, but with lower magnitude, applies for the fully embedded portion as shown in Figure 2.15.

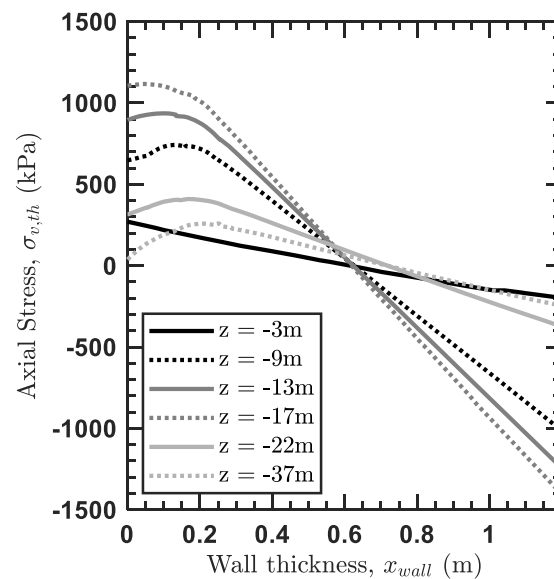


Figure 2.15. Axial stresses developed in the wall at different depths, at steady flux

The axial force in the wall causes a shear action in the slab which presents a peak closed to the wall-slab connection and then dissipates reaching 0 at the slab end on the right (symmetry axis). The axial wall movements affect the slab, which is settling following the settlement of the wall above the null point (Figure 2.13).

The flexural behavior is characterized by a curvature which is partially blocked due to the presence of constraints: the soil and the slabs. Bending moment is hence developed at the extrados (soil-wall interface) because of the tensile axial stresses developed in the vicinity of the pipes. It is higher at the excavated portion with respect to the fully embedded part because of the higher axial stresses (Figure 2.15)

developed in that region. Shear forces are developed mainly at the wall-slab connections due to structural interactions and stress redistribution in the concrete. The wall horizontal displacement (Figure 2.13) and shear force (Figure 2.14) generate axial displacement and axial force in the slab, both of low magnitude.

The third case, EW+ES, involves the simultaneous sum of the two effects previously described. Mutual wall-slab interactions are taking place: the activation of both elements is inducing localized axial force, shear force and bending moment at the wall-slab connection. The horizontal displacements in the wall and slab are, as expected, governed by the slab activation while the wall contribution is marginal. The wall vertical displacement is governed by the wall activation, while the slab vertical displacement follows the upwards curvature given by the slab activation but the shape is shifted downwards consequently to the downward vertical displacement induced by the wall activation and soil shrinkage below the subway tunnel (Figure 2.13). The internal actions in the wall involve, for the axial and shear forces, peaks closed to the wall-slab connection. The bending moment shape is similar to the EW case. The internal actions in the slab are: a tensile force is developed throughout the slab with a major contribution given by the slab activation and a minor, but non-negligible, contribution given by the wall. The shear action is lower in magnitude compared to the EW and ES cases as a consequence of the opposite shear action induced by the ES and EW cases, respectively. The bending moment present a major contribution given by the slab activation and a smaller one due to wall activation (Figure 2.14).

## 2.6 Conclusions

This paper summarizes the results of numerical simulations of a cast-in-place EW wall and ES. Three different heat exchanger design solutions are compared with respect to various aspects that characterize their hydrothermal behavior (*i.e.*, fluid flow velocity, pressure drop, pipe spacing, pipe layout, and base slab activation). Thermally induced mechanical effects are investigated with the emphasis on vertical and horizontal displacements and internal actions on three different wall-slab geothermal activation schemes: EW, ES and EW+ES.

The fluid flow regime inside the pipes plays an important role. Slightly turbulent flow represents the optimum solution as it enables 30% ÷ 40% higher power extraction than a laminar regime in the short term and 10% ÷ 20% higher power extraction over the long term, all without inducing significant thermal effects on the surrounding soil. The pressure drops between the inflow and outflow of the heat exchangers circuit increase with increasing fluid velocity: turbulent regime (*i.e.*,  $v_f = 0.2 \div 0.5$  m/s) allow to maximize the thermal power with limiting the pressure drops to  $\Delta p_f < 0.1$  bar. Pipe spacing and pipe layout have decisive effects on the definition of thermal behavior. The three pipe-layout designs perform in similar ways. The W solution provides slightly higher amount of power extraction but need longer pipe lengths. EW design can be optimized as follows. In cases involving short-term,

intermittent operation (e.g., daily- or weekly-based energy demands, such as for residential heating/cooling), pipe spacing should be as narrow as possible, using a W pipe layout, which of the three examined, is the one that presents the highest effectiveness. Alternatively, Slinky 1 could be employed when budget constraint is paramount: it enables to considerably minimize the quantity of pipe material but performs 4% less than the W shape. In cases involving continuous operation (e.g., supplying energy for industrial needs), wider pipe spacing should be preferable.

Very limited differences in thermo-mechanical behavior were recorded from varying the pipe layouts and spacing. Thermal activation induces a non-uniform temperature distribution in the geostructure which generates axial and transversal deformations, which are partly blocked by the presence of constraints and cause the development of internal actions (i.e., axial and shear force, bending moment). During geothermal operation, mutual wall-slab interactions are recorded. Bending moment seems to be the most severe internal action in the structure. It is worth noting that, conversely to what happens for widely known EG such as energy piles, thermally induced effects in EW and ES involve two concurrent mechanisms: an axial and a bending effect. The concurrent happening of the two mechanisms is due to (i) geometry considerations (i.e., soil and structure constraint the EG deformation in a nonuniform way), (ii) thermal reasons (i.e., the heat exchangers location is non symmetrical with respect to the EG's axis) and to (iii) environmental considerations (i.e., the EG is exposed to air interfaces), generating a nonuniform temperature variation distribution.

# Chapter 3      Hydrothermal interactions in energy walls

**Disclaimer:** The content of this chapter has been published in the following journal paper:

Zannin, J., Ferrari, A., Pousse, M., & Laloui, L. (2020). Hydrothermal interactions in energy walls. *Underground Space*. <https://doi.org/10.1016/j.undsp.2020.02.001>

**My contribution:** Conceptualization, Methodology, Formal analysis, Investigation, Data Curation, Writing – Original Draft, Visualization.

## 3.1 Foreword

Energy geostructures (EGs) employ heat exchangers embedded in concrete geostructures, such as piles, walls, tunnels, and sewers. In this study, energy walls (EWs) are studied with an emphasis on the following objectives: (i) to understand the fundamentals of hydrothermal interactions acting in the vicinity of EWs caused by groundwater seepage in saturated soil; (ii) to highlight hydraulically induced thermal effects and their consequences on the thermal performance of EWs. Extensive three-dimensional hydrothermal finite element analyses were performed considering two groundwater flow conditions: perpendicular and parallel to the EW. The thermal activation of the geostructure locally modifies the flownet with respect to the non-isothermal case because of the temperature dependency of the water properties. Mutual interactions between seepage directions and thermal activation are analysed. Remarkable thermal interactions are detected within the heat exchangers. The thermal behaviour of EGs is highly affected by an incorrect evaluation of the hydraulically induced thermal effects, which may result in an overestimation of the thermal behaviour. Conversely, an efficient thermal design that considers such interactions may increase the thermal potential of EGs.

## 3.2 Introduction

To decrease environmental pollution, satisfy energy requirements, and replace depleting non-renewable energy sources, renewable energies are necessitated. Among the various renewable sources, geothermal energy can significantly contribute towards satisfying these goals, as it represents the second most abundant source of primary energy on Earth (Lee et al., 2007). Different types of geothermal plants exist, and a classification can be established based on the depth of exploitation. Systems operating at depths lower than 400 m are called *shallow geothermal systems* and are characterised by low



temperature and enthalpy. These applications encompass several types, including energy geostructures (EGs). EGs involve regular reinforced concrete geostructures (*i.e.*, piles, diaphragm walls, tunnels, and shafts) with heat exchangers (typically plastic pipes) secured to a reinforcement cage (Adam & Markiewicz, 2009; Brandl et al., 2010b; Laloui & Rotta Loria, 2019). The pipes are subsequently connected to a heat pump to provide and subtract energy to a served structure. The heat pump is connected to a secondary circuit, forming a ground-source heat pump system. Within EGs, soils function as an extraction and storage media. The use of such structures started from the mid-1980s with applications to energy piles and from the mid-1990s to energy walls (EWs) and tunnels (Adam & Markiewicz, 2009; Brandl, 1998). The use of such technologies resulted in increased installations beginning from the mid-2000s (Di Donna et al., 2017; Lund & Boyd, 2016).

Among the various types of EGs, EWs are addressed in this study. Recently, various studies regarding this topic (Amis et al., 2010; Bourne-Webb et al., 2016; Di Donna et al., 2016; Di Donna et al., 2017; Habert & Burlon, 2015; Kürten et al., 2015b; Rui & Yin, 2017; Sterpi et al., 2017; Sun et al., 2013; Xia et al., 2012) have been conducted worldwide but a number of challenges remain. In particular, a complete understanding of thermal exchanges and the consequent behaviour of porous materials involved is crucial. However, little evidence on this topic is available in the literature. This phenomenon was investigated in (Kürten et al., 2015a, 2015b) through a small-scale laboratory test and numerical analyses. The case of a thermo-active wall was investigated in (Cornelio et al., 2016; Di Donna, 2016), where the different thermal behaviour of heat exchangers with and without groundwater flow in soil was highlighted.

The study of the thermal behaviour of EG pairs with a thorough understanding of the mechanism of soil around an EG. However, none of the abovementioned publications have presented a detailed study on hydrothermal effects in soil and the consequent thermal response of heat exchangers. Hence, the objectives of this study are twofold: *(i)* to analyse non-isothermal flow in EWs; *(ii)* to highlight hydraulically induced effects on the thermal exploitation of thermo-active walls.

The accomplishment of both objectives requires the following: *(i)* hydrothermal couplings to be considered such that various multiphysical phenomena involved in EG operations are included; and *(ii)* three-dimensional (3D) models to be employed, which include *(a)* different groundwater flow directions in soil, *(b)* a full description of heat exchanger location and related fluid flow in pipes. The problem is addressed from different scales: from the infrastructure scale (order of magnitude of  $10^2 \text{ m}^3$ ) to the heat exchanger scale (order of magnitude of  $10^{-1} \text{ m}^3$ ). Mutual interactions between these two different scales are highlighted and employed to explain the variations in thermal behaviour based on environmental conditions. Such evaluations are essential to estimate the thermal potential of a site equipped with EWs.

### 3.3 Numerical modelling of hydrothermal behaviour of EWs

To achieve the objectives, extensive numerical analyses involving a high number of thermo-hydraulic parameters were performed. When analysing the seepage around an embedded infrastructure, two limit cases for the groundwater velocity direction may be relevant: perpendicular and parallel to the infrastructure (Figure 3.1).

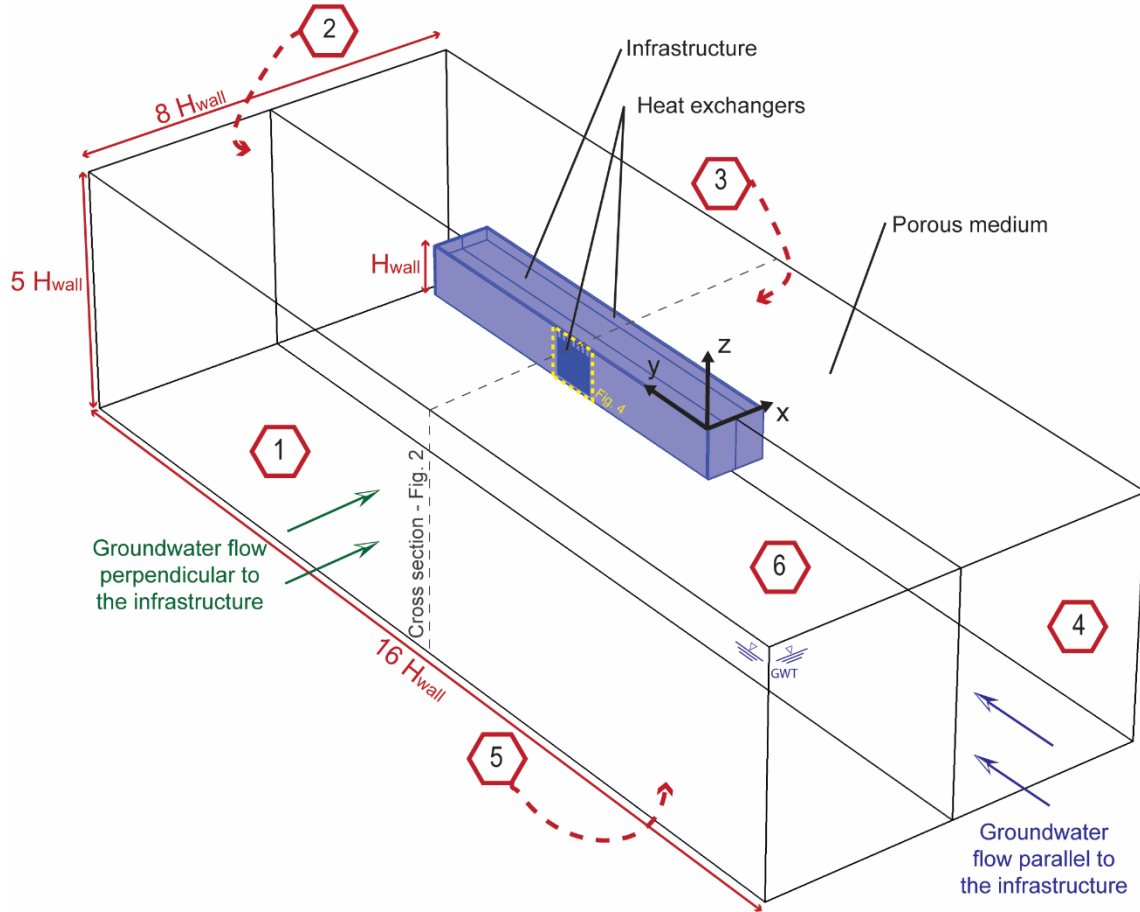


Figure 3.1 3D model, indicators of groundwater flow directions and boundary conditions: 1- Left; 2- Rear; 3- Right; 4- Front; 5- Bottom; 6- Top

In the case of EWs, several heat exchange modes occur. The wall geometry presents soil on one side and air at the top portion of the excavated side. When a geostructure is thermally activated, a heat carrier fluid (HCF) is circulated inside the embedded pipes, and heat is exchanged by convection within the HCF and by conduction through the walls of the pipes. Heat is exchanged by conduction in the concrete wall and the surrounding soil. The presence of groundwater flow in the geomaterials propagates the heat around the geostructure (convection) in the seepage direction. At the top part of the excavated side, a heat exchange between the wall and air occurs. This problem is governed by the thermal and hydraulic properties of the materials and the existing boundary conditions. The wall–air interface can be modelled using convective boundary conditions (Bourne-Webb & da Costa Goncalves, 2016). Moreover, the non-

isothermal fluid flow in the heat exchangers must be included. The convective heat transfer at the excavated side may be important for the quantification of thermal behaviour of the EGs; however, it is not presented herein as the focus of this study is on the hydrothermal interactions towards the unexcavated side. Figure 3.2 shows the structural geometry.

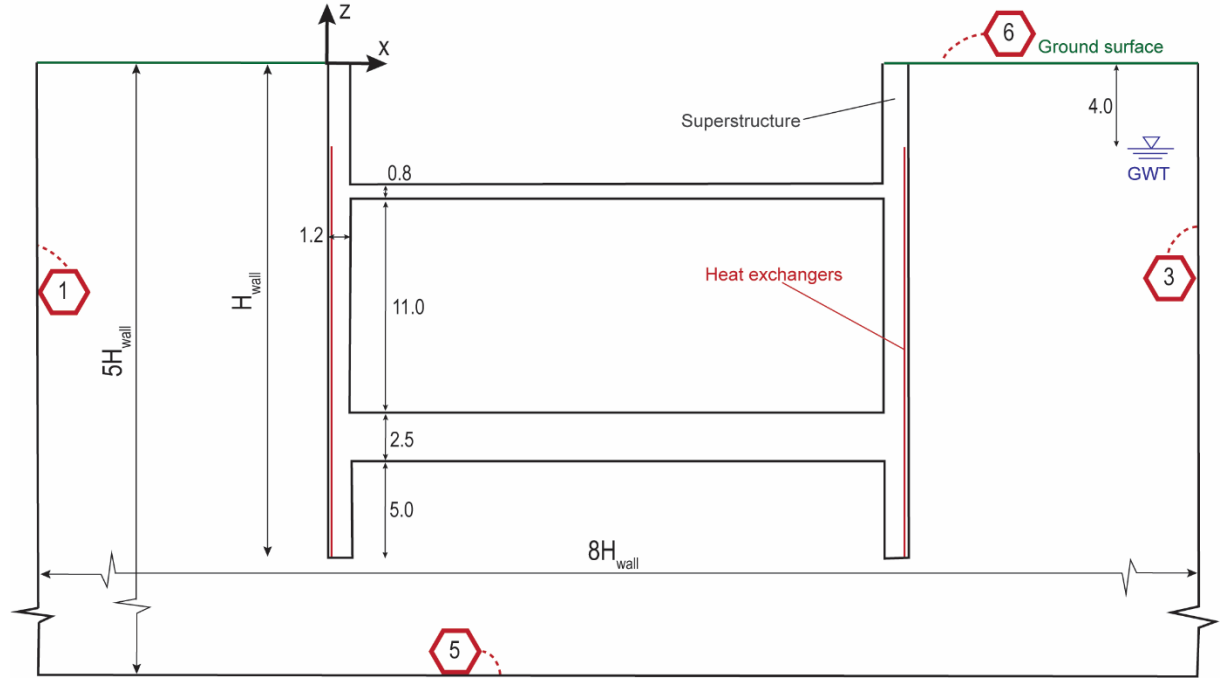


Figure 3.2 Cross section of the infrastructure (Note: the figure is not scaled, dimensions in metres)

### 3.3.1 Mathematical formulation

Commercial software Comsol Multiphysics® (COMSOL Inc., 2018) was employed to perform the hydrothermal numerical analyses. Both soil and concrete were considered as porous media composed of a solid matrix and a liquid phase (Bourne-Webb et al., 2016; Dean et al., 2005; Diamond, 1999; Dupray et al., 2014; Kearsley & Wainwright, 2001, 2002; Kumar & Bhattacharjee, 2003). The hydrothermal coupling in the porous media was considered through the local thermal equilibrium hypothesis, which assumes the pointwise equality of temperature in solid and liquid phases (Nield, 1998; Nield & Bejan, 2006). The pipes were composed of tubes filled with a fluid in motion.

The governing equations are the following. The mass conservation equation is applied to the fluid phase of the porous materials:

$$\frac{\partial}{\partial t}(n\rho_w) + \text{div}(\rho_w \mathbf{v}_{rw}) = 0 \quad (3.1)$$

where  $t$  is the time,  $\rho_w$  the fluid density,  $n$  the porosity, and  $\mathbf{v}_{rw}$  the fluid velocity defined by Darcy's law, which can be written by considering the hypothesis of homogeneous and isotropic porous media as follows:

$$\mathbf{v}_{rw} = -k \mathbf{grad} \left( z + \frac{p_w}{\gamma_w} \right) \quad (3.2)$$

where  $k$  is the hydraulic conductivity,  $p_w$  the fluid pressure, and  $\gamma_w = \rho_w g$ , where  $g$  represents the acceleration due to gravity. The hydraulic conductivity is expressed as a function of the geometric permeability  $k^*$  of the porous material, fluid density  $\rho_w$ , fluid dynamic viscosity  $\mu_w$ , and  $g$ , as follows:

$$k = \frac{k^* \rho_w g}{\mu_w} \quad (3.3)$$

The groundwater flow regime in the porous medium is considered to be laminar (Vulliet et al., 2016).

The energy conservation equation is split into two parts: one related to porous materials and another related to fluid flow in heat exchangers. The portion referred to as the porous materials (*i.e.*, soil and concrete) is:

$$\text{div}(\lambda \mathbf{grad}(T)) = \rho C_p \frac{\partial T}{\partial t} + \rho_w C_{p,w} \mathbf{v}_{rw} \cdot \mathbf{grad}(T) \quad (3.4)$$

where  $\rho C_p$  is the effective volumetric heat capacity at constant pressure, defined as

$$\rho C_p = (1 - n) \rho_s C_{p,s} + n \rho_w C_{p,w} \quad (3.5)$$

with  $C_{p,s}$  and  $C_{p,w}$  the heat capacities at constant pressure of the solid and fluid phases, respectively;  $\rho_s$  is the solid matrix density;  $T$  is the temperature;  $\lambda$  is the effective thermal conductivity of the porous medium evaluated as:

$$\lambda = (1 - n) \lambda_s + n \lambda_w \quad (3.6)$$

where  $\lambda_s$  and  $\lambda_w$  are the thermal conductivities of the solid and fluid phases, respectively.

The energy conservation equation related to the incompressible fluid flow in the heat exchangers accounts for the convective heat transfer within the fluid and the conductive heat transfer through the pipe wall (Batini et al., 2015):

$$\rho_f c_f A_p \frac{\partial T_{bulk,f}}{\partial t} + \rho_f c_f A_p \mathbf{u}_f \cdot \mathbf{grad}(T_{bulk,f}) = \text{div}[A_p \lambda_f \mathbf{grad}(T_{bulk,f})] + \dot{q}_p \quad (3.7)$$

with  $\rho_f$ ,  $c_f$ ,  $T_{bulk,f}$ ,  $\mathbf{u}_f$ ,  $\lambda_f$  the bulk density, specific heat at constant pressure, bulk temperature, tangential velocity, and thermal conductivity of the circulating fluid, respectively.  $A_p$  is the pipe cross section. The heat flux per unit length exchanged through the pipe wall is accounted for by  $\dot{q}_p$ , which is defined as:

$$\dot{q}_p = (UP_p)_{eff} (T_{ext} - T_{bulk,f}) \quad (3.8)$$

Where

$$(UP_p)_{eff} = \frac{2\pi}{\frac{1}{r_{int} + \frac{1}{\lambda_p} \ln\left(\frac{r_{ext}}{r_{int}}\right)}} \quad (3.9)$$

is related to an effective value of the pipe heat transfer coefficient (internal film and wall resistances);  $P_p = 2\pi r_{int}$  is the wetted perimeter of the pipe cross section;  $r_{int}$  and  $r_{ext}$  are the inner and the external radii, respectively;  $T_{ext}$  is the external temperature of the pipe;  $h_{int} = \frac{Nu \lambda_p}{d_h}$  is the convective heat transfer coefficient for the fluid inside the pipe;  $\lambda_p$  is the thermal conductivity of the pipe wall;  $d_h = 4A_p/P_p$  is the hydraulic diameter;  $Nu$  is the Nusselt number, which, from the theory of fluid dynamics, is a function of the Reynolds,  $Re$  and Prandtl,  $Pr$  numbers.

$$Nu = \max(3.66; Nu_{turb}) \quad (3.10)$$

where  $Nu_{turb}$  can be evaluated using the Gnielinski formula for the turbulent regime (Gnielinski, 1976):

$$Nu_{turb} = \frac{\left(\frac{f_D}{8}\right)(Re - 1000)Pr}{1 + 12.7\sqrt{\frac{f_D}{8}}(Pr^{2/3} - 1)} \quad (3.11)$$

$$f_D = \left[ -1.8 \log_{10} \left( \frac{6.9}{Re} \right)^{-1/2} \right] \quad (3.12)$$

with  $f_d$  the friction factor (for extremely low relative roughness) using the formulation of Colebrook (Colebrook et al., 1939; Haaland, 1983).

For a fluid flow in a pipe,  $Re$  is defined as:

$$Re = \frac{u_{f,i} r_{int}}{\nu_f} \quad (3.13)$$

where  $\nu_f$  is the kinematic viscosity of the fluid.

To obtain a hydrothermal coupling in pipes, the Navier–Stokes equations for incompressible fluid flows in pipes (Barnard et al., 1966) were employed.

### 3.3.2 Material characterisation

The modelled soil profile is related to a uniform, isotropic, sandy-gravelly layer (Batini et al., 2015). Concrete is modelled as an impermeable porous medium (Asadi et al., 2018; Bourne-Webb et al., 2016; Dean et al., 2005; Kearsley & Wainwright, 2001; Kim et al., 2003). The pipes were made of high-density polyethylene and the circulating fluid was water, as summarised in Table 3.2. Water was present inside the pipes and inside the porous media. The input parameters for water were as follows: density  $\rho_w$ , dynamic viscosity  $\mu_w$ , thermal conductivity  $\lambda_w$ , and heat capacity  $C_{pw}$ . All of them are temperature-dependent parameters, as shown in Figure 3.3.

Table 3.1 Material properties

	Material	Porosity $n$ (-)	Solid density $\rho_s$ (kg/m <sup>3</sup> )	Geometric Permeability $k^*$ (m <sup>2</sup> )	Heat capacity at constant pressure $C_{p,s}$ (J/(kg K))	Thermal conductivity $\lambda_s$ (W/(m K))
<i>Soil</i>	Sandy Gravelly Moraine	0.35	2735	$10^{-10}$	890	1.50
<i>Infrastructure</i>	Concrete	0.10	2722	-	837	2.00
<i>Pipes</i>	HDPE	-	-	-	-	0.42

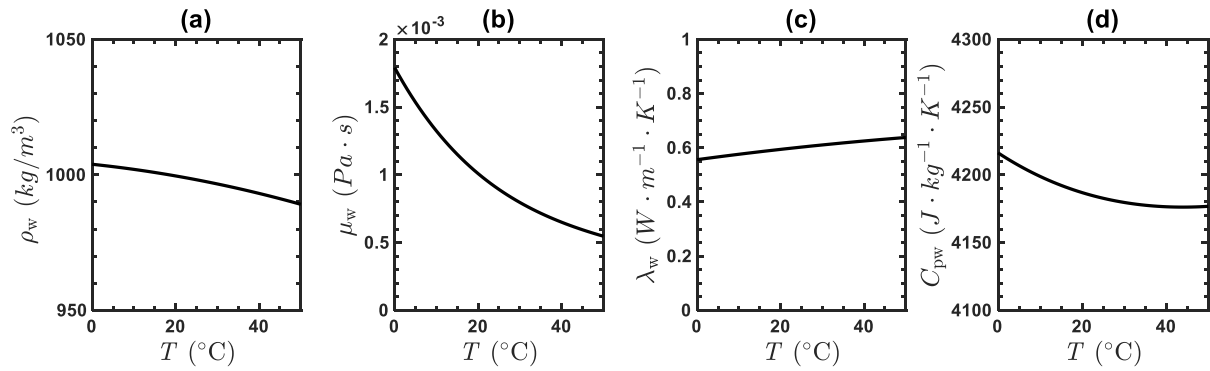


Figure 3.3 Temperature-dependent water properties: (a) Density, (b) Dynamic viscosity, (c) Thermal conductivity, (d) Heat capacity

### 3.3.3 3D model; boundary and initial conditions

The underground infrastructure that accommodates an excavated underground space was modelled based on the following geometrical features: wall thickness  $t_{wall} = 1.20\text{ m}$ , wall height  $H_{wall} = 25.5\text{ m}$ , longitudinal length  $L_{wall,tot} = 8H_{wall}$ , raft width  $L_{raft} = 30\text{ m}$ , and raft height  $h_{raft} = 2.50\text{ m}$ . The full 3D model accounts for the following dimensions in the  $x$ ,  $y$ , and  $z$  coordinates:  $8H_{wall}$ ,  $16H_{wall}$ , and  $5H_{wall}$ , respectively (Figure 3.1 and Figure 3.2). The groundwater table (GWT) is located 4 m below the ground surface, and the undisturbed soil temperature is fixed to  $T_{soil} = 15\text{ }^{\circ}\text{C}$  to represent the average temperature at the shallow depth of the soil in the European climate. Heating and cooling operations were simulated. Six W-shaped heat exchanger loops were modelled at the central portion of the geostructure (Figure 3.1), which could fit into 3 m panels (Figure 3.4). They were buried in the concrete wall and located 15 cm from the wall–soil interface. After a detailed analysis, only six loops were used: after the 6<sup>th</sup> pipe loop (included), the behaviour of the heat exchangers remained constant (see Section 3.4.2).

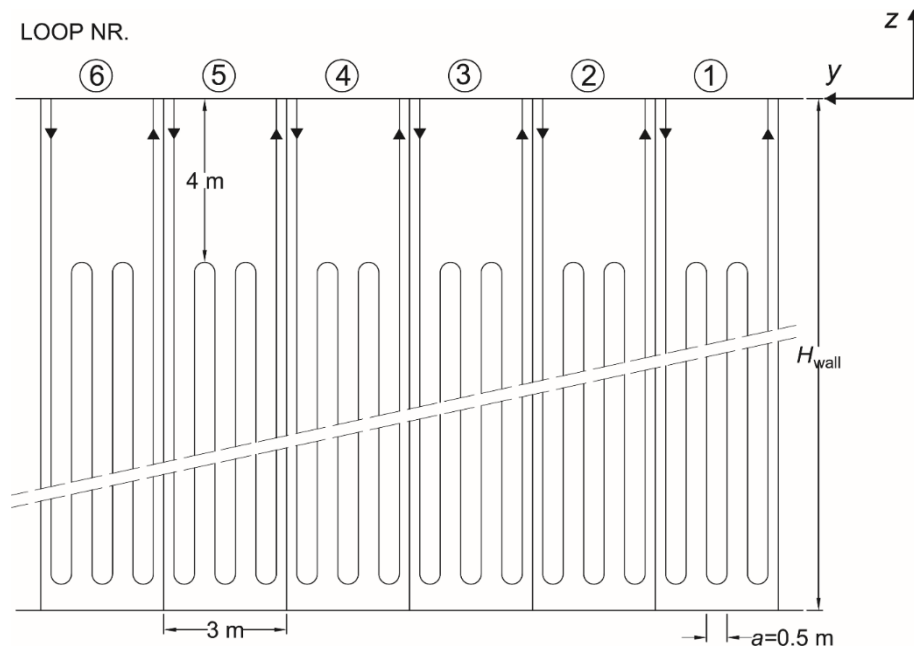


Figure 3.4 Pipe loop configuration and numbering (Note: zoom-in as indicated in Figure 3.4)

The finite element model included tetrahedral, vertex, and edge elements. The pipes and concrete wall were discretised with elements having dimensions that range between 10 cm (closer to the pipe) to 1 m (external portions of the wall). For the surrounding soil, the mesh became coarser as it propagated farther from the EG. The infrastructure included 1'077'366 elements, while the entire geometry contained 1'637'677 elements. Subsequently, two different submodels were set up to analyse the two main groundwater flow directions. Those models differed only by the applied boundary conditions (Figure 3.1 and Table 3.2). For both models, the air zone inside the infrastructure was adiabatic (see Section 3.3).

Table 3.2 Boundary conditions for groundwater flow perpendicular to the wall, where  $H$  represents the total hydraulic head,  $\mathbf{n}$  is the unitary outflow normal vector to the selected surface, and  $\dot{\mathbf{q}}$  is the heat flux (Note: “b.c.” stands for boundary condition)

Boundary nr.	Perpendicular groundwater flow		Parallel Groundwater flow	
	Hydraulic b.c.	Thermal b.c.	Hydraulic b.c.	Thermal b.c.
1	$H = -4.0 \text{ m}$	$T = 15 \text{ }^{\circ}\text{C}$	$\mathbf{n} \cdot \rho_w \mathbf{v}_{rw} = 0$	$\mathbf{n} \cdot \dot{\mathbf{q}} = 0$
2	$\mathbf{n} \cdot \rho_w \mathbf{v}_{rw} = 0$	$\mathbf{n} \cdot \dot{\mathbf{q}} = 0$	$H = \begin{cases} -7.5 \text{ m} \\ -11.0 \text{ m} \\ -18.0 \text{ m} \end{cases}$	$\mathbf{n} \cdot \dot{\mathbf{q}} = 0$
3	$H = \begin{cases} -5.25 \text{ m} \\ -6.5 \text{ m} \\ -9.0 \text{ m} \end{cases}$	$\mathbf{n} \cdot \dot{\mathbf{q}} = 0$	$\mathbf{n} \cdot \rho_w \mathbf{v}_{rw} = 0$	$\mathbf{n} \cdot \dot{\mathbf{q}} = 0$
4	$\mathbf{n} \cdot \rho_w \mathbf{v}_{rw} = 0$	$\mathbf{n} \cdot \dot{\mathbf{q}} = 0$	$H = -4.0 \text{ m}$	$T = 15 \text{ }^{\circ}\text{C}$
5	$\mathbf{n} \cdot \rho_w \mathbf{v}_{rw} = 0$	$T = 15 \text{ }^{\circ}\text{C}$	$\mathbf{n} \cdot \rho_w \mathbf{v}_{rw} = 0$	$T = 15 \text{ }^{\circ}\text{C}$
6	$\mathbf{n} \cdot \rho_w \mathbf{v}_{rw} = 0$	$T = 15 \text{ }^{\circ}\text{C}$	$\mathbf{n} \cdot \rho_w \mathbf{v}_{rw} = 0$	$T = 15 \text{ }^{\circ}\text{C}$

The imposed temperature at the groundwater inflow boundary and at boundaries 1 and 4 (Figure 3.1) was set to  $T_{soil} = 15 \text{ }^{\circ}\text{C}$ . The solvers were used in the analysis: a stationary solver where the thermal and hydraulic boundary conditions were applied; a time-dependent solver that used the stationary solution as the initial condition, in which the system was geothermally activated, and lasted 50 days to attain a steady-flux condition. The groundwater flow was determined by imposing different hydraulic heads at the inflow and outflow boundaries. The following undisturbed average groundwater flow velocities were considered: 0.5, 1.0, and 2.0 m/d.

The pipes have an inner diameter of 25 mm and an outer diameter of 32 mm. The circulating fluid in the pipes is water. It has an imposed inflow velocity of 0.5 m/s. Winter and summer operations were simulated by imposing a constant inflow temperature in the pipes of  $T_{IN,W} = 5 \text{ }^{\circ}\text{C}$  and  $T_{IN,S} = 25 \text{ }^{\circ}\text{C}$ , separately. The choice of the thermal input were selected to enable: (i) short-term thermal responses to be detected, similarly to the intermittent operation reported by (Xia et al., 2012), and (ii) steady flux conditions, which is representative of long-term continuous operations. The pipes in the shallower 4 m of the structure were perfectly insulated (thermal conductivity of the pipe wall was set to 0 W/m/K). This is typically performed in practice to limit thermal effects from the ground surface. In this case, the location depth of the pipes was coincident with the GWT.

### 3.4 Results

The results of the numerical simulations are presented here, focusing on 3D seepage around the underground infrastructure. For various groundwater velocities, the results of the isothermal



analyses (*i.e.*, without geothermal activation) are compared with the wall heating and cooling cases (*i.e.*, summer and winter modes, respectively).

The analysis of hydrothermal interactions on EWs involve two non-isothermal processes occurring simultaneously: fluid flow in pipes and thermal diffusion (plus groundwater seepage) in soil. Once the system is geothermally activated, both are time-dependent processes of different time and space scales. Particularly, soil temperature diffusion evolves with time and space. In the hypothesis of a uniform, homogeneous, and isotropic soil mass in a two-dimensional (2D) plain strain case at the steady-state regime, the case of a fully saturated porous medium heated from the side has been presented by Nield & Bejan, 2006. In that case, the soil domain was bounded by adiabatic surfaces on the top and bottom and constant temperatures (hot and cold, separately) were applied on the left and right sides. Gravity acceleration was vertical and oriented downwards, while the water saturating the porous medium was still. The resulting effect was a buoyancy-driven flow near the heated side and a downward-directed flow toward the cooled side (Figure 3.5). The circular flow is described by a boundary layer in the vicinity of the heated/cooled side. The magnitude of the velocity field decreases with increasing distance from the sides. The gravity acting on the density variations ( $\rho(T) g$ ) induces a buoyancy-driven flow in the vicinity of the wall-soil interface in the case of wall heating because of the temperature dependency of water density and dynamic viscosity. The opposite occurs during cooling.

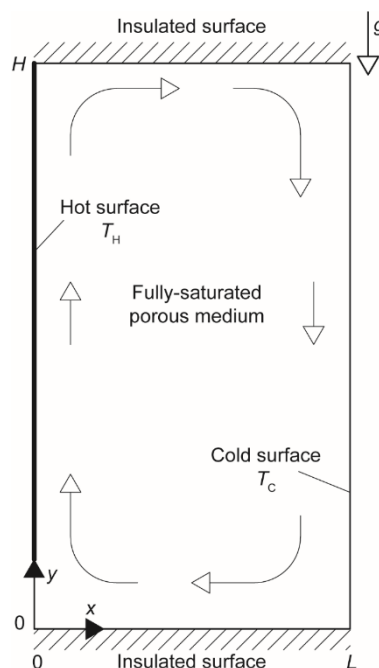


Figure 3.5 2D model of a fully saturated porous medium heated from the side (adapted from Nield & Bejan, 2006)

Unlike such a case, for a three-dimensional thermo-active wall as shown in Figure 3.1 and Figure 3.2, heating occurs on one side only and no bottom boundary is required because the soil volume below the wall is considered in the model. Moreover, the top boundary is related to the ground surface and the right boundary is placed sufficiently far from the wall to prevent any border effects. Such geometric

variations induce a circular flow around the EW with a predominant velocity flow at the wall–soil interface and a significant velocity decrease with increasing distance from the EW. An example is shown in Figure 3.6.

If the water saturating the soil is moving because of the groundwater flow, different results are expected depending on the seepage direction induced by the fluid-structure contact. Two main seepage directions are studied herein: groundwater flow perpendicular and parallel to the infrastructure.

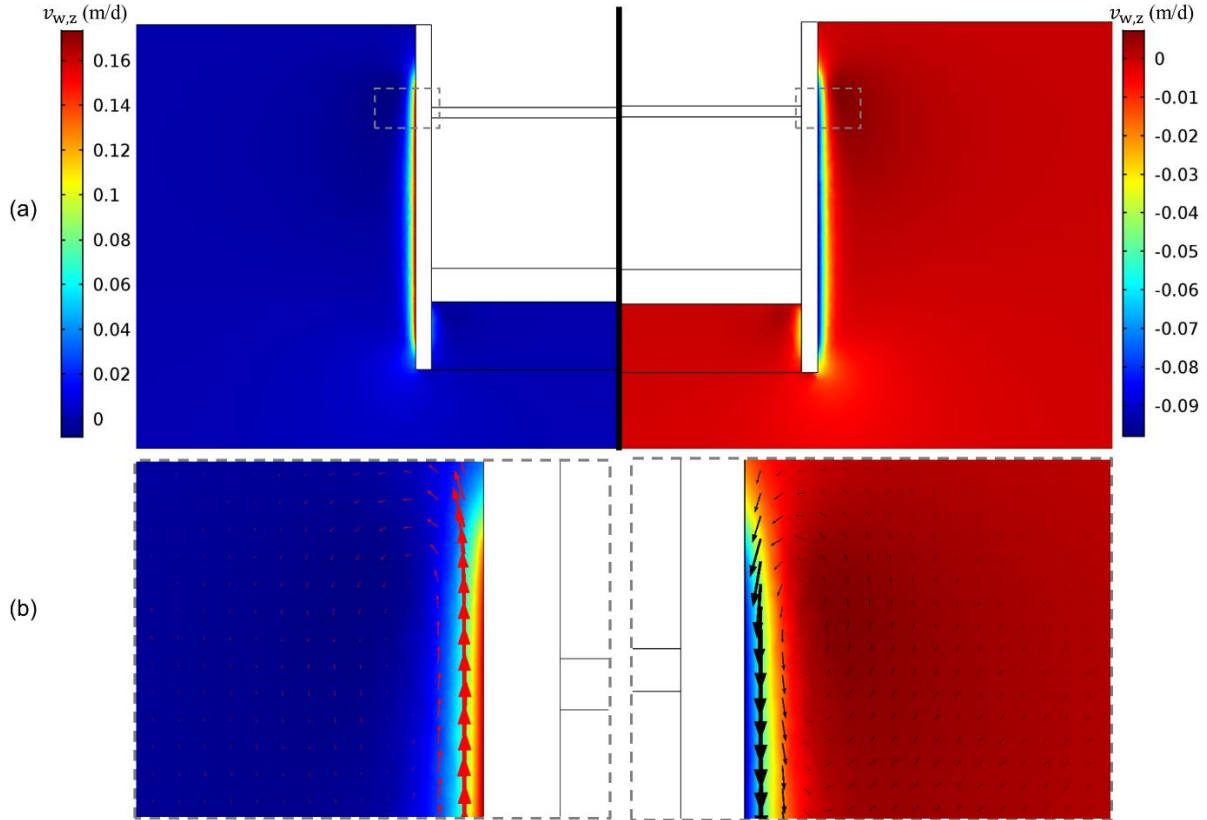


Figure 3.6 (a) Contour plot of the vertical component of the groundwater velocity ( $v_{w,z}$ ) zoomed in the vicinity of the geo-structure; (b) Zoomed-in image of selected zones with arrows indicating the groundwater velocity vector for wall heating (left) and cooling (right)

### 3.4.1 Groundwater flow perpendicular to the infrastructure

When the direction of seepage is perpendicular to the wall, the undisturbed groundwater flow is directed on the  $x$ -direction, intersecting the infrastructure at the longest edge and generating a border effect on the two longitudinal sides of the wall. In the portion of the wall that is not affected by the border effect (Figure 3.7), the groundwater touches the wall in the perpendicular direction; hence, seepage around the infrastructure occurs (*i.e.*, water flows downwards, subsequently below the infrastructure, and finally upwards again on the right side of the infrastructure). At the wall–soil interface, the seepage is governed by the vertical component of the velocity vector,  $v_{f,z}$ , which is lower with respect

to the undisturbed velocity at the far field ( $v_{f, far\ field} \approx v_{f,x}$ ). On average, considering the range of undisturbed groundwater velocity mentioned in Section 3.3.3, the fluid velocity at the wall–soil interface is  $\approx \frac{1}{8}$  to  $\frac{1}{3}$  that of  $v_{f, far\ field}$ . For the left-side wall of Figure 3.7, the velocity at the wall–soil interface changes slightly with temperature exchange: during wall heating, the velocity decreases (the opposite for cooling). For a  $\Delta T \cong \pm 10\ ^\circ\text{C}$ , where  $\Delta T$  represents the temperature difference between soil and the HCF, the corresponding velocity variation is  $\Delta v_{f,z} = \mp 0.01\ \text{m/d}$ . The opposite occurs at the wall located at the right side of the infrastructure.

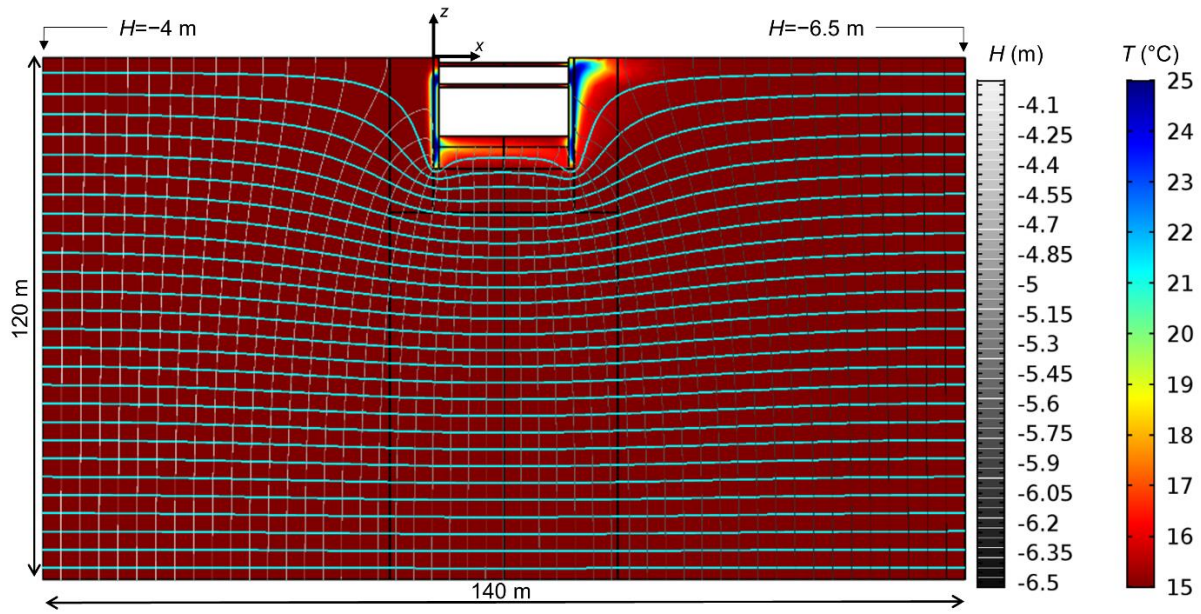


Figure 3.7 Temperature contour plot for groundwater flow perpendicular to the infrastructure with flownet: streamlines (light blue) and equipotential lines of the hydraulic head (H, grayscale)

In studying hydraulically induced thermal interactions, it is interesting that the seepage direction is parallel to the thermal exchange; hence, the circular motion induced by thermal activation apart from that of the EW is not visible. Further, the heat propagated in the seepage direction.

Moreover, the seepage direction was perpendicular to the position of the pipe loops; hence, no hydraulically induced thermal interactions occurring between adjoining pipe loops were detected. Conversely, because the heat propagated from one wall to the other (from left to right, on Figure 3.7), the left wall demonstrated a slightly higher ( $\pm 1\ \text{W/m}^2$ ) power extraction/injection with respect to the right wall. The distance between the two walls was large in this case; hence, differences in terms of thermal behaviour could be considered negligible in this range of groundwater velocities.

### 3.4.2 Groundwater flow parallel to the infrastructure

In this case, the undisturbed groundwater flow is parallel to the infrastructure direction ( $v_{f,y}$ ); hence, the groundwater flow intersects the geostructure in the shortest edge, generating a seepage laterally and below the infrastructure. A border effect occurs, which affects a portion of the infrastructure for a longitudinal length of  $d_{b,y} \cong 3.5H_{wall}$ . Apart from the regions affected by the border effect, the groundwater flow is directed in the  $y$ -direction, while the heat transfer occurs on the  $xz$  plane, perpendicular to the groundwater flow. According to the mathematical formulation in Section 3.3.1, when the structure is thermally activated, the velocity vector is subjected to a modification with respect to the isothermal case. During winter operation (*i.e.*, wall cooling), the distributions of water density and dynamic viscosity induce a circular groundwater motion in addition to the thermo-active wall directed downwards at the wall–soil interface. The opposite occurs during heating. This effect occurs at every adjoining cross section perpendicular to the EW; hence, it affects the overall flownet where the thermal exchange occurs. As shown by the longitudinal cross section at the wall–soil interface (Figure 3.8), the streamlines present an upward and downward velocity component for summer and winter operations, respectively.

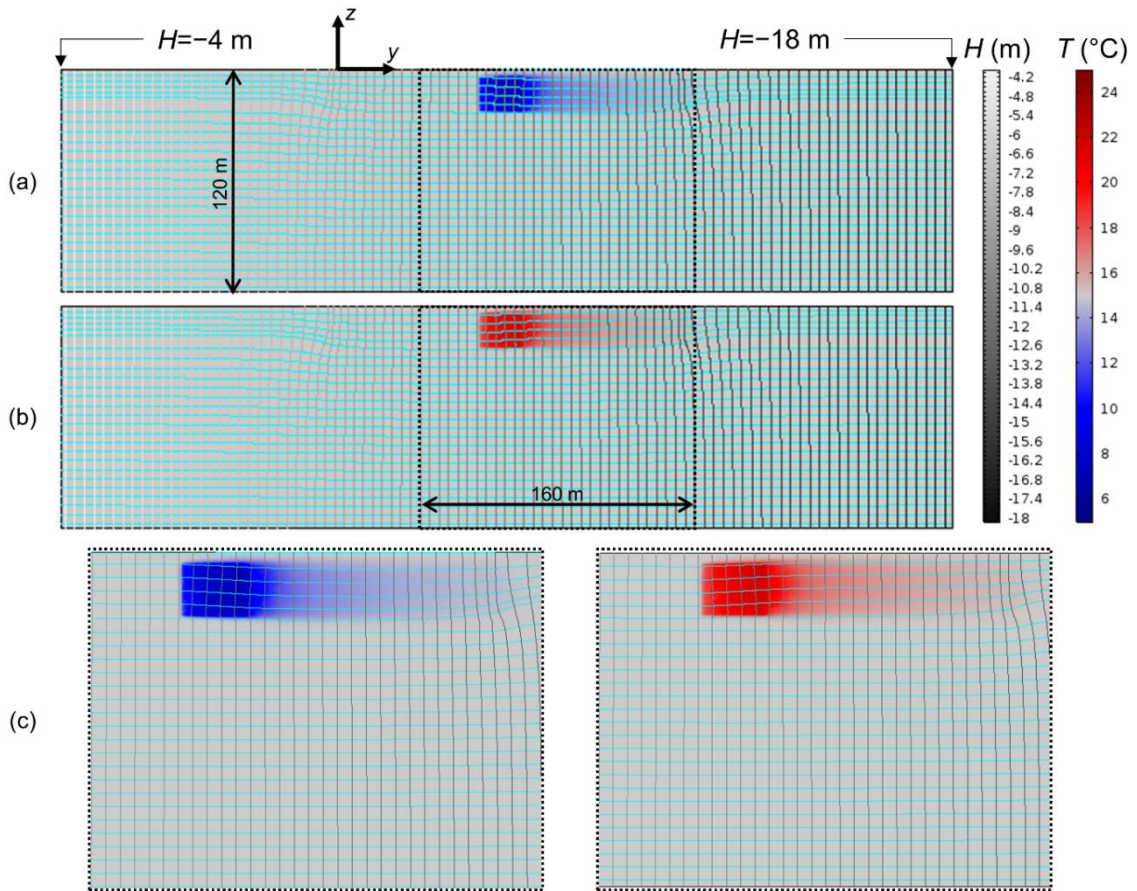


Figure 3.8 Temperature contour plot for groundwater flow parallel to the infrastructure with flownet: streamlines (light blue) and equipotential lines of the hydraulic head [m] (greyscale). (a) winter operation, (b) summer operation, (c) zoom-in image of selected zones.

The local modification of the vertical component of the velocity vector ( $\Delta v_{f,z}$ ) depends on the average temperature difference between the wall and soil ( $\Delta T_{s-w,av}$ ), while it is independent of the depth location and the undisturbed groundwater velocity because the buoyancy-driven flow is due to the gravity forces, which depend only on temperature (Nield & Bejan, 2006). A vertical component of the velocity vector,  $\Delta v_{f,z} = v_{f,z}$ , is generated only because of the thermal actions. In the thermally affected soil region, the local variation of  $v_{f,y}$ ,  $\Delta v_{f,y}$ , varies as a function of  $\Delta T_{s-w,av}$  and the undisturbed groundwater velocity (Figure 3.9).

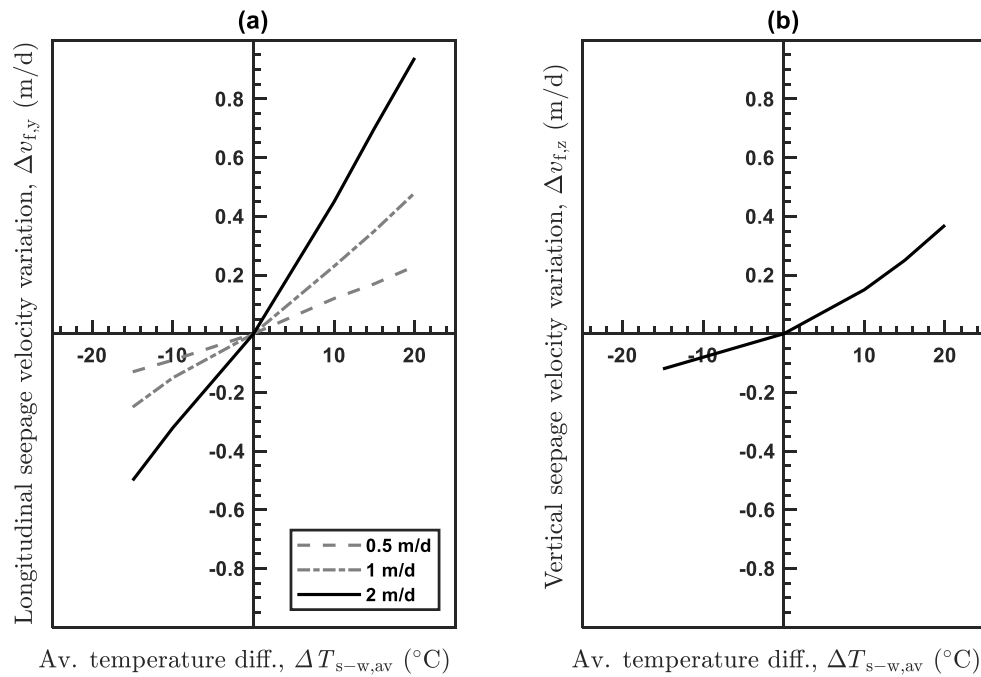


Figure 3.9 Variation in the y (a) and z (b) components of the groundwater velocity vector evaluated at the wall–soil interface with the average temperature difference.

The hydrothermal interactions in the porous medium affected the behaviour of the heat exchangers because the pipe loops were placed parallel to the groundwater flow direction. The seepage propagated the heat in the direction of the groundwater flow; hence, the soil temperature changed along the y-direction, modifying the power extraction/injection of adjoining pipe loops, as shown in Figure 3.10. The heat exchangers on the right and left walls performed equally. A comparison with the case without groundwater flow is also reported in Figure 3.10.

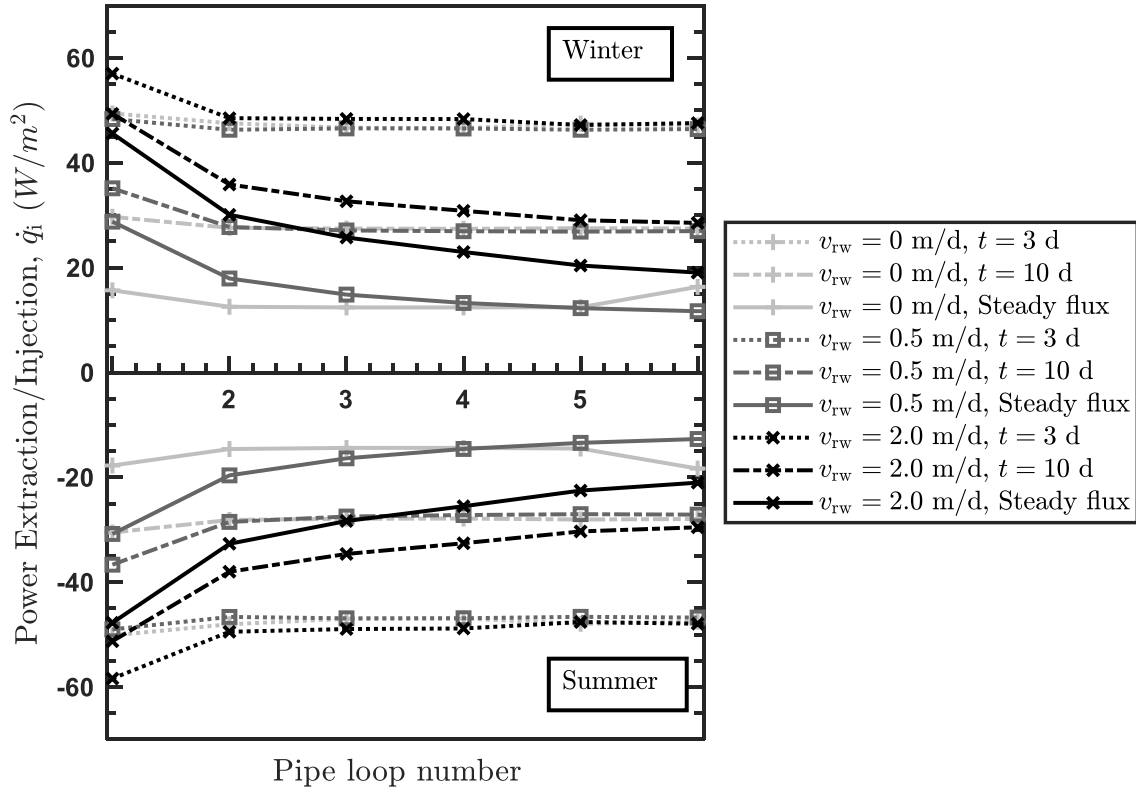


Figure 3.10 Evolution of the power extraction/injection of adjoining pipe loops with time for different values of groundwater velocity. The pipe loops are numbered as in Figure 3.4.

After the 6<sup>th</sup> pipe loop, which is located at a distance  $d = 0.85H_{wall}$ , the power extraction/injection,  $\dot{q}$ , stabilises. Moreover, the heat exchange varies with the magnitude of the undisturbed groundwater velocity (convection); hence, a higher groundwater flow ensures a higher heat exchange. The decrement in  $\dot{q}$  with the loop number is a function of time and is significant at the steady state: the performance of the 6<sup>th</sup> loop is halved with respect to the 1<sup>st</sup> loop. It is noteworthy that, after the 6<sup>th</sup> panel, the performance of the heat exchangers with groundwater parallel to the infrastructure is similar to the condition of groundwater perpendicular to the infrastructure of the same undisturbed velocity. Finally, in the case of groundwater flow parallel to the infrastructure, a detailed evaluation of the hydrothermal interactions should be performed.

### 3.5 Conclusions

Various aspects of 3D non-isothermal seepage related to the EWs of shallow infrastructures were presented in this study, based on 3D hydrothermal finite element analyses. Two main seepage directions were studied: groundwater perpendicular and parallel to the infrastructure. The main findings



of this study were related to (i) the definition of the non-isothermal flownet for the case of EWs, and the definition of hydrothermal interactions related to groundwater flow (ii) perpendicular and (iii) parallel to the infrastructure longitudinal direction.

Starting from analytical solutions for the 2D case, a preliminary overview on how temperature locally modified the flownet could be obtained. Extending those findings to the 3D case in the presence of EWs (or, more generally, to every plane EG), the temperature dependency of water density and dynamic viscosity affected the work done by gravity forces, thereby inducing a circular motion on the side of the thermo-active element. A buoyancy-driven flow near the wall–soil interface occurred when the wall was heated. A downward flow in the soil at an increasing distance to the wall balanced the process. The opposite occurred when the wall was cooled. It is noteworthy that when addressing EGs, the problem was time dependent because the temperature distribution along the heat exchangers was not constant and the volume of soil affected by thermal exchange varied with time.

When the flow was directed perpendicularly with respect to the infrastructure direction, seepage flow occurred with the groundwater flowing below the infrastructure and subsequently upwards on its other side. In such conditions, a superposition exists between the groundwater direction and the circular motion generated by the thermal activation of the wall (parallelism condition), and the process is driven by seepage. Hence, while the circular motion is not visible, the variation of the groundwater velocity near the wall–soil interface during thermal activation can be measured. Moreover, thermal exchange occurred perpendicularly to the plane where the heat exchangers were placed; hence, no hydraulically induced thermal interactions occurred between adjoining pipe loops. Finally, the heat was propagated in the direction of the seepage path; hence, the heat in the soil propagated from one wall towards the other wall. Because of the large distance between the two walls, differences in power extraction/injection were negligible. If the distance between the two walls decreased (*e.g.*, in the case of a trench), then hydraulically induced thermal interactions might be more dominant.

In the case of groundwater flowing parallel to the infrastructure, the seepage was perpendicular to the direction of thermal exchange. Consequently, the circular motion induced by the thermal activation of the wall was highly visible because it occurred on a plane perpendicular to the seepage flow. The wall heating induced a buoyancy-driven flow near the wall–soil interface, which was balanced by a downward flow with increasing distance from the wall. The opposite occurred for wall cooling. Consequently, the flownet in the portion of the soil affected by the thermal exchange was locally modified. The water propagated along a y-axis spiral-shaped trajectory, showing a buoyancy-driven motion in the  $xz$  plane. At the wall–soil interface, a local modification of the velocity vector occurred in the  $y$  and  $z$  components. Finally, the seepage direction is parallel to the position of the heat exchangers. This condition generates hydraulically induced thermal effects between adjoining pipe loops because the heat is propagated by the groundwater flow, thereby affecting the thermal exchange of the pipe loops in the vicinity.

Finally, some considerations related to the power extraction/injection potential considering different groundwater directions are noteworthy. For perpendicular groundwater flow, the component of the groundwater velocity vector that is inducing the convective heat transfer is  $v_{f,z}$  at the wall–soil interface. Because of the seepage path, the magnitude of  $v_{f,z}$  is  $\frac{1}{3} \div \frac{1}{8}$  times smaller than the undisturbed groundwater velocity (the deeper the wall, the smaller is  $v_{f,z}$ ).

For parallel groundwater flow, the magnitude of the velocity vector at the wall–soil interface is similar the undisturbed velocity ( $v_{f,y}$ ); hence, it is much higher with respect to the corresponding perpendicular case. Therefore, the power extraction/injection for parallel flow conditions is higher than that for the perpendicular case; however, because of the hydraulically induced thermal interactions, the thermal performance of adjoining loops decreases and after a number of panels, it stabilises around values similar to the corresponding case with groundwater perpendicular to the wall. In presence of significant groundwater flow parallel to the wall, it is crucial to consider hydraulically induced thermal interactions at the design stage. An incorrect thermal design that does not consider the thermal interactions between consequent pipe loops may result in an overestimation of the thermal potential by ~50% (Figure 3.10). On the contrary, an accurate heat exchanger design that minimises thermal interactions allows the thermal behaviour of the structure to be improved significantly.

### Acknowledgements

The authors wish to acknowledge the support of the European Commission via the Marie Skłodowska-Curie Innovative Training Networks (ITN-ETN) project TERRE 'Training Engineers and Researchers to Rethink Geotechnical Engineering for a Low Carbon Future' (H2020-MSCA-ITN-2015-675762).





# Chapter 4 Early-stage thermal performance design of thermo-active walls implemented in underground energy infrastructures

**Disclaimer:** The content of this chapter has been submitted as a journal paper and it is currently under review:

Zannin, J., Ferrari, A., Larrey-Lassalle, P., & Laloui, L. (accepted, 2020). Early-stage thermal performance design of thermo-active walls implemented in underground energy infrastructures. *Geomechanics for Energy and the Environment*.

**My contribution:** Conceptualization, Methodology, Formal analysis, Investigation, Data Curation, Writing – Original Draft, Visualization.

## 4.1 Foreword

Energy geostructures represent an innovative technology in the sustainable energy agenda and are useful to satisfy the energy needs of the built environment. They are usually involving geostructures such as piles, walls, tunnels, shafts, sewers. The application of such technology to infrastructure projects, may represent a good thermal potential because of the large surfaces that can be thermally activated. This study deals with thermo-active walls (energy walls, EW), which are retaining structures used to sustain the sides of excavations. Key features related to their thermal design are here tackled and a design methodology is proposed. The heat exchange modes involving EWs and the surrounding materials (concrete, soil, air) are studied by means of an extensive campaign of three-dimensional hydro-thermal finite element simulations featuring for the non-isothermal flow in the heat exchangers as well as all other heat exchange modes. The results are firstly presented in terms of charts related to the thermal behavior of the heat exchangers under different hydro-thermal environments. Finally, a methodology for the early-stage thermal performance design based on a flowchart is proposed: the results of this work enable to have a tool that may be helpful for the design and the decision-making process to easily incorporate energy geostructures in engineering design.

## 4.2 Introduction

Geothermal energy is recognized to be one of the most important renewable and sustainable energy sources on earth (Lund & Boyd, 2016) and many different technologies exist for capturing this energy. This work relates on a particular type of shallow geothermal applications: energy geostructures (EG) (Laloui & Rotta Loria, 2019). EG, also termed thermo-active geostructures, are innovative civil engineering geostructures that couple the structural role with a heat exchanger role. The transition from regular geostructures to EG is quite simple, it only requires heat exchangers to be installed and secured to the reinforcing cage whenever a new geostructure is needed. Some of the main advantages of such technology are that energy (i) is continuously available, regardless of weather conditions, (ii) it is available almost everywhere and (iii) it is usable in a wide range of applications (Amis et al., 2010; Barla et al., 2019; Bidarmaghz & Narsilio, 2018; Cousin et al., 2019; Makasis et al., 2018; Mimouni et al., 2014; Mimouni & Laloui, 2015; Sailer et al., 2019; Sterpi et al., 2020). Possible applications of EG are (but not limited to): (i) heating and cooling of civil engineering structures (residential or commercial buildings, industries, etc.) (Brandl, 2006, 1998; Laloui et al., 2006; Nicholson et al., 2014), (ii) production of hot water for agricultural needs (Carella & Sommaruga, 1999), (iii) de-icing of decks', bridges' and roads' pavements (Dupray et al., 2014; Eugster, 2007). The EG technology is being developed over the last decades (Di Donna et al., 2017) and shows a good potential for the energy production (Brandl, 2006) allowing to satisfy heating and cooling needs of the built environment.

In this paper thermo-active walls, termed energy walls (EW), are studied. Typical examples of EW are singly- and multi-floored underground infrastructures (*e.g.*: train stations, underground car parks, basements of high-rise buildings, etc...) and shallow cut-and-cover tunnels (Bourne-Webb et al., 2016; Di Donna et al., 2016; Loveridge et al., 2020; Rui & Yin, 2017; Shafagh et al., 2020; Soga & Rui, 2016; Sterpi et al., 2017, 2020). Among various types of EG, EW represent a relatively new technology and, consequently, a number of challenges exist. First of all, the heat transfer modes and the interactions between the EW and the surrounding materials are not fully understood yet. Secondly, analysis and design methods as well as guidelines for the thermal and mechanical design of EW are missing.

This paper deals with the definition of the thermal performance of EWs and aims at presenting a methodology for the early-stage thermal performance design. The main characteristics of the hydrothermal behavior of EG that must be accounted for in the thermal performance design are firstly outlined. Secondly, the features of a numerical model employed to investigate the hydrothermal behavior of EW are presented. Then, the results of an extensive campaign of numerical analyses (*i.e.*, parametric analyses) are presented in terms of charts that describe the thermal potential of installing EWs in different thermal environments and geometrical conditions. Finally, a design methodology with a sound theoretical basis that links heat transfers, fluid dynamics and seepage in porous media is presented by means of a flowchart. Such tool can easily be employed by designers to investigate the thermal potential of exploiting EWs at a known site.

## 4.3 Materials and methods

### 4.3.1 Hydro-thermal phenomena involved with thermo-active walls

Thermal activation of walls and, more generally, of geostructures involves multiphysical phenomena interacting at two different scales: the infrastructure scale (i.e. lengths of  $10^0$  to  $10^3$  m), as reported and described by Zannin et al. (2020), and the heat exchanger (HE) scale. At the HE scale (i.e. lengths of  $10^{-2}$  to  $10^0$  m), a fluid is flowing, at non-isothermal conditions, in the pipes and exchanging heat with the surroundings. Mutual, concurrent, interactions between such two scales are taking place during thermal activation and consequently affect the hydrothermal behavior. To thoroughly account for all such phenomena, the tool used to investigate this topic is 3D hydrothermal finite element modelling. To describe the thermal performance of EWs in different environmental and geometrical conditions, an extensive campaign of numerical, parametric, analyses has been carried out and it is described in the following sections.

### 4.3.2 Features of the numerical analyses

To perform the analyses, a portion of an underground infrastructure is modelled by means of the finite element software Comsol Multiphysics®. The dimensions of the model in the x, y, z coordinates are:  $8 H_{wall} + L_{tunnel}$ ,  $8 H_{wall}$ ,  $5 H_{wall}$ , respectively (Figure 4.1) where  $H_{wall}$  is the EW height and  $L_{tunnel}$  is the tunnel width. The soil and concrete are considered as isotropic and homogeneous porous media. The soil is fully saturated by water. Six adjacent heat exchanger pipe loops (Zannin et al., 2020) are modelled as linear entities embedded in the concrete walls.

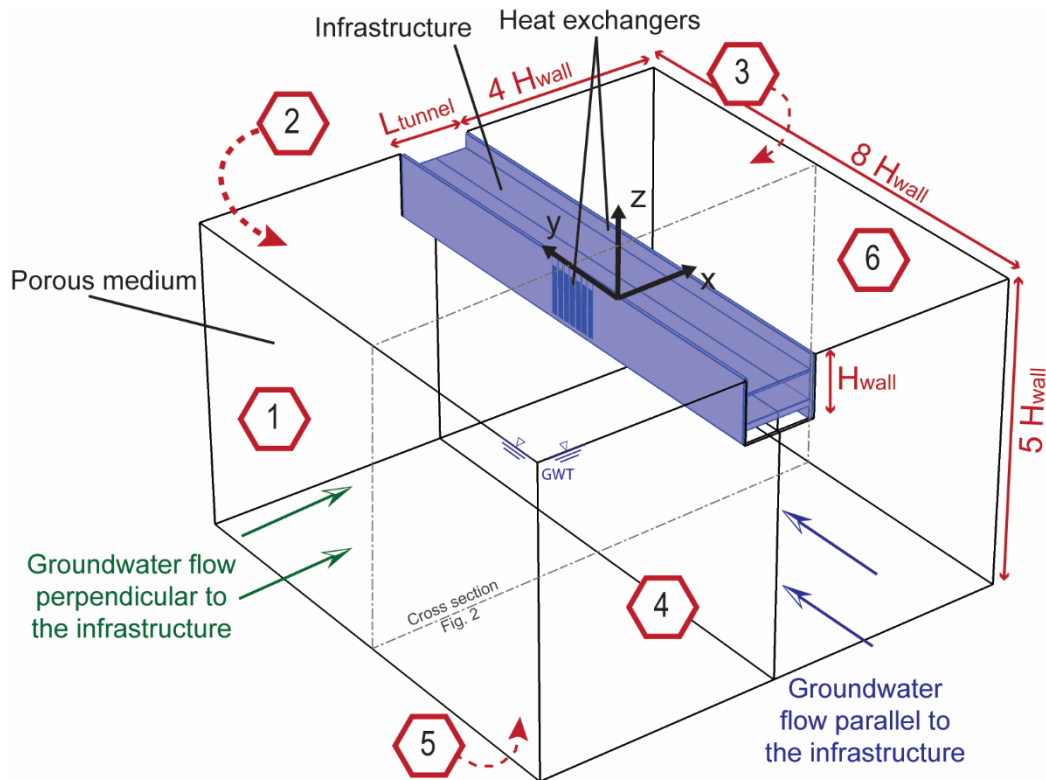


Figure 4.1 View of the 3D model with indications of the boundaries: 1-left; 2-rear; 3-right; 4-front; 5-bottom; 6-top

The HE pipes present an outer diameter of 32 mm and an inner one of 25 mm. Water has been chosen as circulating fluid, with an inflow velocity and a temperature as specified in Section 4.3.4. The pipe layout presents a vertical W configuration.

The model formulation is reported in the Annex A. The model mesh is created with the following features: (i) the HEs have a maximum mesh size of 10 cm; (ii) the infrastructure has a mesh size that range from 10 cm in the vicinity of the HEs to 1 m; (iii) the soil mesh is of 1 m in the vicinity of the EG and it get coarser farther from the underground infrastructure.

The analysis is divided in two solvers: the first is a stationary one, where the thermal and hydraulic boundary conditions are applied. The second is a time dependent solver, that takes the solution of the stationary solver as initial condition. The fluid flow in the pipes is here enabled (i.e., geothermal activation). The details of the thermal input are specified in Section 4.3.4.

The model performance is firstly tested by reproducing the experimental test carried out at the Shanghai Natural History Museum (Xia et al., 2012). The numerical model geometry presented at Figure 4.1 was adapted to account for the experimental data reported for the Shanghai test (Sun et al., 2013; Xia et al., 2012). All the model input data are reported in the Annex B. The comparison results are reported in terms of the heat carrier fluid inflow ( $T_{f,in}$ ) and outlet ( $T_{f,out}$ ) temperatures showing closed agreement (Figure 4.2).

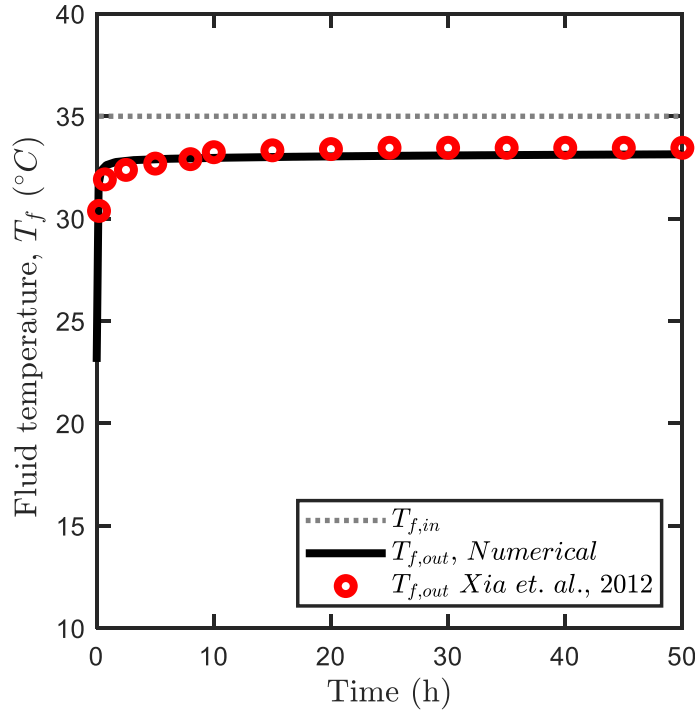


Figure 4.2 Model performance test: simulation of the Shanghai test (Xia et al., 2012) including a comparison among the experimental data and the numerical results

Considering the complex geometry of the model (Figure 4.1), various boundary conditions have to be set. Referring to the numbered boundaries on Figure 4.1, thermal and hydraulic boundaries are set to account for two groundwater flow directions. Table 4.1 summarizes the selected conditions.

Table 4.1 - Thermal and hydraulic boundary conditions (the numbered boundaries refer to Figure 4.1, Figure 4.3 and Table 4.2)

Boundary nr.	Perpendicular groundwater flow		Parallel Groundwater flow	
	Hydraulic b.c.	Thermal b.c.	Hydraulic b.c.	Thermal b.c.
1	$H = -4 \text{ m}$	$T_{1,4}(z)$ (eqt. (4.1))	$\mathbf{n} \cdot \rho_w \mathbf{v}_{rw} = 0$	$\dot{q}_{bc,i} = \mathbf{n} \cdot \dot{\mathbf{q}} = 0$
2	$\mathbf{n} \cdot \rho_w \mathbf{v}_{rw} = 0$	$\dot{q}_{bc,i} = \mathbf{n} \cdot \dot{\mathbf{q}} = 0$	$H = \begin{cases} -7.5 \text{ m} \\ -11.0 \text{ m} \\ -18.0 \text{ m} \end{cases}$	$\dot{q}_{bc,i} = \mathbf{n} \cdot \dot{\mathbf{q}} = 0$
3	$H = \begin{cases} -5.25 \text{ m} \\ -6.5 \text{ m} \\ -9.0 \text{ m} \end{cases}$	$\dot{q}_{bc,i} = \mathbf{n} \cdot \dot{\mathbf{q}} = 0$	$\mathbf{n} \cdot \rho_w \mathbf{v}_{rw} = 0$	$\dot{q}_{bc,i} = \mathbf{n} \cdot \dot{\mathbf{q}} = 0$
4	$\mathbf{n} \cdot \rho_w \mathbf{v}_{rw} = 0$	$\dot{q}_{bc,i} = \mathbf{n} \cdot \dot{\mathbf{q}} = 0$	$H = -4 \text{ m}$	$T_{1,4}(z)$ (eqt. (4.1))
5	$\mathbf{n} \cdot \rho_w \mathbf{v}_{rw} = 0$	$T_5$	$\mathbf{n} \cdot \rho_w \mathbf{v}_{rw} = 0$	$T_5$
6	$\mathbf{n} \cdot \rho_w \mathbf{v}_{rw} = 0$	$T_6$	$\mathbf{n} \cdot \rho_w \mathbf{v}_{rw} = 0$	$T_6$

where  $H$  is the total hydraulic head,  $\mathbf{n}$  represents the normal outflow unit vector,  $\rho_w$  is the water density,  $\mathbf{q}$  the flow vector and  $\dot{q}_{bc,i}$  the heat flux through the  $i$ -th boundary.  $T_{1,4}(z)$  is the temperature ( $^{\circ}\text{C}$ ) distribution along the depth ( $z$ , in meters) aiming at approximating the near-surface geothermal gradient in the shallower 10 m of the subsoil profile:

$$T_{1,4}(z) = \begin{cases} T_6 - z \frac{T_5 - T_6}{10\text{m}} & \text{for } 0 < z \leq -10 \text{ m} \\ T_6 & \text{for } z < -10 \text{ m} \end{cases} \quad (4.1)$$

with  $T_5$  and  $T_6$  as from Table 4.2.

The hydraulic head boundary allows to set different undisturbed groundwater flow velocity ( $v_{gw}$ ) scenarios: in this study  $v_{gw}$  ranges from 0 m/d to 2 m/d. Different wall geometries are studied: the total wall height varies between 25.5 m to 40.0 m. The height of the excavated zone remains as indicated in Figure 4.3, while only the embedded height varies.

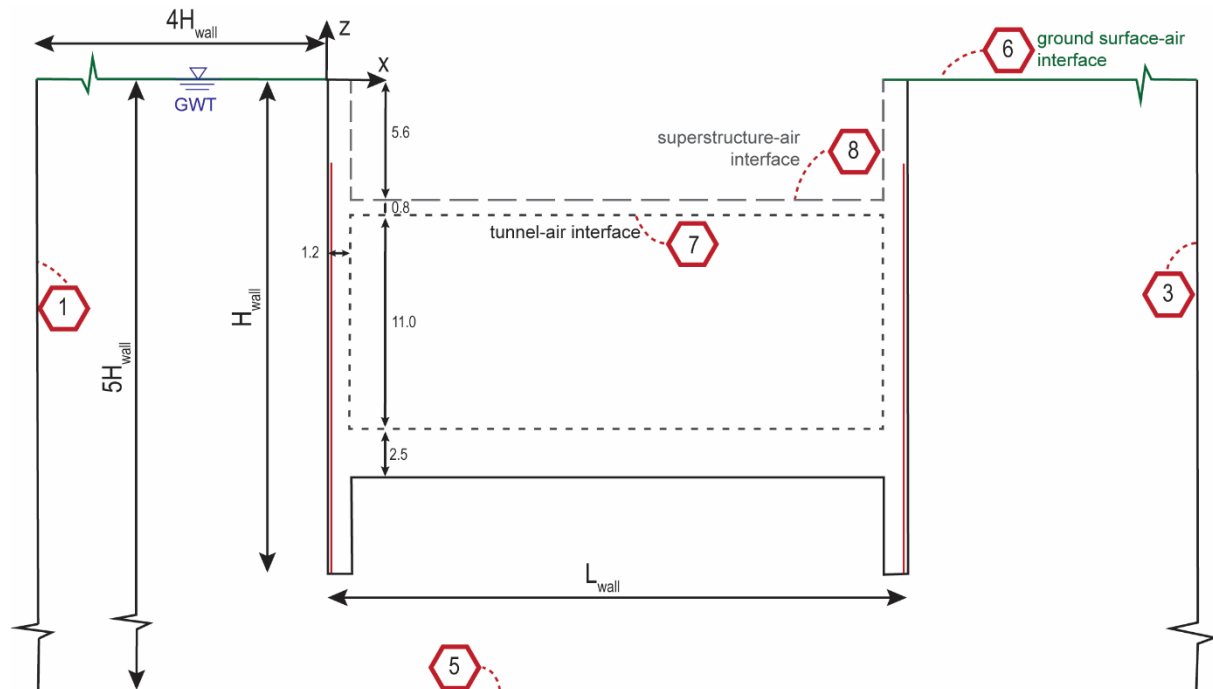


Figure 4.3 Cross section view with indication of the boundaries (NOTE: the figure is not scaled)

The thermal behavior of the EW may considerably be affected by the hydro-thermal interactions between the wall and the airflow in the tunnel (Bourne-Webb & da Costa Goncalves, 2016; Bourne-Webb et al., 2016). In some conditions, the heat exchanged in this portion of the structure (*i.e.* at the wall-air interface) may be predominant: it is the combination between the air flow velocity and the tunnel air temperature that defines the heat exchange. In finite element analyses, convective boundary conditions can be employed to describe this phenomenon, avoiding modelling the complete airflow circulation in the tunnel. This is a flux boundary condition described as:

$$\dot{q}_{bc,i} = \mathbf{n} \cdot \dot{\mathbf{q}} = h_{a,i}(T_{a,i} - T_{amb}) \quad (4.2)$$

where  $h_{a,i}$  is the convective heat transfer coefficient,  $T_{a,i}$  the temperature of the  $i$ -th boundary and  $T_{amb}$  is the temperature of the porous medium at the wall-air interface.

It is particularly difficult to describe and to monitor the air environment in tunnels with rectangular cross section (Peltier et al., 2019), and there is a clear lack of monitored sites (Bourne-Webb et al., 2016). The air temperature in tunnels varies with: the distance from the entrance region, the depth of the tunnel, the influence of the external temperature, the thermal energy released by the passage of trains, the energy dissipated by trains during braking, the crowding of train stations, and eventually the presence of a lighting system. In this work, the temperature values for the air in the tunnel have been chosen after a dedicated literature review on shallow train tunnels located in Germany, France, Austria and United Kingdom (Adam, 2008; Brandl et al., 2010a; Consulenti, 1994; IC Consulenti ZT GmbH, 2005; MacDonald, 2004; Schlosser, 2007). The air flow velocity is directly connected with the convective heat transfer coefficient (Bourne-Webb et al., 2016). The selected reference values, in this study range between  $2.5 \text{ W/m}^2/\text{K}$  and  $25.0 \text{ W/m}^2/\text{K}$ .

Moreover, two other environments are exchanging heat with the EW: a portion of the superstructure and the ground surface (Figure 4.3, see 8 and 6). At 8, the internal conditions of a building are simulated: the temperature is set at  $18^\circ\text{C}$  accounting for “near-zero” airflow. At 6, the temperature ranges from  $2^\circ\text{C}$  to  $30^\circ\text{C}$  aiming at encompassing various thermal environments typical of European climates including worst case scenarios defined as very cold and very hot climates (average temperatures in Helsinki, Finland (Finnish Meteorological Institute, 2019) during winter and in Palermo, Italy (Servizio Meteorologico dell’Aeronautica Militare, 2019) during summer), and an average airflow velocity of  $2.5 \text{ m/s}$  is accounted. A summary is given in Table 4.2.

Table 4.2 Boundary conditions at the wall-air interfaces (the boundary conditions names refer to Figure 4.3)

	Boundary	$T_{\min}$	$T_{\max}$	$v_{\text{air}, \min}$	$v_{\text{air}, \max}$
5	bottom	$9^\circ\text{C}$	$15^\circ\text{C}$	-	-
6	ground surface	$2^\circ\text{C}$	$30^\circ\text{C}$	$0 \text{ m/s}$	$5 \text{ m/s}$
7	tunnel-air interface	$10^\circ\text{C}$	$15^\circ\text{C}$	$0 \text{ m/s}$	$5 \text{ m/s}$
8	superstructure-air interface		$18^\circ\text{C}$	$0 \text{ m/s}$	-

To test the impact of each boundary condition on the thermal exploitation, a dedicated set of preliminary sensitivity analyses has been carried out, referring to the configurations described in Table 4.3. For such analysis  $h_{a,i}$  at the tunnel level is set to  $25.0 \text{ W/m}^2/\text{K}$  only.



Table 4.3 Configurations used for the boundary conditions comparison

Configuration	Description of the b.c.
Config. 1	6, 7, 8 thermally insulated
Config. 2	7 active, 6 and 8 thermally insulated
Config. 3	6, 7 active, 8 thermally insulated
Config. 4	6, 7, 8 active

Neglecting the heat exchanges between the wall and the air (*config. 1*) may lead to a critical underestimation of the thermal potential. On the other hand, accounting for the heat exchanges on a portion of the superstructure may overestimate the thermal potential (*config. 4*): in real applications, at shallow depths, the pipes may be thermally insulated to avoid major thermal losses in the top part of the excavation. Consequently, *config. 3* has been adopted for the rest of this study.

#### 4.3.3 Material properties of the involved materials

The soil description has been chosen to enable a thermal characterization typical of fine- and coarse-grained materials. From a hydraulic viewpoint, the chosen geometric permeability is the one typical for coarse-grained materials (Vulliet et al., 2016; Zannin et al., 2020) as higher groundwater flow velocities are expected to occur for coarser materials rather than for finer ones. The infrastructure is made of concrete and the heat exchanger pipes are made of high-density polyethylene (HDPE). Water is the circulating fluid inside the HEs and the saturating medium in the soil. The details are described in Table 4.4.

A broad variety of hydro-thermal environments in the soil and at the air interfaces are simulated by varying several parameters (Table 4.5). The variations in soil thermal conductivity ( $\lambda_s$ ) aim at encompassing the majority of shallow subsoil materials, while in the case of concrete ( $\lambda_c$ ), thermal conductivity varies in function of a number of parameters, such as the aggregate mix composition and water content (see Section 4.4.2).

Table 4.4 Material properties

	Material	Porosity $n$ (-)	Density $\rho_s$ (kg/m <sup>3</sup> )	Geometric Per- meability $k^*$ (m <sup>2</sup> )	Heat capacity at constant pressure $C_p$ (J/(kg K))	Thermal conductivity $\lambda$ (W/(m K))
<i>Soil</i>	Coarse grained	0.35	2735	$10^{-10}$	890	1.5 to 3.5
<i>Structure</i>	Concrete	0.10	2722	-	837	0.7 to 2.0
<i>Pipes</i>	HDPE	-	-	-	-	0.4

#### 4.3.4 Definition and choice of the thermal input

The choice of the thermal input is key to define the thermal behavior of the heat exchangers. The selected numerical model includes the convective and conductive heat transfers within the fluid, the pipe material, the concrete, the soil and the air. In a real application, the thermal input imposed by the heat pump to the primary circuit is to satisfy the (total or partial) energy demand of the served superstructure. Since this study deals with the preliminary design stages of a project, a number of challenges related to the selection of the thermal input exist.

First, a broad variety of energy demand curves exist for different types of civil engineering structures and of shallow geothermal applications. It is difficult to define a reliable thermal input that can be representative of all the possible conditions, for winter and summer operations. Secondly, the elements constituting the EG present a response which differs with time and space (Li & Lai, 2015) depending on the material characterization and on the ongoing multiphysical phenomena, inducing mutual hydro-thermal interactions (Zannin et al., 2020). Thirdly, accounting for a dynamic thermal input implies a high computational cost and high number of needed runs.

A trade-off can be found by using relatively short-time constant temperature inputs, to detect the response of the EG both in the transient and steady flux conditions, giving a comprehensive overview of the thermal behavior of the heat exchangers when either short term (intermittent) or long term constant modes are selected (Xia et al., 2012). With a constant temperature input, the thermal response of the HEs is linear depending on the inflow temperature (Figure 4.4), but some correlations to the dynamic response can be done. It is possible to evaluate the dynamic thermal behavior of the heat exchanger by applying the Duhamel principle: the dynamic problem can be solved by accounting for a sequence of infinitesimal impulses of different amplitudes, as shown in (Li & Lai, 2015). Moreover, at the early stages of an EG design, the energy demand curve may not yet be defined with enough accuracy. For all these reasons, a constant with time temperature input is set. To account for temperature limits that are usually prescribed for EGs (*i.e.* soil temperature to be maintained between 0 °C and 50 °C), the inflow temperature of the fluid ( $T_{f,in}$ ) in the pipes is set at 5 °C and 25 °C for winter and summer operation,

respectively, to have an average temperature difference between the fluid in the pipes and the soil of  $\pm 10$  °C, as showed in Figure 4.4. The power extraction/injection rate ( $\dot{q}$ ) expressed in  $W/m^2$ , of the heat exchanger loop can be quantified (Batini et al., 2015; Sterpi et al., 2020) as the enthalpy drop between the inflow and the outflow sections:

$$\dot{q} = \frac{A_P \rho_f C p_f v_f \Delta T_f}{A_W} \quad (4.3)$$

where  $\rho_f$ ,  $C p_f$  and  $v_f$  represent the density, heat capacity and velocity of the circulating fluid,  $\Delta T_f$  is the fluid temperature difference between the pipe outflow and the inflow, and  $A_W$  is the equipped surface of the wall.

A constant with time fluid velocity in the pipes of 0.5 m/s is also imposed to attain turbulent regime. The duration of the analyses is set to 50 days which has proven to be sufficient in order to reach the steady flux domain.

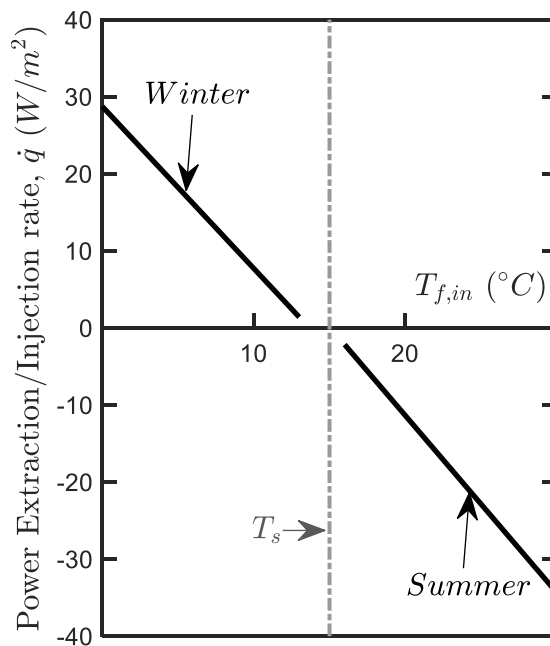


Figure 4.4 Thermal response of a heat exchange loop at steady flux varying the inflow temperature input.

## 4.4 Results and discussion

The results of the numerical analyses are here described, focusing on the heat exchanger scale, highlighting the thermal response of the HEs. The results are given in terms of charts that relate to selected times allowing to detect the short term and the steady flux response. The time dependent HE

response is firstly described. Secondly, design charts aiming at highlighting the effects of soil thermal characterization are proposed. Then, a section is dedicated to determining the structural thermal characterization. A flowchart to be employed for the early-stage thermal performance design is eventually proposed. Table 4.5 summarizes the ranges of the studied parameters introduced in Section 4.3.2.

Table 4.5 Ranges of values for the studied parameters

	$\lambda_s$	$\lambda_c$	$T_5$	$T_6$	$T_7$	$v_{gw}$	$T_{f,in}$	$H_{wall}$
<i>min</i>	1.5 W/m/K	0.7 W/m/K	9 °C	2 °C	10 °C	0 m/d	5 °C	25.5 m
<i>max</i>	3.5 W/m/K	2.0 W/m/K	15 °C	30 °C	15 °C	2 m/d	25 °C	40.0 m

The HE's thermal response is evaluated in terms of power extraction/injection rate as from equation (4.3). A fluid velocity and a temperature are imposed at the pipe inlet while the fluid temperature at the outflow is monitored. The time dependency of the thermal response of the HE to a constant with time thermal input (section 4.3.4) leads to the definition of two zones (Figure 4.5): an initial, time dependent portion (the duration depending on the fluid velocity, the pipe loop length and shape) in which the heat exchanges are governed by the heat capacity and the thermal conductivities of the involved materials, called “transient”, and a time-independent phase where the heat exchanges are governed by the thermal conductivities of the materials only (steady flux).

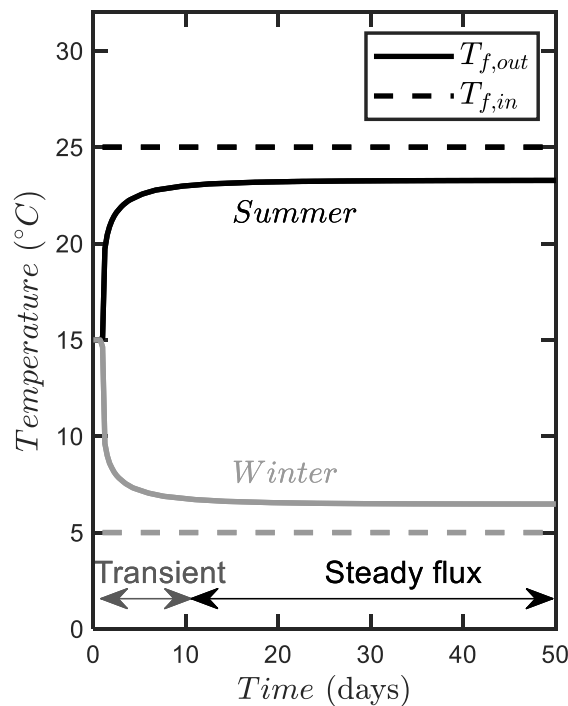


Figure 4.5 Applied thermal input with indication of the heat transfer conditions

In transient conditions, the volume of materials affected by the heat flow is quickly increasing with time: the soil portion affected by the thermal exchange is in the order of the decimeter to the meter scale. The presence, if any, of groundwater flow is interacting with the increasing soil volume in which the heat exchange takes place. Due to this interaction, for short term response, the seepage may not remarkably enhance the behavior of the HEs. The impact of groundwater flow in enhancing the heat transfer process increases approaching steady flux conditions. As a consequence of the spatial evolution of the heat exchange processes in the soil, the power injection/extraction rate decreases with time.

Once steady flux is reached, the thermal response of the HEs is time independent. This condition is reached after an activation time in the order of 10 days and allows for the definition and analysis of long term energy exploitation scenarios (Xia et al., 2012). The soil volume involved in the heat exchange reaches its definitive evolution and it is recorded on the scale of few meters around the EG. If groundwater flow is present, the soil volume affected by the thermal exchanges is much larger depending on the direction and magnitude of the seepage. In this condition, mutual interactions among the seepage and the heat exchangers are taking place: on one hand the seepage affects the heat exchanges by moving the heat in the space, and on the other hand the thermal activation induces local seepage variations (Zannin et al., 2020).

To study the time-dependent behavior of the heat exchangers' response, three time steps are studied that aim at giving a comprehensive overview of the time-dependent heat transfer rates. The selected ones are: 2, 5, 50 days, where the first aims at defining the short-term response (*e.g.* representing highly intermittent heat pump functioning), the second gives an average value for the transient condition, and the third defines a measure of the long-term seasonal performance.

#### 4.4.1 Thermal behaviour of the energy geostructure in different environmental conditions

In the following section, charts (Figure 4.7 and Figure 4.8) are presented showing the power extraction/injection rate ( $\dot{q}$ , on the y axis) with groundwater velocity ( $v_{gw}$ , on x axis), for two different groundwater directions and soil thermal conductivities. In both cases, the results refer to the first pipe loop number (*i.e.* the one showing a higher performance), hence neglecting any hydraulically induced thermal interaction. In the next figures, all the results refer to a concrete thermal conductivity of  $2.0 \text{ W/(m K)}$ . The importance of this key parameter on the results will be further discussed in section 4.2.

To examine the effect of increasing the number of HE loops, Figure 4.6 shows the decrement of the power extraction/injection rate of adjoining heat exchanger' loops, for selected groundwater flow velocities parallel to the wall.

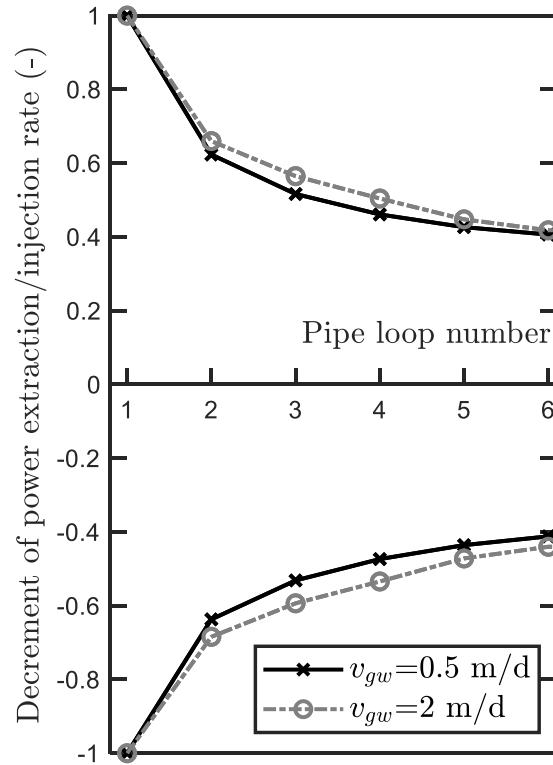


Figure 4.6 Power extraction/injection rate of adjoining pipe loops in the case of groundwater flow parallel to the wall

In the charts presented in Figure 4.7 and Figure 4.8 it is possible to detect the time-dependent decrease (in absolute value) of the thermal behavior of the HEs moving from transient to steady flux conditions. It is worth noting how the results for the condition of groundwater flow parallel to the wall are higher with respect to the correspondent case in perpendicular groundwater flow conditions. This is expected, because the magnitude of  $v_{gw}$  for parallel flow is higher with respect to the correspondent case in perpendicular flow due to the seepage. On the contrary, in the parallel flow case, hydraulically-induced thermal interactions among adjoining loops affect the thermal behavior as shown in Figure 4.6. Such results may be useful to have a preliminary estimation of the energy potential achievable from the heat exchangers embedded in retaining walls for an early-stage thermal performance design of the EG. In Figure 4.7 and Figure 4.8, the symbol T indicates the undisturbed soil temperature (i.e., at the far field).

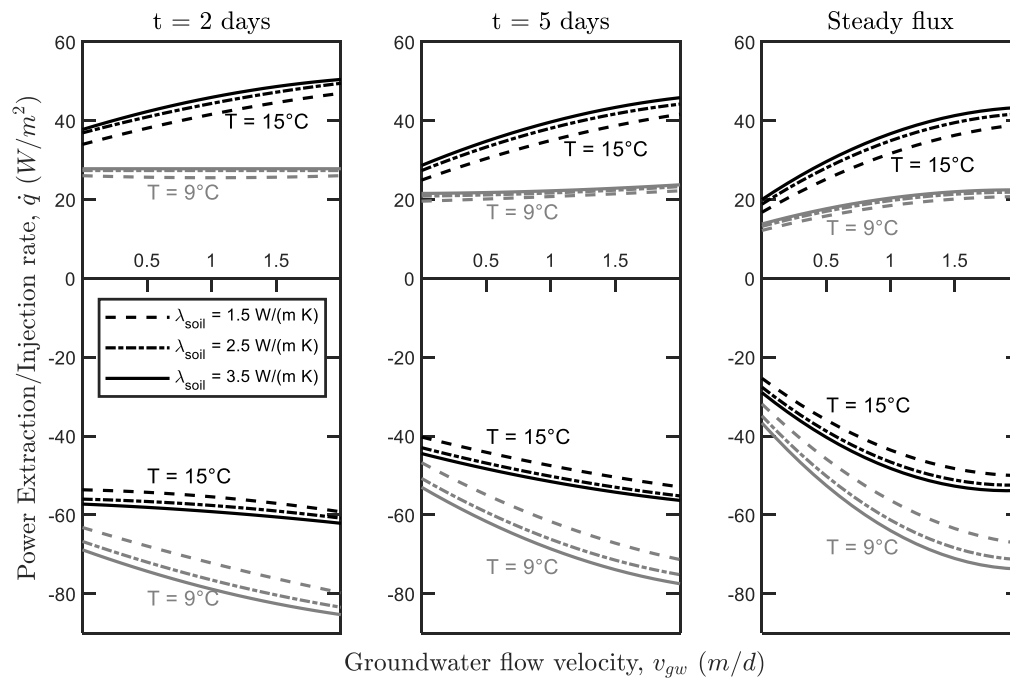


Figure 4.7 Charts for groundwater flow parallel to the wall

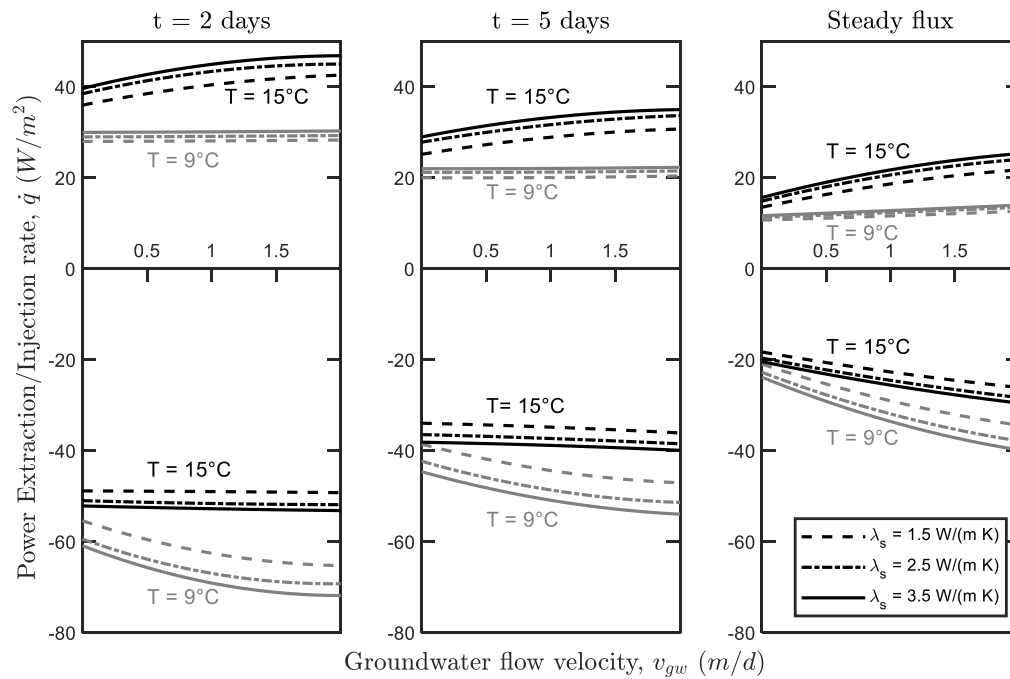


Figure 4.8 Charts for groundwater flow perpendicular to the wall

#### 4.4.2 Effect of the thermal characteristics of the structure

The role of structural thermal characterization on the thermal behavior of the heat exchangers is here presented and discussed. Thermal properties of concrete (i.e., the structural material) are typically affected by seven parameters (Asadi et al., 2018): humidity conditions, age, temperature, water-cement ratio, fine aggregate fraction, type of admixture and total aggregate volume fraction. Moisture content and temperature have a major importance: thermal conductivity in saturated conditions is 50% higher than that in dry conditions (Zhang et al., 2015). Additionally, experimental studies showed that thermal conductivity increases about 6% every 1% increment of moisture content (Valore, 1980). Aggregate type is another important parameter because concrete is composed by aggregates for about  $60\% \div 80\%$  of his volume. Thermal conductivity raises by raising the coarse aggregate volume fraction and keeping the sand ratio unchanged (Zhang et al., 2015). Density is another major parameter: an increase of density induces an exponential increase of thermal conductivity (Asadi et al., 2018).

Thermal conductivity of concrete is a property that can, to some extent, be engineered: for EG applications, one could choose a concrete type with higher properties with respect to other alternatives, but the long-term soil-structure interactions and the implications on thermal behavior are hardly definable at the design stage. They depend very much on the hydro-thermal interactions among the materials. In the case of EW, the interactions between the wall and the air at the excavated side and between the wall and the soil at the other side are additional interaction that may locally affect the thermal properties of the structure. To consider such scenarios, in this study, concrete thermal conductivity is being varied from  $0.7 \text{ W/(m K)}$  to  $2.0 \text{ W/(m K)}$  (Asadi et al., 2018). The following set of charts (Figure 4.9 and Figure 4.10) aims at giving ranges of values of power extraction/injection rate with groundwater flow velocity for different combinations of concrete and soil thermal conductivities. Again, the charts relate to the first pipe loop, without considering the hydraulically induced thermal interactions.

Per each concrete thermal conductivity value, a surface is identified. Minimum and maximum (absolute) values per each surface relate to low and high soil thermal conductivities, respectively.



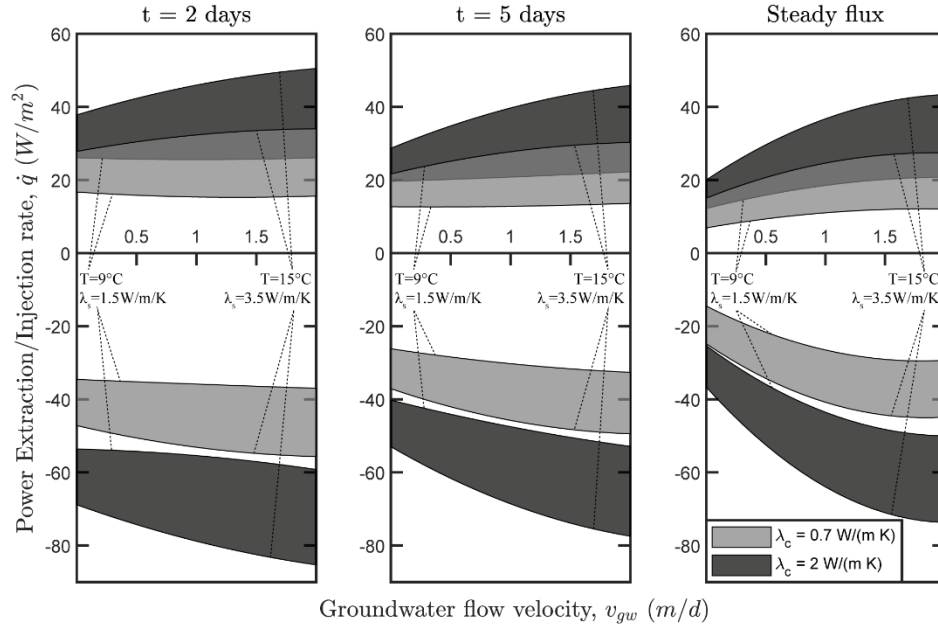


Figure 4.9 Charts with dependency on concrete thermal conductivity for groundwater flow parallel to the wall

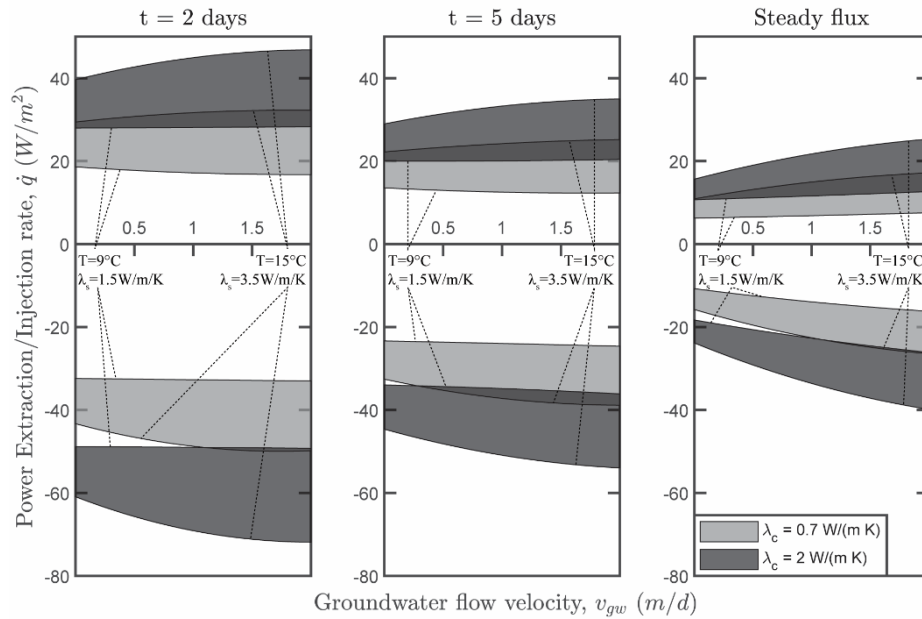


Figure 4.10 Charts with dependency on concrete thermal conductivity for groundwater flow perpendicular to the wall

#### 4.5 A flowchart for the early-stage thermal performance design

This section aims at linking subsoil characteristics and air environment conditions to the energy quantities achievable with EWs by defining a flowchart that can be used not only as a tool for the preliminary thermal design of EWs, but also for the decision-making process to decide if to involve EGs in an infrastructure project. The required input parameters are related to basic hydro-thermal

properties of a site: an estimation of the thermal properties of the involved materials and the possible presence and velocity of groundwater flow that may significantly interact with the infrastructure. The flowchart follows two steps: initially, based on fluid dynamics theory, the main heat exchange mechanism is defined and, secondly, by selecting the input thermal properties, the estimation of the thermal performance of heat exchangers embedded in EWs is done. The objective of this section is to propose a design methodology for energy evaluations at preliminary design stages, in order to reply to the frequently asked question: how much energy is achievable by using this technology at a known site?

#### 4.5.1 Analytical solution and Péclet number for steady flux calculations

To recall some fundamentals from thermodynamics and fluid dynamics, a simple sketch of an EW can be done by considering the case of a porous material constantly heated from the side by a heat source having a rectangular shape (Figure 4.11(a)). In this condition (i.e., steady flux) it is possible to describe the heat transfer process (conduction and convection) in an analytical way. For the case of a porous medium fully-saturated by water, with the liquid phase in movement at a velocity  $\dot{u}_x$ , the problem can be looked at the 2D case as shown in Figure 4.11(b).

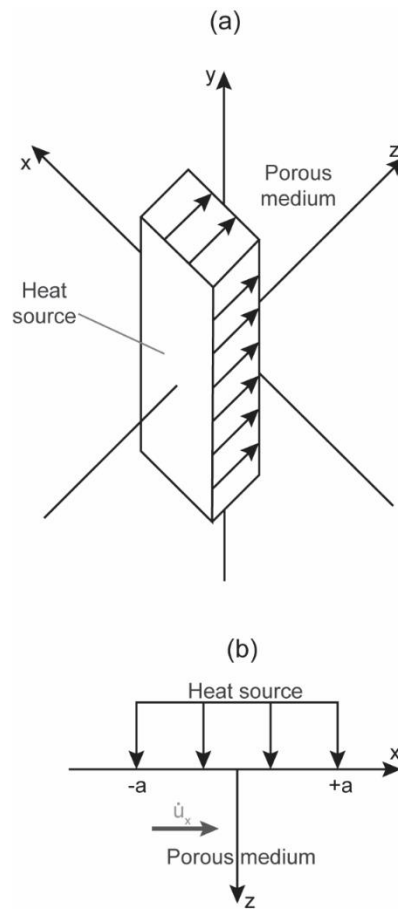


Figure 4.11 Porous medium heated from the side, 3D case (a) and 2D sketch (b)

In such conditions we can determine in which cases the heat exchanges are dominated by conduction ( $Pe < 1$ ) and in which others by convection ( $Pe > 1$ ), by studying the so-called Péclet number ( $Pe$ ). The Péclet number is a dimensionless number that expresses the ratio between the convective and the conductive transport rates in a continuum. In the application to hydro-thermal phenomena, it is equal to the product between the Reynolds ( $Re$ ) and the Prandtl ( $Pr$ ) numbers:

$$Pe = \frac{\text{convective transport rate}}{\text{conductive transport rate}} = Re Pr = \frac{\bar{v}\bar{x}}{\alpha} \quad (4.4)$$

where  $\bar{v}$  and  $\bar{x}$  represent the velocity field and the geometrical length of the considered problem and  $\alpha$  is thermal diffusivity. For the case shown in Figure 4.11(b) we can express:

$$Pe = \frac{\dot{u}_x a}{2\alpha} \quad (4.5)$$

The same result can be alternatively achieved by looking at the following ratio of times (Childs et al., 2000):

$$\begin{aligned} \frac{1}{Pe} &= \frac{\text{time for an element in motion to pass the heat source of width } 2a}{\text{time for the heat to conduct a distance } 2a} \quad (4.6) \\ &= \frac{t_{conv}}{t_{cond}} \begin{cases} \text{if } Pe \gg 1 & \text{convective dominated problem} \\ \text{if } Pe \ll 1 & \text{conductive dominated problem} \end{cases} \end{aligned}$$

where the distance  $2a$  is the width of the heat source (Figure 4.11(b)).

$$t_{conv} = \frac{2a}{\dot{u}_x} \quad (4.7)$$

And

$$t_{cond} = \frac{a^2}{\alpha} \quad (4.8)$$

by invoking the approximation proposed by (Carslaw & Jaeger, 1952) that gives a measure of the spatial extent of the heated region by analyzing the error function.

This knowledge can be applied to the case of EWs by analyzing the 2D case in the following conditions. For groundwater flow parallel to the wall the distance  $2a$  can be seen as the longitudinal length of the thermo-active walls of the infrastructure (it may range between  $10^0$  m to  $\approx 10^3$  m) and  $\dot{u}_x$  as the magnitude of the undisturbed groundwater velocity at the wall-soil interface (range: from 0 m/d to  $\approx 2.0$  m/d). For groundwater flow perpendicular to the wall, the seepage at the wall-soil interface is directed vertically, hence the distance  $2a$  can be seen as the wall height (range: from  $10^0$  m to  $\approx 10^2$  m) and  $\dot{u}_x$  as the magnitude of the groundwater velocity at the wall-soil interface (which is significantly

lower with respect to the undisturbed groundwater velocity ( $v_u$ ) because of the seepage path, usually  $\frac{1}{3}v_u$  to  $\frac{1}{8}v_u$ ) (Zannin et al., 2020).

In engineering applications, usually, Péclet number is high, hence the limit value that separates the conductive- to the convective-dominated regime has to be studied for low values of the parameter  $a$ , defined as the half of the length of a wall panel (e.g., diaphragm walls are usually composed of 1.5 ÷ 3.0 m long adjoining concrete panels) for the case of groundwater parallel to the wall, and as a half of wall height for the case of groundwater perpendicular to the wall. Thermal diffusivity is being studied in the range between  $1 \cdot 10^{-7} \text{ m}^2/\text{s}$  and  $2 \cdot 10^{-6} \text{ m}^2/\text{s}$  (Vulliet et al., 2016).

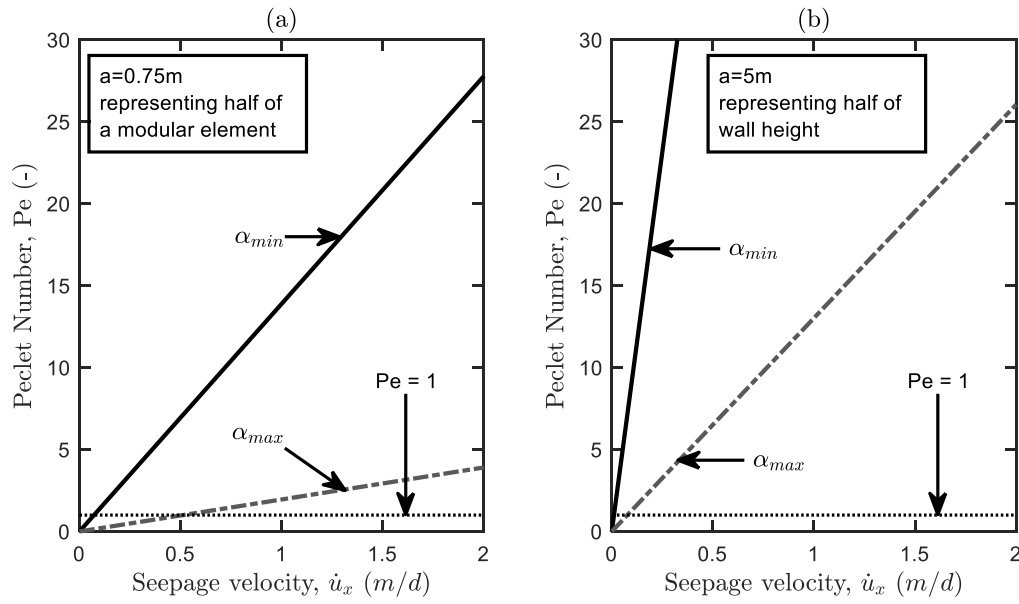


Figure 4.12 Evaluation of Péclet number with groundwater flow velocity for (a) parallel and (b) perpendicular groundwater flow with respect to the wall

The evaluation of the maximum limiting value of velocity to reach the condition  $Pe < 1$  can be consequently done: for parallel groundwater flow,  $v_u = \dot{u}_x \leq 0.5 \text{ m/d}$ . For perpendicular groundwater flow,  $\dot{u}_x \leq 0.1 \text{ m/d}$  which corresponds to an undisturbed velocity  $v_u \sim (0.3 \div 0.8) \text{ m/d}$ . Concluding, a velocity value of  $v_u = 0.5 \text{ m/d}$  can be used as a separator between the two main heat exchange modes.

#### 4.5.2 Proposition of a flowchart for early-stage thermal performance design

To propose a flowchart that is based on such results and theoretical principles, the definition of the conditions and implications of each heat exchange mode are needed.

In case of conductive-dominated regime (i.e., when a groundwater table is not present or  $v_u < 0.5 \text{ m/d}$ ), the long-term sustainability of the project has to be guaranteed. It is essential to ensure an adequate thermal recharge to the soil mass to avoid any unacceptable long term temperature variation

(Fromentin et al., 1999). An optimum functioning mode is represented by the case where cooling and heating operations are balanced. In the case of convective-dominated regime, a designer must mind that the heat storage is inhibited because of the fluid flow that dissipates the heat in the surrounding soil mass.

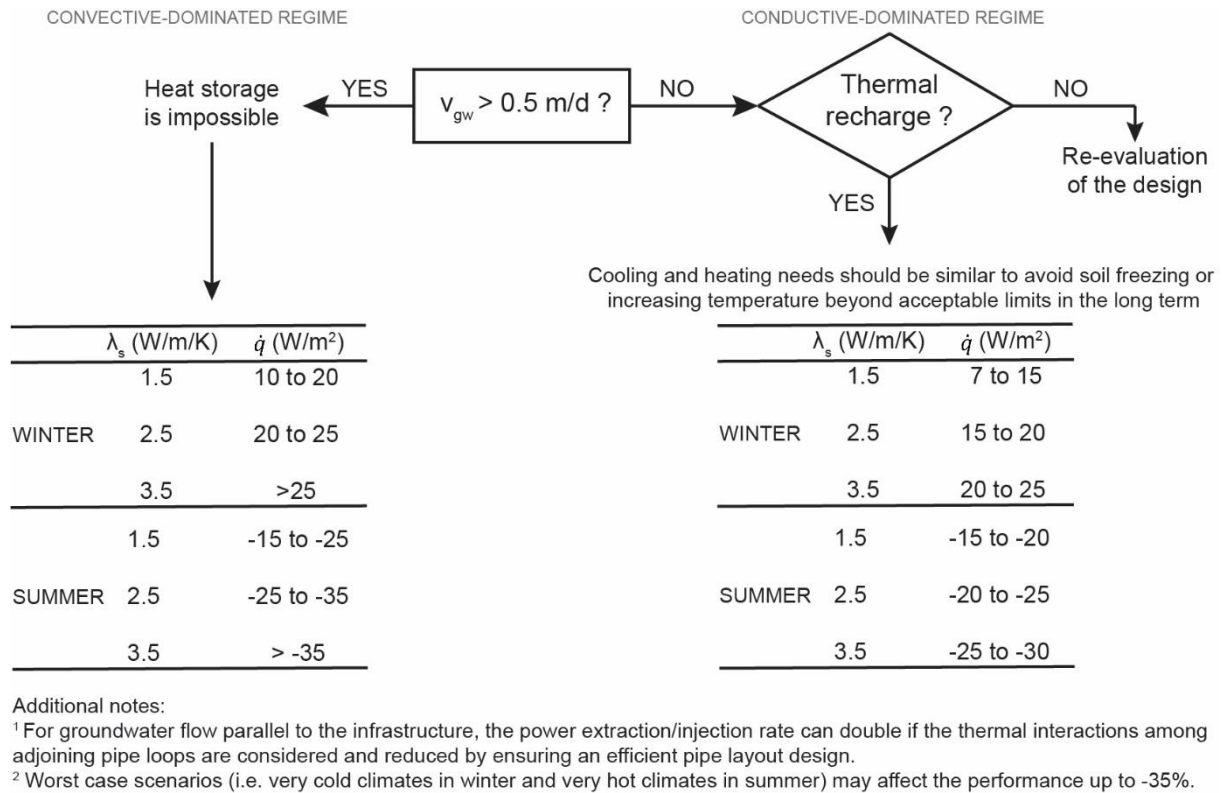


Figure 4.13 Flowchart for early-stage thermal performance design of energy walls

## 4.6 Conclusions

This paper summarizes some concepts of hydro-thermal interactions applied to EWs and presents a methodology for early-stage thermal performance design of such EGs.

A portion of an energy infrastructure is numerically modelled, and the thermal behavior is discussed with reference to different environmental conditions. The presence of groundwater flow in the soil on one hand enhances the heat exchanges but on the other hand induces adverse hydraulically induced thermal interactions among adjoining pipe loops. The performance of one heat exchanger loop in the case of parallel groundwater flow conditions is greater with respect to the perpendicular groundwater flow case. Within this framework, the time-dependent nature of the heat exchangers response is highlighted. The structural thermal characterization plays a non-negligible role, a precise quantification of the thermal conductivity is hardly feasible due to the broad range of values available in the literature,

the dependency on many parameters (such as density and degree of saturation) and the long term interactions with the soil. Consequently, the response of the heat exchangers may considerably vary.

A methodology for early-stage thermal performance design of EW is then proposed. It is based on a sound theoretical basis that helps to account for the multiphysical phenomena acting and interacting one another (thermodynamics, fluid dynamics) at different scales. Once basic hydro-thermal characteristics of a site are known, a flowchart gives values for power extraction/injection rates expressed in  $\text{W/m}^2$  of thermo-active surface, for heating and cooling operations.

This methodology will help designers to have a preliminary quantification of the energy achievable by equipping an infrastructure with EWs, during the early-stage design phases. Moreover, such a methodology may have an impact on the decision making process when the question is whether or not to install thermo-active elements on a planned infrastructure project. The data included in this design tool represent a conservative estimation of the power rate because of the definition of steady flux conditions with respect to the selected thermal input.

Finally, EWs show a good potential for energy exploitation. Average values for power extraction/injection rate range between  $10 \text{ W/m}^2$  and  $50 \text{ W/m}^2$ . The early-stage thermal performance design methodology presented here may represent a decisive tool for designers to close a gap between researchers and practitioners, enabling such technology to be more widely used.

### **Acknowledgements**

The authors wish to acknowledge the support of the European Commission via the Marie Skłodowska-Curie Innovative Training Networks (ITN-ETN) project TERRE 'Training Engineers and Researchers to Rethink Geotechnical Engineering for a Low Carbon Future' (H2020-MSCA-ITN-2015-675762).



## Part 2 : Thermomechanical behavior





# Chapter 5      Extension of Winkler's solution to non-isothermal conditions for capturing the behaviour of plane geostructures subjected to thermal and mechanical actions

**Disclaimer:** The content of this chapter has been published in the following journal paper:

Zannin, J., Rotta Loria, A. F., Llabjani, Q., & Laloui, L. (2020). Extension of Winkler's solution to non-isothermal conditions for capturing the behaviour of plane geostructures subjected to thermal and mechanical actions. *Computers and Geotechnics*.

**My contribution:** Conceptualization, Validation, Writing – Original Draft, Visualization.

## 5.1 Foreword

Before this study, no analytical models had been made available for describing the behaviour of plane geostructures subjected to thermal and mechanical actions. This knowledge gap notably represented a limitation for investigations about the behaviour of so-called energy geostructures, which are subjected to the considered actions due to their geothermal heat exchanger and structural support roles. In this study, the first analytical model that allows describing the behaviour of plane geostructures subjected to thermal and mechanical actions is presented. This model extends Winkler's solution to non-isothermal conditions for quantifying the effects of temperature variations, axial loads, transversal loads and bending moments applied to plane geostructures resting on an elastic soil mass. The model is applied to the analysis of an elementary unit represented by a single beam as well as to more complex plane geostructures using the superposition principle. The obtained results are compared with predictions deriving from more rigorous yet time-consuming numerical analyses, showing close agreement. This result makes the developed analytical model a useful tool for scientific and engineering purposes, paving the way for future developments in this scope.

## 5.2 Introduction

The behaviour of geostructures involves mutual interactions between structural elements and the ground. Conventionally, interactions between geostructures and the ground have mainly been

caused by mechanical actions. Currently, a rising number of situations involve geostructures that are subjected to a variety of multiphysical actions. When dealing with so-called energy geostructures, which involve dual structural support and geothermal heat exchanger role, thermal and mechanical actions that must be considered for analysis and design purposes are typically encountered (Laloui & Rotta Loria, 2019).

A variety of modelling approaches can be employed to address the interactions occurring between geostructures and the ground. Examples of these approaches include analytical and numerical models, with the former being preferred to the latter especially at early stages of analysis and design (e.g., geotechnical and structural) due to their simplified yet representative description of reality.

Since the 18th century, Coulomb (Coulomb, 1776) and Winkler (Winkler, 1867) have addressed the analytical modelling of the interaction between geostructures and the surrounding ground. Winkler's theory of subgrade reaction has been developed resorting to the previous investigations and employed for analysing problems related to horizontal footings (Terzaghi, 1955), retaining walls (Ménard & Bourdon, 1965) and piles (Coyle & Reese, 1966; Frank & Zhao, 1982). The analytical solution associated with Winkler's theory describes a beam foundation resting on a soil mass composed by a series of closely spaced, linear elastic and independent springs, whose stiffness (called modulus of subgrade reaction) governs the relationship between the pressure exerted by the soil to the foundation and the deflection. Winkler's solution can be applied to describe the behaviour of plates, in addition to beams, although limitations in the resulting predictions are typically observed due to the lack of continuity at the foundation edges. A variety of models have been proposed to improve Winkler's solution with respect to the limitations above. In these models, in addition to the parameter associated with the stiffness of the spring, the soil is described using one or two parameters that include the effects of additional flexural elements, virtual shear layers, pre-tensioned membranes, etc. (Hétyenyi, 1946, 1950; Kerr, 1965; Pasternak, 1954; Reissner, 1937). A description of such models has been proposed by Hétyenyi (Hétyenyi, 1946) and Selvadurai (Selvadurai, 1979), and explicates models characterised by one, two, or three parameters. In general, the subgrade reaction modulus included in Winkler's solution can be related relatively easily to the elastic properties of soils. In contrast, the second and third parameters included in the models above are sometimes difficult to estimate because they do not necessarily have a physical meaning. For this reason, Winkler's solution is often employed for practical purposes to provide approximate yet representative estimations of reality.

Applications of analytical models based on Winkler's solution typically address horizontal footings and vertical retaining structures. Substantial differences among the previous two applications reside in the determination and calibration of the Winkler's subgrade reaction modulus. For horizontal footings, several theoretical, semi-empirical and empirical definitions are widely available in the literature (e.g., (Barden, 1963b, 1962; Biot, 1937; Galin, 1943; Selvadurai, 1979; Terzaghi, 1955; Vesic, 1961b; Vesic, 1961a; Vesic & Johnson, 1963)). For vertical retaining structures, the complexities of the problem

geometry make theoretical estimations complicated and extensive validations of semi-empirical and empirical procedures against field testing are often employed (e.g., (Balay, 1984; Fages & Bouyat, 1971; Ménard & Bourdon, 1965; Monnet, 1994; Schmitt, 1995; Terzaghi, 1955)).

Before this study, all of the available analytical models for describing the interaction between plane geostructures and the ground allowed a description of the influence of sole mechanical actions. In other words, no analytical soil-structure interaction models for plane geostructures have been made available for capturing the influence of thermal actions, potentially applied in conjunction with mechanical actions. Looking at this knowledge gap, this paper presents the formulation and application of an analytical model based on an extension of Winkler's solution to non-isothermal conditions for describing the behaviour of plane geostructures subjected to thermal and mechanical actions. This model is developed with particular reference to energy geostructures, although it may be employed for the analysis of other relevant problems that are increasingly encountered in science and engineering.

In the following, the proposed analytical model is derived and discussed first. Then, the model is applied to the analysis of problems of increasing complexity and the obtained results are compared with those of more rigorous yet time-consuming numerical analyses. Finally, concluding remarks that can be drawn from this work are summarised.

## 5.3 Analytical model for plane geostructures subjected to thermal and mechanical actions

### 5.3.1 Fundamentals

In this study, a beam is defined as a structural element having one dimension (length,  $L$ ) that is much greater than the other two (breadth,  $b$ , and height,  $h$ ). Winkler's solution is employed to describe the behaviour of beams resting on an elastic soil mass. Winkler's solution is based on the widely known Euler-Bernoulli theory of beams (circa 1750, as appears in Truesdell (Truesdell, 1960)). Such a theory allows writing the relationship between the deflection and the loads characterising any beam and obtaining the fourth-order differential equation that governs the problem. In small deformations, Euler-Bernoulli theory involves that straight lines or planes normal to the neutral axis of the beam remain straight and normal to the considered axis after deformation. This feature allows expressing the bending moment proportionally to the second derivative of the deflection.

Based on the previous premises, Winkler's solution resorts to the three following hypotheses. (i) The subgrade reaction modulus,  $k_s$ , is independent of the pressure and involves the same response for both loading and unloading. (ii) The value of  $k_s$  does not vary in space. (iii) The springs work unidirectionally and independently of each other. The previous hypotheses involve the following practical considerations. (i) The soil follows a linear elastic behaviour, which makes the solution representative and

suitable for the analysis of limited deformation levels (so-called serviceability conditions). (ii) The soil reaction is uniformly distributed among the springs, which makes the solution unsuitable to describe rigid beams but particularly appropriate to model flexible beams. (iii) Any influence caused by actions in the soil outside the beam length cannot be captured, which makes the solution suitable to provide accurate estimates of action effects along the beam only.

In the following, the adopted sign convention is that of structural mechanics. Positive deflections and rotations are directed downwards and clockwise, respectively, and tensile forces are considered as positive. Unless otherwise specified, reference is made to one-dimensional conditions.

### 5.3.2 Influence of thermal and mechanical actions on plane geostructures

Thermal and mechanical actions applied to geostructures result in a variety of effects for the structure and the ground. Thermal actions are typically associated with temperature variations within and around geostructures. Mechanical actions are typically associated with axial loads, transversal loads and bending moments.

The temperature variations caused by thermal actions are typically non-uniform and can be idealised as composed of two contributions (Figure 5.1): a constant distribution of temperature variation over the cross-section of the structure,  $\Delta T_a$ , inducing an axial effect, and a linear distribution of temperature variation over the cross-section of the structure,  $\Delta T_c$ , inducing a bending effect. The uniform and linear temperature variations can be evaluated as:

$$\Delta T_a = \frac{\Delta T_2 + \Delta T_1}{2} \quad (5.1)$$

$$\Delta T_c = \frac{\Delta T_2 - \Delta T_1}{2} \quad (5.2)$$

The axial and bending effects resulting from the previous temperature variations can be associated with a thermally induced axial strain and curvature, respectively. Prevention of these effects results in the development of axial loads and bending moments, respectively. The effects of generally distributed mechanical loads are axial and transversal displacements, rotations of the neutral axis, axial and shear forces, as well as bending moments.

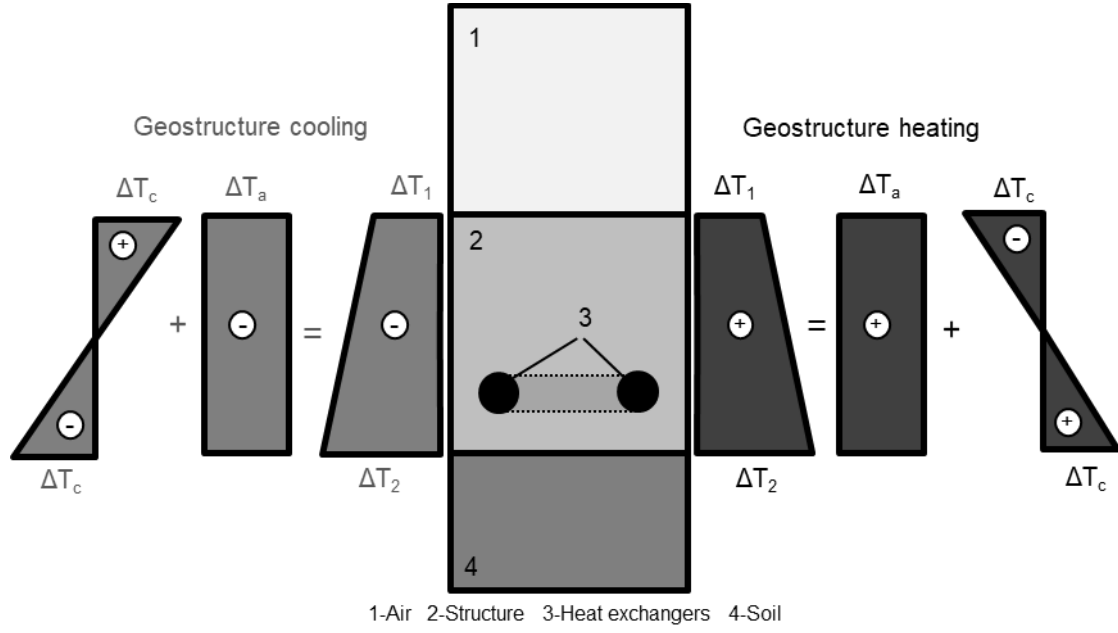


Figure 5.1 Idealised schematic of the temperature variation within the cross-section of a plane geostructure interfacing, from one side, the air, and from the other side, the ground. The considered schematic can refer to a slab resting on the ground or to the exposed portion of a retaining wall.  $\Delta T_1$  and  $\Delta T_2$  refer to the temperature variations at the geostructure-air and geostructure-soil interfaces, respectively.

### 5.3.3 Degree of freedom: definition for axial and flexural actions

The concept of degree of freedom is a powerful means to address the effects caused by temperature variations applied to geostructures (Laloui & Rotta Loria, 2019): it expresses the development of a relevant physical quantity to its value under free thermal deformation conditions. Before this study, the degree of freedom was applied to describe axial effects caused by thermal actions applied to geostructures (Laloui et al., 2003); in contrast, no applications of this parameter were reported to address flexural effects caused by thermal actions applied to geostructures. In the following, the degree of freedom is defined and employed to address both axial and flexural effects caused by constant and linear distributions of temperature variations applied to geostructures.

A constant distribution of temperature variation,  $\Delta T_a$ , applied along a geostructure free to move at its ends causes the development of a free thermally induced axial strain,  $\varepsilon_f^{th}$ , as

$$\varepsilon_f^{th} = \alpha \Delta T_a \quad (5.3)$$

where  $\alpha$  is the linear thermal expansion coefficient of the material. A linear distribution of temperature variation applied along a geostructure free to move at its ends causes the development of a free thermally induced curvature,  $\chi_f^{th}$ , as

$$\chi_f^{th} = \frac{\alpha}{I} \int_A y_h \frac{2\Delta T_c}{h} dA = \frac{2\alpha\Delta T_c}{h} \quad (5.4)$$

where  $I$  is the moment of inertia of the cross-section,  $A$ , and  $y_h$  is the coordinate along the geostructure height,  $h$ .

A partial restraint applied to a geostructure by any given boundary condition (e.g., the presence of the ground and a connected structure) yields to the development of an observed axial deformation and curvature that are a fraction of the ones under free thermal deformation conditions. The previous consideration involves that only a portion of axial deformation and curvature is developed with respect to those under free deformation conditions, while a portion of axial deformation and curvature is blocked.

The previous considerations inherently yield to the definition of the degree of freedom. The degree of freedom associated with axial effects,  $DOF_a$ , can be defined as:

$$DOF_a = \frac{\varepsilon_o^{th}}{\varepsilon_f^{th}} \quad 0 \leq DOF_a \leq 1 \quad (5.5)$$

where  $\varepsilon_o^{th}$  represents the observed thermally induced axial strain. The degree of freedom associated with flexural effects,  $DOF_c$ , can be defined as:

$$DOF_c = \frac{\chi_o^{th}}{\chi_f^{th}} \quad 0 \leq DOF_c \leq 1 \quad (5.6)$$

where  $\chi_o^{th}$  represents the observed thermally induced curvature.

Internal actions develop as a consequence of the blocked portion of deformations. The restraint of a constant distribution of temperature variation causes a thermally induced axial force. The restraint of linear distribution of temperature variation causes a thermally induced bending moment (which explicates a tensile action at one side of the cross-section and a compressive action at the other side). The observed thermally induced axial force,  $N_o^{th}$ , and bending moment,  $M_o^{th}$ , caused by the previous temperature variations can be quantified as

$$N_o^{th} = N^{th} = AE\alpha\Delta T_a(1 - DOF_a) \leq N_b^{th} \quad (5.7)$$

$$M_o^{th} = M^{th} = EI \frac{2\alpha\Delta T_c}{h}(1 - DOF_c) \leq M_b^{th} \quad (5.8)$$

where  $N_b^{th}$  and  $M_b^{th}$  are the axial force and bending moment under completely blocked deformation conditions, respectively.

Figure 5.2 shows parallelism between the axial and flexural effects caused by constant and linear distributions of temperature variations in a geostructure, highlighting the link between the relevant degree of freedom and the development of deformations and internal actions. The cases of a structure free to

deform, completely restrained (i.e., blocked), and partly restrained by varying magnitudes of constraints are considered.

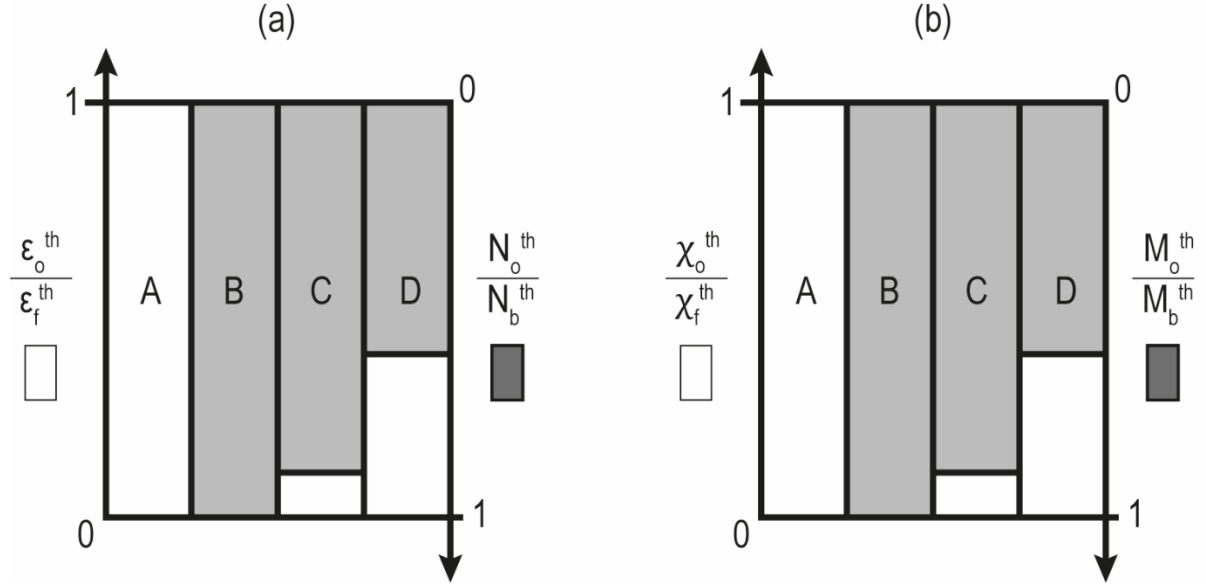


Figure 5.2 Qualitative development of deformations and internal actions caused by (a) constant and (b) linear distribution of temperature variations in a geostructure: (A) free case, (B) completely restrained case, (C) partly restrained case with significant prevention of deformations, and (D) less restrained case with less significant prevention of deformations.

#### 5.3.4 The analytical model

From Euler-Bernoulli theory, the rotation,  $\theta(x)$ , the bending moment,  $M(x)$  and the shear force,  $V(x)$ , characterising any infinitely small element of a beam as a consequence of the application of thermal and mechanical actions inducing flexural effects (e.g., non-uniform distribution of temperature variations or distributed loads perpendicular to the beam axis) respectively read

$$\theta(x) \approx \tan \theta(x) = \frac{dy(x)}{dx} \quad (5.9)$$

$$M(x) = -EI \frac{d^2y(x)}{dx^2} - EI\chi_f^{th} \quad (5.10)$$

$$V(x) = \frac{dM(x)}{dx} \quad (5.11)$$

where  $x$  is the relevant coordinate axis and  $y$  is the deflection. In addition to the previous actions, axial forces,  $N$ , can characterise any element of a beam due to the application of thermal and mechanical actions (e.g., uniform distributions of temperature variations or mechanical forces applied normal to the beam transversal cross-section). Consideration of one-dimensional conditions involves neglecting any extension or contraction of the beam within its cross-section due to the considered actions. The present



model can be formulated by analysing the equilibrium of a beam element resting on an elastic soil of length  $dx$  in its deformed configuration (Figure 5.3(a)).

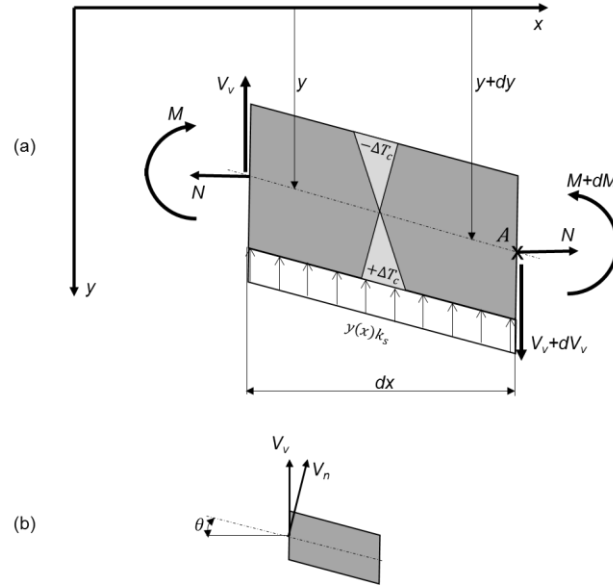


Figure 5.3 Schematic of (a) the equilibrium of a beam element of length  $dx$  and (b) the geometric decomposition of shear actions.

Vertical equilibrium gives

$$\frac{dV_v}{dx} = y(x)k_s \quad (5.12)$$

where  $V_v$  is the vertical shear force, which can be correlated to the normal shear force,  $V_n$  (Figure 5.3(b)):

$$V_n = V_v \cos \theta - N \sin \theta \approx V_v - N \frac{dy}{dx} \quad (5.13)$$

The generalised shear action is evaluated by modifying equation (5.11) to account for the two components of the shear force. The following expression is obtained

$$V(x) = -EI \frac{d^3 y(x)}{dx^3} - EI \frac{d\chi^{th}}{dx} + N \frac{dy(x)}{dx} \quad (5.14)$$

The moment equilibrium around point A, divided by  $dx$ , can be written as follows (neglecting second-order terms):

$$\frac{dM}{dx} = V_v - N \frac{dy}{dx} \quad (5.15)$$

Substituting equation (5.10) into (5.15), differentiating with respect to  $x$  and considering equation (5.12), the differential equation of the elastic line is obtained for this problem:

$$EI \left( \frac{d^4 y}{dx^4} + \frac{d\chi^{th^2}(x)}{dx^2} \right) - N \frac{d^2 y(x)}{dx^2} + k_s y(x) = 0 \quad (5.16)$$

Equation (5.16) has a solution of the type:

$$y(x) = (C_1 e^{\alpha x} + C_2 e^{-\alpha x}) \cos \beta x + (C_3 e^{\alpha x} + C_4 e^{-\alpha x}) \sin \beta x \quad (5.17)$$

with:

$$\alpha = \sqrt{\lambda^2 + \frac{N}{4EI}} \quad (5.18)$$

$$\beta = \sqrt{\lambda^2 - \frac{N}{4EI}} \quad (5.19)$$

where  $\lambda$  is called the characteristic of the system. The term  $1/\lambda$  is called the characteristic length, as defined by Hétenyi (Hétenyi, 1946), and it is a useful parameter to express the problem solution as a function of the non-dimensional parameter  $\lambda L$ , called relative stiffness of the beam. The parameter  $\lambda$  reads

$$\lambda = \sqrt[4]{\frac{k_s}{4EI}} \quad (5.20)$$

The integration constants,  $C_1, C_2, C_3$  and  $C_4$  can be defined by imposing the boundary conditions and solving the system of equations (5.9)(5.10) and (5.17). The resolution of this system allows extending the classical Winkler's solution to non-isothermal conditions. In this work, a code has been developed to solve this system using the software Wolfram Mathematica 11 (Wolfram Research, 2019).

### 5.3.5 Analysis of simple plane geometries

The obtained analytical model can straightforwardly address the effects caused by arbitrary thermal and mechanical actions applied to *simple plane geometries*: geostructures (e.g., beams) of finite dimensions resting on a Winkler-type soil mass that are arbitrarily restrained by boundary conditions and subjected to loading (Figure 5.4). This capability resorts to the superposition principle (i.e., an essential constituent of the elastic theory employed herein). Based on this principle, the effects caused by arbitrary combinations of loading actions can be considered as the sum of the effects caused by single actions solved separately. Accordingly, the deflection, rotation, bending moment, shear force and normal force can be considered as made of two contributions: one component caused by any thermal action and another component caused by any mechanical action. The generalised axial force resulting from a thermal and mechanical action can hence be defined for any element of a beam as:

$$N = N^{th} + N^m \quad (5.21)$$

where the superscripts th and m stand for “thermal” and “mechanical”, respectively.

From the previous considerations, it results

$$y(x) = y^{th}(x) + y^m(x) \quad (5.22)$$

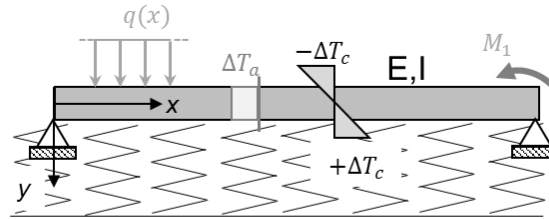
$$\theta(x) = \theta^{th}(x) + \theta^m(x) \quad (5.23)$$

$$M(x) = M^{th}(x) + M^m(x) \quad (5.24)$$

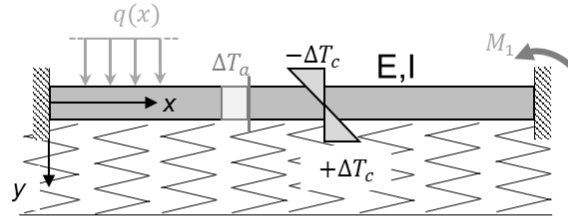
$$V(x) = V^{th}(x) + V^m(x) \quad (5.25)$$

The influence of any thermal loading configuration (e.g., a constant or a linear distribution of temperature variation) along the beam can be quantified by imposing the boundary conditions and, consequently, by determining the four integration constants from equation (5.17). The influence of any mechanical loading configuration (e.g., a concentrated mechanical force) can be addressed by employing the method of initial conditions as detailed in Appendix B.

(a) - Hinged



(b) - Fixed



(c) - Partly restrained

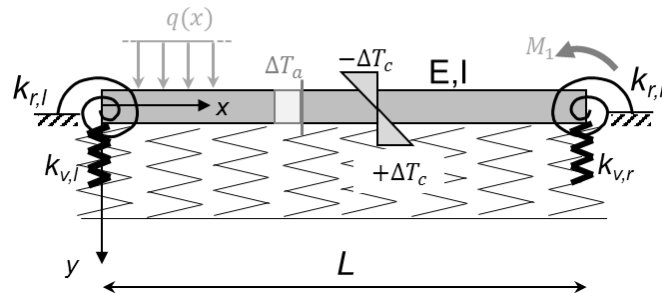


Figure 5.4 Examples of simple plane geometries characterised by different boundary conditions: (a) hinged, (b) fixed and (c) partly restrained

### 5.3.6 Analysis of complex plane geometries

The obtained analytical model can also effectively address the effects of arbitrary combinations of thermal and mechanical actions on *complex plane geometries*: geostructures composed by multiple elements mutually connected one another (e.g., cut-and-cover structures, structures involving wall-slab and wall-anchors intersections, mat foundations and multi-floored structures) that are partly or entirely surrounded by a Winkler-type soil mass and subjected to loading (Figure 5.5). In the present context, this capability is again related to the superposition principle. Relevant simple plane geometries can be considered as an elementary unit for more complex plane geometries. The effects of thermal and mechanical actions applied to these geometries can be addressed straightforwardly. Once such action effects are obtained, they can be considered as boundary loads for the other unit(s) composing the complex plane geometry. From the foregoing, general combinations of thermal and mechanical actions can be solved for all the elementary units constituting any complex geometry, thus yielding a complete procedure for addressing the related response.

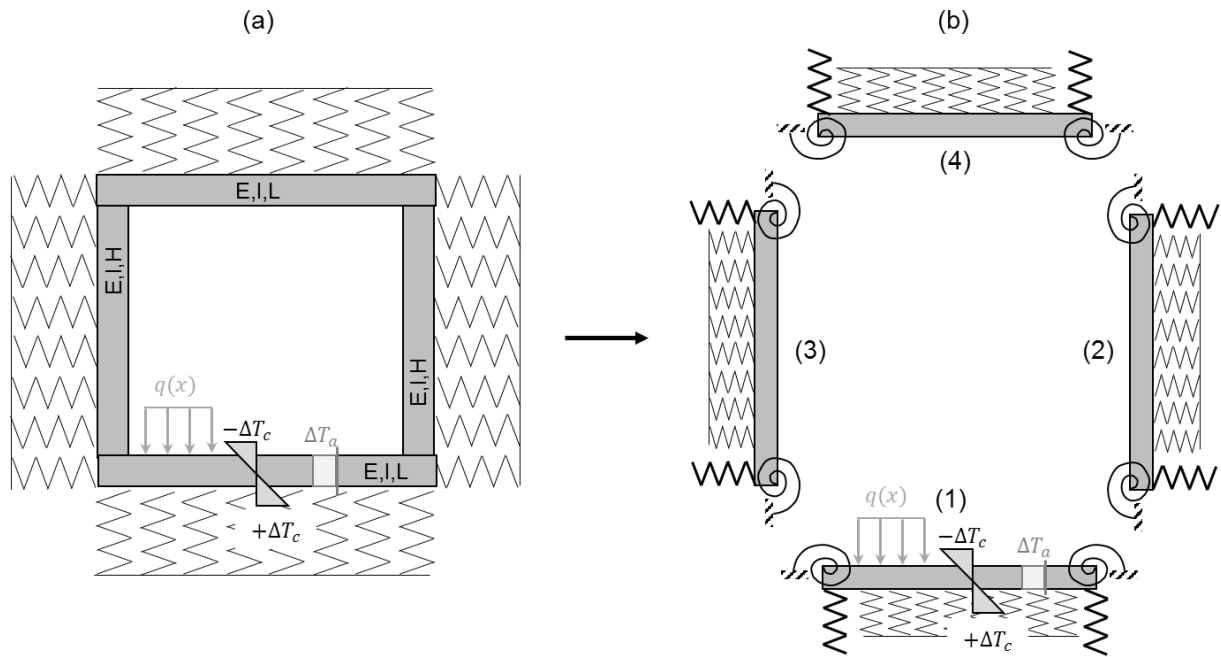


Figure 5.5 Example of (a) a complex plane geometry (i.e., a cut-and-cover tunnel) and (b) a related geometrical decomposition approach into four simple plane geometries

### 5.3.7 Boundary conditions

Three possible conditions can characterize beams, such as general geostructures: completely free conditions, completely restrained conditions, or partly restrained conditions (Figure 5.4). The most common condition encountered in practice corresponds to a situation wherein beams are partly

restrained at their ends (transversal  $(k_{v,l}, k_{v,r})$  and rotational  $(k_{r,l}, k_{r,r})$  springs are considered at each end of the structure in such cases). In some cases, the restraint characterising beams could be so high that completely restrained conditions may be representative of reality.

A summary of the mathematical formulations allowing to consider the discussed boundary conditions is detailed in Table 5.1. Consideration of these formulations allows resolving the problems addressed by the obtained analytical model.

Table 5.1 Boundary conditions for selected cases

	Fixed	Hinged	Free	Partly restrained
Conditions	$y(0) = y(L) = 0$ $\theta(0) = \theta(L) = 0$	$y(0) = y(L) = 0$ $M(0) = M(L) = 0$	$M(0) = M(L) = 0$ $V(0) = V(L) = 0$	$y(0) = \frac{V(0)}{k_{v,l}}$ $\theta(0) = -\frac{M(0)}{k_{r,l}}$ $y(L) = -\frac{V(L)}{k_{v,r}}$ $\theta(L) = \frac{M(L)}{k_{r,r}}$

### 5.3.8 Modulus of subgrade reaction

The modulus of subgrade reaction,  $k_s$ , is a key parameter to address the response of geostructures. This parameter does not represent an intrinsic characteristic of soils, but it depends on the soil properties, geostructure dimensions, geometry and rigidity, and the spatial distribution of the applied loads (Delattre, 2001; Selvadurai, 1979; Terzaghi, 1955). While Terzaghi (Terzaghi, 1955) proposed charts for the determination of  $k_s$  based on the results of an experimental campaign, other authors proposed empirical relations linking  $k_s$  to parameters such as the Young's modulus of soils,  $E_s$ , the Poisson's ratio,  $\nu_s$ , or the foundation breadth,  $B$  (Barden, 1963b, 1962; Biot, 1937; Galin, 1943; Vesic, 1961b; Vesic, 1961a; Vesic & Johnson, 1963). Table 5.2 summarises some widely established empirical formulations to estimate  $k_s$ . A practical application for the determination of  $k_s$  is presented in Appendix C.

Table 5.2 Determination of  $k_s$  from empirical formulations

Formula	Reference
$k_s = \frac{0.65E_s}{B(1-\nu_s^2)}$	(Barden, 1963b, 1962)
$k_s = \frac{\pi E_s}{2B(1-\nu_s^2) \ln \frac{L}{B}}$	(Galin, 1943), recalled in (Selvadurai, 1979)
$k_s = \frac{1}{B} \left[ 0.65 \sqrt{\frac{E_s B^4}{EI}} \right] \frac{E_s}{1-\nu_s^2}$	(Vesic, 1961b; Vesic, 1961a), (Vesic & Johnson, 1963)
$k_s = \frac{E_s}{B(1-\nu_s^2)}$	Meyerhof and Baieke
$k_s = \frac{0.95E_s}{B(1-\nu_s^2)} \left[ \frac{E_s B^4}{(1-\nu_s^2)EI} \right]^{0.108}$	(Biot, 1937)

## 5.4 Application and validation of the analytical model – simple plane geometries

### 5.4.1 General

The literature is rich in investigations addressing with the classical Winkler's solution the effects of mechanical actions (e.g., concentrated and variably distributed forces and moments) on the behaviour of plane geostructures (Hétyenyi, 1946; Selvadurai, 1979). In contrast, no investigations addressing the effects of thermal actions have ever been made available before this study. Looking at such a challenge, the proposed extension of Winkler's solution is employed in this section to address the effects of thermal actions (e.g., a unitary linear distribution of temperature variation) on the behaviour of a geostructure characterised by a simple plane geometry. Complementary comments about the effects of thermal (and mechanical) actions on the behaviour of geostructures are eventually reported.

### 5.4.2 The problem

In the following, beams characterised by hinged and partly restrained boundary conditions are considered. Perfectly fixed conditions are not treated as they represent a trivial case: displacements are entirely blocked, and internal actions are constant everywhere. In other words, the deflection and rotation are equal to zero, and the internal actions reach their constant maximum values by definition of entirely blocked conditions.

Hinged conditions aim at representing the behaviour of beams characterised by connections with an infinite transversal stiffness and zero rotational stiffness at their ends. Such conditions do not represent realistic conditions usually encountered in engineering. Partly restrained conditions aim at representing the behaviour of beams connected with other structural elements that are common in practice (e.g., wall-

slab connections, such as for cut-and-cover structures). In the following, when considering partly restrained conditions, symmetric boundary conditions at the ends of the beam are considered:  $k_{v,l} = k_{v,r} = k_v$  and  $k_{r,l} = k_{r,r} = k_r$ . For both of the considered boundary conditions, the subgrade reaction modulus reads  $k_s = 10^6 \div 10^8$  N/m<sup>3</sup>, aiming at encompassing soft to stiff soils, respectively (Selvadurai, 1979; Terzaghi, 1955). Complementary input parameters characterising the considered problem are presented in Table 5.3. The rationale of considering a linear distribution of temperature variation of  $\Delta T_c = 1.0$  °C is that it provides a unitary response of the modelled problem. In particular, as long as the hypothesis of a reversible response of the soil (and structure) holds, temperature variations of  $\Delta T_c = 10.0$  °C and  $\Delta T_c = -1.0$  °C, for example, yield to results that are ten times higher and opposite compared to those discussed here, respectively.

Table 5.3 Input parameters for the modelling of the considered problem

$L$ (m)	$h$ (m)	$B$ (m)	$\Delta T_c$ (°C)	$E$ (Pa)	$k_r$ (Nm/rad)	$k_v$ (N/m)
10.0	0.5	1.0	1.0	$25.0 \times 10^9$	$1.0 \times 10^9$	$1.0 \times 10^8$

To validate the capabilities of the present analytical model in addressing the considered problem, comparisons with the results of numerical models have been made (the details of the numerical models are highlighted in Appendix C). In this context, two problems have been considered: (i) a beam resting on a spring foundation and (ii) a beam resting on a continuum medium. In the first case, the analytical and numerical modelling results perfectly match (error of 0%): this result fully validates the capability of the proposed extension of Winkler's solution in capturing the effects of thermal actions with respect to a numerical modelling technique considering the same problem (this capability is also observed for mechanical actions). In the second case, differences between the analytical and numerical modelling results are observed: these differences are critically discussed in the following.

### 5.4.3 Comparison between analytical and numerical modelling results

The comparison between analytical and numerical modelling results is reported in Figure 5.6. In the following, considerations related to deflections, rotations and internal actions are reported, and a discussion resorting to the concept of degree of freedom is eventually proposed.

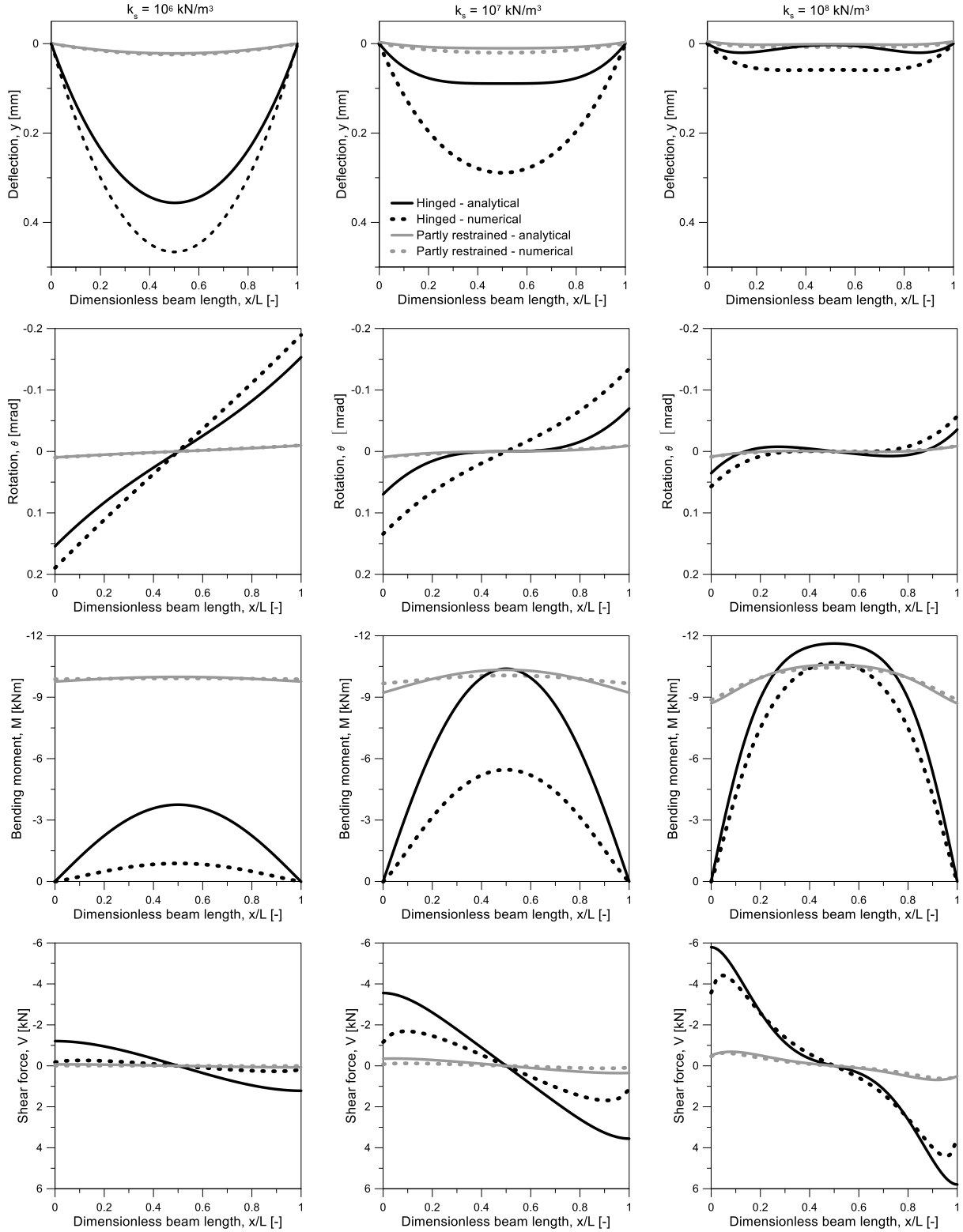


Figure 5.6 Thermo-mechanical response of a geostructure resting on different soil conditions and subjected to a linear distribution of temperature variation: comparison between analytical and numerical models



#### 5.4.3.1 Deflection and rotation

The following considerations apply irrespective of the considered static scheme. For very stiff soils (e.g.,  $k_s = 10^8$  N/m<sup>3</sup>), the relative stiffness  $\lambda L$  is relatively high and thus the deflection is concentrated in the vicinity of the boundaries. It follows that the conditions at one end of the beam do not affect the results at the other end of the beam and the deflection at the mid-span is nearly zero. As suggested by Hétenyi (Hétenyi, 1946), the solution of this problem can be simplified by a superposition of two semi-infinite beams. For soft soils (e.g.,  $k_s = 10^6$  N/m<sup>3</sup>), the relative stiffness  $\lambda L$  is relatively low. The maximum deflection takes place at the midpoint of the beam. Following the classification proposed by Hétenyi (Hétenyi, 1946), the solution of this problem can be found by considering the beam as finite. The maximum values of rotation are recorded at the beam ends. Zero rotation is evaluated at the mid-span of the beam, showing an anti-symmetric distribution.

The following considerations apply with reference to the static scheme. Hinged conditions allow for free rotation at the boundaries and null vertical deflection. Under these conditions, the beam displaces downwards showing a maximum at its mid-span and zero deflection at the boundaries. Rotation is maximum (in absolute value) at the boundaries and goes to zero at the mid-span. At the considered location, the deflection presents a minimum. Partly restrained conditions affect the magnitude of the deflection and rotation. The deformed shape is the same as for hinged conditions, but characterised by a lower magnitude.

By comparing the analytical and numerical modelling results, some remarks can be highlighted. The analytical model suffers from a lack of continuity between the springs and at the sides of the beam. This feature does not characterise the employed numerical model. Therefore, deflection and rotation are generally underestimated by the analytical modelling results compared to the numerical modelling results. Such discrepancies in the results could be partly recovered by employing a two-parameter model such as that reported by Pasternak (Pasternak, 1954). The differences between the analytical and numerical modelling results are higher for lower rotational boundary constraints. If there is some rotational stiffness at the boundaries, the results of the analytical model approach the numerical ones.

#### 5.4.3.2 Internal actions

The following considerations apply irrespective of the considered static scheme. Bending moment and shear forces develop because of the applied loads as well as the presence and significance of constraints. In entirely free deformation conditions, a beam subjected to a linear thermal load would deflect downwards and be subjected to zero thermally induced internal actions. In partly or fully restrained conditions, a constraint to the beam bending causes a tensile force in the upper part of the cross-section as a consequence of cooling thermal loading, while a compressive force in the lower part as a

consequence of heating thermal loading. The correspondent bending moment shape is towards the beam extrados.

The following considerations apply with reference to the static scheme. By definition of hinged conditions, bending moment is equal to zero at the boundaries of the beam and presents a maximum at the mid-span of the beam. In these conditions, bending is only restrained by the soil reaction. In partly restrained conditions, the observed bending moment follows equation (5.8)). The higher the boundary rotational stiffness, the flatter the bending moment distribution. Because of the definition of the shear force (equation (5.11)), shear actions are maximum when high bending moment variations develop along the beam. For flatter bending moment distributions, the shear force approaches zero. It follows that maximum values are recorded at the beam ends for hinged conditions, showing an anti-symmetric distribution.

By comparing the analytical and numerical modelling results, some remarks can be highlighted. While the obtained formulation of Winkler's solution underestimates deflections and rotations compared to numerical results considering a continuum soil mass, it overestimates internal actions. The smaller the rotational boundary constraint, the higher the discrepancy among the analytical and numerical modelling results. For partly restrained conditions, the results match satisfactorily.

#### 5.4.3.3 Interpretation of the results using the concept of degree of freedom

Hinged conditions represent a lower bound of the flexural effects that are likely to characterise plane geostructures. The reason for this is because the rotational stiffness is given only by the presence of the soil. It follows that the soil stiffness plays a paramount role in the definition of flexural behaviour. The stiffer the soil, the lower the deflection and the rotation, the higher the internal actions and the smaller the  $DOF_c$ . The softer the soil, the higher the deflection and the rotation, and the lower the internal actions:  $DOF_c \rightarrow 1$  when  $k_s \rightarrow 0$ .

Fully blocked conditions represent an upper bound of the flexural effects that are likely to characterise plane geostructures. In such conditions, rotational and transversal stiffness are blocked by the definition of the boundary conditions (i.e.,  $DOF_c = 0$ ). As the deformation is completely blocked for whatever soil stiffness, bending moment reaches its maximum constant value along the beam length as shown in equation (5.8) for  $DOF_c = 0$ .

Partly restrained conditions represent an intermediate case among hinged and fixed conditions. Consequently, the associated  $DOF_c$  lays between the values that characterise beams under fixed and hinged conditions. The definition of  $DOF_c$  depends on both the soil and the boundary stiffness. A softer soil allows for higher deflection and rotation, and a flatter distribution of internal actions with respect to a stiffer soil. Regarding the rotational boundary stiffness, the higher  $k_r$ , the smaller the deflection and the

rotation, and the flatter the distribution of the internal action reaching a constant value while approaching to fixed conditions ( $DOF_c \rightarrow 0$ ).

#### 5.4.4 Considerations about axial and flexural effects caused by thermal actions

This section aims at providing insights about the modelling of a beam on a Winkler-type soil mass subjected to transversal (i.e., flexural) and axial loads. Transversal loads can be associated, for example, with transversally distributed or concentrated mechanical forces as well as with linear distributions of temperature variations. Axial loads can be associated with axial mechanical forces or constant distributions of temperature variations. Linear distributions of temperature variation induce a transversal action along beams. Constant distributions of temperature variations induce a variation of the deflected shape. The effect of a positive (e.g., tensile) axial load, coming from thermal or mechanical actions reduces the deflection. Conversely, a negative (e.g., compressive) axial load increases the transversal displacement. The limitation of the proposed analytical model is that it is not able to thoroughly quantify axial displacements because of the unidirectional definition (transversal only) of the springs with respect to the beam neutral axis.

### 5.5 Application and validation of the analytical model – complex plane geometries

#### 5.5.1 General

In this section, the proposed extension of Winkler's solution is used to investigate the effects of thermal and mechanical actions (e.g., linear distribution of temperature variation and transversal distribution of mechanical load) on the behaviour of a geostructure characterised by a complex plane geometry. While applying the proposed decomposition procedure to the analysis of the considered structure, the main objective of the following developments is to highlight the redistribution of loading conditions within complex plane geometries.

#### 5.5.2 The problem

A cut-and-cover tunnel with an aspect ratio  $L/H = 1$ , with  $H = L = 10.0$  m, which is embedded in a uniform soil mass, represents the considered complex plane geometry (Figure 5.5). Each beam composing the considered geostructure presents a cross-section of  $h = B = 1.0$  m. The spring foundation representing the soil mass is characterised by a subgrade reaction modulus of  $k_s = 1.8 \times 10^7 \text{ N/m}^3$ . For simplicity, the same value of  $k_s$  is considered for the beams lying horizontally

and vertically. A detailed treatment of the validity of this assumption is reported elsewhere (Balay, 1984; Fages & Bouyat, 1971; Monnet, 1994; Terzaghi, 1955). The boundary conditions per each beam involve rotational springs of  $k_r = 5.0 EI/H = 10.4 \times 10^8 \text{ Nm/rad}$ , and transversal springs for horizontal and vertical elements of  $k_{v,H} = 30.0 EI/L^3 = 6.25 \times 10^7 \text{ N/m}$  and  $k_{v,V} = 2.0 EA/L = 5.0 \times 10^9 \text{ N/m}$ , respectively. Details on the boundary conditions calibration are reported in section 5.5.4.

To address the capabilities of the present analytical model in solving the considered problem, comparisons with the results of numerical models have been made (the details of the numerical models are highlighted in Appendix D). In this context, two problems have been considered: (i) a numerical model employing beam elements for the cut and cover structure, and spring elements for the soil; (ii) a numerical model where the structure is modelled using beam elements and the soil is modelled as a continuum elastic medium with the elastic parameters calibrated following the formulation proposed by Selvadurai (Selvadurai, 1979) and Vesic (Vesic, 1961a).

The material constituting the geostructure is reinforced concrete with Young's modulus  $E = 25.0 \text{ GPa}$ , Poisson's ratio  $\nu = 0.2$  and linear thermal expansion coefficient of  $\alpha_{th} = 10^{-5} \text{ 1/}^\circ\text{C}$ . The numerical models employing the continuum medium idealisation present the following parameters:  $E_s = 2.5 \times 10^7 \text{ N/m}^2$  and  $E_s = 3.5 \times 10^7 \text{ N/m}^2$  for the one calibrated following (Selvadurai, 1979; Vesic, 1961a), respectively. Poisson's ratio is set to  $\nu_s = 0.3$ . The applied loading conditions are a linear distribution of temperature variation of  $\Delta T_c = 1.0 \text{ }^\circ\text{C}$  and a distributed load, downwards directed, acting on the bottom beam of magnitude  $q = 1.0 \text{ kN/m}$ . The rationale of considering a linear distribution of temperature variation of  $\Delta T_c = 1.0 \text{ }^\circ\text{C}$  applies to the consideration of a distributed mechanical load of  $q = 1.0 \text{ kN/m}$ .

### 5.5.3 Analysis approach

This section expands on the steps allowing to model complex plane geometries such as a cut-and-cover tunnel using the proposed analytical model and decomposition analysis approach. The considered cut-and-cover structure can be decomposed in four single beams. Boundary conditions and loading conditions for each beam have to be detailed to ensure continuity and a correct redistribution of actions throughout the structure.

The solution method is based on five steps (Table 5.4). Step 1: the equilibrium of the bottom beam (1) is solved considering  $q$  and  $\Delta T_c$ . Step (2): the equilibrium of beam (2) is solved by imposing the rotation and the shear force coming from beam (1) at one boundary (the shear force for beam (2) represents the axial force for beam (1)). Step 3: the same procedure considered in Step 2 is applied to resolve the equilibrium of beam (3). Step 4: the equilibrium of beam (1) is re-assessed by adding the axial action coming from the shear force distribution in beams (2) and (3). Step 5: the upper beam (4) is solved by

imposing rotations coming from beams (2) and (3) and transversal displacements coming from beam (1) (assuming that beams (2) and (3) settle/heave as rigid bodies). Such boundary conditions lead to a discontinuity in bending moment between beams (2), (3) and (4), but this discrepancy tends to zero, ensuring a suitable calibration of the boundary conditions (rotational and transversal stiffness). For this reason, in the following, a procedure for estimating and calibrating the boundary conditions is proposed.

Table 5.4 Steps for resolving the cut-and-cover structure employing the proposed analytical model

Step number	Beam number	Input parameters	Output parameters
1	Base beam (1)	$q; \Delta T_c$	$y_{1,1}(x); \theta_{1,1}(x); M_{1,1}(x); V_{1,1}(x)$
2	Right vertical beam (2)	$\theta_2(0) = \theta_1(L)$ $N_2 = Q_1(L)$	$y_2(x); \theta_2(x); M_2(x); V_2(x)$
3	Left vertical beam (3)	$\theta_3(0) = \theta_1(0)$ $N_3 = Q_1(0)$	$y_3(x); \theta_3(x); M_3(x); V_3(x)$
4	Base beam (1)	$q; \Delta T_c$ $N_1 = Q_2(0) = -Q_3(L)$	$y_{1,2}(x); \theta_{1,2}(x); M_{1,2}(x); V_{1,2}(x)$
5	Top beam (4)	$\theta_4(0) = \theta_3(H)$ $\theta_4(L) = \theta_2(H)$ $y_4(0) = y_{1,2}(0)$ $y_4(L) = y_{1,2}(L)$	$y_4(x); \theta_4(x); M_4(x); V_4(x)$

It is worth noting that the foregoing analysis approach could be applied to any arbitrary loading scenario and plane geometry. For example, a slightly more complex problem than the one considered here could consist in a cut-and-cover structure with more than one beam subjected to thermal actions. Such a problem may be adequately addressed following a similar procedure than the one described above.

#### 5.5.4 Calibration of boundary conditions

In this section, a procedure for calibrating the rotational and transversal boundary conditions is presented. Such a procedure aims to be as general as possible, so that it may be used to tackle frequent problems in engineering when different variably connected elements are present (e.g., perpendicular and variably inclined connections, wall-anchors, etc). In the following, two components of stiffness are considered: the structural (subscript “SS”) and the soil-structure interaction (subscript “SSI”).

##### 5.5.4.1 Rotational stiffness

The structural stiffness,  $k_{r,SS}$ , is related to the frame rigidity and can be determined by employing the so-called displacement method, as described in Connor & Faraji (Connor & Faraji, 2016).

This method is employed here with reference to the structure shown in Figure 5.7 (a-c). The value of  $k_{r,SS}$  is bounded by an upper bound (fixed condition) and a lower bound (hinged condition). The upper bound relates to a case where the rotation is blocked by the presence of a fixed end. The bending moment  $M^*$  applied at the frame angle induces a rotation of  $M^*(4EI/L)^{-1}$  radians. The stiffness of the equivalent rotational spring is therefore  $4.0 EI/L$  Nm/rad (Figure 5.7 (a)). The lower bound is characterised by the beam hinged at its ends (Figure 5.7 (b)). The equivalent rotational stiffness is thus  $3.0 EI/L$  Nm/rad. It follows that if the rotation is partly restrained, the spring structural stiffness reads (Figure 5.7 (c))

$$k_{r,SS} = \frac{m^* EI}{L} \quad \text{with } m^* = 3.0 \text{ to } 4.0 \quad (5.26)$$

The whole structure is also constrained by the presence of soil all around, which is partly restraining the rotations. The rotational stiffness  $k_{r,SSI}$  is the one exerted by the soil-structure interaction in the portions not accounting for the beam of interest. This contribution can be estimated by applying a unit moment,  $M^*$ , to a beam that is fixed at one end and supported by the spring foundation along its length (Figure 5.7 (d-e)). A first estimation of  $k_{r,SSI}$ ,  $k_{r,1}$ , can be obtained by dividing the unit moment  $M^*$  by the rotation  $\theta_1$  and subtracting the structural flexural stiffness, equal to  $EI/L$  for this case (Figure 5.7 (d)). The final evaluation of  $k_{r,SSI}$  is done by applying the same method to the structure with a replacement of the fixed end with a rotational spring of stiffness  $k_{r,1} + k_{r,SS}$  (Figure 5.7 (e)).

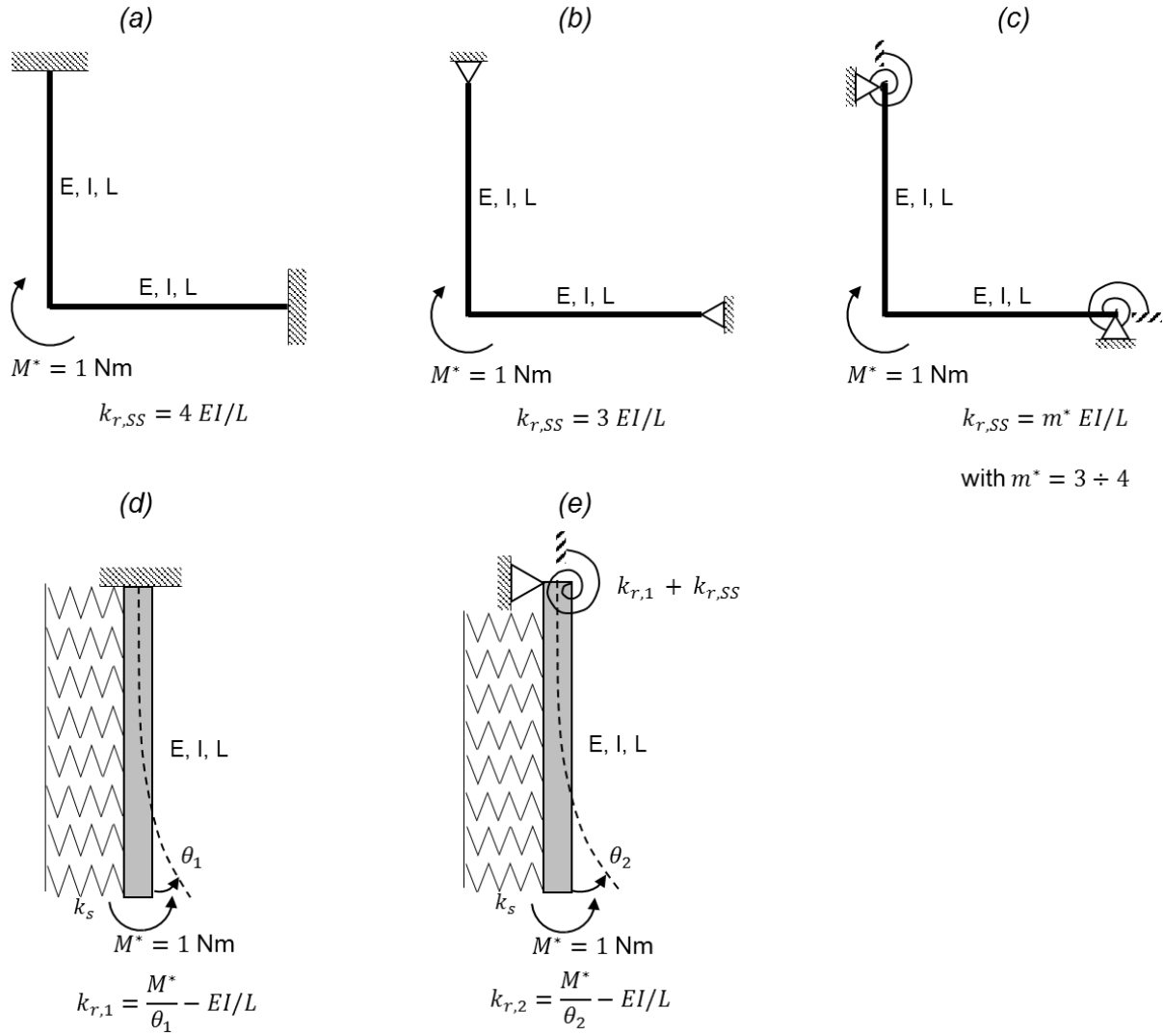


Figure 5.7 Determination of structural rotational stiffness: (a) fixed case, (b) hinged case, (c) partly restrained case. Determination of the soil-structure interaction rotational stiffness: (d) first estimation and (e) final estimation

The equivalent rotational spring,  $k_r$ , can be estimated by summing the two components previously highlighted:

$$k_r = k_{r,SS} + k_{r,SSI} \quad (5.27)$$

Figure 5.8 shows the relationship between the dimensionless rotational stiffness and the beam geometry. Each line in the plot contains the sum of the evaluations described in Figure 5.7, providing upper and lower bounds for different soil conditions. In all cases, the soil subgrade reaction modulus,  $k_s$ , is multiplied by the beam height,  $h$ , to give results that are independent to the beam height. The results depicted for  $k_s h = 0 \text{ N/m}^2$  include the stiffness given by the structure only. The difference between these results and those obtained for  $k_s h \neq 0 \text{ N/m}^2$  denotes the contribution of the soil-structure interaction.

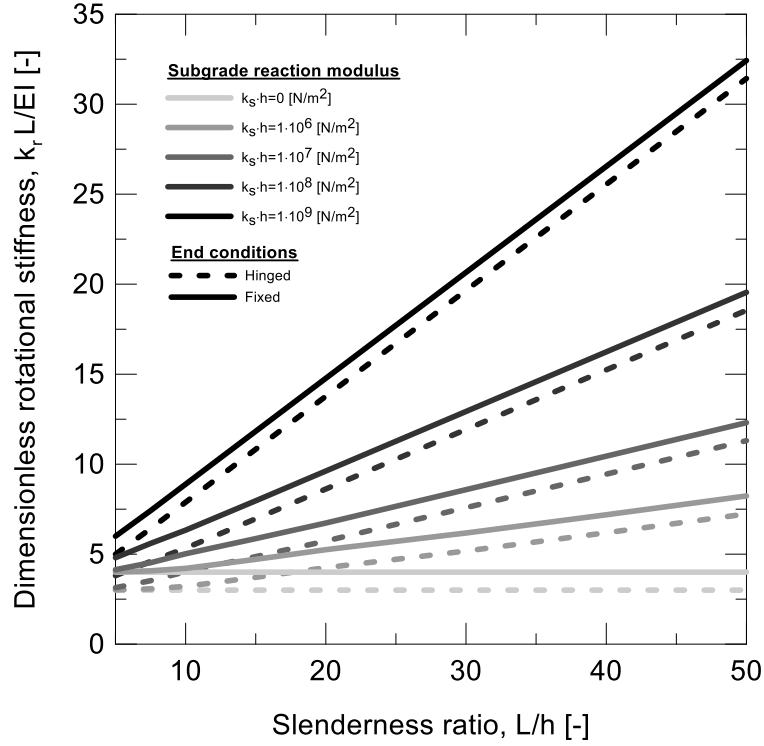


Figure 5.8 Relationship between the dimensionless rotational boundary stiffness and the beam geometry that can be used to calibrate the rotational boundary condition

#### 5.5.4.2 Transversal stiffness

The evaluation of the transversal stiffness has to account for four components (Figure 5.9 (a)): the bottom connection,  $k_{v,c1}$ , the axial stiffness of the structural element,  $k_{v,a}$ , the top connection,  $k_{v,c2}$ , and the soil-structure interaction,  $k_{v,SSI}$ .

Such conditions can be represented by four springs in series. This approach yields to the following formulation of the equivalent transversal stiffness,  $k_v$ :

$$k_v = \frac{1}{\frac{1}{k_{v,a}} + \frac{1}{k_{v,c1}} + \frac{1}{k_{v,c2}} + \frac{1}{k_{v,SSI}}} \quad (5.28)$$

As Winkler's solution does not consider any friction between the soil and the structure, this aspect is neglected.  $k_{v,a}$  relates to the axial stiffness of a beam as follows:

$$k_{v,a} = \frac{EA}{L} \quad (5.29)$$

In many cases,  $k_{v,a}$  is considerably higher with respect to the other components, hence it can often be neglected in equation (5.28): depending on the geometry details, such element may behave as a rigid body that is not deforming axially, but it only transfers the loads to the surrounding structures.  $k_{v,c1}$  and



$k_{v,c2}$  can be determined by considering the following upper and lower bound cases (Figure 5.9 (b-d)). The upper bound is represented by the stiffer case (fixed ends, Figure 5.9 (b)), while the lower bound involves free rotation at the ends (hinged ends, Figure 5.9 (c)). Following the same methodology shown for the rotational spring, it follows that the connection stiffness,  $k_{v,ci}$ , can be evaluated as (Figure 5.9 (d)):

$$k_{v,ci} = v^* \frac{EI}{L^3} \quad \text{with } i = 1,2 \text{ and } v^* = 1.5 \div 7.5 \quad (5.30)$$

For the determination of the soil-structure interaction vertical stiffness, different methodologies should be employed for the analysis of (i) the horizontal beams and of (ii) the vertical walls. For horizontal beams,  $k_{v,SSI}$  is estimated by considering the static scheme shown in Figure 5.9 (e-f). The first step is to consider a beam fixed at one end and subjected to a unit transversal load,  $P^*$ .  $k_{v,1}$  is evaluated by dividing  $P^*$  by the correspondent vertical displacement,  $y_1$ , and subtracting the structural transversal stiffness,  $3.0 EI/L^3$ . The second and final step is to consider the same beam solved by replacing the fixed boundary with  $k_{v,1}$  and  $k_r$ , (Figure 5.9 (f)). The vertical stiffness for the second step,  $k_{v,2}$  can be similarly evaluated. It follows that

$$k_{v,SSI} = k_{v,2} \quad (5.31)$$

For vertical beams, the determination of their transversal boundary stiffness is based on their mechanical response. In the considered problem, the two vertical beams behave symmetrically. Their transversal boundary stiffness can therefore be estimated as the axial stiffness of a half of a horizontal beam.

$$k_{v,vertical} = \frac{EA}{L/2} \quad (5.32)$$

Figure 5.10 shows the estimation of  $k_v$  through the relationship between the transversal stiffness and the geometry details. This chart includes the steps described in Figure 5.9 (b-e). Only the case  $k_{v,c1} = k_{v,c2}$  is included in the charts. The soil subgrade reaction modulus,  $k_s$ , is multiplied by the beam height,  $h$ , to give results that are independent to the beam height.

The results depicted for  $k_s h = 0 \text{ N/m}^2$  include the stiffness given by the structure only. The difference between these results and those obtained for  $k_s h \neq 0 \text{ N/m}^2$  denotes the contribution of the soil-structure interaction.

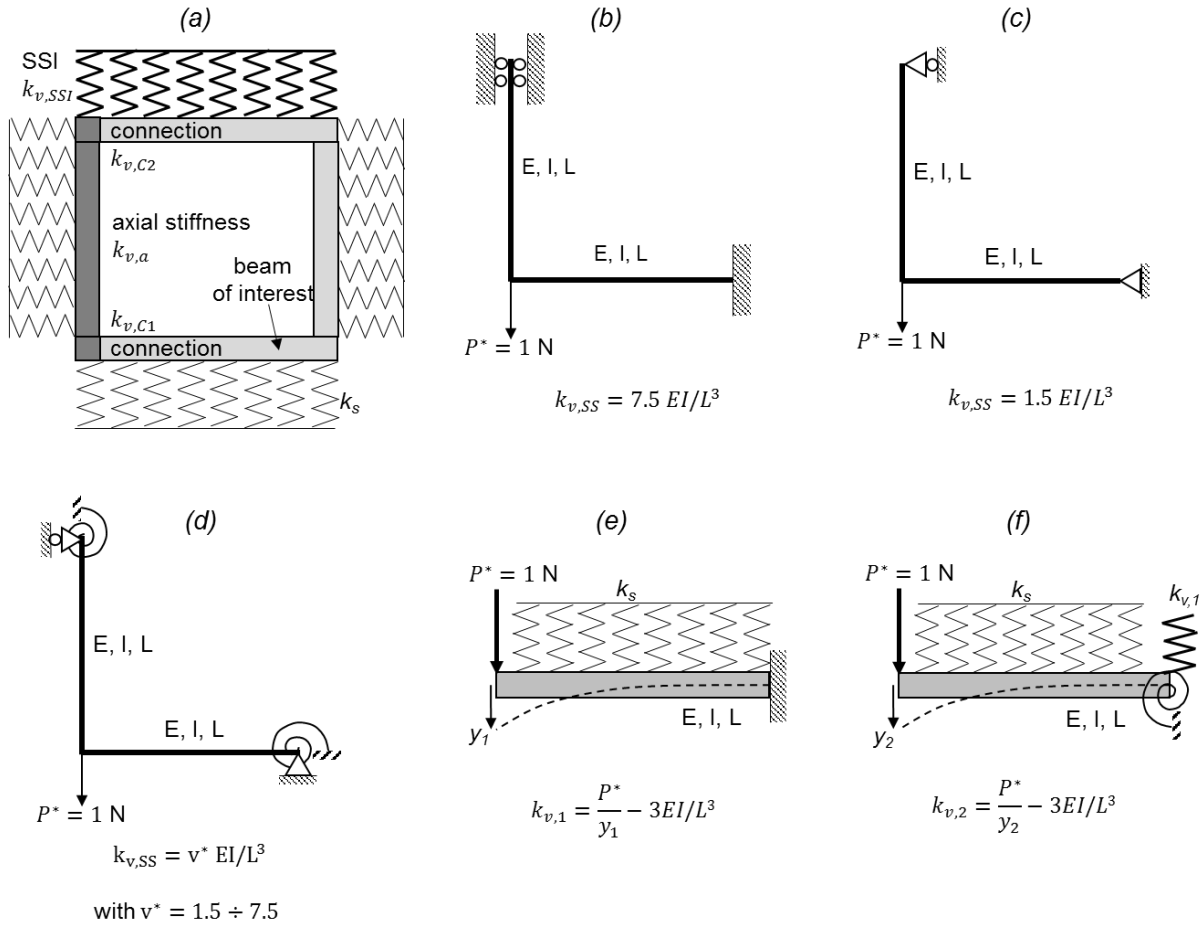


Figure 5.9 (a) Components to be considered for the evaluation of the transversal stiffness boundary condition. Determination of the structural transversal stiffness at the connections: (b) fixed case, (c) hinged case, (d) partly restrained case. Determination of the soil-structure interaction transversal stiffness: (e) first estimation and (f) final estimation

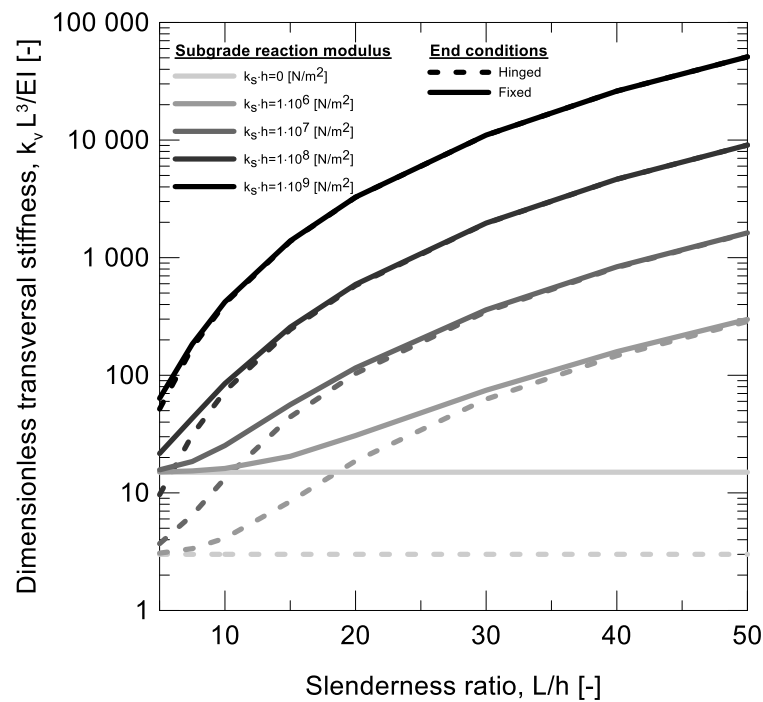


Figure 5.10 Relationship between the dimensionless transversal boundary stiffness and the beam geometry that can be used to calibrate the transversal boundary condition

### 5.5.5 Comparison between analytical and numerical modelling results

In the following, the response of the modelled cut-and-cover structure is addressed with reference to the considered action effects (depicted for each portion of the structure), by distinguishing the influence of thermal and mechanical actions.

Deflections are shown in Figure 5.11. A close correspondence between the analytical and numerical modelling results is observed when addressing the influence of the thermal load. The predicted structural response is in fact very similar in all cases, highlighting a slight underestimation of the deflections only when considering the spring foundation models (numerical and analytical). Due to the end stiffness definition, the deflections of the lower beam are minimal (lower than 0.1 mm). Due to the downward bending of the lower beam, the two walls displace towards the inner part of the structure, while the upper beam moves upward. The whole structure slightly moves upward due to the soil reaction against the lower beam. A more significant difference between the analytical and numerical modelling results is observed when addressing the influence of the mechanical load. The spring foundation models considerably underestimate the horizontal beam displacements. The shape of the deflection is similar, thus confirming that Winkler's solution can be used to estimate the differential settlements of footings, but is unsuitable to thoroughly capture actual settlements, especially when dealing with particularly rigid structures.

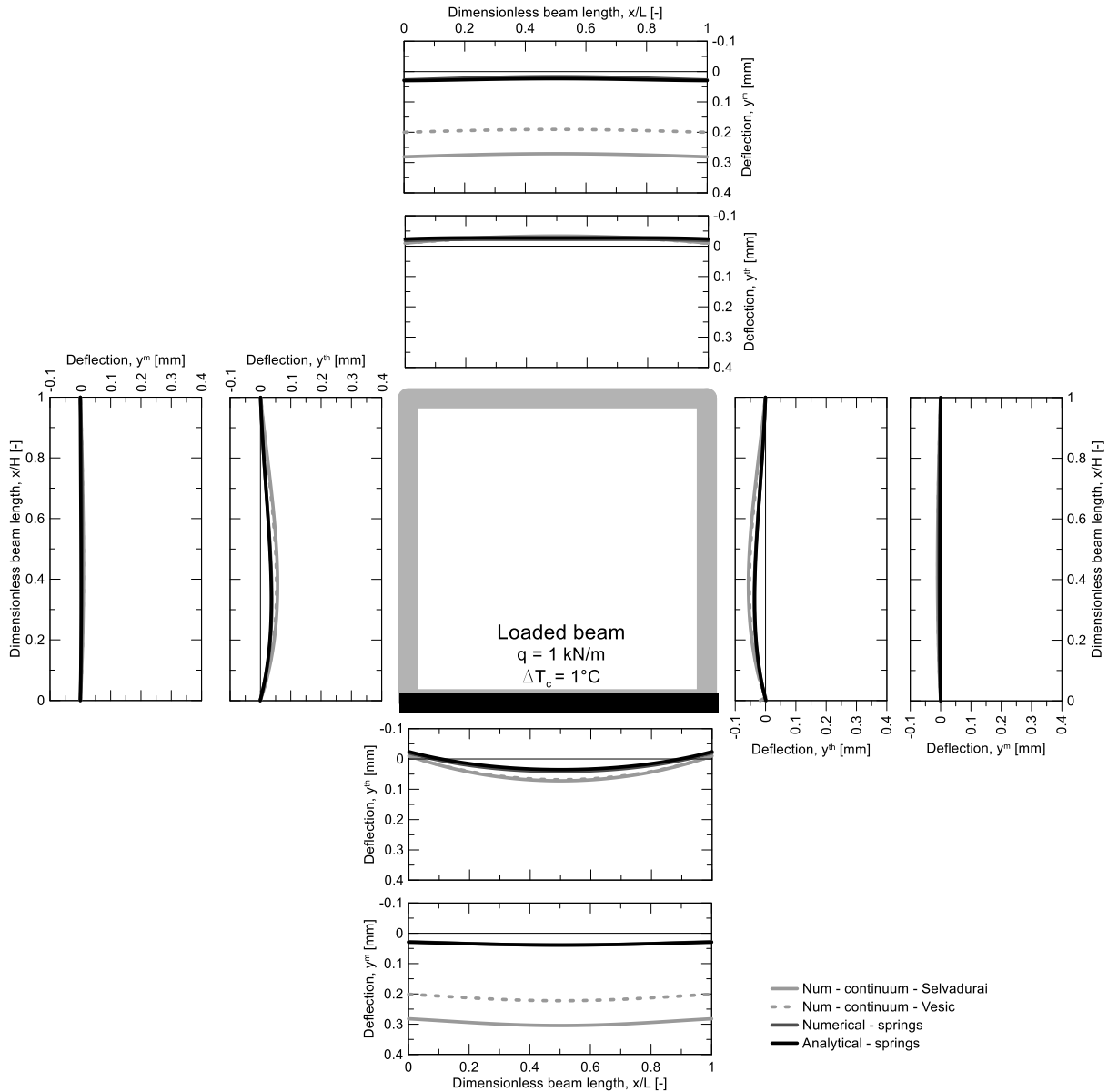


Figure 5.11 Response of a cut-and-cover structure with  $L/H=1$  subjected to thermal and mechanical loading to the bottom beam only: deflection

Rotations are shown in Figure 5.12. A close correspondence between the analytical and numerical modelling results is observed when addressing the influence of both the thermal and mechanical load. The analytical and numerical modelling results with spring foundation slightly underestimate rotations. The thermal load affects rotations in the whole structure, thus inducing much higher rotations at the edges of the cut-and-cover with respect to the distributed mechanical load. The distributed mechanical load induces a flatter displacement profile, hence involving rotations that are very small compared to those caused by thermal loading.

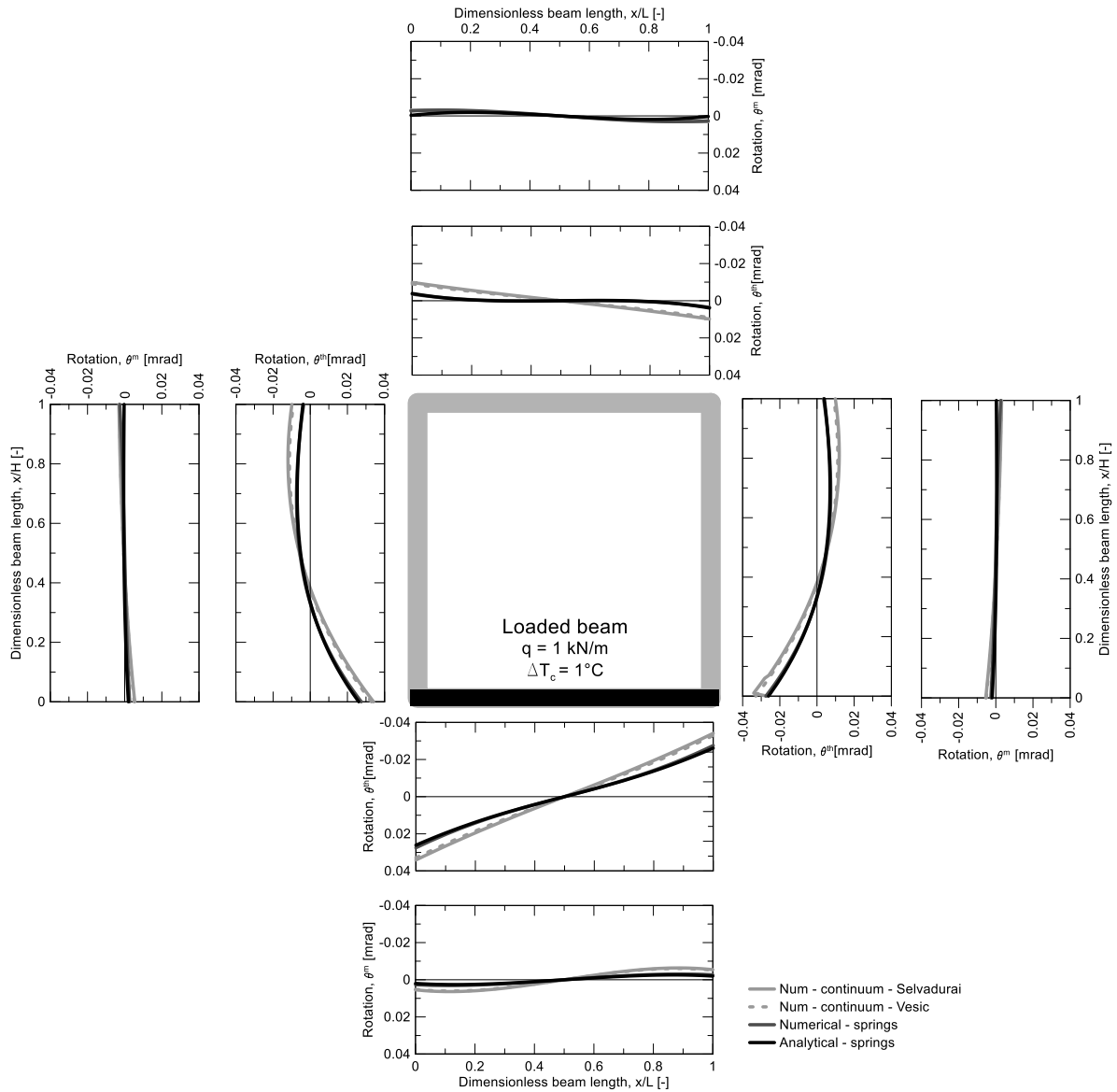


Figure 5.12 Response of a cut-and-cover structure with  $L/H=1$  subjected to thermal and mechanical loading to the bottom beam only: rotation

Bending moments are shown in Figure 5.13. A close correspondence between the analytical and numerical modelling results is observed when addressing the influence of both the thermal and mechanical loads. The thermal load induces a rotation that is notably restrained at the boundaries, while a bending moment distribution that is flatter but high in magnitude, with values higher compared to the distributed load. Models with spring foundation slightly overestimate internal actions in the bottom beam. The mechanical load induces a bending moment that is nearly-zero, hence the thermal load is determining significant effects in the structure.

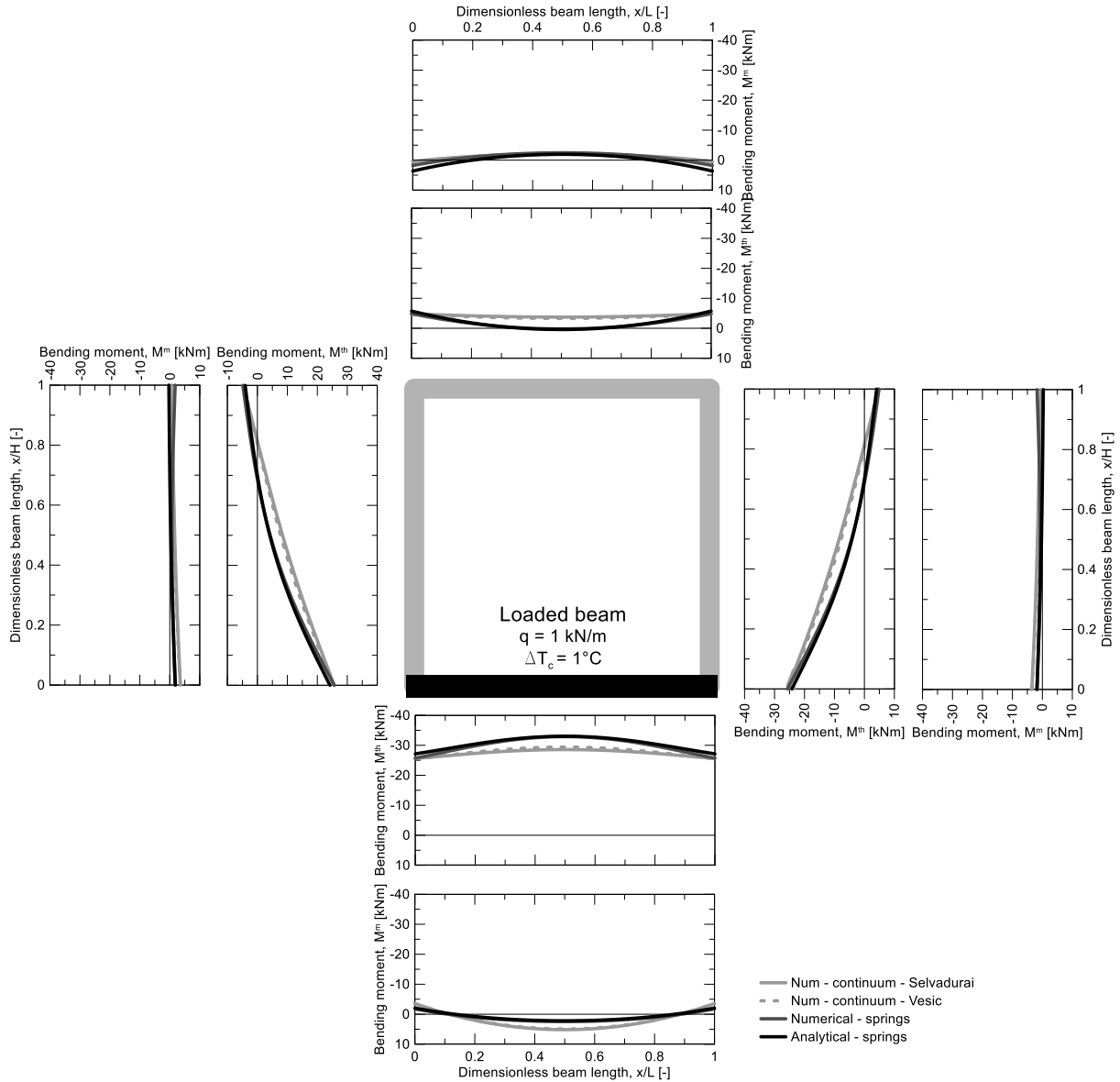


Figure 5.13 Response of a cut-and-cover structure with  $L/H=1$  subjected to thermal and mechanical loading to the bottom beam only: bending moment

Shear forces are detailed in Figure 5.14. A satisfactory correspondence among the analytical and numerical modelling results is recorded for thermal and mechanical loads. The thermal load causes shear actions in the entire structure, consequently to the bending moment distribution. The distributed load induces shear forces only in the horizontal beams due to the nature of the applied load (transversal to horizontal beams). The sign of shear action induced by  $\Delta T$  is opposite to that of  $q$ . It follows that they delete each other. However, if the thermal load takes the opposite sign, the total shear force would sum the two.

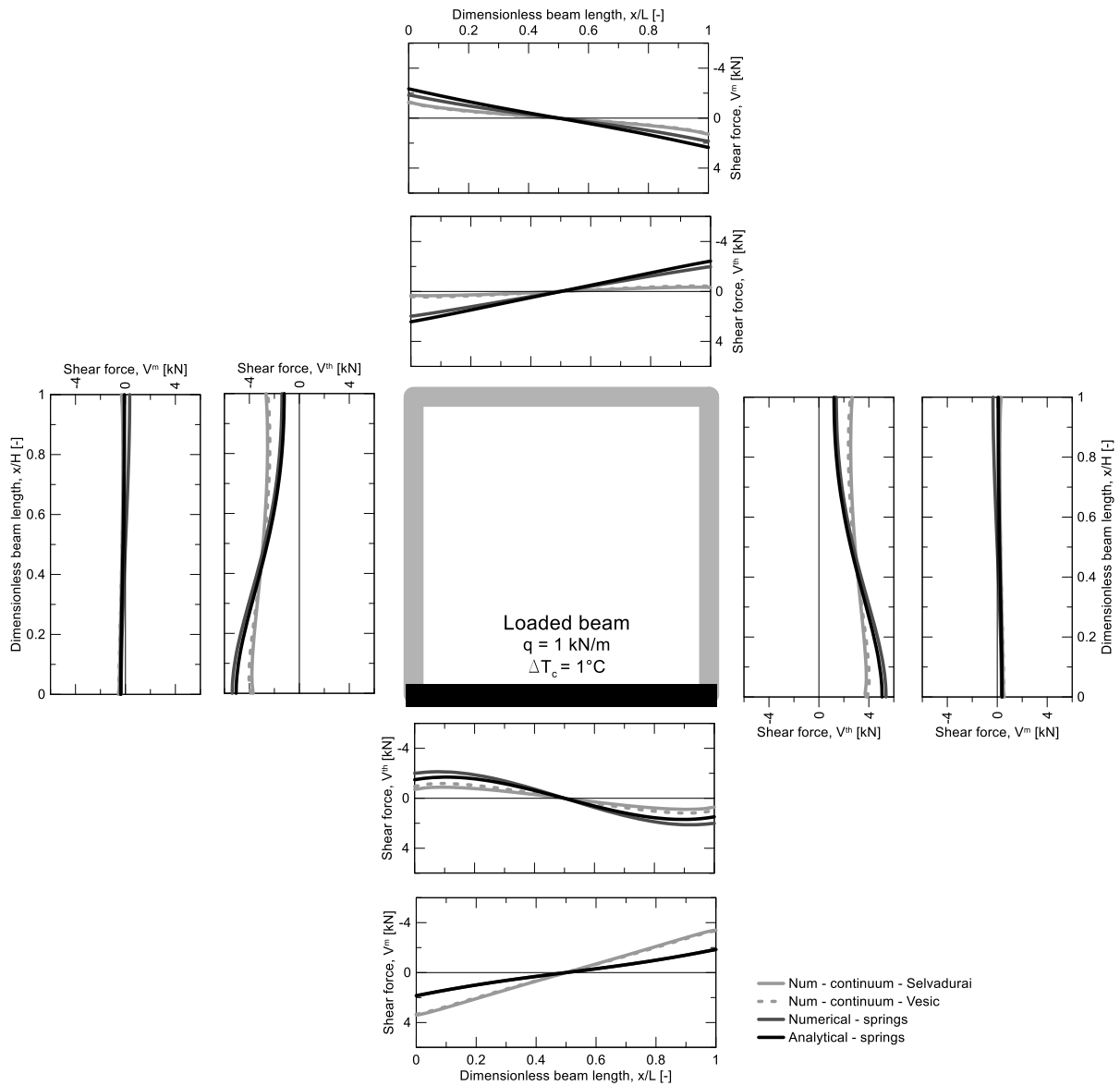


Figure 5.14 Response of a cut-and-cover structure with  $L/H=1$  subjected to thermal and mechanical loading to the bottom beam only: shear force

## 5.6 Concluding remarks

This study aims at taking a step forward towards a detailed assessment of the thermo-mechanical behaviour of plane geostructures subjected to thermal and mechanical actions by proposing an analytical model for capturing the effects of the considered perturbations. The proposed model extends Winkler's solution to non-isothermal conditions for quantifying the effects of actions that include, without being limited to, temperature variations, axial loads, transversal loads and bending moments applied to plane geostructures resting on an elastic soil mass. The model formulation resorts to a theoretical analysis of the influence of thermal and mechanical actions applied to geostructures, as well as to a new

definition of degree of freedom for capturing the influence of axial and flexural effects caused by thermal actions.

By resorting to novel charts and mathematical procedures that can be employed to calibrate appropriate boundary conditions for the analysis of simple and complex plane geostructures, the work highlights aspects of paramount importance for the modelling of plane geometries. A comparison between analytical and numerical modelling results highlight that the proposed extension of Winkler's solution can capture with accuracy problems of varying complexity as long as similar hypotheses are employed in the analyses. This work provides a useful tool for both engineering and scientific purposes, enabling a novel approach to tackle this subject.





# Chapter 6 Analytical modelling of energy geostructures: applications and advanced analytical models

## 6.1 Introduction

This chapter is a continuation of Chapter 5 and relates to analytical modelling of thermomechanical behavior focusing on energy geostructures. Many analytical models are available in the literature for tackling problems related to soil-structure interaction, but little evidence is available on tackling non-isothermal soil-structure interaction. In the following, further applications of the proposed analytical model as well as the definition of alternative models that are extended to non-isothermal conditions are proposed, reporting examples for horizontal and vertical geostructures.

This chapter is structured in three parts. Firstly, the Winkler model is applied to the case of an energy pile, to a three-span continuous beam and to a partly embedded energy wall. Secondly, the two-parameters soil model (Pasternak, 1954; Selvadurai, 1979) is then extended to non-isothermal conditions and applied to a single beam. Thirdly, the Winkler solution including a linearly varying reaction modulus in non-isothermal condition is proposed and applied to a vertical retaining structure. Each of these three parts is meant as a stand-alone sub-chapter. For each of them, introductive concepts, model description, validation, results and discussion as well as concluding remarks are reported.

## 6.2 Applications of the Winkler model in non-isothermal conditions to energy geostructures

### 6.2.1 Laterally loaded energy pile

#### 6.2.1.1 General

This section aims at analyzing the thermomechanical behavior of energy piles, studying the pile transversal behavior (Bowles, 1974; Wood, 2004). Conventional analysis on energy piles is usually devoted to studying the pile axial behavior (Amatya et al., 2012; Batini et al., 2015; Knellwolf et al., 2011; Laloui et al., 2006; Mimouni & Laloui, 2014; Ravera et al., 2019; Rotta Loria, 2018; Rotta Loria & Laloui, 2017a; Rotta Loria et al., 2020; Rotta Loria & Laloui, 2019; Sutman et al., 2020; Sutman et al., 2015, 2017, 2019; Wang et al., 2016). Such findings are here extended to the case of laterally loaded piles in non-isothermal conditions. It is well documented in the literature that the thermal activation of

piles involves the application of a constant distribution of temperature variation throughout the pile cross section usually due to the radial presence of heat exchangers and to the axisymmetric nature of the heat exchanges with the surrounding materials (i.e., uniform materials radially to the pile). Uniform temperature variation throughout the whole pile length give rise to modifications in the axial stress/strain state of the pile. For this reason, energy piles and energy pile groups are usually analyzed in their axial behavior only.

The analytical solution proposed here, is the same presented in Chapter 5 (i.e., extension of the Winkler solution in non-isothermal conditions) (Zannin et al., 2020) where the pile is subjected to any arbitrary mechanical load distribution at his head (i.e., axial force, transversal force and/or bending moment) and it is axially loaded through a constant distribution of temperature variation throughout the whole pile length,  $\Delta T_a$ . At deformed conditions, any additional axial load (e.g., thermal, mechanical) impacts on the transversal behavior if axial deformation is partly blocked ((Hétenyi, 1946)). To give an example, an analogy can be done with the classical Euler buckling instability problem applied to a rod.

#### 6.2.1.2 The problem

The energy pile (EP) is represented by a continuous beam of a given elastic stiffness  $EI$ , in contact with the soil represented by independent, unidirectional springs of stiffness  $k_s$ . The pile is partly vertically constrained at its head and at its base by means of two springs of stiffness  $k_{head}$  and  $k_{base}$ , respectively (Knellwolf et al., 2011; Laloui et al., 2006; Mimouni & Laloui, 2014). The loading conditions are represented by a concentrated transversal force,  $P$ , a concentrated bending moment,  $W$ , applied at the pile head and a constant distribution of temperature variation,  $\Delta T_a$ , throughout the whole pipe length. The reference system has origin at the pile head, with the x-coordinate directed towards the pile toe and the y-coordinate directed towards the left (Figure 6.1).

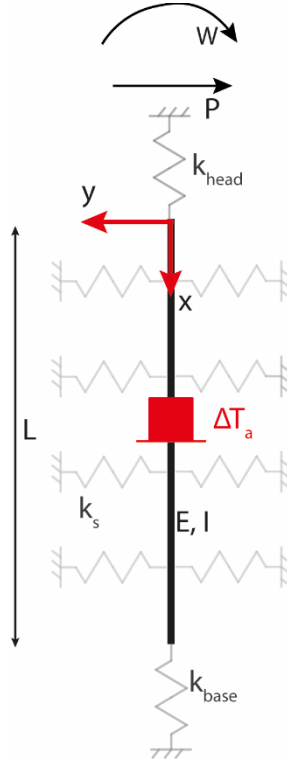


Figure 6.1 Scheme of the modelled problem: the transversally loaded EP

The fourth-order differential equation to be solved reads:

$$EI \left( \frac{d^4 y}{dx^4} + \frac{d\chi^{th^2}(x)}{dx^2} \right) - N \frac{d^2 y(x)}{dx^2} + k_s y(x) = 0 \quad (6.1)$$

Which has a solution:

$$y(x) = (C_1 e^{\alpha x} + C_2 e^{-\alpha x}) \cos \beta x + (C_3 e^{\alpha x} + C_4 e^{-\alpha x}) \sin \beta x \quad (6.2)$$

Where

$$\lambda = \sqrt[4]{\frac{k_s}{4EI}} \quad (6.3)$$

$$\alpha = \sqrt{\lambda^2 + \frac{N}{4EI}} \quad (6.4)$$

$$\beta = \sqrt{\lambda^2 - \frac{N}{4EI}} \quad (6.5)$$

The boundary conditions are set as:

$$\begin{cases} M(0) = W \\ V(0) = P \\ M(L) = 0 \\ V(L) = 0 \end{cases} \quad (6.6)$$

The solution of this system of four equations allows to determine the four integration constants  $C_1, C_2, C_3, C_4$  and consequently the problem is solved.

### 6.2.1.3 Validation against analytical solution available in the literature

A validation against results available in the literature is reported here. Many examples of analytical solutions applied to laterally loaded piles are reported in the literature. The one chosen here, presents the Winkler solution applied to a pile loaded at his head with a concentrated force,  $P$ , and the solution is reported in Wood, 2004. Under these loading conditions, the pile behaves as an “infinitely long pile” if the characteristic length is

$$\lambda L \geq 6 \quad (6.7)$$

While for smaller values of  $\lambda L$ , it behaves as a “short pile” (Wood, 2004). The solution proposed by Wood is compared with the analytical solution proposed here. The chosen geometry (Figure 6.1) and materials present the features presented in Table 6.1

Table 6.1 Input parameters for the comparison with the analytical solution available in Wood, 2004

	Symbol	Value
Subgrade reaction	$k_s$	$10^6 \text{ N/m}^3$
Pile Young's Modulus	$E$	$25 \text{ GPa}$
Pile width	$h$	$1 \text{ m}$
Pile breadth	$b$	$1 \text{ m}$
Pile length	$L$	$40 \text{ m}$
Transversal force	$P$	$10 \text{ kN}$

Figure 6.2 shows the comparison among the two solutions for deflection. A very satisfactory agreement among the two solutions is found.

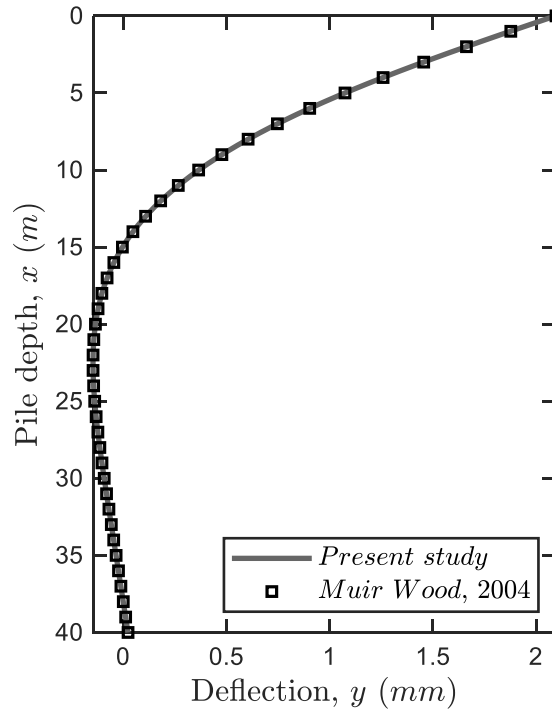


Figure 6.2 Comparison between the analytical results presented in this study with the ones proposed by Wood, 2004

#### 6.2.1.4 Results and discussions

Different cases are analyzed in this section and they include the application of thermal and mechanical loading conditions. Firstly, the pile is subjected to unitary thermal and mechanical actions. Then, it is subjected to a combination of thermomechanical actions representative of a worst-case scenario useful to highlight the most severe cases when thermal actions play major roles in thermomechanical behaviour. Additionally, different static schemes (i.e., mechanical boundary conditions) are used. The pile is, generally, partly restrained at its head in terms of axial and transversal displacements and rotation, usually because of the presence of structural elements (e.g., rafts, columns, etc...) composing the superstructure. At its base, the pile is constrained by the presence of soil. The boundary conditions applied at the base are usually set as free displacements and rotations as the only constraint is represented by the soil (Bowles, 1974; Wood, 2004). The axial base stiffness depends on the nature of the soil. Piles in stiff soil strata may be represented with a fixed end condition, while piles in more compressible materials may be represented by a looser end condition. For this reason, this model employs two different axial springs at the head and at the base that can be set to model the presence of head and base constraints. The thermal component of the generalized axial force throughout the pile (equation (5.21)), is hence computed as:

$$N^{th} = - \frac{\alpha \Delta T_a L}{\frac{L}{EA} + \frac{1}{k_{head}} + \frac{1}{k_{base}}} \quad (6.8)$$

where  $A$  represent the pile cross section and  $k_{head}$  and  $k_{base}$  are strictly positive and they are expressed in  $N/m$ . The mechanical component of the generalized axial force throughout the pile (equation (5.21)) is set as:

$$N^m = 0 \quad (6.9)$$

as no external axial loads are included here. They could, potentially, be included in the computation by using a similar approach as the one proposed with thermal actions.

It follows that, if  $k_{head} \rightarrow 0$  and/or  $k_{base} \rightarrow 0$ , the pile is free to axially deform when subjected to thermal actions (i.e.,  $DOF_a \rightarrow 1$ ) and thermal actions will not affect the flexural behavior ( $N^{th} \rightarrow 0$ ). Conversely, if  $k_{head} \rightarrow +\infty$  and/or  $k_{base} \rightarrow +\infty$ , the pile is completely axially constrained (i.e.,  $DOF_a \rightarrow 0$ , blocked axial deformation) and the thermal load has an impact on the flexural behavior as thermally-induced stresses develop. At intermediate conditions, the pile axial displacement may be partly blocked. In such conditions (i.e.,  $DOF_a < 1$ ), the blocked portion affects the pile flexural behavior.

Two different pile configurations are studied here, aiming at representing realistic conditions: (i) at fixed conditions, when the pile present stiff head and base constraints ( $k_{head} = k_{base} \rightarrow +\infty$ ); (ii) at intermediate conditions, when the base restraint is much higher than the head one ( $k_{head} \ll k_{base}$ ).

For the sake of completeness, when applying this model and including compressive axial loads, one should verify that the magnitude of the compressive load,  $N$ , is lower than the Eulerian ultimate load, that would generate buckling instability. In all the analyzed cases here, this condition is verified.

In the following, two examples are given. Firstly, the application of unitary thermal and mechanical loads is presented. Then, the description of a worst-case scenario is reported. Conclusions are eventually highlighted.

#### 6.2.1.4.1 Case I - application of unitary loads

The first analysis is devoted to the analysis of the same geometry presented in section 6.2.1.3, but the pile is subjected to unitary thermal and mechanical loads. This choice was made to analyze the geosstructural response when thermal and mechanical loads have the same magnitude. The findings arising from such analysis can then be extended to more realistic conditions by using the superposition principle.

The input data employed in this study are presented in Table 6.2. Such choice of geometry and material allows to encompass the cases presenting non-dimensional parameter  $\lambda L < 6$  and  $\lambda L > 6$ , following the classification proposed by Hétenyi, 1946 and Wood, 2004.

Table 6.2 Input parameters for the evaluation of the pile behavior under unitary loads

	Symbol	Value
Subgrade reaction	$k_s$	$10^6 \div 10^8 \text{ N/m}^3$
Pile Young's Modulus	$E$	$25 \text{ GPa}$
Pile width	$h$	$1 \text{ m}$
Pile breadth	$b$	$1 \text{ m}$
Pile length	$L$	$40 \text{ m}$
Concentrated transversal force	$P$	$1 \text{ kN}$
Concentrated bending moment	$W$	$1 \text{ kNm}$
Constant distribution of temperature variation	$\Delta T_a$	$1^\circ\text{C}$

The results of such analysis are presented in the following figures, for the fixed (Figure 6.3, Figure 6.4) and intermediate (Figure 6.5, Figure 6.6) static schemes. In the following figures, continuous lines report the results for the pile subjected to mechanical loads only (“m”), while the dotted lines report the results for the pile subjected to thermomechanical loads (“m+th”). In some of the following figures, the dotted lines are hardly visible as the difference between the two analyzed cases is very limited.

The deflection presents a maximum value at the pile head, following the sign of the applied external mechanical loads. The magnitude of the deflection is lower for stiffer soils. The effect induced by  $\Delta T_a$  is an increase of the positive maximum deflection, following the sign of the applied thermal load. Heating induces a uniform compression throughout the pile length resulting in an increase (in absolute value) of the pile deflection with respect to the non-isothermal case.

Rotation is here free at the head; hence a negative rotation is computed, following the sign of the applied loads. A positive  $\Delta T_a$  causes an absolute increment of rotation throughout the whole pile length.

Bending moment present its maximum values (i.e., positive and negative) in the vicinity of the head, where the mechanical loads are applied. At the head, bending moment assumes the value of the external load, while it is negative with increasing depth. The location of the maximum negative moment depends on the soil stiffness: the stiffer the soil, the closer the maximum negative moment to the pile head. The maximum bending moment would be located at the head for an infinitely stiff soil. A positive  $\Delta T_a$  enhances the maximum and minimum bending moment.

Shear force is maximum at the pile head consequently to the applied external mechanical load. A positive  $\Delta T_a$  tends to increase shear effects.



For deflection, rotation, bending moment and shear force, the opposite applies for a negative  $\Delta T_a$ , given the same distribution of mechanical loads (Figure 6.1). The same concept applies to all the static schemes analyzed here.

The percent differences ( $\delta_i$ ) between the thermomechanical ( $m+th$ ) and the mechanical only ( $m$ ) cases shows relatively low values, with peaks that go up to  $0.3\% \div 0.6\%$  for the fixed static scheme. Concerning the intermediate static scheme, the difference is one order of magnitude lower with respect to the fixed case.

Such results show that, when the magnitude of thermal and mechanical loads is comparable, no major issues on the flexural behavior of energy piles arise, if the pile is correctly designed to sustain the mechanical actions.

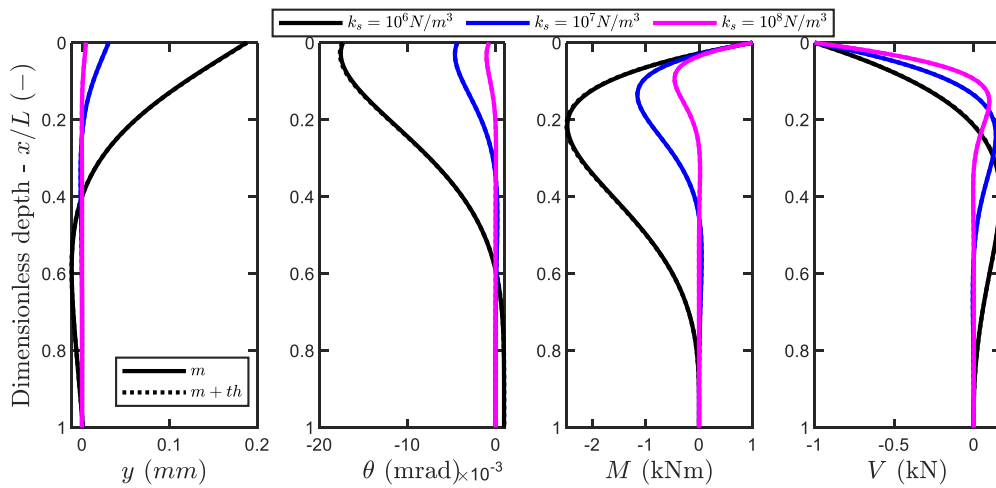


Figure 6.3 Thermomechanical behaviour of an energy pile subjected to unitary thermal and mechanical loads, the selected static scheme is fixed (i.e.,  $k_{head} = k_{base}$ )

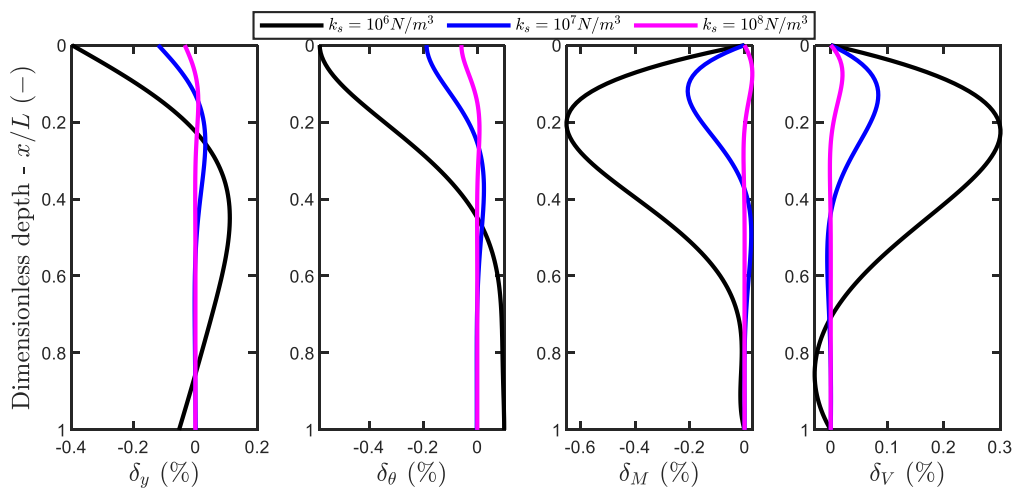


Figure 6.4 Differences between the mechanical only case and the thermomechanical one presented in Figure 6.3

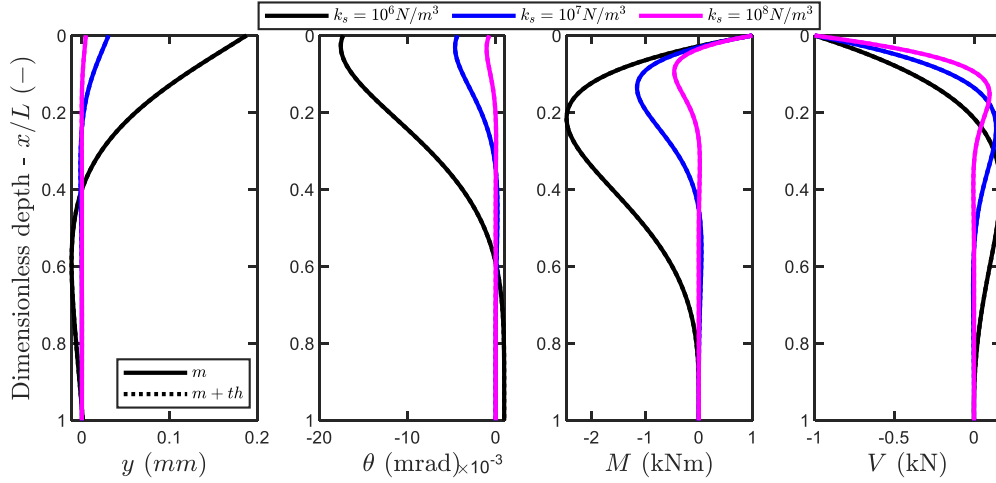


Figure 6.5 Thermomechanical behaviour of an energy pile subjected to unitary thermal and mechanical loads, the selected static scheme is intermediate (i.e.,  $k_{head} \ll k_{base}$ )

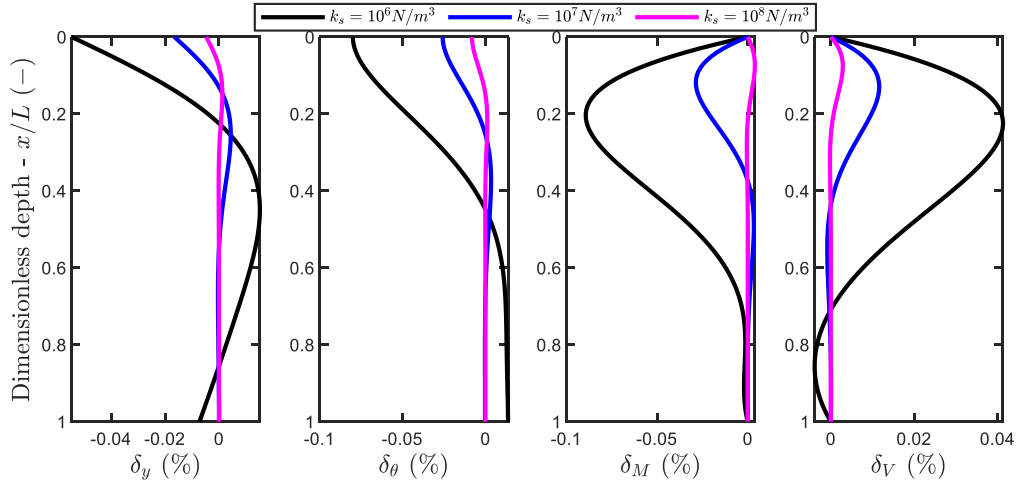


Figure 6.6 Differences between the mechanical only case and the thermomechanical one presented in Figure 6.5

#### 6.2.1.4.2 Case II – worst-case scenario

This section relates to the definition of a worst-case scenario and the comparison between the thermomechanical and mechanical only loading configurations. The goal of this section is to identify possible realistic conditions and analyze the impact of the thermally induced mechanical effects from a design viewpoint.

The analysis proposed at Section 6.2.1.4.1 shows the impact of thermal loads for cases where the magnitude of thermal and mechanical loads is similar. Realistic conditions may differ from it. For example, piles may be subjected to considerably high mechanical actions (i.e., in the range of several thousand times higher than the ones proposed at Sec. 6.2.1.4.1) while thermal actions may be of few dozen times as the ones reported at Sec. 6.2.1.4.1. In such case, the impact of thermal actions would be even more limited than the one reported at Sec. 6.2.1.4.1. So, a question rises up: is there any realistic case where

the impact of thermal loads may represent an interesting condition from a design perspective? This section aims at investigating this point.

It is well documented in the literature (Rotta Loria, 2018; Rotta Loria et al., 2020) that thermal effects in energy piles are stronger for long piles, as there is a linear dependency between the thermal load and the pile length. For such reason, a worst-case scenario when dealing with thermal actions could be defined as a long energy pile loaded with low magnitude mechanical actions and a relatively high constant distribution of temperature variation. In other words, it relates to an over-designed pile which is thermally activated. Two analyses are, again, carried out: (i) firstly, the pile is axially fixed ( $k_{head} = k_{base} \rightarrow +\infty$ ); (ii) secondly, the pile is at intermediate conditions ( $k_{head} \ll k_{base}$ ).

The input data employed in this study are presented in Table 6.3.

Table 6.3 Input parameters for the evaluation of the pile behavior subjected to a worst-case scenario loading condition

	Symbol	Value
Subgrade reaction	$k_s$	$10^6 \div 10^8 \text{ N/m}^3$
Pile Young's Modulus	$E$	$25 \text{ GPa}$
Pile width	$h$	$1 \text{ m}$
Pile breadth	$b$	$1 \text{ m}$
Pile length	$L$	$40 \text{ m}$
Concentrated transversal force	$P$	$10 \text{ kN}$
Concentrated bending moment	$W$	$10 \text{ kNm}$
Constant distribution of temperature variation	$\Delta T_a$	$35^\circ\text{C}$

Figure 6.7 and Figure 6.9 show the results for the thermomechanical behavior. The same macroscopic behavior for either deflection, rotation and internal actions as for the previous case (see Figure 6.3 and Figure 6.5) is identified. The magnitude of the percent difference between the thermomechanical and the mechanical only cases reaches higher values with respect to those reported at Figure 6.4 and Figure 6.6. For the fixed case, absolute value differences (Figure 6.8) go up to around 20% for deflection and rotation, 30% for bending moment and 12% for shear force are recorded. At the intermediate case, differences (Figure 6.10) of around one order of magnitude less than the fixed conditions are recorded, consistently with what reported at Sec. 6.2.1.4.1.

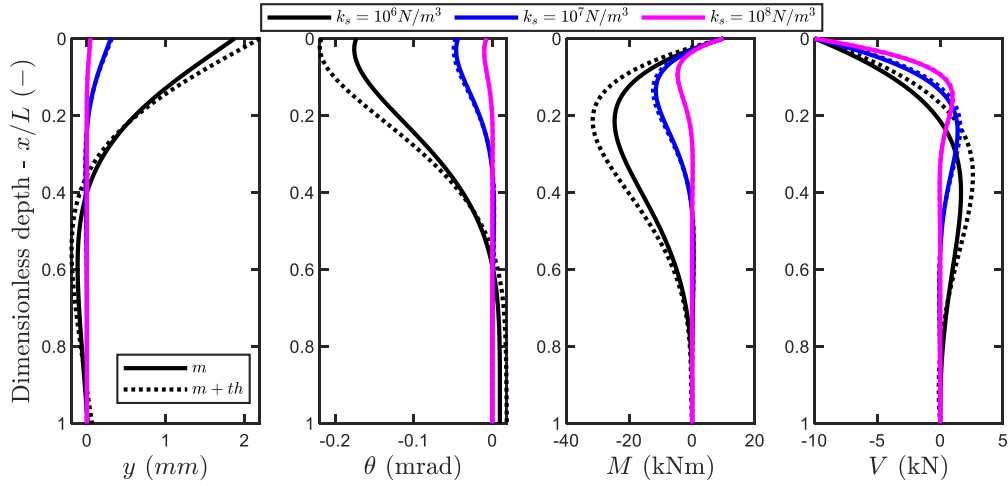


Figure 6.7 Thermomechanical behaviour of an energy pile subjected to thermal and mechanical loads, the selected static scheme is fixed (i.e.,  $k_{head} = k_{base}$ )

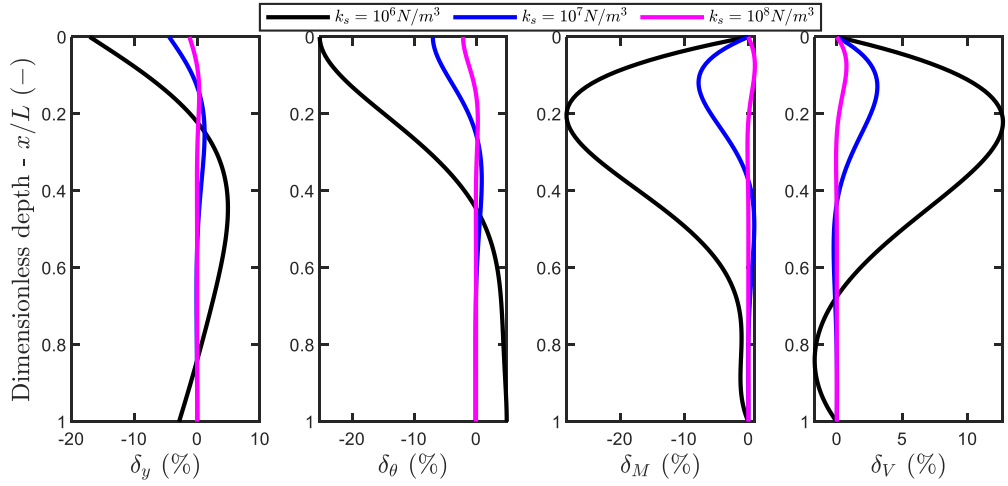


Figure 6.8 Differences between the mechanical only case and the thermomechanical one presented in Figure 6.7

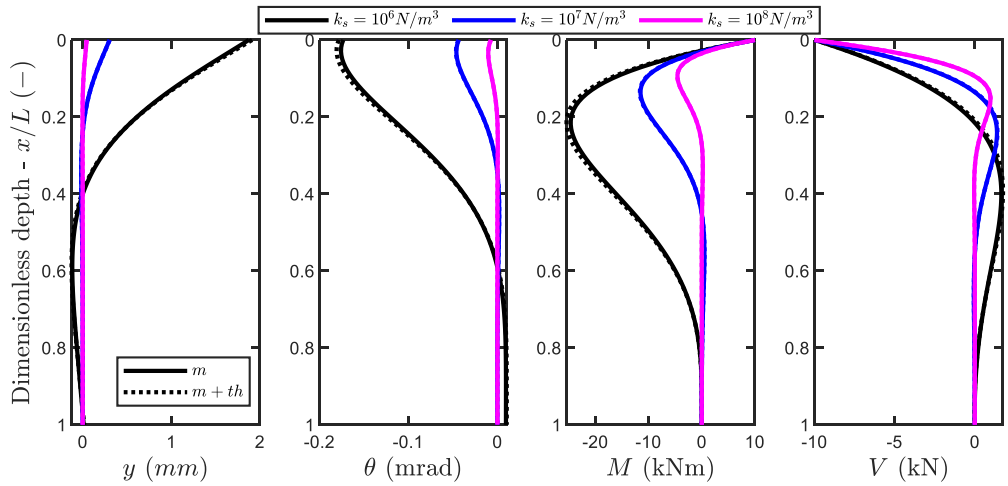


Figure 6.9 Thermomechanical behaviour of an energy pile subjected to thermal and mechanical loads, the selected static scheme is intermediate (i.e.,  $k_{head} \ll k_{base}$ )

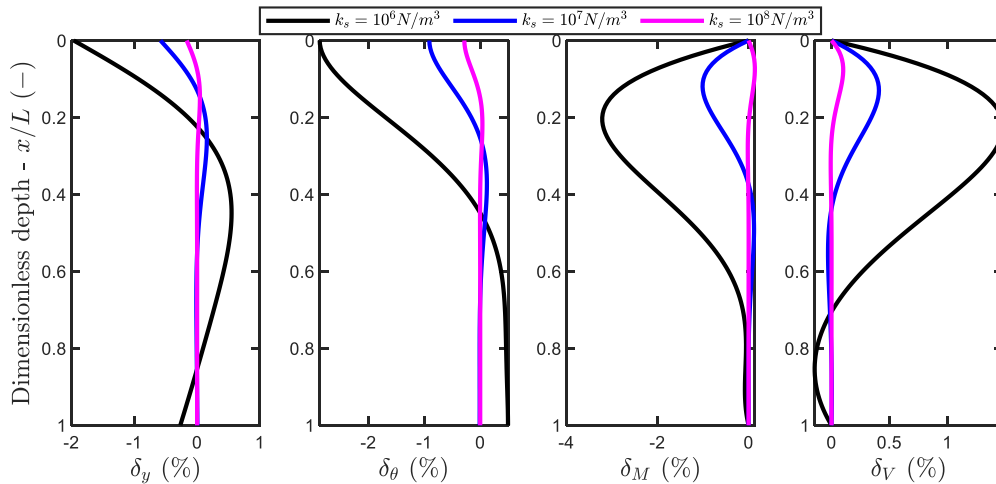


Figure 6.10 Differences between the mechanical only case and the thermomechanical one presented in Figure 6.9

### 6.2.1.5 Concluding remarks

This section highlighted the example of the Winkler model, extended to non-isothermal conditions, for the analysis of energy pile thermomechanical behavior. Insights on the model formulation are reported and results are presented. Thermal actions show their maximum effects on the transversal behavior of an energy pile when the pile is completely axially blocked at his head and at his base. If the pile is partly free to move at its head, the differences between the thermomechanical and the mechanical only loading conditions reduce of one order of magnitude with respect to the fixed (i.e., fully blocked) conditions.

Two different loading scenarios are analyzed. Firstly, the case of unitary thermomechanical actions is investigated showing that the thermal effects are very limited in terms of either deflection and internal actions. Secondly, a worst-case scenario is identified, showing that thermal effects may have an increasing impact when moving from partly constrained to fixed conditions. Worst-case scenarios, from a thermal viewpoint, are identified as oversized piles, such as long, thick piles that are subjected to low-magnitude mechanical actions and to a constant distribution of temperature variation.

## 6.2.2 Application to a complex plane geometry: the three-span continuous beam

### 6.2.2.1 General

In this section, the application to a continuous beam composed by three consecutive spans is presented. The goal is to study geometry variation and subgrade reaction stiffness variations along a continuous beam subjected to a linear distribution of temperature variation. The same concept could be extended to any other thermomechanical loading configuration. Examples of possible applications of this model in the context of energy geostructures could be: a horizontal beam resting on different

materials or a vertical footing (e.g., retaining structure) resting on a layered soil deposit or, alternatively, a foundation with a cross section that varies in space.

### 6.2.2.2 The problem

The formulation for this problem is similar to the one presented on Chapter 5 and in Sec. 6.2.1. The studied beam is divided in three spans, following the  $x$ -coordinate,  $x_i$ , development (Figure 6.11).

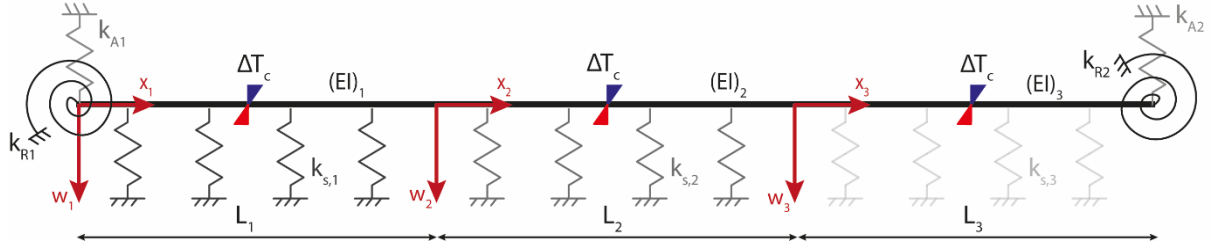


Figure 6.11 Schematic view of a beam composed by three consecutive spans resting on a spring foundation and bounded by rotational and transversal springs.

The solution can be found by solving the differential equation in each of the three portions and ensuring continuity at the connections.

The fourth order differential equation governing the problem reads:

$$(EI)_i \left( \frac{d^4 y_i}{dx_i^4} + \frac{d\chi_i^{th^2}(x_i)}{dx_i^2} \right) - N_i \frac{d^2 y_i(x_i)}{dx_i^2} + k_{s,i} y_i(x_i) = 0 \quad (6.10)$$

Which has a solution of the type:

$$y_i(x_i) = (C_{1,i} e^{\alpha_i x_i} + C_{2,i} e^{-\alpha_i x_i}) \cos \beta_i x_i + (C_{3,i} e^{\alpha_i x_i} + C_{4,i} e^{-\alpha_i x_i}) \sin \beta_i x_i \quad (6.11)$$

where  $i = 1, 2, 3$  represents the three spans that compose the beam.

$$\alpha_i = \sqrt{\lambda_i^2 + \frac{N_i}{4(EI)_i}} \quad (6.12)$$

$$\beta_i = \sqrt{\lambda_i^2 - \frac{N_i}{4(EI)_i}} \quad (6.13)$$

$$\lambda_i = \sqrt[4]{\frac{k_{s,i}}{4(EI)_i}} \quad (6.14)$$

It follows that the problem needs the quantification of 12 integration constants (i.e., four per each span). They are determined by imposing the boundary conditions and the continuity conditions at each span connection.

$$\left\{ \begin{array}{l} y_1(0)k_{A1} = V_1(0) \\ \theta_1(0)k_{R1} = M_1(0) \\ y_1(L_1) = y_2(0) \\ \theta_1(L_1) = \theta_2(0) \\ M_1(L_1) = M_2(0) \\ V_1(L_1) = V_2(0) \\ y_2(L_2) = y_3(0) \\ \theta_2(L_2) = \theta_3(0) \\ M_2(L_2) = M_3(0) \\ V_2(L_2) = V_3(0) \\ y_3(L_3)k_{A2} = -V_3(L_3) \\ \theta_3(L_3)k_{R2} = -M_3(L_3) \end{array} \right. \quad (6.15)$$

### 6.2.2.3 Results and discussions

In this section, results on different parametric analyses are reported. The three-span beam is defined presenting the spans 1 and 3 as identical, while the parametric analyses proposed here below are studied on the span 2.

The problem, per each span, is controlled by the dimensionless characteristic  $(\lambda L)_i$ , where  $i = 1, 2, 3$  and it stands per each span of the beam. By definition,  $\lambda_i$ , as defined at chapter 5, is function of  $k_{s,i}$  and  $(EI)_i$  hence parametric analyses on  $k_{s,i}$ ,  $(EI)_i$  and  $L_i$  are here proposed.

Results on the parametric analysis on the subgrade reaction,  $k_{s,i}$  are firstly reported together with comments on the effect of  $L_i$ . Results on parametric analysis on the beam stiffness,  $(EI)_i$  and the impact of  $L_i$  are eventually proposed.

The following dimensionless parameters are introduced:

$$r = k_{s,2}/k_s \quad (6.16)$$

$$n = L_2/L \quad (6.17)$$

$$s = (EI)_2/EI \quad (6.18)$$

Where

$$k_s = k_{s,1} = k_{s,3} \quad (6.19)$$

$$L = L_1 = L_3 \quad (6.20)$$

$$EI = (EI)_1 = (EI)_3 \quad (6.21)$$

The input parameters for the following parametric analyses are presented in Table 6.4

Table 6.4 Input parameters for the parametric analyses

	Symbol	Value
Subgrade reaction	$k_s$	$10^6 \text{ N/m}^3$
Young's Modulus	$E$	$25 \text{ GPa}$
Beam height	$h$	$1 \text{ m}$
Beam breadth	$b$	$1 \text{ m}$
Beam length	$L$	$40 \text{ m}$
Subgrade reaction of second span	$k_{s,2}$	$= r k_s$
Stiffness of second span	$(EI)_2$	$= s EI$
Length of second span	$L_2$	$= n L$
Dimensionless subgrade reaction	$r$	$-\infty, 0.1, 1, 10, 100, 1000, +\infty$
Dimensionless length	$n$	$0.01, 10, 100$
Dimensionless stiffness	$s$	$-\infty, 0.1, 1, 10, 100, 1000, +\infty$
Linear distribution of temperature variation	$\Delta T_c$	$1^\circ\text{C}$

#### 6.2.2.3.1 Parametric analysis on $k_s$

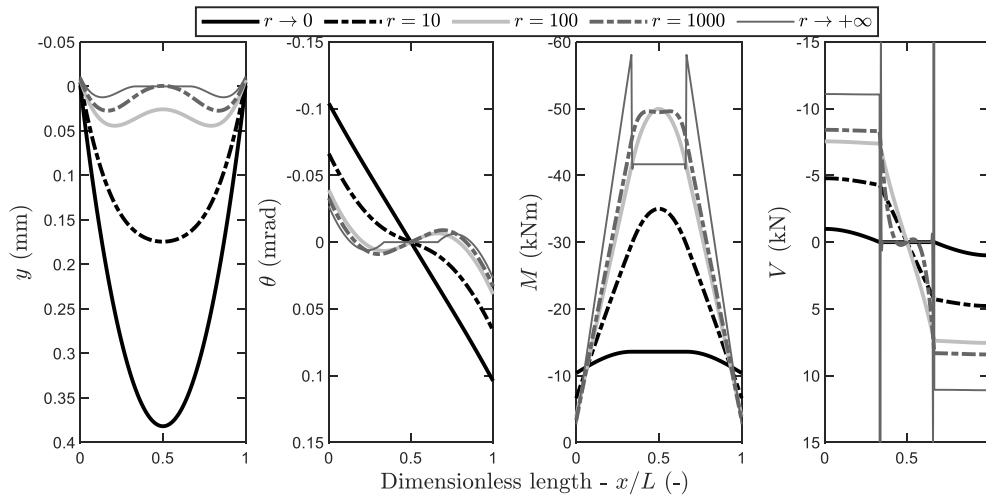
In the following, the dimensionless length is set as  $n = 1$ . Figure 6.12 shows the results for this analysis.

When  $r \rightarrow 0$  it means that  $k_{s,2} \rightarrow 0$ , so the beam at the second span is free to deform because it is not constrained by the presence of the soil. Internal actions are entirely taken by the spans at the two sides. It follows that the beam accommodates large deflections and rotations and small internal actions.

For increasing values of  $r$  (i.e.,  $r = 10 \div 1000$ ),  $\lambda_2$  increases with  $r$ , driving the beam behavior from the one of a “short beam”, where the deflection is maximum at the mid-point, towards the one of “two infinitely long beams”, where the deflection is concentrated at the vicinity of the external boundaries, as reported by Hétenyi, 1946, and presented in Chapter 5. Increasing  $r$ , the magnitude of deflection and rotation decreases, while the magnitude of internal actions increases.

For  $r \rightarrow +\infty$ , it follows that  $k_{s,2} \rightarrow +\infty$  which means that the beam lays on an infinitely rigid support. Hence, zero rotations are recorded, which means constant deflection (and equal to zero). Internal actions are concentrated in the vicinity of the connections with the second span and exhibit very high, concentrated values for bending moment and shear force.



Figure 6.12 Results for the parametric analysis on  $k_s$ 

If we add an analysis also on the effect of the length of the second span,  $L_2$ , results are reported in Figure 6.13.

For low  $L_2$  length (i.e.,  $n = 0.01$ , Figure 6.13a), the value of  $(\lambda L)_2$  do not change much because the decrease of  $L_2$  is compensated with an increase of  $\lambda_2$ . It follows that the behavior of the beam is the one typical for a “short beam”, with maximum deflection and moment at the mid-point and maximum rotation and shear action at the beam ends. Increasing  $r$ , deflection and rotation decrease, while internal actions increase. The maximum values for internal actions are recorded at the second beam span.

For high  $L_2$  length (i.e.,  $n = 10$ , Figure 6.13b) and increasing  $r$ , the beam exhibits a change in its behavior, moving from a “short beam” towards the one of “two infinitely long beams”. Deflection and rotation are higher for low values of  $r$ , while internal actions are higher for high  $r$  values. Again, the maximum of internal actions is concentrated towards the connections with the second span.

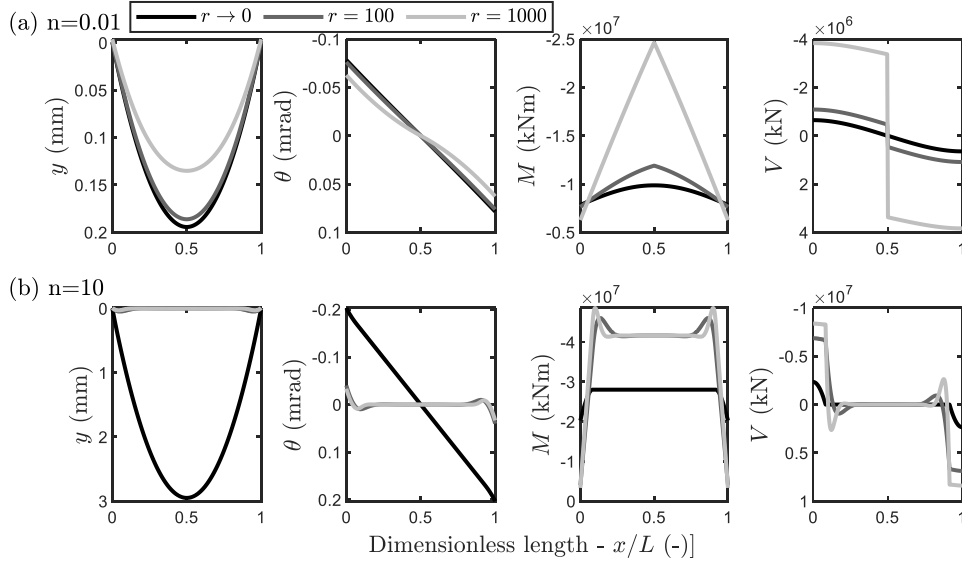


Figure 6.13 Results for the parametric analysis on  $k_{s2}$  and  $L_2$  for (a) low  $L_2$  length and (b) high  $L_2$  length

#### 6.2.2.3.2 Parametric analysis on $EI$

In the following, the dimensionless length is set to  $n = 1$ . Figure 6.14 shows the results for this analysis.

When  $s \rightarrow 0$ , it means that  $(EI)_2 \ll EI$ . It follows that it is like that the second span do not exist hence the beam is free to deform at the connections with the second span. Deflection and rotation are maximum at the connections with the second span and internal actions are null at the second span.

For low value of  $s$  (i.e.,  $s = 0.1$ ) the behavior is the one typical for “two infinitely long beams”, while increasing  $s$ , the behavior moves to the one typical for “short beams”. This is because  $\lambda_2/\lambda$  increases with  $s$ , driving the overall beam behavior.

When  $s \rightarrow +\infty$ , the second span is a rigid body, with  $(EI)_2 \rightarrow +\infty \gg EI$ . The second span behaves as a rigid body; hence it does not deflect but it can only rigidly rotate. It follows that the full rotation is shown by the first and third spans. Bending moment at the second span diverges because the structure is extremely rigid, hence capable to sustain an internal action with an infinite magnitude. It follows that also shear force is very high throughout the beam.

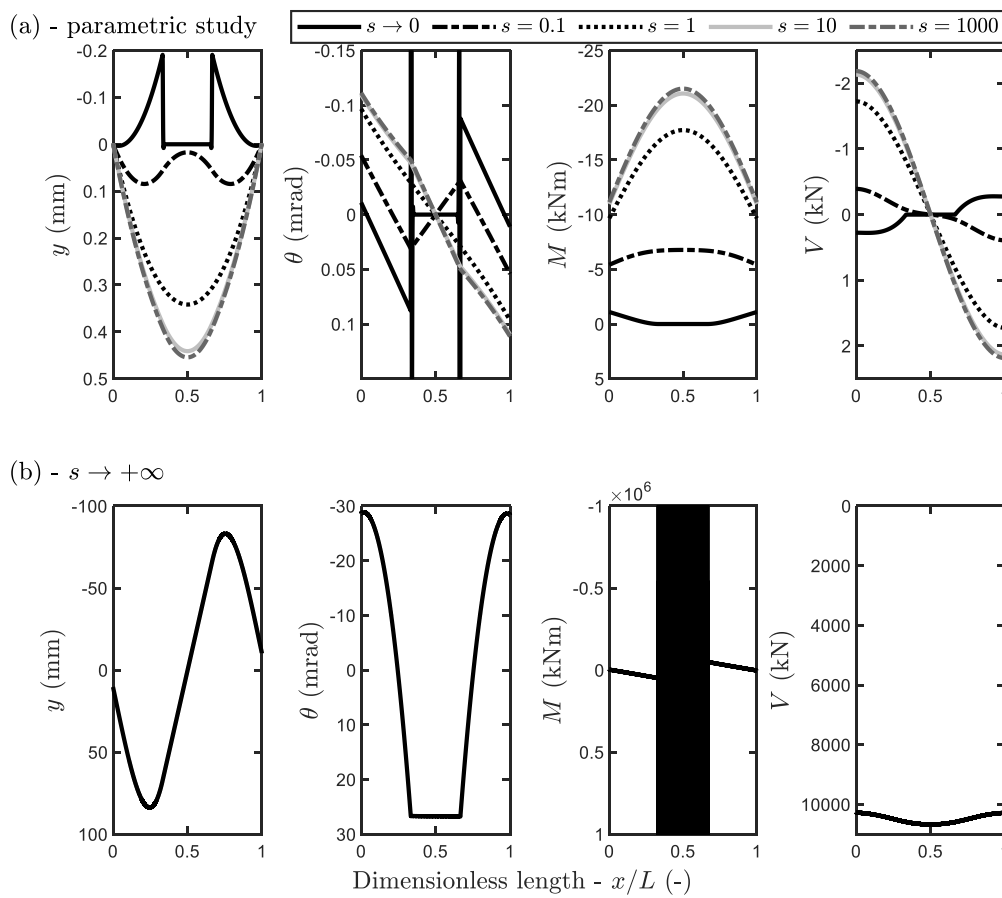


Figure 6.14 Results for the parametric analysis on  $EI$ : (a) parametric study on  $s$ ; (b) highlight for the case  $s \rightarrow +\infty$

If we add an analysis also on the effect of the length of the second span,  $L_2$ , results are reported in Figure 6.15.

For low value of  $n$  (i.e.,  $n = 0.01$ ), the characteristic of the whole system  $\lambda L$  remains quasi constant because the variation (i.e., increase) in  $\lambda_2$  is compensated by a very low value of  $L_2$ . It follows that, for the analyzed case, the beam behavior follows the one of a “short beam”, with a behavior roughly independent to  $s$ .

For higher  $n$  values (i.e.,  $n = 10$ ), the behavior strongly depends on the definition of the second span. If  $\lambda_2$  is low (i.e.,  $s = 0.1$ ), lower values of deflection, rotation and internal actions are recorded throughout the whole beam. If  $\lambda_2$  is high (i.e.,  $s = 10$ ), the behavior of the second span is the one typical for “two infinitely long beams”, showing markedly higher deflection, rotation and internal actions with respect to the previous case. Particularly, internal actions for high  $\lambda_2$  are two orders of magnitude higher than the ones for low  $\lambda_2$  values, because  $(EI)_2 > EI$ .

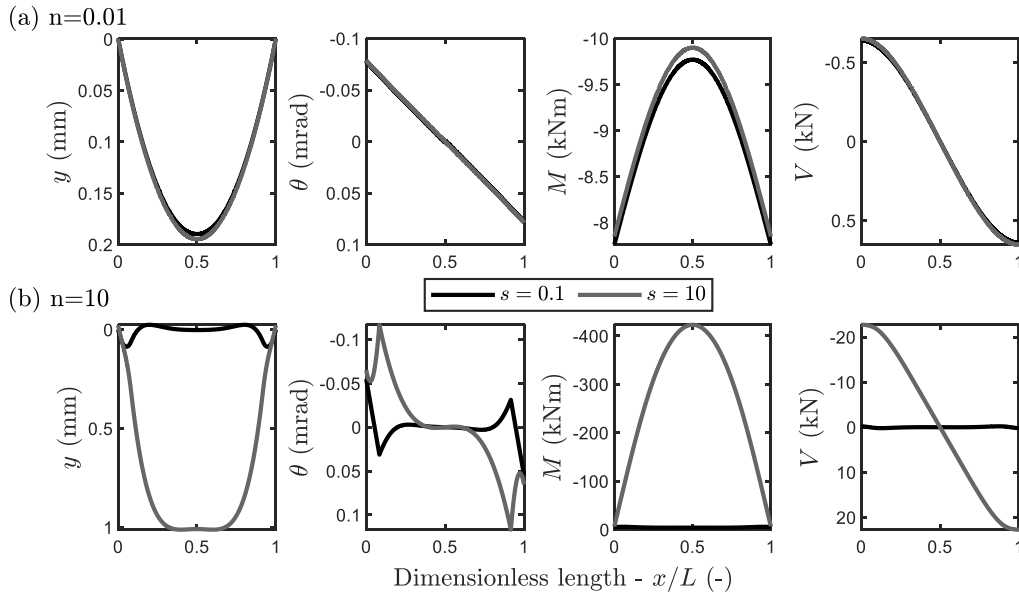


Figure 6.15 Results for the parametric analysis on  $EI_2$  and  $L_2$  for (a) low  $L_2$  length and (b) high  $L_2$  length

#### 6.2.2.4 Concluding remarks

This section presents the application of this analytical model to a complex plane geometry represented by a continuous beam formed by three consecutive spans. The thermomechanical behavior of the geostructure subjected to a linear distribution of temperature variation is presented. Example of applications of the findings proposed here are: a geostructure laying on a layered profile, or a geostructure with variations of cross section properties.

Firstly, a parametric analysis on the effect of different subgrade reaction modulus is proposed. If the central span lays on a less stiff subgrade reaction modulus with respect to the lateral ones, deflection and rotation are concentrated towards the central spans, while internal actions are mostly taken by the external spans. The opposite is reported for a stiffer subgrade reaction. If a dependency on the relative length among the spans is added, the overall behavior of the geostructure is governed by the definition of the characteristic of the system,  $\lambda L$ .

Secondly, a parametric analysis on the effect of different beam stiffness (i.e.,  $EI$ ) is proposed. If the central span is less stiff with respect to the lateral spans, deflection and rotation are concentrated towards the connections among the central and the lateral spans. Internal actions are taken by the lateral spans. The opposite is reported for the case of a central span stiffer than the lateral ones. If a dependency on the relative length among the spans is added, the overall behavior of the geostructure is governed by the definition of the characteristic of the system,  $\lambda L$ . Concentration of deflection, rotation or internal actions are recorded at the span connections.

In conclusion, a continuous beam subjected to variations in the definition of the subgrade reaction or of the cross-section stiffness, show different behavior depending on the quantification of the characteristics of the system. Moreover, concentration of deflection, rotation or internal actions are recorded at the connections between the spans, which means that the design of such connections should be carefully investigated. A similar approach to the one presented here, could be employed also to tackle geometries with more than one (or two) connected beams, such as the case of a partly embedded retaining structure connected with a slab, or a pile-raft foundation. In such cases, the system of equations that govern the problem should consider the presence of localized thermally and mechanically induced concentrated actions (i.e., axial and transversal forces, bending moment) as boundary conditions.

### 6.2.3 Partly embedded energy wall

#### 6.2.3.1 General

This section aims at proposing a slight variation of the analytical model proposed in Chapter 5 for analyzing the soil-structure interaction in non-isothermal conditions of vertical retaining walls. After an introductive part, the model is stated, and it is then compared with results coming from numerical analyses. Concluding remarks are eventually reported.

Several methods for soil-structure interaction applied to vertical retaining structures (e.g., retaining walls, piled walls, sheet piles/walls, multi-floored anchored/propped walls, etc...) exist (Bond & Harris, 2008; Clayton et al., 2014; Powrie, 2018; Selvadurai, 1979). Analytical methods are usually employed to analyze ultimate limit state (ULS) conditions, empirical methods, numerical and semi-analytical models are employed to address ULS and serviceability limit states (SLS) (Bolton et al., 1989; Bond & Harris, 2008; Burland et al., 1981; Potts & Fourie, 1984; Powrie, 1996; Rowe, 1952). Among the analytical and semi-analytical models, various variations of the Winkler's subgrade reaction models were developed to analyze vertical retaining structures. Main focus was given to the subgrade reaction definition (Balay, 1984; Delattre, 2001; Delattre & Marten, 2003; Monnet, 1994), mainly through empirical evaluations (Schmitt, 1995; Simon, 1995), and to the definition of automatic solvers accounting for elasto-plasticity (Fages & Bouyat, 1971). No evidence is available in the literature regarding the non-isothermal analysis of vertical retaining structures through analytical models such as the Winkler one.

In the following, the analysis of a partly embedded energy wall during summer operation is studied. The problem is firstly stated, derived and solved. The results are presented and compared with those coming from a numerical, finite element model. Concluding remarks are eventually reported.

### 6.2.3.2 The problem

A partly embedded retaining wall is considered here. It represents a vertical retaining wall exposed to an excavation on the top portion and fully embedded at the bottom. To consider the possible interactions with horizontal structural elements at the top and bottom of the excavated side (e.g., slab), the vertical structure is divided in two portions (two adjoining beams), mutually connected through the application of suitable boundary conditions (Figure 6.16). The model is exactly as the one employed in Chapter 5, with the only difference that lays in the definition of the subgrade reaction modulus: in this section, the evaluation of  $k_s$  is performed through the Chadeisson's chart, proposed by Monnet (Monnet, 1994).

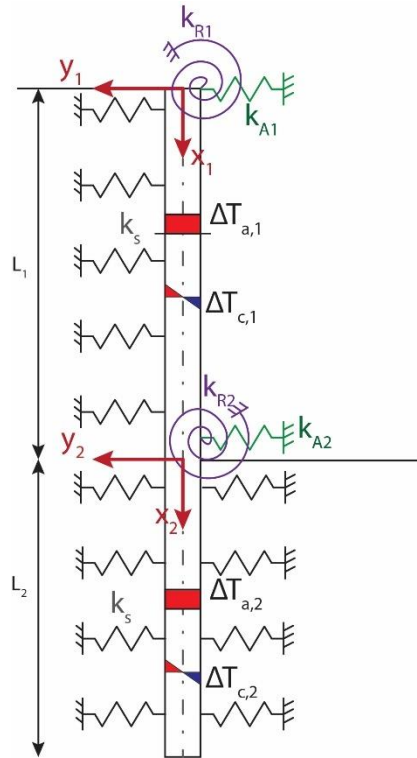


Figure 6.16 Geometry of the partly embedded wall

The considered geometry and loading conditions refer to the experimental data reported at Chapter 7, and collected during the execution of a Thermal response test (TRT) carried out at an underground train station in Geneva (Switzerland). The wall is composed of two portions (Figure 6.16), the top one exposed to the excavation of length  $L_1$ , and the bottom one fully embedded in the soil, of length  $L_2$ . The wall-slabs interactions at the excavated side are schematized through rotational ( $k_{Ri}$ ) and transversal ( $k_{Ai}$ ) springs, calibrated as from section 5.5.4. The wall is axially fixed at its head and at its base. Each portion of the wall is subjected to a constant distribution of temperature variation ( $\Delta T_{a,i}$ ) and to a linear distribution of temperature variation ( $\Delta T_{c,i}$ ). The input parameters are reported in Table 6.5.

Table 6.5 Input parameters for the study of the partly embedded wall

	Symbol	Value
Subgrade reaction	$k_s$	$3 \cdot 10^7 \text{ N/m}^3$
Wall Young's Modulus	$E$	25 GPa
Wall width	$h$	1 m
Wall breadth	$b$	1 m
Wall length (top beam)	$L_1$	11.6 m
Wall length (bottom beam)	$L_2$	8.1 m
Rotational boundary stiffness	$k_{R1}$	$7.4 \cdot 10^7 \text{ Nm/rad}$
Transversal boundary stiffness	$k_{A1}$	$10^{20} \text{ N}$
Rotational boundary stiffness	$k_{R2}$	$7.4 \cdot 10^8 \text{ Nm/rad}$
Transversal boundary stiffness	$k_{A2}$	$10^{20} \text{ N}$
Vertical (axial) boundary stiffness	$k_h$	$10^{20} \text{ N}$
Constant distribution of temperature variation	$\Delta T_{a,1}$	8 °C
Linear distribution of temperature variation	$\Delta T_{c,1}$	6 °C
Constant distribution of temperature variation	$\Delta T_{a,2}$	10 °C
Linear distribution of temperature variation	$\Delta T_{c,2}$	3 °C

Additionally, continuity in bending and shear force are imposed at the contact among the two beams. The solution procedure is iterative (2 iterations): firstly, the top beam is solved, then the bottom one is solved accounting for the boundary internal actions coming from the top beam. Then, the top beam is solved again including the internal actions coming from the bottom beam as boundary conditions. In this way, continuity is ensured at the connection among the two beams.

### 6.2.3.3 Results and discussion

In the following, the analytical results are compared with numerical ones. The numerical model features the wall and the slabs modelled as continuum elements, following the mathematical formulation reported in the Appendix A. Additional insights on the numerical model will be reported at Chapters Chapter 7 and Chapter 8. Results are presented in Figure 6.17 and are discussed in the following.

The wall deflects towards the heated side, i.e., towards the soil side. The presence of slabs and of the soil partly restrains the deflection. A general closed agreement between the two solutions is recorded. Higher discrepancies are highlighted at the wall toe, where the analytical solution shows higher displacements than the numerical one. This is due to the modelling of the mechanical boundary conditions as free, in the analytical model.

The sign convention for bending moment is as follows: moment is positive when the fibers in tension are at the extrados. The wall heating induces expansion at the extrados and contraction at the intrados. Such deflection is partly blocked by the presence of the soil and structure, hence the resulting internal

action is a traction at the intrados and a compression at the extrados which follows on a negative bending moment. Maximum bending moment is recorded at the excavated zone, which is the portion of the wall that undergoes the strongest temperature gradient between the extrados and the intrados. The fully embedded portion undergoes to a lower temperature gradient because the heat is exchanged by conduction within the same materials all around the wall. It follows that the temperature distribution in the fully embedded portion is mainly a constant distribution,  $\Delta T_{a,2}$ , while the bending component,  $\Delta T_{c,2}$ , is of lower magnitude (i.e., related only to the fact that the heat exchangers are placed non symmetrically with respect to the wall axis). Closed agreement between the analytical and numerical results is recorded.

Thermally induced shear force is of low magnitude, with a maximum (in absolute value) at the wall-slab interaction. For shear force, the discrepancy between the analytical and the numerical results is higher with respect to deflection and bending moment.

The analytical model tends to slightly overestimate internal actions with respect to the numerical one. At the excavated portion of the structure, the analytical results are always higher than the numerical results. Conversely, in the fully embedded portion, the analytical solution shows a maximum peak value located at the wall-slab interaction and then it reduces in magnitude until it is zero at the wall toe consequently to the boundary condition definition (i.e., free end) which allows for deflection and null internal actions. In the fully embedded portion, the numerical model results are slightly higher in magnitude with respect to the analytical one, showing a peak at the wall toe, which is a consequence of the quasi-null deflection captured at the same location (Figure 6.17).

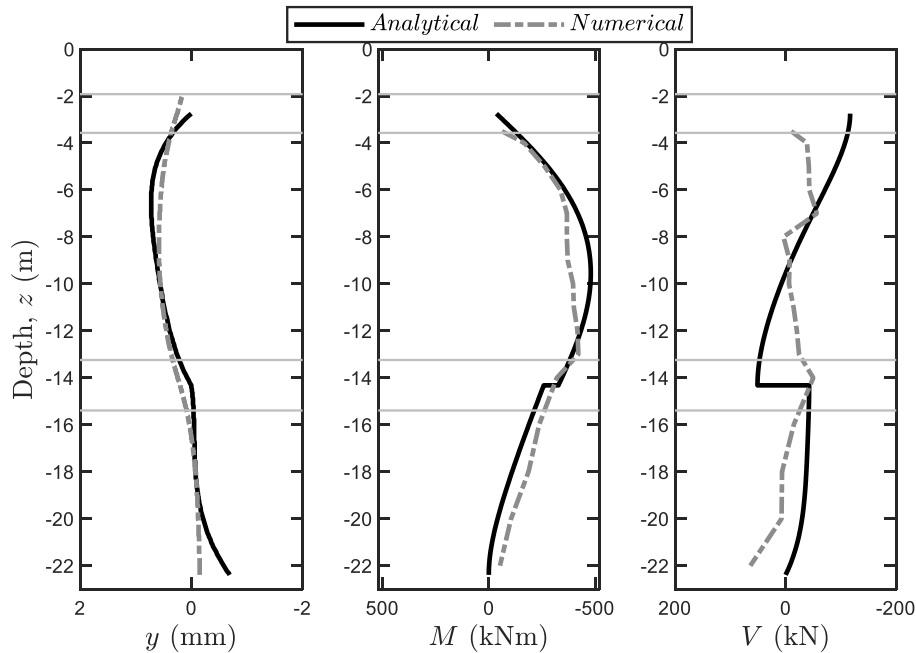


Figure 6.17 Results for the partly embedded wall: analytical results compared with numerical ones



#### 6.2.3.4 Concluding remarks

In this section, the application of the extension to non-isothermal conditions of the Winkler's model was applied to a case study of a partly embedded energy wall. The model was firstly detailed, highlighting the input parameters. The results were then compared with the ones coming from numerical analyses, showing closed agreement.

During thermal activation, uniform and linearly variable temperature variations should be included in the thermomechanical analysis. The bending behavior of the energy wall shows small deformations transversal to the wall axis because of the high stiffness imposed by the structure and its boundaries. Bending moment and shear actions develop mainly at the excavated side, showing traction at the intrados fibers.

Further insight on the geometry chosen here will be deeply investigated in *Part 3* of this thesis, as it relates to an EG where the authors have carried out some experimental investigations.

### 6.3 Extension of the two-parameters soil model to non-isothermal conditions

In this section, the extension to non-isothermal conditions of a new analytical model is presented. The solution is similar to the one presented in Chapter 5, but the soil-structure interaction is here modelled by means of two parameters. A family of models is well documented in the literature, called the two-parameters soil models, but no evidences on the analysis in non-isothermal conditions have been made available before.

In the following, general introductory concepts are presented, followed by the model definition. The application to a single beam subjected to a linear distribution of temperature variation is then proposed. Eventually, concluding remarks are reported.

#### 6.3.1 General

In this analytical model, the soil is idealized as composed by springs, independent one another and transversal to the geostructure's neutral axis (i.e., exactly as the classical Winkler's one), and a virtual shear layer laying at the contact between the spring and the geostructure (Figure 6.18). The role of the virtual shear layer is to create a connection among the springs and to restore mechanical interaction among adjacent springs.

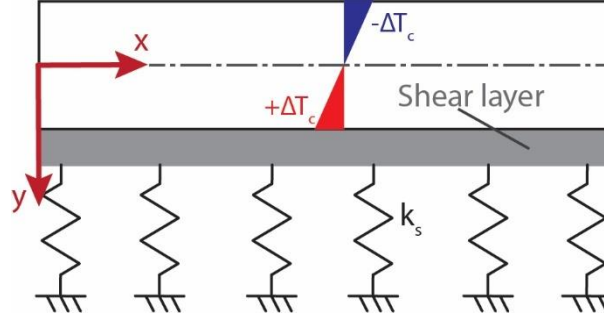


Figure 6.18 Sketch of a beam lying on a two parameters soil model

The virtual shear layer can be defined in various ways: as a thin elastic membrane under constant tension (Filonenko-Borodich, 1940, 1945), as an elastic beam (Hétyenyi, 1946), as an incompressible vertical layer which deforms in transversal shear only (Pasternak, 1954), or it can also be reconstructed by imposing restrictions to the admissible displacement and stress of an elastic layer (Reissner, 1958; Vlasov, 1949b, 1949a). Many of the available models proposed in the literature (Filonenko-Borodich, 1940, 1945; Hétyenyi, 1946; Kerr, 1965; Pasternak, 1954) use different notations, but the shape of the differential equation that governs the problem is the same, hence the solution is of the same type.

The two parameters that come into play in this model are the subgrade reaction modulus,  $k_s$ , and the shear modulus of the virtual shear layer,  $G_p$ . The calibration of the two parameters is an essential feature for a correct employment of this models.  $k_s$  and  $G_p$  can be determined following Vlasov's approach. It is worth noting that  $G_p$  do not have a real physical meaning, but it can be somehow correlated to the shear modulus of soil. In the following,  $k_s$  and  $G_p$  are calibrated following Vlasov's interpretation (Selvadurai, 1979):

$$k_s = \frac{E_s}{1 - \nu_s^2} \int_0^{H_s} \left( -\frac{1}{H_s} \right)^2 dz = \frac{E_s}{H_s(1 - \nu_s^2)} \quad (6.22)$$

$$G_p = \frac{1}{2} \int_0^{H_s} \frac{E_s}{1 + \nu_s} \left( 1 - \frac{z}{H_s} \right)^2 dz = \frac{H_s E_s}{6(1 + \nu_s)} \quad (6.23)$$

where the subscript "s" stands for soil,  $E_s$  represent the Young Modulus,  $\nu_s$  the Poisson ratio,  $H_s$  the height of the soil layer below the geostructure (Selvadurai, 1979) and  $z$  the vertical, downwards directed, coordinate centered at the soil-geostructure interface.  $G_p$  becomes equal to the soil's shear modulus,  $G_s$ , for  $H_s = 3$ . This is the case considered in the following.

A particular condition is for  $G_p \rightarrow 0$ . In such case, the solution of the two-parameters soil model is the same as for the Winkler model.

In the following, the two-parameters soil model is applied to an elementary unit composed by a single beam bounded by transversal and rotational boundary conditions and the results are compared with the Winkler model, to highlight the effect of introducing the second parameter,  $G_p$ .

### 6.3.2 The problem

The elementary unit considered is composed by a single beam resting on a two-parameters soil medium and bounded at the edges by a transversal and rotational springs of stiffness  $k_A$  and  $k_R$ , respectively (Figure 6.19). The beam is subjected to a linear distribution of temperature variation throughout the whole length,  $\Delta T_c$ .

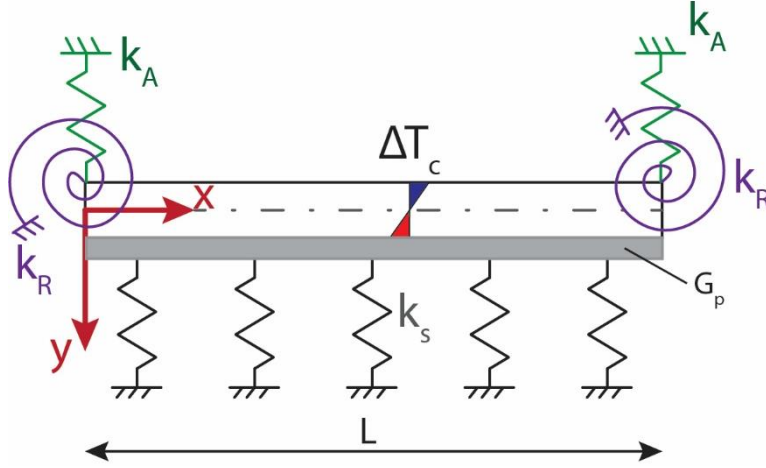


Figure 6.19 Sketch of the elementary unit employed for the two parameters soil model analysis

The fourth-order differential equation that governs the problem is:

$$EI \frac{d^4 y(x)}{dx^4} - G_p b \frac{dy(x)}{dx^2} + k_s b y(x) = 0 \quad (6.24)$$

Where  $EI$  is the beam's bending stiffness,  $y(x)$  the deflection,  $b = 1$  m the unitary width of the beam. The solution for this differential equation is of the type:

$$y(x) = (A_1 e^{\mu \lambda x} + A_2 e^{-\mu \lambda x}) \cos(\beta \lambda x) + (A_3 e^{\mu \lambda x} + A_4 e^{-\mu \lambda x}) \sin(\beta \lambda x) \quad (6.25)$$

$$\mu = \sqrt{1 + \frac{G_p \lambda^2}{k_s}} \quad (6.26)$$

$$\beta = \sqrt{1 - \frac{G_p \lambda^2}{k_s}} \quad (6.27)$$

$$\lambda = \sqrt[4]{\frac{k_s b}{4EI}} \quad (6.28)$$

Where  $A_1, A_2, A_3, A_4$  are the four integration constants to be determined by imposing the boundary conditions. If  $G_p \rightarrow 0$ ,  $\mu \rightarrow \beta$  and the classical Winkler solution is restored.

Rotation,  $\theta(x)$ , bending moment,  $M(x)$  and the generalized shear force,  $V_{gen}(x)$  are determined as:

$$\theta(x) = \frac{dy(x)}{dx} \quad (6.29)$$

$$M(x) = -EI \frac{d^2y(x)}{dx^2} - EI\chi_f^{th} \quad (6.30)$$

$$V_{gen}(x) = \frac{dM(x)}{dx} + G_p b \frac{dy(x)}{dx} \quad (6.31)$$

Where  $\chi_f^{th}$  is the thermally-induced free curvature, as introduced in Chapter 5, and  $V_{gen}(x)$  is also known as the *generalized shear force* as it accounts also for the shear effects induced by the presence of  $G_p$  differently with respect to the shear force as it is introduced in Chapter 5.

The four boundary conditions are:

$$\begin{cases} M(0) = \theta(0)k_R \\ V(0) = y(0)k_A \\ M(L) = -\theta(L)k_R \\ V(L) = -y(L)k_A \end{cases} \quad (6.32)$$

The loading configuration employed in the following is a linear distribution of temperature variation throughout the beam's height,  $\Delta T_c = 1^\circ\text{C}$ .

### 6.3.3 Results and discussions

The input parameters for the following parametric analyses are presented in Table 6.6. The materials are selected from a literature review (Bowles, 1988; Kézdi & Réthati, 1974; Prat et al., 1995) and aim at representing materials of different stiffness that could be encountered in foundation analysis. Geometrical and boundary conditions inputs for the analyses are presented in Table 6.7.

Table 6.6 Input material properties for the analyses reported in this section

Material	$E_s$ [MPa]	$\nu_s$ [-]	$k_s$ [N/m <sup>3</sup> ]	$G_p$ [N/m]
Dense gravel	200	0.3	$1.36 \cdot 10^8$	$7.69 \cdot 10^7$
Stiff clay	20	0.3	$1.36 \cdot 10^7$	$7.69 \cdot 10^6$
Soft clay	5	0.3	$3.40 \cdot 10^6$	$1.92 \cdot 10^6$

Table 6.7 Input parameters for the analyses of a beam on a two-parameters soil model

	Symbol	Value
Concrete Young Modulus	$E$	25 GPa
Concrete thermal expansion coefficient	$\alpha$	$10^{-5} \text{ K}^{-1}$
Beam height	$h$	1 m
Beam breadth	$b$	1 m
Beam length	$L$	20 m
Transversal spring stiffness boundary condition	$k_A$	$10^8 \text{ kN/m}$
Rotational spring stiffness boundary condition	$k_R$	$10^9 \text{ kNm/rad}$
Linear distribution of temperature variation	$\Delta T_c$	$1 \text{ }^\circ\text{C}$

Results for these analyses, together with a comparison with the Winkler model are reported in Figure 6.20. A parametric analysis encompassing different soil conditions is presented.

Deflection, as expected, is maximum for lower soil stiffness. For low  $\lambda L$  values (i.e., low  $k_s$ ), the beam behavior is the one typical for a “single beam” (Hétyenyi, 1946), while if  $\lambda L$  increases, the beam behavior shifts towards the one typical for “two infinitely long beams”. Looking at the differences between the Two-parameters model and the Winkler model, higher discrepancy is recorded for higher soil stiffness. The location of the peaks for deflection, rotation and shear force are slightly shifted in space with respect to the correspondent Winkler case.

Internal actions show the same qualitative shape for the three studied soil conditions. Minimal discrepancies among the two-parameters model and the Winkler model are recorded for bending moment. Higher differences are recorded for higher soil stiffness. Shear force shows higher differences among the two parameters model and the Winkler model. The shear force for the two parameters model is higher with respect to the Winkler model because the virtual shear layer is capable to deform upon shear, hence partly restraining internal actions.

In general, deflection, rotation and internal actions are slightly lower for the two-parameters model with respect to the Winkler model, but no macroscopic differences between the two models are recorded.

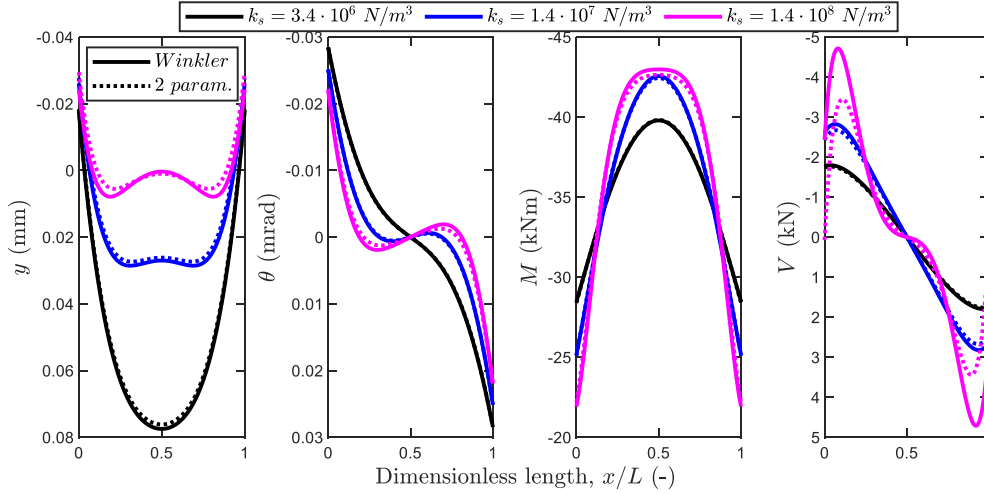


Figure 6.20 Results for the analysis employing the two-parameters soil model: the dotted lines represent the results employing the two-parameters soil model for the cases described in Table 6.6, the continuous line represents the results for the case  $G_p \rightarrow 0$  which corresponds to the Winkler model

#### 6.3.4 Concluding remarks

Two-parameters soil model extends the Winkler model partly recovering continuity in the modelling of the soil-structure interaction. In the two-parameters model presented here, a virtual shear layer is added between the linear springs representing the soil and the beam, partly restoring the mechanical interaction among adjoining springs. The two-parameters soil model is here extended to non-isothermal conditions and the thermomechanical behavior of a beam resting on a two-parameters soil model is studied by loading the beam with a linear distribution of temperature variation.

The model is presented in its mathematical formulation and the application to an elementary unit composed by a single beam is proposed.

Results on the application of the two-parameters model are shown and they are compared with the Winkler model. Modifications among the two models are recorded. In particular, higher differences among the two models are recorded for a stiffer soil, while for a soft soil, the differences among the two models are marginal.

Generally speaking, for deflection, rotation and internal actions, the employment of the two-parameters model with respect to the Winkler model highlights that the macroscopic behavior of the elementary unit does not change among the two employed models. Local variations of deflection and internal actions are recorded, showing little modifications. For shear forces, the highest differences are highlighted as the virtual shear layer, by definition, is capable of partly reducing the shear action by accommodating deformation upon shear.

Possible applications of the two-parameters soil model could relate to horizontal as well vertical footings loaded with thermal and mechanical actions.

## 6.4 Extension of the linearly varying reaction modulus model to non-isothermal conditions

### 6.4.1 General

This section presents the extension of the linearly varying subgrade reaction modulus model to non-isothermal conditions. This model allows for studying the behavior of vertical and horizontal footings laying on geomaterials with a stiffness that varies along the geostructure length.

The main variation with respect to the Winkler model lays in the definition of the subgrade reaction modulus,  $k_s$ . Winkler's model assumes a constant value for  $k_s$ , while in the following,  $k_s$  is defined as a linear function along the geostructure's length. Such feature modifies the problem definition (i.e., the differential equation that governs the problem) and the solution type substantially modifies.

A wide literature is available to address problems related to vertical and horizontal beams laying on a linearly varying subgrade reaction modulus subjected to mechanical actions, in analytical and numerical ways. Examples of this model are related to analytical solutions for horizontal beams subjected to static mechanical actions (Franklin & Scott, 1979; Froio & Rizzi, 2016, 2017; Hétenyi, 1946; Yankelevsky et al., 1989) and to moving mechanical loads (Froio et al., 2018). Numerical (Bowles, 1974; Guo & Weitsman, 2002) and approximate (Clastornik et al., 1986) solutions for mechanically loaded beams, analytical applications of energy theorems (Borák & Marcián, 2014) for analyzing mechanically loaded beams are also reported. Examples on vertical beams relate mainly to piles (Madhav et al., 1971; Randolph, 1981). Main fields of applications of this model are the analysis of: ballasted railway tracks, bridges, beam trusses, pipelines and floating structures.

In the context of energy geostructures, this model allows to determine the deformed shape as well as to quantify internal actions. Main applications of this model could be (but not limited to) energy piles, walls and horizontal geostructures such as slabs, rafts, decks and bridges (e.g., for de-icing applications).

In this section, the model is firstly presented and validated against alternative solutions available in the literature and against numerical results. Results are then presented, focusing on a parametric interpretation. Concluding remarks are eventually reported.

## 6.4.2 The problem

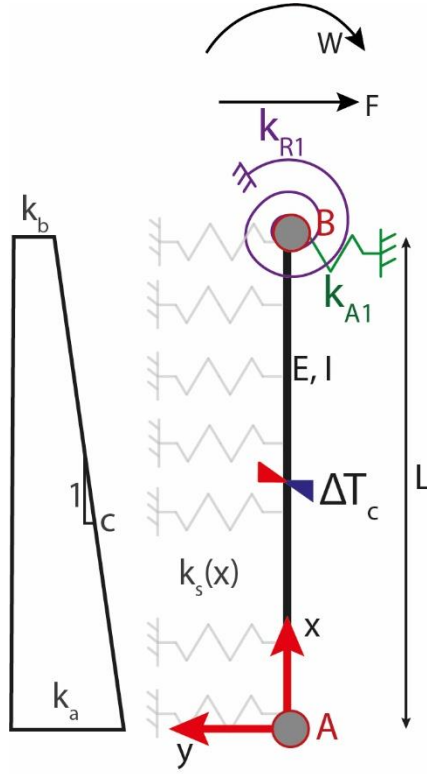


Figure 6.21 Sketch of the problem: a vertical beam laying on a linearly varying subgrade reaction modulus subjected to a linear distribution of temperature variation along the beam axis and to concentrated shear and bending actions at his head

In the following, the subgrade reaction modulus is defined as a linear function of the  $x$ -coordinate,  $k_s(x)$ , where  $k_a$  is the subgrade reaction modulus at the point  $x = 0$ , and  $c$  is the slope (Figure 6.21).

$$k_s(x) = k_a - cx \quad (6.33)$$

Analyzing the equilibrium of an infinitesimal portion of the beam, the differential equation that governs the problem is written as:

$$\frac{EI}{k_a} \frac{d^4 y(x)}{dx^4} + \frac{k_a - cx}{k_a} y(x) = 0 \quad (6.34)$$

where  $E$  is the Young Modulus of the beam,  $I$  is the moment of inertia of the cross section (i.e.,  $I = bh^3/12$  for a rectangular cross section of base  $b$  and height  $h$ ) and  $y(x)$  is the deflection of the beam following the  $x$  coordinate.

The solution can be found by performing a change of variable, from  $x$  to  $\xi$  and consequently re-writing equation (6.33).



$$\xi = \frac{k_a - cx}{k_a} = 1 - \frac{c}{k_a}x \quad (6.35)$$

$$\frac{d^4y}{d\xi^4} + \alpha\xi y = 0 \quad (6.36)$$

with  $\alpha$  being the characteristic length of the system defined as:

$$\alpha = \frac{k_a^5}{c^4EI} \quad (6.37)$$

The solution of the differential equation (6.34), can be written as:

$$y(\xi) = C_1y_1(\xi) + C_2y_2(\xi) + C_3y_3(\xi) + C_4y_4(\xi) \quad (6.38)$$

where  $C_1, C_2, C_3, C_4$  are four integration constants to be determined by imposing the boundary conditions, and  $y_1(\xi), y_2(\xi), y_3(\xi), y_4(\xi)$  are series expansions (Hétenyi, 1946):

$$y_1(\xi) = 1 - \frac{\alpha}{5!}\xi^5 + \frac{6\alpha^2}{10!}\xi^{10} - 6\frac{11\alpha^3}{15!}\xi^{15} + 6 \cdot 11 \cdot 16\frac{\alpha^4}{20!}\xi^{20} - \dots \quad (6.39)$$

$$y_2(\xi) = \xi - \frac{2\alpha}{6!}\xi^6 + 2\frac{7\alpha^2}{11!}\xi^{11} - 2 \cdot 7\frac{12\alpha^3}{16!}\xi^{16} + 2 \cdot 7 \cdot 12\frac{17\alpha^4}{21!}\xi^{21} - \dots \quad (6.40)$$

$$y_3(\xi) = \frac{\xi^2}{2!} - \frac{3\alpha}{7!}\xi^7 + 3\frac{8\alpha^2}{12!}\xi^{12} - 3 \cdot 8\frac{13\alpha^3}{17!}\xi^{17} + 3 \cdot 8 \cdot 13\frac{18\alpha^4}{22!}\xi^{22} - \dots \quad (6.41)$$

$$y_4(\xi) = \frac{\xi^3}{3!} - \frac{4\alpha}{8!}\xi^8 + 4\frac{9\alpha^2}{13!}\xi^{13} - 4 \cdot 9\frac{14\alpha^3}{18!}\xi^{18} + 4 \cdot 9 \cdot 14\frac{19\alpha^4}{23!}\xi^{23} - \dots \quad (6.42)$$

Once the deflection,  $y(\xi)$ , is known, the rotation,  $\theta(\xi)$ , bending moment,  $M(\xi)$  and shear force,  $V(\xi)$ , can be defined as:

$$\theta(\xi) = \frac{c}{k_a} \frac{dy(\xi)}{d\xi} \quad (6.43)$$

$$M(\xi) = -EI \left( \frac{c}{k_a} \right)^2 \frac{d^2y(\xi)}{d\xi^2} - EI\chi_f^{th} \quad (6.44)$$

$$V(\xi) = -EI \left( \frac{c}{k_a} \right)^3 \frac{d^3y(\xi)}{d\xi^3} - EI \frac{d\chi_f^{th}}{d\xi} \quad (6.45)$$

where  $\chi_f^{th}$  is the free thermal curvature, as defined in Chapter 5.

With reference to the geometry showed in Figure 6.21, the following boundary conditions can be set. At  $x = 0$ , the conditions written in terms of the variable  $\xi = \xi_1 = 1$  (equation (6.35)) are:

$$\begin{cases} M(\xi_1) = 0 \\ V(\xi_1) = 0 \end{cases} \quad (6.46)$$

At  $x = L$ , the conditions written in terms of the variable  $\xi = \xi_2 = 1 - \frac{c}{k_a}L$  (equation (6.35)) are:

$$\begin{cases} M(\xi_2) = W - k_{R1}\theta(\xi_2) \\ V(\xi_2) = F - k_{A1}y(\xi_2) \end{cases} \quad (6.47)$$

In the following, the considered loading condition features of concentrated shear force,  $F$ , and bending moment,  $W$ , at the top end and a linear distribution of temperature variation along the geostructure (Figure 6.21).

### 6.4.3 Validation

In this section, the model presented here is validated against analytical results available in the literature (Froio & Rizzi, 2017) and against numerical results.

The input parameters used to perform the validation are presented in Table 6.8.

Table 6.8 Input parameters for the analyses of a beam on a linearly-varying subgrade reaction soil model for the validation against literature and numerical results

	Symbol	Value
Concrete Young Modulus	$E$	25 GPa
Concrete thermal expansion coefficient	$\alpha$	$10^{-5} \text{ K}^{-1}$
Beam height	$h$	1 m
Beam breadth	$b$	1 m
Beam length	$L$	10 m
Transversal spring stiffness boundary condition	$k_A$	0 kN/m
Rotational spring stiffness boundary condition	$k_R$	0 kNm/rad
Concentrated shear force at the top	$F$	10 kN
Concentrated bending moment at the top	$M$	10 kNm
Subgrade reaction modulus at the bottom	$k_a$	$2.66 \cdot 10^7 \text{ N/m}^3$
Slope of the subgrade reaction modulus curve	$c$	$1.33 \cdot 10^6 \text{ N/m}^4$

The parameters chosen in Table 6.8 allows for determining the following non-dimensional parameters (Froio & Rizzi, 2017):

$$\lambda_b = \sqrt[4]{\frac{k_b}{4EI}} = 0.2 \quad (6.48)$$

$$l = \lambda_b L = 2 \quad (6.49)$$

$$\alpha^* = 4(\lambda_b L)^4 = 64 \quad (6.50)$$

$$\beta = \frac{k_a}{k_b} - 1 = 1 \quad (6.51)$$

The numerical finite element model is a 2D plane strain model of a beam laying on a spring foundation with stiffness as from equation (6.33). The mathematical formulation of the model is reported in Appendix D. Input parameters are reported in Table 6.8.

The results of such comparison are reported in Figure 6.22. Closed agreement among the three solutions is revealed for deflection, bending moment and shear force. Rotation is not reported because it is not made available in the literature (Froio & Rizzi, 2017).

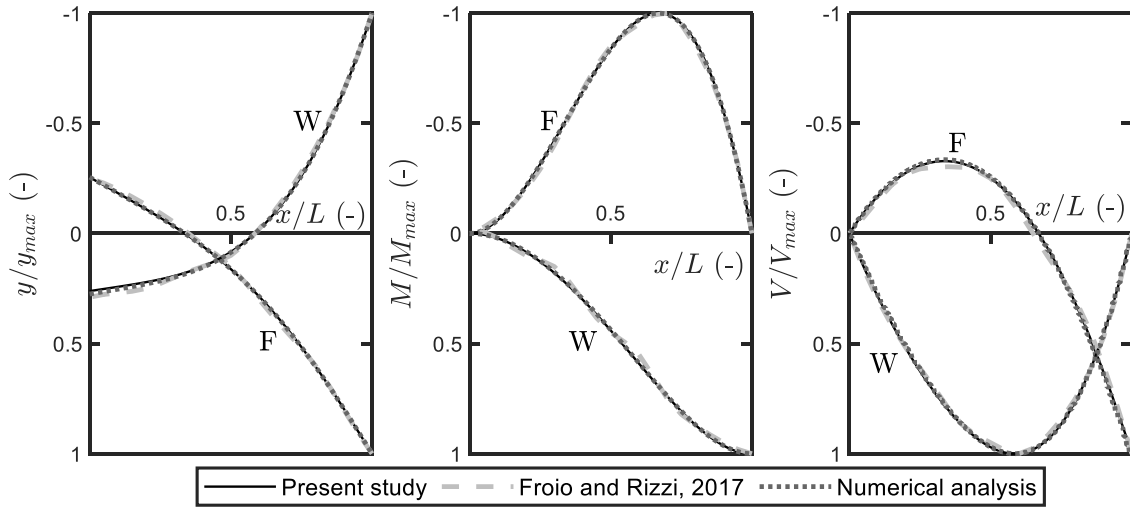


Figure 6.22 Comparison among the analytical, numerical results and the ones available in the literature. The results for the application of a concentrated shear force are denoted with  $F$ , while the results for the application of a concentrated bending moment are denoted with  $W$

#### 6.4.4 Results and discussions

In this section, results related to the application of a unitary linear variation of temperature variation,  $\Delta T_c = 1^\circ\text{C}$ , along the beam are presented.

The following two static schemes are adopted: free beam at his head and partly restrained which adds partial transversal and rotational constraints at the beam head (Figure 6.21), evaluated as  $k_{R1} = 10^9$  Nm/rad and  $k_{A1} = 10^8$  N/m, respectively. A parametric analysis on selected parameters is here proposed. The input parameters are reported in Table 6.9. Results are presented in Figure 6.23. Results are

discussed firstly with reference to the free static scheme and then with reference to the partly constrained static scheme.

Table 6.9 Input parameters for the parametric analyses of a beam on a linearly varying subgrade reaction soil model

	Symbol	Value
Concrete Young Modulus	$E$	25 GPa
Concrete thermal expansion coefficient	$\alpha$	$10^{-5} \text{ K}^{-1}$
Beam height	$h$	1 m
Beam breadth	$b$	1 m
Beam length	$L$	10 m
Transversal spring stiffness boundary condition	$k_A$	$0 \div 10^8 \text{ kN/m}$
Rotational spring stiffness boundary condition	$k_R$	$0 \div 10^9 \text{ kNm/rad}$
Linear distribution of temperature variation	$\Delta T_c$	$1^\circ \text{C}$
Subgrade reaction modulus at the bottom	$k_a$	$10^6 \div 10^8 \text{ N/m}^3$
Dimensionless group: top/bottom relative stiffness of the subgrade reaction modulus	$\beta$	$2 \div 100$

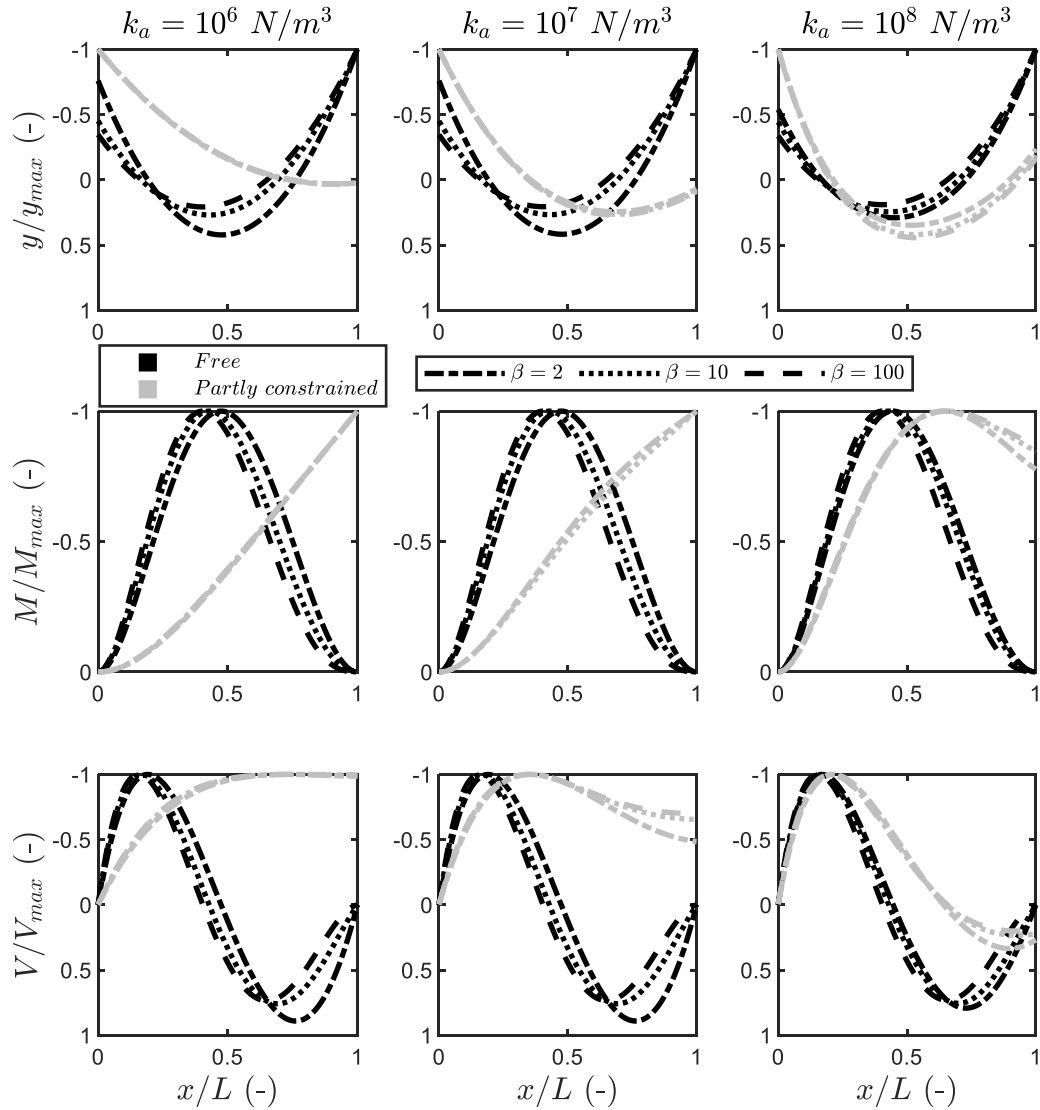


Figure 6.23 Results for the parametric analysis for the beam on a linearly varying subgrade reaction modulus

The free static scheme is characterized by null transversal stiffness at the beam's head. It follows that the beam is free to deflect and rotate at the two extremes (i.e., end constraints are equal). The thermal load is constant throughout the beam and the subgrade reaction stiffness is non-symmetric following the input parameters reported in Table 6.9. It follows that  $y\left(\frac{x}{L} = 1\right) > y\left(\frac{x}{L} = 0\right)$  because of the lower subgrade reaction stiffness at point B. The maximum deflection is hence located between  $\frac{x}{L} = 0$  and  $\frac{x}{L} = 0.5$ . The maximum point moves towards  $\frac{x}{L} = 0$  if  $\beta$  increases. For the classical Winkler case (i.e.,  $k_a = k_b$ ), the maximum deflection would be located at  $\frac{x}{L} = 0.5$ . The overall beam's behavior remains consistent if  $k_a$  increases. The effects of  $\beta$  reduce for increasing values of  $k_a$ , as the flexural degree of freedom reduces, and deflection reduces giving rise to higher internal actions Figure 6.24.

Internal actions develop along the beam. Bending moment is negative throughout the whole beam, consequently to the sign of the applied thermal action. Maximum values for bending moment and shear force are located between  $\frac{x}{L} = 0$  and  $\frac{x}{L} = 0.5$ , consistently with the higher stiffness offered by  $k_s$ . Bending moment shape would be symmetric if  $k_a = k_b$  (i.e., classical Winkler model), whereas for a linearly varying  $k_s(x)$  the maximum point is shifted towards the bottom portion of the beam. Shear force would be perfectly anti-symmetric for the Winkler's model, whereas for a linearly varying  $k_s(x)$  its shape is shifted towards the bottom portion of the beam.

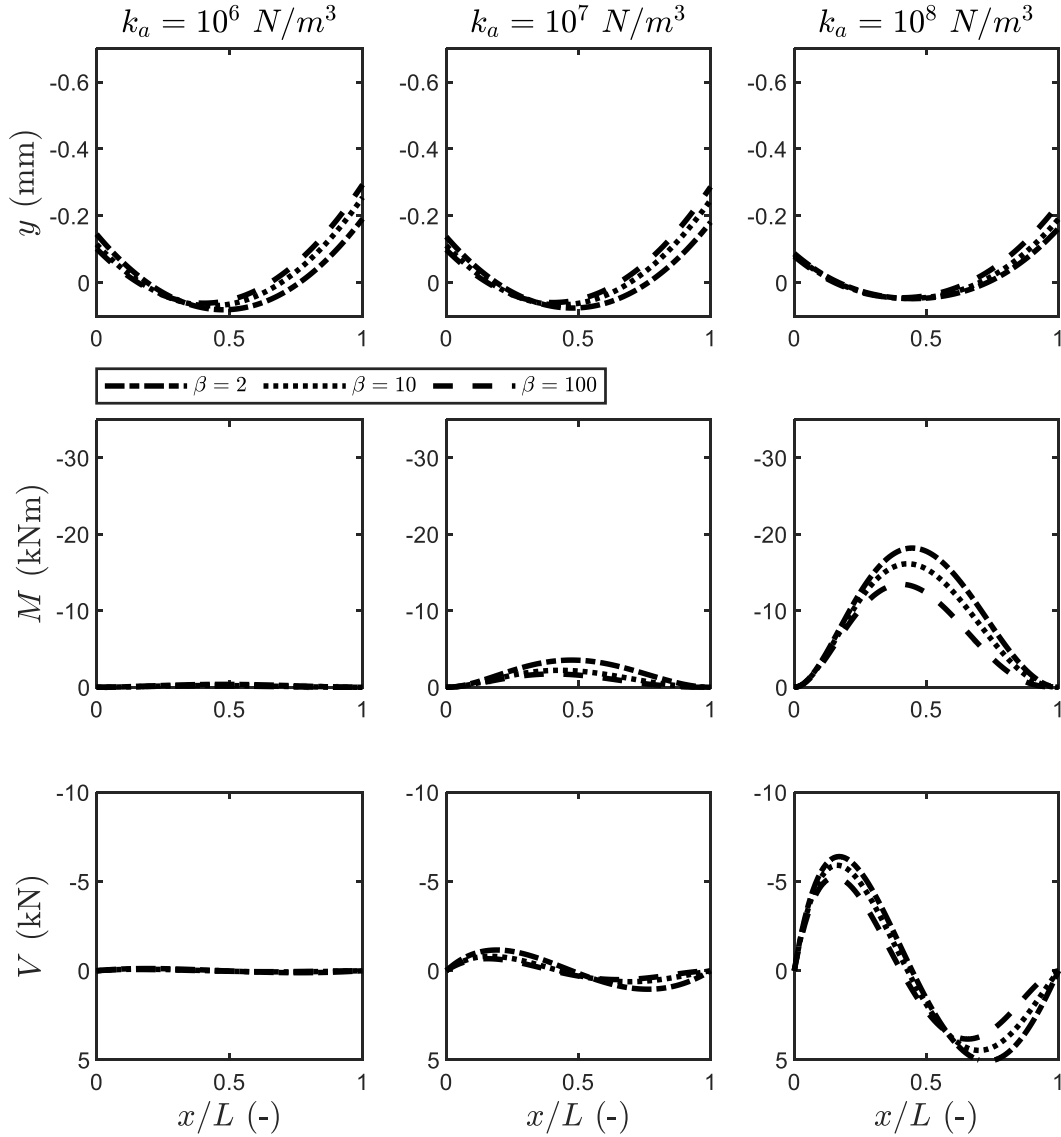


Figure 6.24 Particular over the results for the free static scheme

The partly restrained static scheme presents the aforementioned beam (Figure 6.21, Table 6.8) subjected to a unitary linear distribution of temperature variation and bounded by a partial transversal and rotational restraint at  $x = L$ . Regarding deflection (Figure 6.25), the boundary conditions partly restrain the deflection, hence the beam deflects more where it is free to do it (i.e.,  $0 < \frac{x}{L} < 0.5$ ). Deflection at the point  $\frac{x}{L} = 1$  is very low and it would tend to  $y\left(\frac{x}{L} = 1\right) \rightarrow 0$  for  $k_a \rightarrow +\infty$ . Deflection decreases in magnitude for increasing values of  $k_a$  as the  $DOF_c$  decreases (Figure 6.21).

Negative bending moment develops throughout the whole beam, with higher values located in the vicinity of the partly constrained boundary. The magnitude of internal actions increases with increasing  $k_a$  (Figure 6.21), consequently to the decrease of  $DOF_c$ . Shear force develops throughout the beam, increasing in magnitude with  $k_a$ . Overall, the dependency on  $\beta$  is lower than in the free static scheme, as the effect of boundary conditions (i.e., static scheme) is paramount.

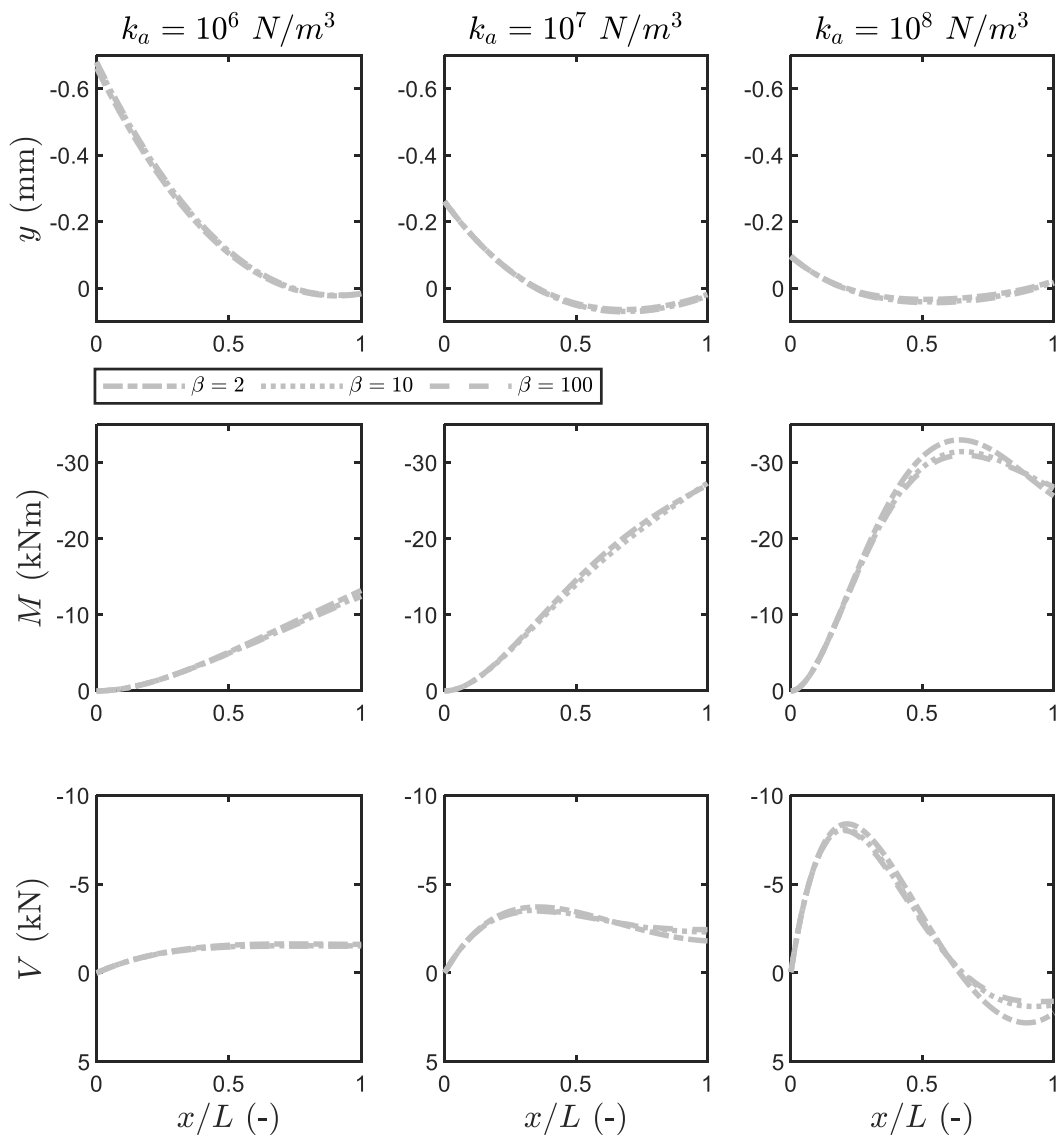


Figure 6.25 Particular over the results for the partly constrained static scheme

### 6.4.5 Concluding remarks

This section introduces a variant to the classical Winkler's subgrade reaction model, by proposing the model related to a linearly varying subgrade reaction, extended to non-isothermal conditions. The model is firstly presented, the solution procedure explained and the boundary conditions are defined. The model behavior is validated against literature results proposed by Froio & Rizzi, 2017 and against numerical results, showing excellent agreement.

The application of thermal loads is then investigated with reference to the application of a unitary linear distribution of temperature variation throughout a vertical beam. A parametric analysis is proposed, focusing on detecting the beam's behavior for different subgrade reaction modulus' definitions as well

for different static schemes. The beam's response is detailed with reference to deflection and internal actions. The choice of the static scheme governs the macroscopic beam behavior (i.e., the overall shape of the beam's response), while the subgrade reaction definition locally modifies the beam's behavior in terms of either deflection (e.g.,  $y(x)$  is higher for lower  $k_s(x)$  stiffness) and internal actions (e.g., the location of internal actions' peaks varies with  $k_s(x)$ ).

Finally, this model is able to capture deflection and internal actions for single beams, subjected to thermal and mechanical actions. Main applications of this model are vertical and horizontal footings subjected to thermal and mechanical actions. In the context of energy geostructures, this model could be employed for the analysis of, but not limited to, vertical elements (e.g., piles, walls, shafts, etc...) as well as to horizontal elements (e.g., decks and pavement roads for de-icing purposes, structural slabs).





## Part 3 : In-situ testing



# Chapter 7 Thermal Response Testing on an underground thermo-active train station in Switzerland

## 7.1 Foreword

Little is known concerning the quantification of the thermal potential of thermo-active underground infrastructures that can serve as a major heating/cooling provider for the built environment. This chapter relates to the full-scale in-situ testing and the numerical modelling of an underground train station in Switzerland equipped with energy geostructures. A portion of the underground energy walls-and-slabs installation at the Lancy-Bachet train station in Geneva (Switzerland) is tested by executing a TRT (i.e., thermal response test).

The content of this chapter is strongly linked with the following Chapter 8, because the experimental, in-situ, activities is composed by a series of different tests carried out from summer 2019 to spring 2020. Chapter 7 contains the details of the tested site and of the experimental setup, the execution and data interpretation of a TRT on energy walls. Chapter 8 expands on investigations related to the wall-tunnel hydrothermal interactions and thermomechanical behavior, including results of further series of heating/cooling tests, and on the determination of the thermal potential of the underground energy infrastructure.

Chapter 7 aims at analyzing the first steps of the in-situ experimental campaign, by detailing the execution of a TRT. TRT is an in-situ test employed to thermally characterize the materials within and around a geostructure. Examples of applications and guidelines for the test execution exist for vertical heat exchangers (e.g., boreholes and energy piles). No informations are available on the execution and data interpretation of TRTs on walls or, more generally, on any geostructure partly interacting with an air environment. Hence, the objectives of this chapter are to reply to the following questions: what type of data can we get from a TRT on walls? How can we monitor the energy gostructure behavior? How does the wall interact with its surrounding environments, and particularly with the tunnel? How should we execute the test? Which preliminary prescriptions can we recommend based on this experience?

## 7.2 Introduction

Thermal activation of shallow underground infrastructures may represent an important source for thermal energy for the built environment. Currently, a rising number of installations employing

shallow geothermal technologies (e.g., energy geostructures, EG) are recorded around the world (Di Donna et al. 2017). In EG, the dual role of geostructures is enhanced: they involve a structural support and a geothermal heat exchanger role. EG have proven to be an efficient and renewable solution for heating/cooling of the built environment (Sutman et al., 2020). The use of thermo-active shallow underground infrastructures (i.e., underground energy infrastructures, UEI) has recently been tackled by the scientific community and shows a promising future. Examples of UEIs could be, but not limited to: underground circular and cut-and-cover tunnels used for transportation and/or services, underground train stations, trenches, sewers. Within UEIs, heat exchangers (i.e., plastic pipes) can be secured to the steel cage of the reinforced concrete geostructure, and they exchange heat with the surrounding materials. Typical geostructural elements that can be thermally-activated within UEIs are: vertical walls (Bourne-Webb et al., 2016), base slabs and the tunnel lining (Cousin et al., 2019).

The knowledge on UEIs is lacking on feedbacks from real monitored installations, whose experience could be critical to fully understand the details on the ongoing multiphysical processes and to propose design optimization strategies and guidelines for future installations. To this regard, a limited number of field experiments are available in the literature. Attempts on understanding the thermal behaviour highlighted that heat exchangers configuration may play a crucial role and wall-tunnel thermal interactions could be non-negligible (Xia et al., 2012; Nicholson et al. 2014). Different thermal performances for energy walls and slabs were highlighted, with the former performing better than the latter (Sterpi et al., 2017, 2018, 2020) but important differences on the thermal behavior could be envisaged because of the different definitions of the air thermal environment. As per the thermomechanical behavior, low-magnitude thermally-induced deformations were registered at the Lainzer U2 line in Vienna (Brandl, 2016) but the rationale for thoroughly describing thermomechanical behavior still remains unclear.

Despite the knowledge acquired from the literature review, more in-depth investigations are required. Firstly, the determination of the thermal potential of UEIs remains unclear. Secondly, the thermal exchanges among the involved materials (i.e., geostructure, soil, air, heat carrier fluid and pipes) must be clearly assessed. Thirdly, the thermomechanical response of the energy geostructure has to be qualitatively and quantitatively detailed.

This chapter deals with the execution of a TRT on an UEI, highlighting fundamental hydrothermal aspects on the UEI operation. The objectives are: (i) to determine the thermal characteristics of the involved materials; (ii) to understand the thermal behavior of the UEI; (iii) to detail the wall-tunnel air interactions during the test; (iv) to determine the suitability and identify a procedure for executing TRTs on UEIs. Additional insights (e.g., thermomechanical behavior, determination of thermal potential) will be further expanded in Chapter 8.

To meet the objectives, an experimental in-situ campaign was undertaken. In the following, the experimental setup details are firstly presented, constituting the baseline for all the experimental results presented in this thesis. Results of the TRT executed in 2019 are secondly presented and discussed. A 3D,

finite element, numerical model, validated against the experimental results, is used to interpret the experimental results. Concluding remarks are eventually reported.

### 7.2.1 Energy geostructures implemented at the CEVA Lancy-Bachet underground train station (Geneva, Switzerland)

The tested site is located in the southwestern part of the city of Geneva, Switzerland (Figure 7.1). A new railway line that connects Geneva to Annemasse (France) has been recently constructed. One of the train stations, Lancy-Bachet, is equipped with energy walls and slabs presenting a total thermo-active surface of around 5000 m<sup>2</sup>. The construction is being finalized and consequently the UEI has never been exploited. The Lancy-Bachet train station is located at the entrance portal of the underground portion of the railway line. The train station represents the entrance point of the underground tunnel portion, going in the direction of Annemasse. The station structure is made of two underground levels (Figure 7.2) where the bottom one (level -2) is the railway level and the top one (level -1) is a technical room. The train station entrance is at the ground level (level 0).

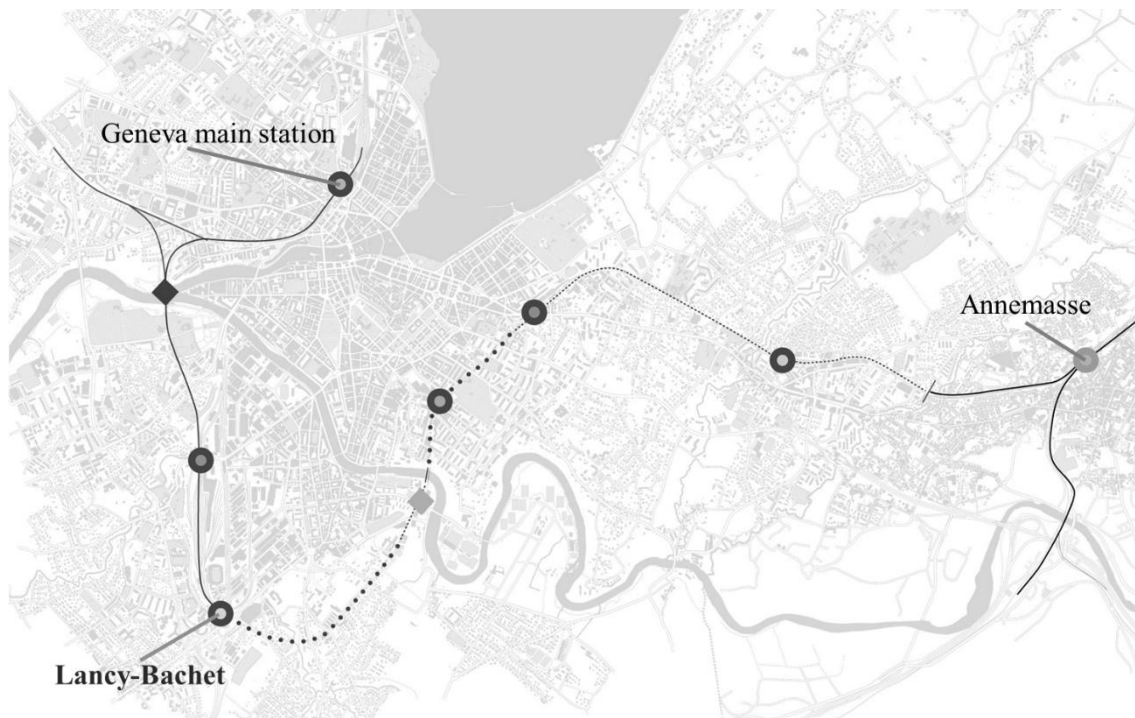


Figure 7.1 Plan view of the new railway line with location of the UEI at Lancy-Bachet (source: [www.ceva.ch/](http://www.ceva.ch/))

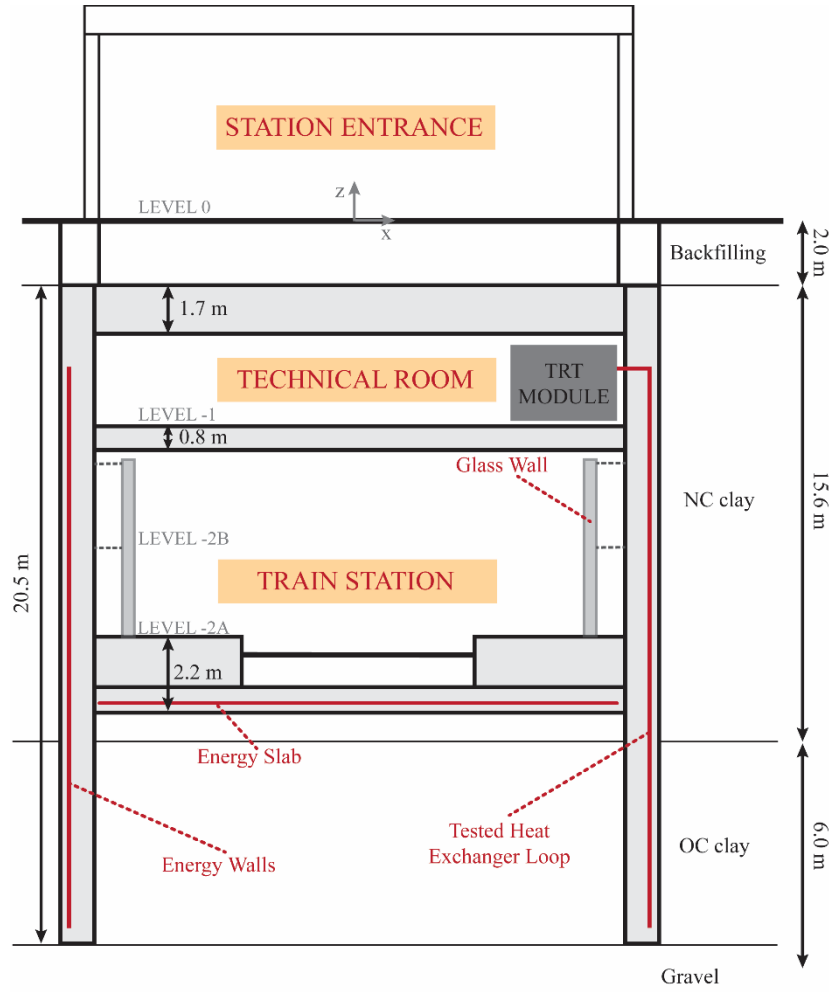


Figure 7.2 Cross section of the Lancy-Bachet underground train station with indication of the heat exchanger locations

All the vertical walls surrounding the train station as well as the base slab of level -2 are equipped with heat exchangers. The vertical walls are equipped with one U-loop every 2.5m in the tunnel longitudinal direction, with a pipe spacing of  $a_w = 0.25$  m and a pipe external and inner diameter  $\phi_{p,ext} = 25$  mm,  $\phi_{p,in} = 23$  mm, respectively. The total length of each heat exchanger circuit in the walls is  $L_{p,w} = 36$  m. The heat exchangers are installed inside the concrete geostructure, attached to the reinforcement cage and are placed at a distance  $c_{f,ws} = 0.20$  m from the wall-soil interface. The walls are  $t_w = 1$  m thick, which means that the heat exchangers are placed at a distance  $d_{pw} = 0.80$  m from the wall-air interface in the tunnel. At level -2, an architectural element composed by a glass wall sustained by a steel structure is installed and partially separates the tunnel in two regions (Figure 7.2). The slab is equipped with heat exchanger loops having a pipe spacing of  $a_s = 0.5$  m. Each loop is installed within a surface  $A_{p,s} = 16 \times 6 = 96$  m<sup>2</sup>. The total heat exchanger length in the slab per each circuit is  $L_{p,s} \cong 200$  m. The heat exchangers are installed at a distance  $c_{f,ss} = 0.40$  m from the slab-soil interface. The slab is  $t_s = 2.2$  m thick, which means that the heat exchangers are placed at a distance  $d_{ps} = 1.75$  m from the slab-air interface in the tunnel. Every heat exchanger circuit in the wall and in the slab is

connected in parallel to the main pipe connections. The whole piping system is eventually collected in a technical room that will serve as thermal central for the future thermal exploitation of the EI. The tested portion is composed by a single heat exchanger U-loop of the wall. During the test period, the train station was not in operation yet, except of sporadic train circulation tests (Section 7.4.1).

The soil profile (Figure 7.2) is characterized by a backfilling layer in the top 2.0 m, a layer of normally-consolidated clay until a depth  $z = -17.6$  m, a layer of slightly overconsolidated clay until  $z = -23.6$  m, and by a layer of compacted gravel at the bottom. The groundwater table is located in the compacted gravel layer (i.e., below the bottom of the wall). The soil deposit is considered to be fully saturated by capillary rise in the clayey geomaterials.

### 7.3 Materials and methods

In this section, the experimental setup is firstly presented. The details of the numerical model used for the interpretation of the results are eventually reported.

#### 7.3.1 Details on the experimental setup

The experimental equipment is installed at two different levels: -1 and -2, which are separated and not communicating with one another. The heat exchangers are connected to the heating module at level -1, while a thermomechanical monitoring system is installed at level -2.

The equipment installed at level -1 is the heating module, called the TRT (i.e., Thermal Response Test) module, developed and presented by Mattsson et al. (2008), which is connected to the heat exchangers circuit (Figure 7.3 (a)). It consists of a flight case of dimensions 60cm x 30cm x 70cm composed by a heating unit and of a dedicated monitoring system which measures: (i) the heat carrier fluid (HCF) temperature and pressure at the inflow and outflow of the heat exchangers; (ii) the internal and external temperature of the module; (iii) the fluid flow inside the heat exchangers; (iv) the electrical consumption. The TRT Module applies a constant thermal power to the heat exchangers, as the one usually employed for standard TRT tests (Gehlin & Hellström, 2000; Gehlin, 2002; Laloui et al., 2006; Mattsson et al., 2008; Sanner et al., 2005).

The equipment installed at level -2 is composed by a thermomechanical monitoring system (Figure 7.3 (b)), specifically designed for this tested site. Behind the glass wall, level -2 is composed of two different sub-levels (named -2A and -2B, as from Figure 7.3 (b)) which are separated by means of a steel grid (i.e., not a solid separation element, but air can pass through it). The design of the monitoring system has been done to allow the measurement of key parameters that govern the heat fluxes and the hydro-thermal heat exchanges between the EG and the tunnel air as well as the mechanical behavior of the tunnel intrados. It allows having a real-time monitoring of: (i) the air temperature and (ii) the wind



velocity in the tunnel, (iii) the structural deformations at the wall intrados. Air temperature and velocity are measured through temperature sensors and anemometers placed at two different locations (Figure 7.3 (c) and (d)). The first one is at the top of the glass wall (i.e., level -2B), giving a measure of the tunnel environment. The second location is at level -2B, monitoring the hydrothermal environment behind the glass wall. The deformation sensors (i.e., 11, uniaxial, vibrating wire strain gauges) are screwed to the wall intrados and they are installed, alternatively, in the vertical and longitudinal directions (Figure 7.3 (e)). The strain gauges read deformation and temperature, hence it is possible to have a measurement of the air temperature distribution in the immediate vicinity of the wall intrados. All the instruments are connected to a datalogger, installed at level -2B. Data acquisition is done manually. Since the geostructure was already partly constructed and the ground surface was a construction site, there is no possibility to install any monitoring system in the soil and inside the wall.

The details of the sensors employed in the monitoring system at level -2 are reported in Table 7.1.

Table 7.1 Details of the sensors employed in the experimental setup for monitoring level -2

	Temperature	Deformation	Wind speed
Name	Roctest/Smartec	Roctest/Smartec	Campbell Scientific
	TH-T	SM-5	Windsentry 03101-L
Range	$-20^{\circ}\text{C} \div +80^{\circ}\text{C}$	$3000 \mu\epsilon$	$0.5 \text{ m/s} \div 50 \text{ m/s}$
Accuracy	$\pm 0.5\% \text{ F.S.}$	$\pm 0.5\% \text{ F.S.}$	$\pm 0.5 \text{ m/s}$
Resolution	$0.1^{\circ}\text{C}$	$1 \mu\epsilon$	$0.05 \text{ m/s}$
Sampling time	5 min	5 min	15 s

A TRT has been conducted following the available standards (GSHPA, 2012). An initial phase of fluid circulation lasted 2 days, followed by the heating phase at a constant thermal power  $Q_{th} = 1 \text{ kW} = 45 \text{ W/m}$  of wall depth, for 24 days.

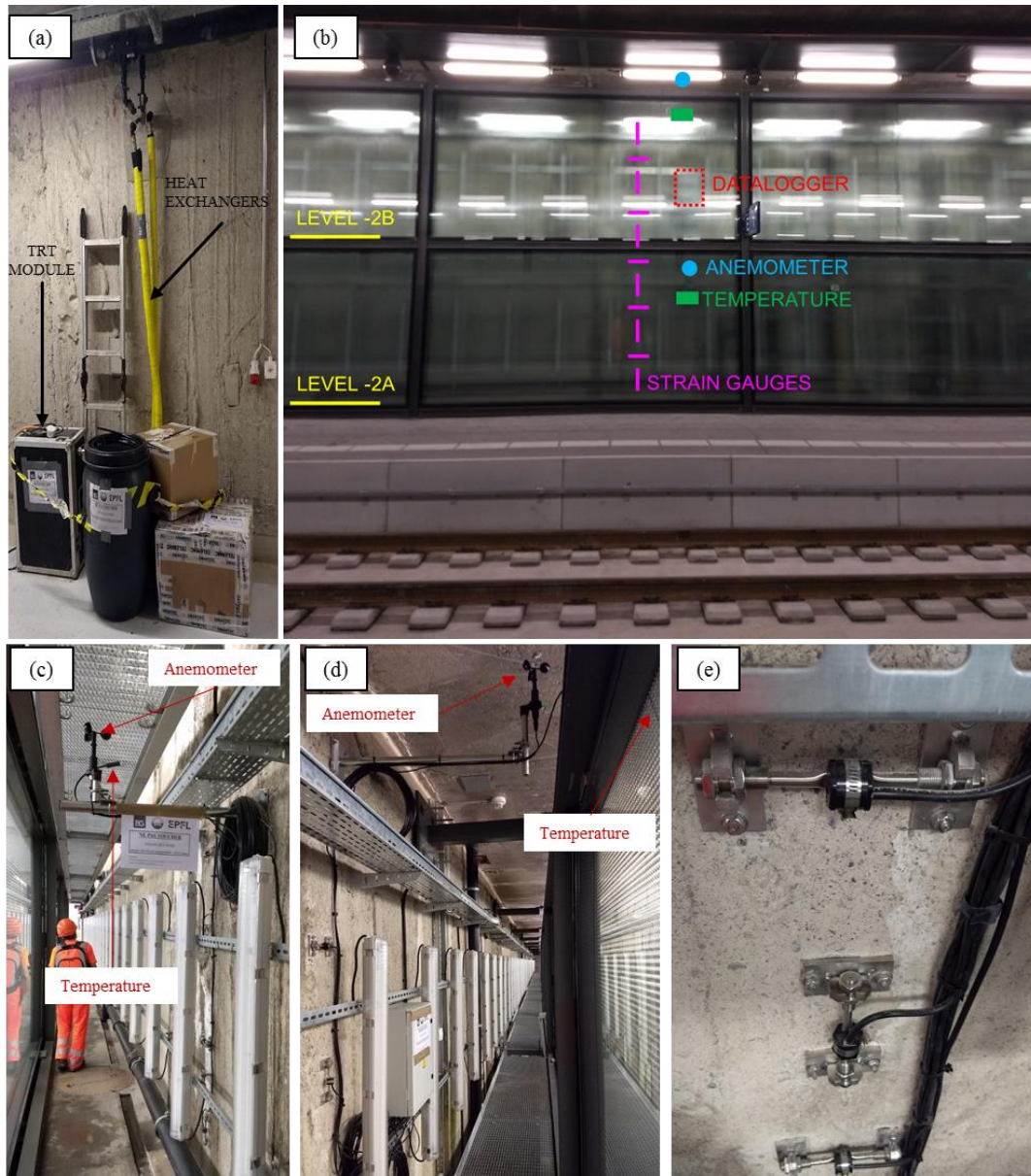


Figure 7.3 Details of the equipment at: (a) level -1; (b) level -2; (c) temperature sensor and anemometer at position -2A; (d) temperature sensor and anemometer at position -2B; (e) partial view of the strain gauges

### 7.3.2 Features of the numerical analyses

Given the complexity of the problem (i.e., geometry) and the lack of literature related to the use of analytical and/or semi-analytical models for interpreting in-situ tests on energy walls and more generally to UEI, numerical analysis is employed. The 3D, hydro-thermal, finite element model used to simulate the in-situ test and to interpret the results, is built using the commercial software Comsol Multiphysics (COMSOL Inc., 2018). The objectives for the numerical analysis are: (i) to determine the thermal characteristics of the materials involved in the heat exchanges; (ii) to give a comprehensive overview of the thermal behaviour of the UEI, highlighting the soil temperature distribution before and

during the test, the volume of materials affected by the thermal exchanges, the direction and magnitude of the wall-tunnel and wall-soil heat fluxes. Some of the parameters measured experimentally are input parameters for the numerical model (e.g., inflow temperature and velocity, boundary conditions), while others are back analysed to calibrate the numerical model to best fit the experimental data (i.e., outflow fluid temperature, thermal characteristics of materials).

The model dimensions are 186 m × 55 m × 100 m in the x,y,z coordinates, respectively (Figure 7.4).

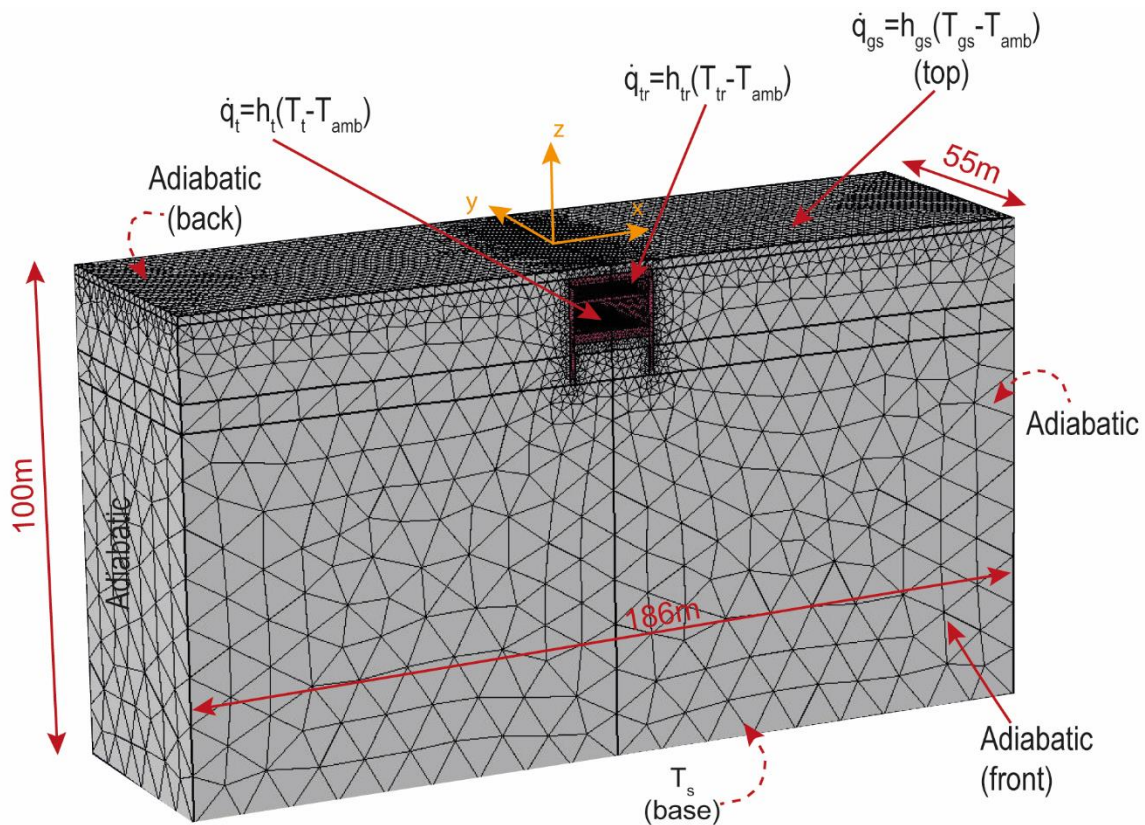


Figure 7.4 Geometry of the numerical model with indication of the boundary conditions

The heat exchangers are modelled following the technical details of the geostructural design. The soil and structure are modelled as fully saturated porous materials. The groundwater is considered in stationary condition with null velocity, hence convective heat exchanges within the soil are neglected. The mathematical formulation for the numerical model is reported in the Appendix A. The model simulates either the initial phase of fluid circulation, allowing to determine the temperature distribution in the materials, as well as the heating phase.

The thermal boundary conditions (Figure 7.4) are as follows: the two vertical surfaces at the sides are adiabatic (i.e., the far field temperature distribution with depth is not affected by the presence of the tunnel and the surface temperature affects the top 15 m, simulating realistic far-field conditions); the front and rear vertical surfaces are adiabatic; the bottom horizontal surface is set to a constant temperature,  $T_s$  (i.e., the soil temperature); the ground surface, technical room and tunnel air interfaces are

simulated by means of convective boundary conditions (i.e., flux conditions,  $\dot{q}_i$ ), setting a coefficient for convective heat transfer,  $h_i$ , and an air temperature  $T_i$ . The determination of  $h_i$  and  $T_i$  are set depending on the experimental monitored data. The non-isothermal fluid flow in the heat exchangers is simulated by means of imposing the experimental time history of fluid inflow temperature and velocity, while the outflow fluid temperature is used to calibrate the model with respect to the experimental results. The solver accounts for a temperature initialization phase, followed by the simulation of the TRT.

## 7.4 Results and discussion

The experimental results are firstly presented. The calibration, validation of the numerical model is then proposed together with a global interpretation of the experimental results. The suitability and execution details on using TRT for detecting the behaviour of UEIs are eventually reported.

### 7.4.1 Experimental results

The results from the TRT module (i.e., at level -1) are firstly presented, followed by the ones from the monitoring system in the tunnel (i.e., at level -2).

The test starts with a fluid circulation phase (i.e., no heating), which lasted 2 days. The duration was chosen after running a preliminary test a few weeks in advance, with a duration of one week, that showed no fluid temperature fluctuations on a day/night basis. The heat injection phase at a constant power  $Q_{th}$  lasted 24 days, which is considered enough to reach the steady state. During the fluid circulation phase, the fluid temperature reached the constant value of  $T_{f,exp} = 17.34$  °C, which represent the average temperature of the wall subjected to the effects linked to the soil, tunnel and ground surface temperatures (Figure 7.5). This value is higher with respect to the average soil temperature values recorded for European climates (Mattsson et al., 2008; Pahud & Matthey, 2001; Rotta Loria & Laloui, 2017a), suggesting that the soil temperature distribution could be affected by the presence of the tunnel. During the heating phase, the shape of the fluid temperature rapidly increases. Two distinct portions are clearly distinguished: an initial transient phase presenting a duration of around  $5 \div 7$  days, is followed by a steady state condition, where the fluid temperature slowly increases with time (Figure 7.5). The temperature difference between the inflow and the outflow remains constant throughout the heating phase and it is equal to  $\Delta T_f = 0.6$  °C. The air temperature inside the technical room is manually recorded by using a thermometer during the fluid circulation phase,  $T_{tr} = 21$  °C and it does not show any day/night fluctuation.

The monitoring system in the tunnel records the air temperature, the wind velocity and the intrados deformations.

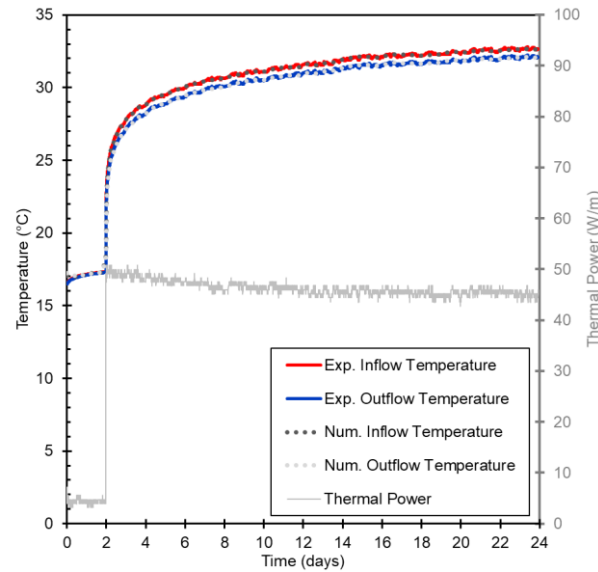


Figure 7.5 Experimental data from the TRT Module (fluid temperature and thermal power) with fitting of the numerical results

Air temperature and wind speed are shown in Figure 7.6. Air temperature shows a periodic behaviour on a daily basis, with a maximum difference between day and night of around  $7^{\circ}\text{C}$  (on date 06.08.2019). A difference between the two measurements (i.e., at levels -2A and -2B, respectively) is notable: the maximum difference is  $4.9^{\circ}\text{C}$  while the minimum one is  $0.3^{\circ}\text{C}$ . Average air temperature values during the whole test duration are  $20.2^{\circ}\text{C}$  and  $18.6^{\circ}\text{C}$  for the positions at levels -2A and -2B, respectively. Such measurements were compared with the meteorological data provided by MétéoSuisse at the Genève-Aéroport measurement station, which is the closest to the site. The tunnel air temperature recorded at level -2B shows a close correlation with the meteorological data: the average day and night temperature differences are  $+14.5\%$  and  $-19.2\%$ , respectively. The tunnel temperature is lower during the day while it is higher during the night with respect to the external air temperature. Such strong correlation among the tunnel and the external air temperature is induced by the closed distance between the UEI and the tunnel entrance. The UEI is located at the thermal and hydrodynamic entrance region (Laloui & Rotta Loria, 2019; Peltier et al., 2019), which means that the tunnel temperature distribution is still under development within the tunnel length.

Air speed shows a highly scatter behaviour. The anemometer at level -2B shows higher and more frequent recordings with respect to the one at level -2A. Such difference is due to the presence of the glass wall that strongly modifies the aerodynamics of the environment. Maximum recorded values reached  $2.3 \pm 0.5$  m/s at level -2B and  $1.5 \pm 0.5$  m/s at level -2A. As presented in Table 7.1, the sensors are not able to record air speed lower than 0.5 m/s. Being the recorded values very scatter, it follows that for around 96% of the time, the wind speed was  $v_w < 0.5$  m/s. Some train circulation tests were ongoing at the moment of the installation of the sensors, and an increase of air speed due to the train passage was recorded.



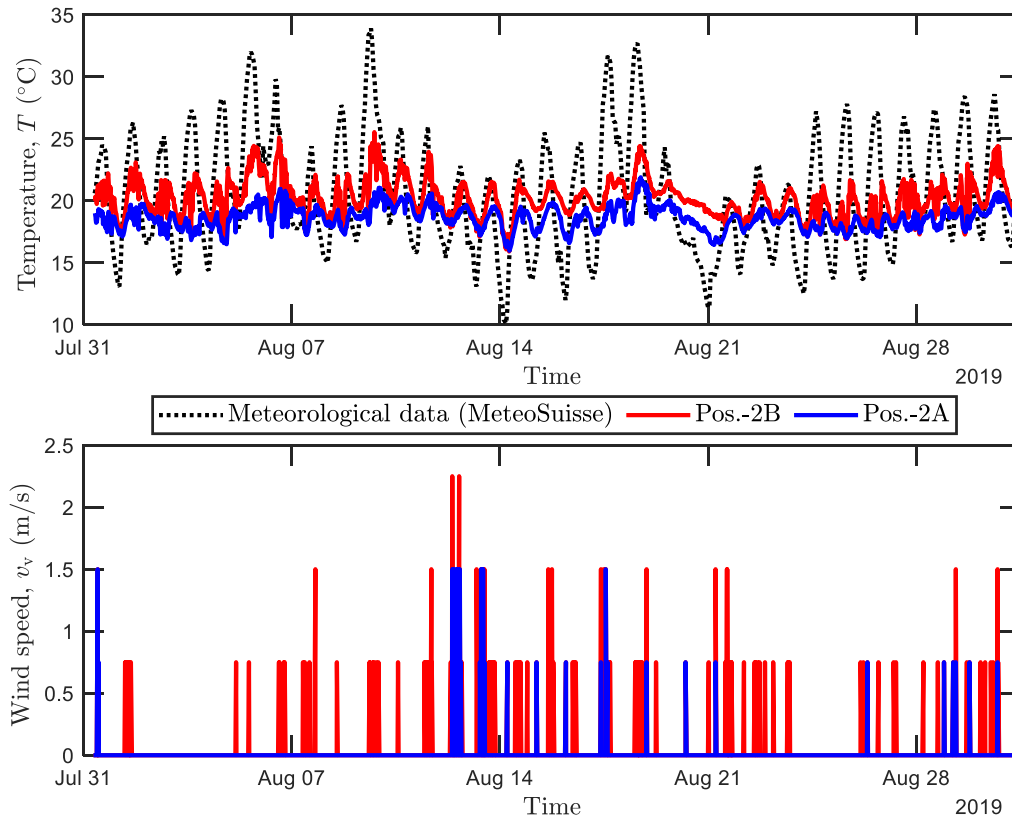


Figure 7.6 Experimental data for temperature and wind velocity during the test execution

The temperature recorded by the strain gauges give a global view of the temperature distribution at the wall-air interface along the tunnel wall height,  $h$  (Figure 7.7). Average values show that the intrados temperature increases with height (i.e., the shallower the hotter). The average temperature difference between the recordings at the top and bottom is  $2.5 \pm 0.5^\circ\text{C}$ . The envelopes of maximums and minimums per each sensor show differences of  $5.0 \pm 0.5^\circ\text{C}$  and  $2.0 \pm 0.5^\circ\text{C}$ , respectively. The temperature recorded at the wall-air interface is higher with respect to the one recorded at levels -2A and -2B, respectively.

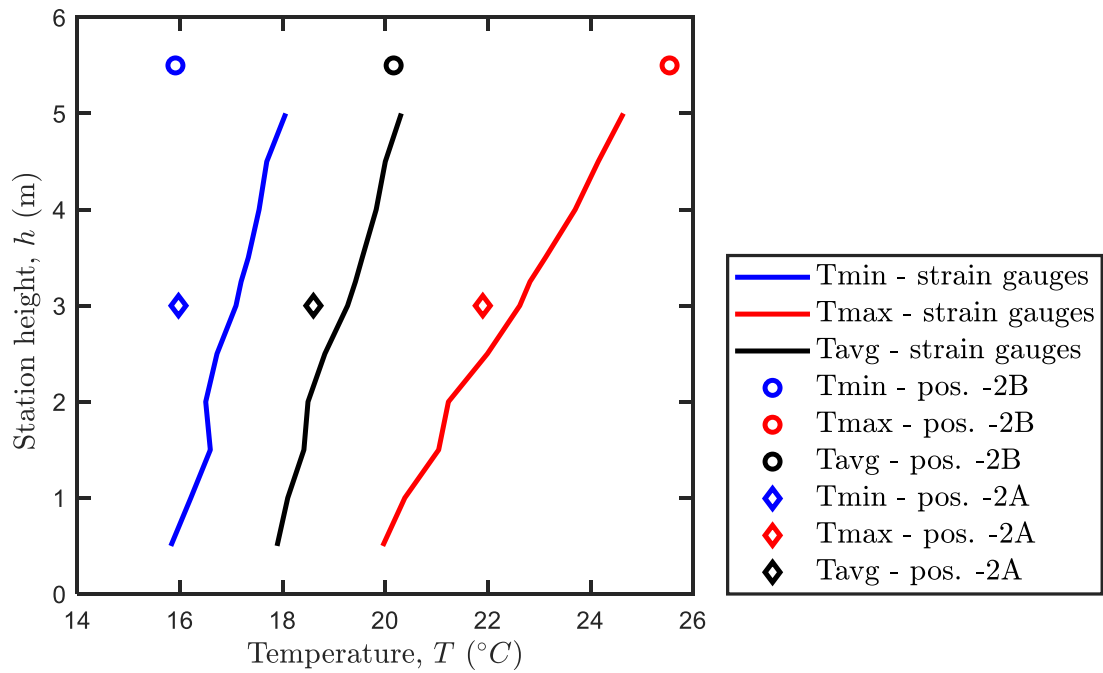


Figure 7.7 Comparison among temperature recorded by the strain gauges and by the temperature sensors

#### 7.4.2 Numerical modelling: calibration, validation and interpretation of the experimental results

The simulation of the fluid circulation phase needs to start with a realistic temperature profile in the materials. For this reason, the model is initialized at a uniform temperature,  $T_s$  (i.e., the undisturbed soil temperature), and a 10-year transient analysis takes place. Such duration was chosen to ensure to have the model response independent to the initial conditions. After 6 years of simulations, the model responds periodically, hence a duration of 10 years is considered sufficient to realistically initialize the model. The temperature profiles for the boundary conditions during the initialization phase are shown in Figure 7.8 and are described here. The surface air temperature was evaluated based on the monthly average temperature over the last 10 years measured by MétéoSuisse at the Genève-Aéroport meteo station. The measured technical room air temperature presents low seasonal variations because the room is a non-ventilated, yet very voluminous, space. The tunnel air temperature was calibrated on experimental data for the period from August 2019 to March 2020 (details at section 8.3.1). Further details on these aspects are presented at section 8.3.

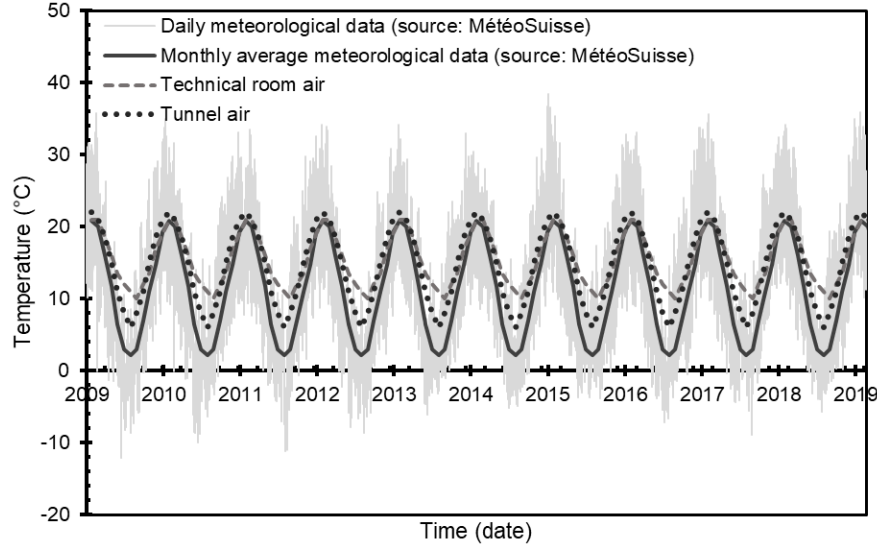


Figure 7.8 Temperatures of the air boundary conditions used for the numerical model initialization

Ground surface, technical room and tunnel are all modelled as convective boundaries (i.e., as from Figure 7.4:  $\dot{q}_{gs}$ ,  $\dot{q}_{tr}$ ,  $\dot{q}_t$ , respectively). It means that the heat flux,  $\dot{q}_i$ , at each boundary is:

$$\dot{q}_i = h_i(T_i - T_{amb}) \quad (7.1)$$

where  $h_i$  represents the convective heat transfer coefficient,  $T_i$  the air temperature and  $T_{amb}$  the temperature of the solid.  $h_i$  is linked to the air velocity and it was calibrated following the available correlations proposed by (Guo et al., 2011; Lee et al., 2009; Peltier et al., 2019).  $h_i$  was chosen as:  $h_{gs} = 10$  W/m<sup>2</sup>/K,  $h_{tr} = 3$  W/m<sup>2</sup>/K,  $h_t = 4$  W/m<sup>2</sup>/K, for the ground surface, technical room and tunnel, respectively; the first representing a wind speed of around 1 m/s and the latter as “quasi-zero”. For the heat exchangers, the experimentally-recorded inflow tangential fluid velocity,  $u_f = 0.8$  m/s and the time history of inflow temperature (Figure 7.5) were imposed. The internal pipe diameter was set to  $d_{int} = 25.4$  mm having a thickness of  $t_p = 2.3$  mm and a thermal conductivity of  $\lambda_p = 0.4$  W/m/K (i.e., high density polyethylene).

$T_s$  was varied to obtain an average temperature in the tubes equal to that measured by the TRT module during the water circulation phase. This correspondence takes place for  $T_s = 14.6^\circ\text{C}$ , which is in line with the expected values for the European climate.

This numerical analysis shows that the temperature profile in the vicinity of the geostructure is strongly affected by the boundary conditions. Particularly, a volume of soil that extends up to a few meters around the geostructure is affected by a temperature difference  $\geq 1^\circ\text{C}$  between summer and winter. The soil temperature is perturbed up to a distance of around 30 m from the tunnel. At larger distances, the soil temperature distribution is the one typical of soils in free conditions: the effect of ground surface is present in the top 15 m while at deeper depths the temperature remains constant and equal to  $T_s$ . The temperature of the HCF is affected by seasonal effects. Before the start of the heating phase of the TRT,



the average fluid temperature is  $T_{f,num} = 17.30^\circ\text{C}$  which is very closed to the experimental value,  $T_{f,exp} = 17.34$ .

The second phase of the numerical analysis simulates the TRT during the heating phase at constant power. The ground surface and tunnel air temperatures are the time series measured during the test (Figure 7.6). The technical room air temperature was measured equal to  $T_{tr} = 21^\circ\text{C}$ .

The first objective was to estimate the thermal characteristics of the involved materials (i.e., soil and concrete). An issue related to the unicity of the solution exists: having only one experimental result, it is impossible to uniquely determine thermal conductivity for soil and concrete. Concrete thermal conductivity could realistically vary between  $\lambda_c = 1.0 \div 1.7 \text{ W/m/K}$  (Asadi et al., 2018; Bourne-Webb et al., 2016; Valore, 1980; Zhang et al., 2015). Soil thermal conductivity (i.e., normally-consolidated clay and slightly over-consolidated clay in saturated conditions) could realistically be evaluated as  $\lambda_s = 1.0 \div 2.5 \text{ W/m/K}$  (Laloui & Rotta Loria, 2019; Vulliet et al., 2016). Thermal capacity and density are fixed to:  $Cp_c = 850 \text{ J/kg/K}$ ,  $\rho_c = 2722 \text{ kg/m}^3$ ,  $Cp_s = 1000 \text{ J/kg/K}$ ,  $\rho_s = 2011 \text{ kg/m}^3$  for concrete and soil, respectively. A sensitivity analysis on thermal capacity effects was done, showing little variations of the EG thermal behaviour. Concrete thermal conductivity is here fixed to different values encompassing the aforementioned range of expected values and soil thermal conductivity is evaluated to best match the experimental results (Table 7.2). The comparison between the experimental and numerical results is performed at the outflow fluid temperature,  $T_{f,out}$ , which is known, and it is not an input parameter of the numerical model. The error is evaluated as  $T_{f,out,num} - T_{f,out,exp}$ , and it is reported at Table 7.2. Closed agreement between the experimental and numerical results is reported. Seasonal variations of soil and concrete thermal conductivities could, at this stage, not be excluded as wetting and drying processes in all the porous materials could saturate/desaturate the porous media consequently to infiltrations from the ground surface caused by rainfalls, snow or dry periods. For this reason, experimental tests during winter period are planned, as reported at section 8.3.3. In the following, the numerical results for  $\lambda_c = 1.7 \text{ W/m/K}$  and  $\lambda_s = 1.4 \text{ W/m/K}$  are reported as it represents the best fitting to the experimental results.

Table 7.2 Evaluation of thermal conductivity for concrete and soil: determination of soil thermal conductivity to best match the experimental results for a given concrete thermal conductivity

Concrete thermal conductivity $\lambda_c \left( \frac{\text{W}}{\text{m K}} \right)$	Soil thermal conductivity $\lambda_s \left( \frac{\text{W}}{\text{m K}} \right)$	Absolute numerical-experimental error at steady state ( $^\circ\text{C}$ )
1.7	1.4	0.014
1.5	1.9	0.026
1.2	2.1	0.044
1.0	2.4	0.045

The second and third objectives introduced at section 7.2, relates to giving a comprehensive overview of the thermal behaviour of the UEI, which is discussed in terms of: (i) temperature profile of the materials upon heating, (ii) heat fluxes, (iii) evolution of bulk temperature in the heat exchangers and (iv) intrados tunnel temperature.

Figure 7.9 reports the evolution with time of the temperature distribution within and around the UEI. At the beginning of the heating phase, only the concrete is affected by thermal exchanges. The soil is then strongly affected by thermal exchanges because of the vicinity of the heat exchangers: the heat exchangers-soil heat flux remains quasi-constant throughout the test. As time passes, steady state conditions approach and the soil volume involved in the heat exchanges increase. At the end of the test, the model suggests that a soil portion of thickness 1.5 m around the energy wall is affected by a temperature variation  $> 1^{\circ}\text{C}$  with respect to its initial temperature distribution.

The bulk temperature of the HCF is time dependent. During the initial phase of heating, the temperature in the heat exchangers abruptly rises. Approaching towards the steady state, the HCF temperature distribution becomes quasi linear and remains unchanged throughout the test.

The direction and intensity of the heat fluxes as well as the temperature distributions in the UEI during and after the test are here presented. At the beginning of the heating phase, the temperature difference between the heat carrier fluid (HCF) and the soil was higher than the one between the HCF and the tunnel. Consequently, the heat flux was dominated by the HCF-soil component. The temperature distribution inside the concrete geostructure evolves with time. At the beginning of heating and during a portion of the transient condition, the intrados temperature is higher than the HCF, it follows that the heat flux is directed from the tunnel towards the HCF. The tunnel, in this phase, acts as a thermal resistance rather than a conductor. This is visible in Figure 7.9(b) and Figure 7.10 where a positive heat flux denotes a flux vector directed towards the positive x-axis (i.e., from the wall towards the soil). The tunnel is located at depths (i.e., z coordinate) between  $-7.5$  m and  $-14$  m and the positive heat flux with magnitude of around  $+7.5 \text{ W/m}^2$  is clearly visible. When the HCF temperature increases, it becomes higher than the tunnel, hence the heat flux reverses. It reaches its stationary condition at around  $-5 \div -10 \text{ W/m}^2$  (Figure 7.9(c,d) and Figure 7.10). At the wall extrados (Figure 7.9(b,c,d) and Figure 7.10), the heat flux abruptly increases and then it remains constant throughout the whole heating phase at around  $25 \div 35 \text{ W/m}^2$ , which is 3  $\div$  5 times higher than the one at the wall intrados.

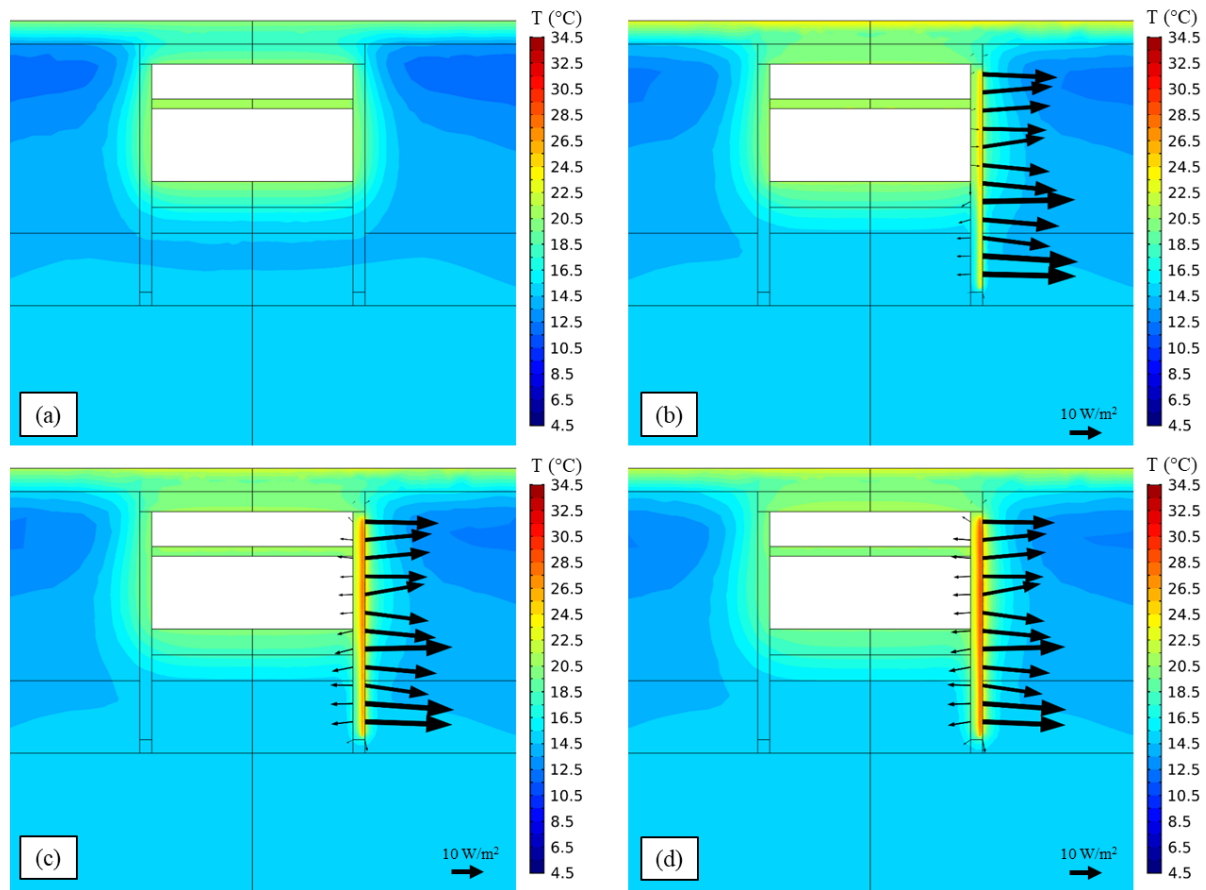


Figure 7.9 Temperature contour plot (a-d) with indication of the heat flux at the EW intrados and extrados (b,c,d only) for the following time steps: (a) before the test, (b) after 1 day of test, (c) at the end of the transient phase and (d) at the end of the test

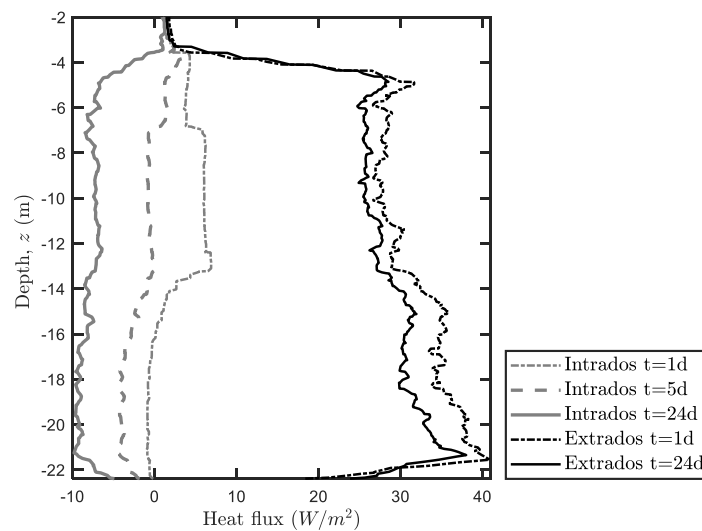


Figure 7.10 Magnitude of the heat flux at the wall intrados and extrados

Figure 7.11 shows the intrados temperature at two different dates: 21/08/2019 and 29/08/2019 (i.e., after 16 and 24 days of heating). Thermal photos were taken and compared with the numerical results, showing closed agreement. The longitudinal thickness of the thermally affected zone is of 1.6 m and 2.0 m for the two dates, respectively. The intrados temperature varies between  $20 \div 22^\circ\text{C}$  on 21/08/2019, and between  $20 \div 23^\circ\text{C}$  on 29/08/2019. It follows that the temperature distribution inside the wall is nonuniform: it shows a maximum located in the vicinity of the HCF and affecting the whole wall thickness and it decreases until a minimum point at the wall-tunnel interface.

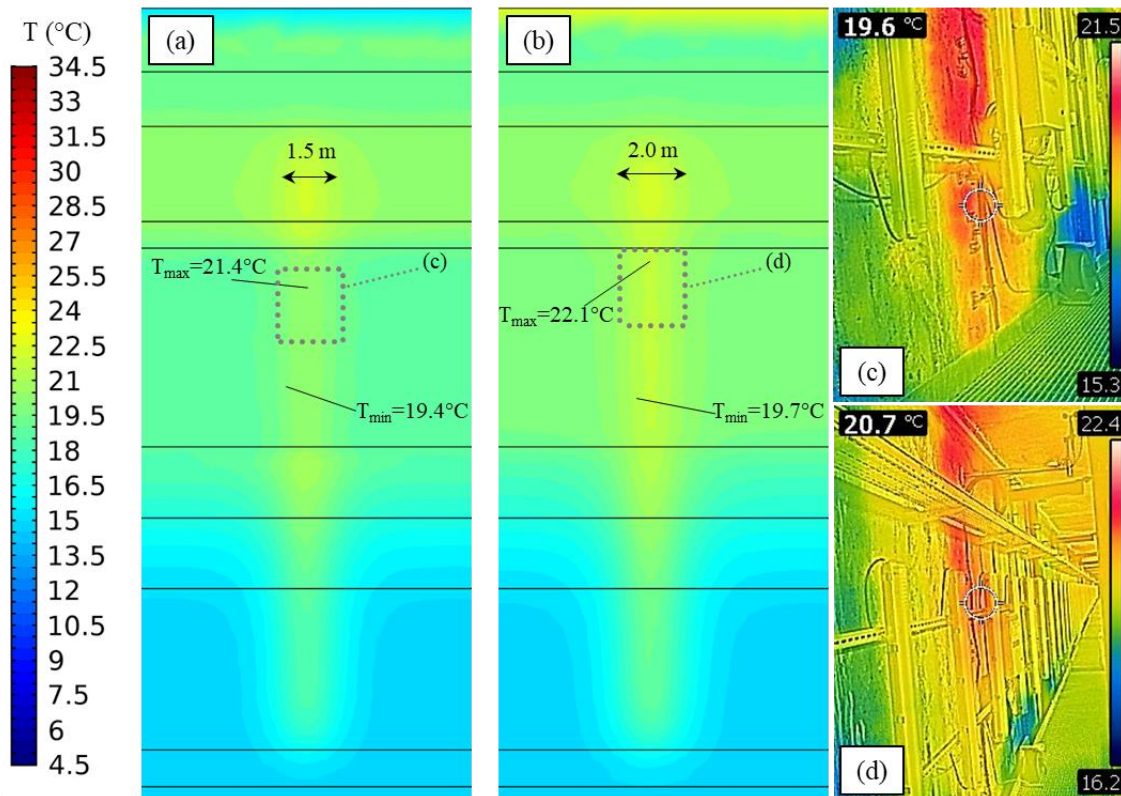


Figure 7.11 Comparison among numerical (a,b) and experimental (c,d) results related to the wall intrados temperature: (a) numerical temperature contour plot at the wall intrados on date 21/08/2019, (b) numerical contour plot at the wall intrados on date 29/08/2019, (c) thermal photo taken on date 21/08/2019, at level -2B, (d) thermal photo taken on date 29/08/2019, at level -2B

## 7.5 Is TRT suitable for underground energy infrastructures?

This section discusses the details on the execution of TRTs applied to UEIs and, more generally, to any geostructure partially in contact with an air interface. No literature evidence on this topic is available. Moreover, no feedbacks, execution manuals nor legislative standards for the test execution and data interpretation are available.

TRT-type heating input was extensively used to determine the soil thermal characteristics for vertical heat exchangers (Gehlin 2002; Mattsson, Steinmann, and Laloui 2008) and energy piles, and to detect the thermomechanical behaviour of the EG (Mimouni & Laloui, 2015; Rotta Loria & Laloui, 2017a, 2017b). Consequently, the first challenge was to understand what knowledge the execution of TRT on UEIs could bring, knowing that the focus should be given on determining the thermal behavior and potential of the UEI. Based on the foregoing presented results, the main feedbacks are reported here.

Firstly, one should verify that the following prescriptions are fulfilled when carrying out the test: (i) the fluid circulation phase should last long enough such that possible day/night fluid temperature variations are recorded; (ii) the heating phase should last long enough such that the steady state condition within the heat exchangers is successfully reached. To this regard, the typical heating duration used for vertical heat exchangers (i.e. one week) should be taken as a lower boundary case. The longer and/or the complex the heat exchanger circuit, the longer the heating phase should be to ensure to reach the steady state; (iii) the interpretation of the results requires a detailed knowledge of the thermal environments in the vicinity of the EG. The definition of the initial temperature profile within and around the UEI is crucial; (iv) if the thermal environments around the UEI are not known with enough accuracy, the installation and use of a dedicated in-situ monitoring system is strongly advised; (v) the interpretation of the results should account for all possible heat exchange modes taking place within and around the UEI. Consequently, the use of numerical models seems to be the most accurate tool, in view of the geometry complexities. Attempts of determining the soil thermal conductivity employing analytical models (Carslaw & Jaeger, 1952; Mattsson et al., 2008) were done in the case presented in this study. The strongly transient wall-tunnel heat exchanges made the heat flux directions and magnitude of very difficult definition, leading to the need of using numerical models to fully understand the ongoing thermal processes.

Finally, it can be concluded that this in-situ test allows for replying to the challenge related to the determination of the thermal characteristics of the involved materials if a correct assessment and monitoring, if needed, of the relevant boundary conditions is thoroughly done.

## 7.6 Concluding remarks

This chapter summarizes the results on the first part of the experimental campaign related to in-situ testing of an energy wall at the Lancy-Bachet underground train station in Geneva, Switzerland. A TRT has been executed on a portion of the thermo-active elements during the final steps of construction (i.e., geostructural construction was finished, but the railway was not in operation yet). A dedicated monitoring system was designed and installed in the tunnel. A numerical model (i.e., hydro-thermal) was validated against the experimental results and used to interpret the thermal response of the UEI.

The experiment showed that there is a closed relation between the tunnel and the surface temperature, with limited wind effects inside the tunnel. The thermal input in the heat exchangers induces a temperature difference of around 15°C, which induces a non-uniform temperature distribution inside the EW. The numerical results show that the undisturbed soil temperature was  $T_s = 14.6^\circ\text{C}$  and a sensitivity analysis was performed to calibrate the numerical model on the experimental results. The determination of the initial temperature profile in the materials was paramount: an accurate determination and monitoring of all boundary conditions (i.e., ground surface, technical room and tunnel temperature and air velocity) must be done to ensure a realistic simulation. The thermal characteristics of the concrete and soil were numerically calibrated and different combinations of concrete and soil thermal conductivities were identified to best match the experimental results. The elaboration of the numerical results highlighted that the wall-soil heat flux is considerably higher than the wall-tunnel one. The wall-tunnel heat flux must be carefully studied as his behaviour seems to be strongly transient with time. The intrados temperature is affected by thermal exchanges and the numerical results show good agreement with respect to thermal photos taken during the experiment.

Additionally, preliminary prescriptions and hints for a successful execution and data interpretation of TRT on UEIs are reported. Variations with respect to the available guidelines for TRT execution on borehole heat exchangers and/or energy piles are suggested. The data interpretation should account for all heat exchange modes within and around the UEI.

Concluding, the portion of the UEI tested in this study can deliver a thermal power of 1 kW without reaching limiting values for temperatures within and around the heat exchangers. This chapter represents a first step towards a better understanding of the behaviour of UEIs. This example relates to the first UEI in Switzerland, and among the first in the world, paving the road for a deeper understanding and future energy exploitation. Further insights on the thermo-hydro-mechanical aspects involved in UEI operation are presented in Chapter 8.



# Chapter 8 On the determination of the thermo-hydro-mechanical behavior and the quantification of thermal potential of an underground energy infrastructure

## 8.1 Foreword

The use of underground infrastructures as thermal energy source may represent an important renewable energy source for the built environment. Underground infrastructures such as subway/railway stations, traffic shallow tunnels, basements of buildings can be thermally activated by inserting heat exchangers connected to the steel cage of underground infrastructures. The large surfaces exposed to the soil may guarantee an important thermal potential for extracting and storing energy in the ground. Some of the main challenges involved with the development of underground energy infrastructures are related to: (i) understanding the thermal exchanges with the air environments (e.g., tunnels, stations, basements, etc...) and with the surrounding materials, (ii) detecting the thermomechanical behavior of the UEI and (iii) quantifying the thermal potential and detailing the best thermal exploitation modes. Such challenges are tackled here with reference to a case study developed at the underground energy infrastructures installed at the Lancy-Bachet underground train station in Geneva (CH). An experimental campaign involving thermal tests on a portion of the energy walls was carried out. The results are interpreted through the employment of additional numerical analyses, validated against the experimental results, that allowed to have a global view of the thermo-hydro-mechanical concurrent processes. Important, seasonal hydrothermal UEI-tunnel interactions were recorded. The thermomechanical behavior was defined by non-uniform temperature distributions throughout the structure, inducing concurrent axial and bending thermally induced actions. The evaluation of the thermal potential of the entire installation allows to identify the high thermal potential and particularly the important contribution given by heat storage employing underground energy infrastructures.

## 8.2 Introduction

The objective of this chapter is to expand on insights related to the experimental testing campaign on underground energy infrastructures, providing, discussing and interpreting detailed thermo-hydro-mechanical results, and to define and quantify the thermal potential of the Lancy-Bachet EG installation. Understanding the behavior of underground energy infrastructures is a challenging topic as



it represents multidisciplinary aspects where soil and structural mechanics, fluid dynamics and energy are all linked together.

Little information is available on the thermo-hydro-mechanical behavior of vertical and horizontal ge-structures characterizing UEI. Some of the main examples of real world installations are related to underground infrastructures in Vienna, Austria (Brandl, 2016), applications on subway lines in London (Nicholson et al., 2014; Soga et al., 2015), Paris (Delerablée et al., 2018), Barcelona (Shafagh et al., 2020) and Shanghai (Sun et al., 2013; Xia et al., 2012). Such publications report fewer details who make difficult to thoroughly understand thermal, hydraulic and mechanical aspects (Loveridge et al., 2020). Other publications refer to numerical (Bourne-Webb & da Costa Goncalves, 2016; Bourne-Webb et al., 2016; Di Donna et al., 2016; Makasis et al., 2018, 2020, 2019; Zannin et al., 2020), analytical studies or to scaled models (Dong et al., 2019; Kürten et al., 2015a, 2015b) developed at the laboratory scale. Such studies partly tackle all the involved aspects, focusing on specific topics such as, for example, the thermomechanical behavior or hydrothermal aspects.

In this chapter, the knowledge acquired in the previous sections of this thesis (i.e., hydrothermal aspects as detailed in Chapter 3 and Chapter 4, thermomechanical aspects tackled in Chapter 5, Chapter 6 and execution of in-situ testing activity as reported in Chapter 7) is applied to the case study offered by the Lancy-Bachet UEI installation. Within this framework, a series of heating and cooling tests was carried out on a portion of the energy walls, by replacing the TRT module employed in Chapter 7 with a heat pump which allows to perform heating and cooling tests simulating real conditions. By monitoring the thermo-hydro-mechanical behavior of the thermo-active underground train station, the results are reported in terms of: (i) thermal behavior of the involved materials, (ii) hydraulic behavior of the fluid circulating in the heat exchangers, (iii) mechanical behavior of the tested energy wall subjected to heating and cooling. Numerical and analytical models, built and validated against the experimental results, are used to interpret the experimental results and to simulate the realistic, future hydrothermal behavior allowing to quantify the thermal potential of such installation.

In this chapter, hydrothermal aspects are firstly tackled, followed by thermomechanical analysis. Experimental results are presented, discussed and interpreted with the help of numerical simulations and analytical models, validated against experimental results, which allow to have a complete picture of the thermo-hydro-mechanical aspects involved in UEI operation. Thirdly, the thermal potential of the underground energy infrastructure is evaluated, allowing for determining the total energy quantities for satisfying thermal needs of the surrounding built environment and for identifying the most suitable thermal demand curve that maximizes the thermal performance of underground energy infrastructures. Concluding remarks are eventually reported.

## 8.3 Hydrothermal behavior

This section contains the experimental results from the in-situ testing campaign undertaken at the underground energy infrastructure installation at Lancy-Bachet, Geneva (CH).

Firstly, the experimental results that allow for the determination of the wall-tunnel hydrothermal interactions are presented, with emphasis on the thermal characterization, comparison with respect to the external air, the analysis of the wind velocity inside the tunnel. Secondly, the yearly profile of the temperatures at the air environments is evaluated. Thirdly, the test results where the wall is subjected to heating and cooling are presented. Then, comparison with numerical results are presented and discussed.

### 8.3.1 Tunnel behavior

The tunnel hydrothermal behavior is continuously monitored thanks to the monitoring system detailed in 7.3.1. The tunnel hydrothermal behavior is here detailed with reference to: (i) the seasonal temperature profile with correlation to the external environmental temperature; (ii) the wind velocity profile and the interactions with the train passage effects; (iii) the wall seasonal temperature distribution with height.

The tunnel temperature profile is analyzed with reference to the measurements performed from August 2019 to March 2020. The monitored results are compared with the temperature measurements taken by Météo Suisse at the Genève-Aéroport meteo station. Such measurements allow for the correct assessment of the boundary conditions of the numerical model.

Looking at the thermal interactions between the tunnel and the external temperature profiles, two different behaviors are reported (Figure 8.1). During summer (from August to mid-October) the tunnel temperature follows a periodic behavior on a daily basis, and it is lower than the external temperature during the day and higher at night. The difference between the tunnel and the external temperatures is, in absolute terms, about 6 °C and 4 °C for day and night, respectively. This behaviour is clearly visible as reported in Figure 7.6. The tunnel temperature varies between  $12.0 \pm 0.5^\circ\text{C}$  and  $30.0 \pm 0.5^\circ\text{C}$ . The temperature recorded at position -2B is generally higher than that at position -2A.

During winter, the tunnel temperature behaves periodically on a daily basis and it is always (i.e. during day and night) higher than that recorded outside (Figure 8.1). The difference between the tunnel temperature and the external temperature is about  $3 \div 5^\circ\text{C}$ . The tunnel temperature varies between  $+6.5 \pm 0.5^\circ\text{C}$  and  $+13.0 \pm 0.5^\circ\text{C}$ . The external temperature varies between  $-2.5^\circ\text{C}$  and  $13.0^\circ\text{C}$ . The temperature values measured in positions -2A and -2B are generally in line with each other. The values in position -2B have lower minimum values than the -2A measurement.

The wind speed profile shows an important variation between summer and winter (Figure 8.1). In the summer (Figure 7.6), wind speed values are recorded sporadically. There is a limited difference between the values measured at positions -2A and -2B.

During winter (Figure 8.2 and Figure 8.3) the wind speed values are more frequent and higher compared to those measured during the summer. Two different behaviors are identified: before and after the start of train traffic (as of 15 December 2019). Train traffic significantly modifies the air flow in the tunnel. This behavior is described in detail in Figure 8.3. Figure 8.3a clearly shows how the overall airflow behavior has changed before and after the beginning of train circulation. Figure 8.3b reports the differences within the periodical daily behavior (i.e., when trains are running) and the periodical night behavior (i.e., no train traffic). Figure 8.3c shows the correlation between air speed measurements and the passage of trains at three different times of a typical day (i.e., morning, afternoon, evening). The time-tables of train passages are detected from the timetable available at the station. The peaks of the air speed values coincide perfectly with the train passages. Such behavior is continuously reported until the time of writing of this thesis.

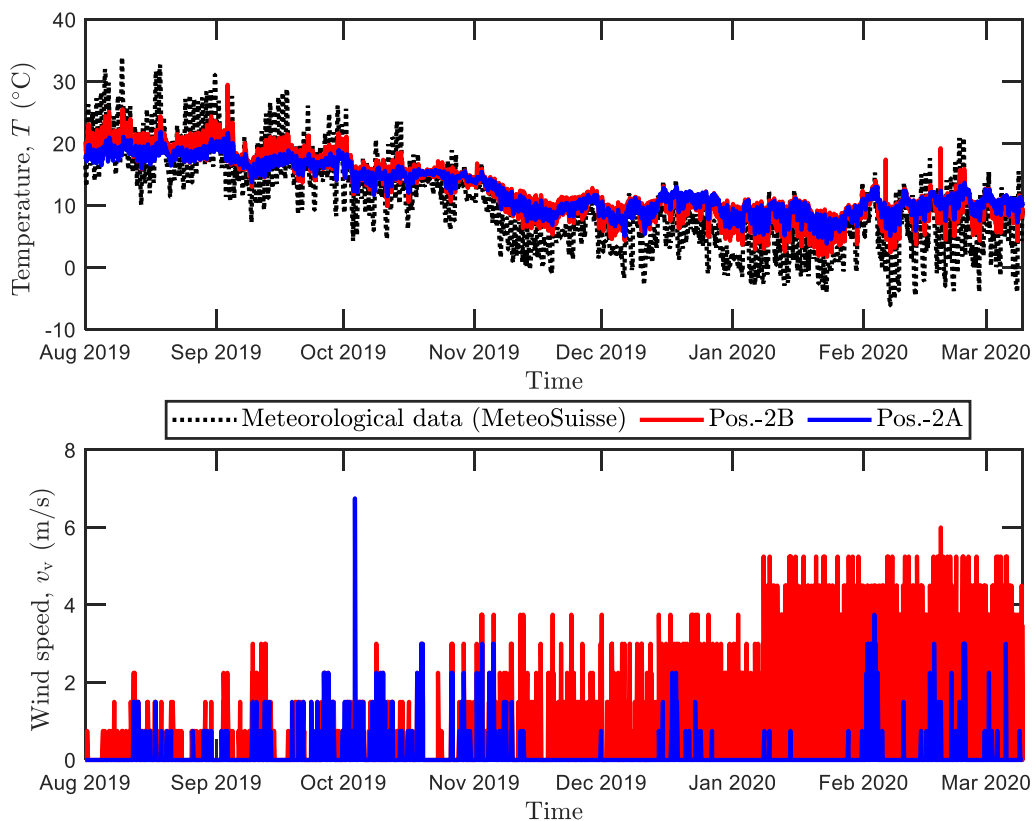


Figure 8.1 Tunnel air temperature profile and wind velocity from summer to winter behavior

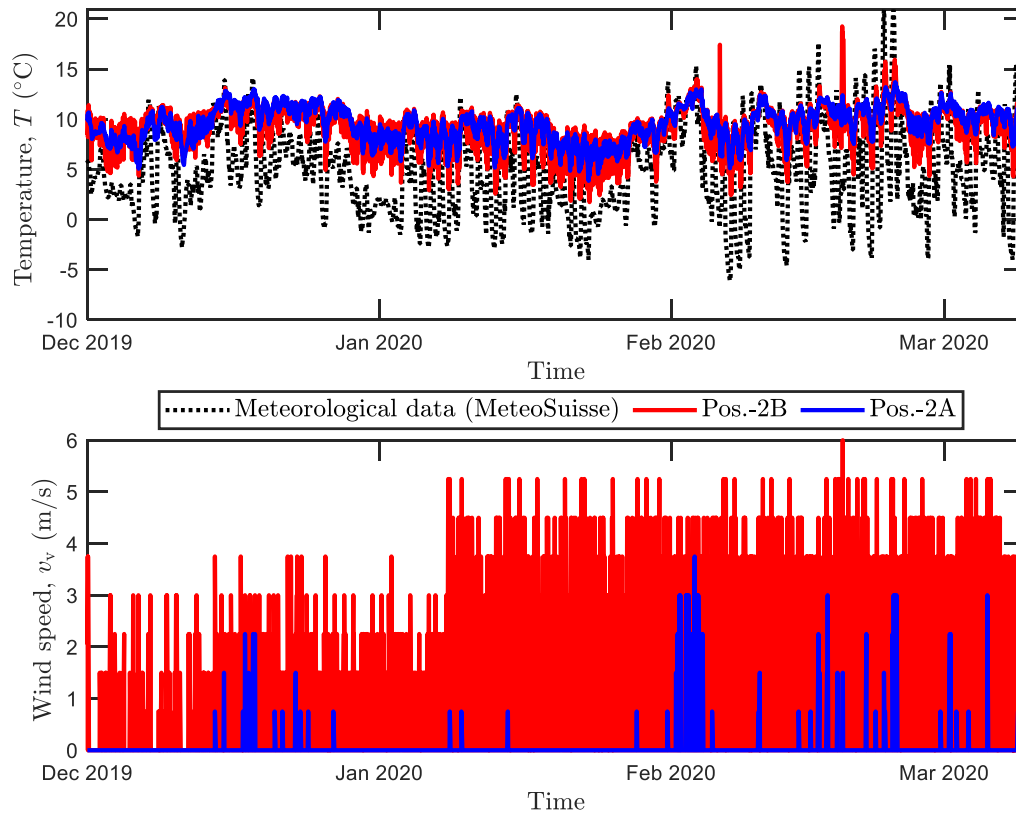


Figure 8.2 Tunnel air temperature profile and wind velocity: zoom-in to analyze the winter behavior

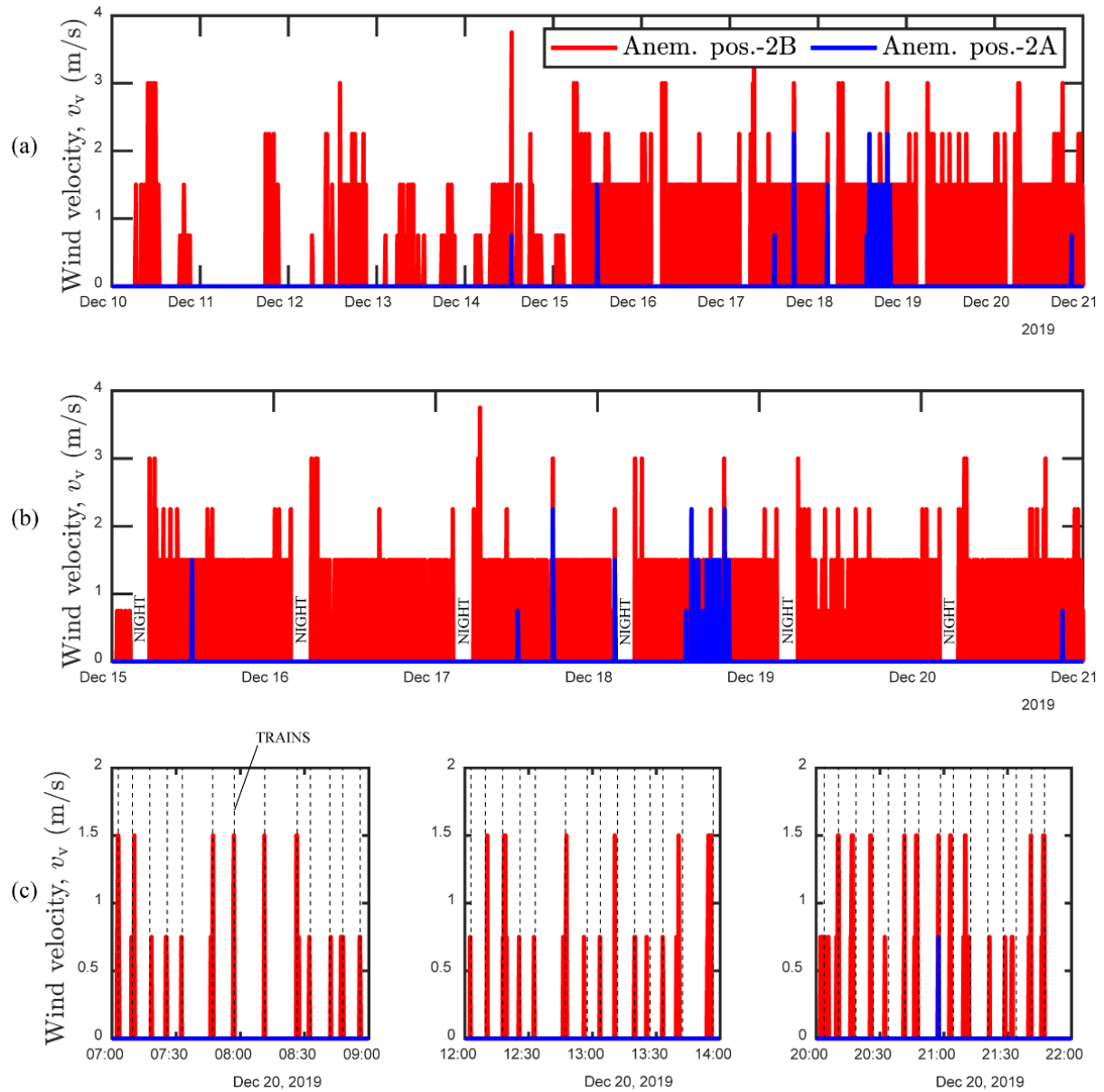


Figure 8.3 Analysis of the wind speed: (a) behavior before and after the beginning of train circulation; (b) behavior during few days after train circulation, definition of the differences between day and night behaviors; (c) zoom-in at three different times during a typical day and correlations between the measurements and the train passages

The analysis of the air temperature distribution at the intrados along the height of the tunnel wall is presented here. The temperature varies significantly on a seasonal basis, therefore two distinct analyses are made for summer and winter. The air temperature during summer (Figure 7.7) varies between  $16.0 \pm 0.5$  °C and  $27.5 \pm 0.5$  °C, with a difference of about 2 °C between the upper part (pos. -2B) and the lower part (pos. -2A). The wall is warmer at the top and cooler at the bottom. Differences of approximately 0.5 °C are recorded between the temperature measured at the wall intrados and that measured at approximately 1 m.

The air temperature during winter (Figure 8.4) varies between  $5.0 \pm 0.5$  °C and  $15.0 \pm 0.5$  °C, with a difference of  $2 \div 5$  °C between the top (pos. -2B) and bottom (pos. -2A). The wall is warmer at the top and cooler at the bottom. The difference between the measurement at the intrados and the measurement at approximately 1 m is more pronounced than during summer. Differences of approximately 1.5 °C at the lower part (pos. -2A) and 3 °C at the upper part (pos. -2B) are detected.

The difference between summer and winter behaviors could be explained by the increase in air velocity induced by trains circulation, which significantly affects the temperature in front of the glass wall (Figure 7.2), but a boundary layer regime exists behind the glass wall because such zone is slightly affected by train passage (see the blue curve in Figure 8.3). The average temperature of the wall in the winter period is 11.0 °C.

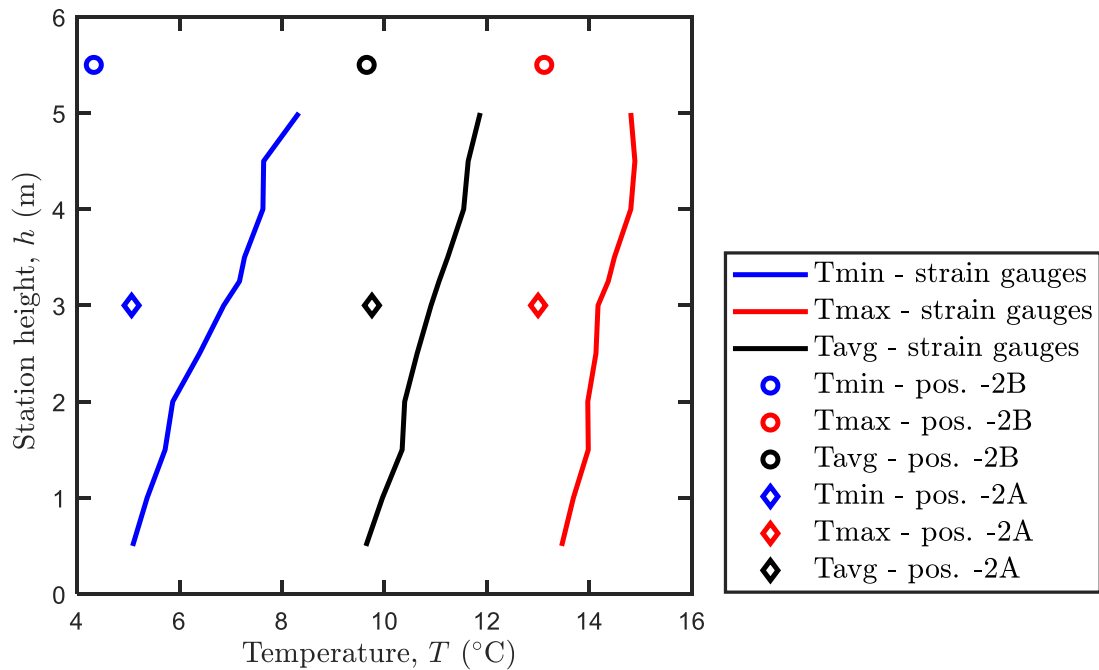


Figure 8.4 Temperature profile with wall height during winter

### 8.3.2 Definition of the yearly temperature profiles at the environments in the vicinity of the underground energy infrastructure

The measurements taken from summer to winter allow to reconstruct the yearly temperature profiles of the environments located in the vicinity of the UEI and that affect the thermal exploitation. Such values, which are summarized in Table 8.1, are also used as boundary conditions for the numerical model that simulates the in-situ tests and that it is used to define the thermal potential of the UEI.

Table 8.1 Determination of the temperature yearly profiles for each boundary condition

	External temperature (ground surface)	Tunnel temperature	Technical room tem- perature
	$T_{gs}$ (°C)	$T_t$ (°C)	$T_{tr}$ (°C)
Jan	2,2	6,0	11,0
Feb	2,9	8,0	10,0
Mar	6,9	11,0	12,0
Apr	11,0	15,0	13,5
May	14,7	18,5	17,0
Jun	19,2	21,0	19,0
Jul	20,8	22,0	21,0
Aug	20,0	21,0	21,0
Sep	16,0	18,5	18,5
Oct	11,7	15,0	16,0
Nov	6,4	11,0	13,5
Dec	2,9	8,0	11,5

### 8.3.3 Thermal activation tests

The results of the experimental campaign are presented in this section. The equipment used during this type of tests consists of a water-to-air heat pump (HP) located at level -1 (Figure 8.5), which replaces the TRT module presented at Chapter 7. In addition to the HP, a dedicated hydrothermal monitoring system is designed on purpose for this installation. Such monitoring system allows for a continuous measurement (i.e., one record every 30 seconds) of: (i) inflow and outflow fluid temperature,  $T_{f,in}$  and  $T_{f,out}$ , respectively; (ii) the flowrate,  $\dot{V}$ , of the circulating fluid, which is water; (iii) the air temperature at the HP ventilator,  $T_{ventilator}$ ; (iv) the technical room temperature undisturbed from the HP functioning,  $T_{techroom}$ . Moreover, thermal photos were taken at the end of each test, to analyze the wall intrados temperature distribution at the -2 level.

The tests have been carried out in the period from December 2019 to March 2020 and they relate to heating and cooling of the heat carrier fluid (HCF) at constant temperature, simulating real summer and winter operations, respectively. The heat pump allows for setting a user-defined  $T_{f,in}$ , the HP automatically sets its time-dependent behavior of the internal circulation pump (i.e., settings of flowrate) to ensure the best functioning and the respect of the maximum and minimum internal temperatures to avoid any excessive heating and/or fluid freezing.

The objectives of such tests are to reach limiting values (maximum and minimum) of the HCF temperature representative of future UEI operations. In other words, such tests aim at representing worst case scenarios in terms of temperature difference imposed to the UEI from a thermomechanical viewpoint, and best-case scenarios in terms of thermal exploitation (i.e., highest thermal power).

In this section, the results for heating and cooling tests are reported, focusing on the details of the HP behavior. Results of the thermal photos are eventually presented.

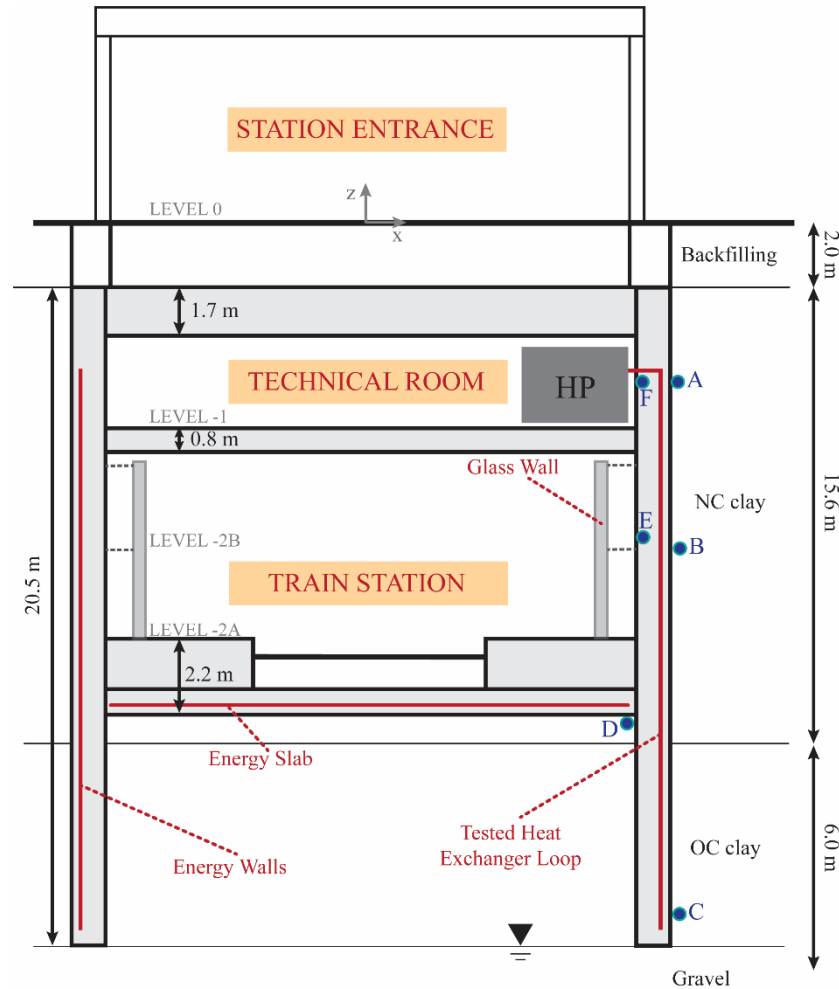


Figure 8.5 Cross section with indication of the location of the heat pump

#### 8.3.3.1 Heating tests

Two heating tests were run in December 2019 and February 2020. The period of the year in which the tests were carried out was imposed by the construction site's tight schedule. Heating tests represent the summer behavior of an UEI: the heat is injected in the ground to produce cold air used for air conditioning of the superstructure. The heating test performed in this context aim at achieving high



temperature levels in the range of values normally employed in low enthalpy geothermal applications and for heat storage operations (Gao et al., 2015; Gehlin, 2016; Nordell et al., 2015; Reuss, 2015; Witte & Van Gelder, 2007).

During heating tests (i.e., summer operation), the HCF is therefore cooled by exchanging heat with the pipes, the wall, the ground and the tunnel, which are at a lower temperature than that imposed by the heat pump. As a result, the wall and the soil are heated. Finally, the heat pump, via its refrigerating internal cycle, produces cold air.

The first test consists of a heat injection at constant temperature by fixing  $T_{f,in} = 50.0$  °C. The observed HP behavior is continuous and cyclic, with about 2 cycles per hour (Figure 8.6). The heat pump is switched on for about 15 minutes, when  $T_{f,in}$  rises to the set value, and then for about 15 minutes it decreases a little to allow thermal recharging around the heat exchangers.  $T_{f,in}$  varies between  $45.0 \div 56.5$  °C.  $T_{f,out}$  varies because of the imposed  $T_{f,in}$ , with a slight time shifting of a few seconds. The maximum variation is  $\Delta T_{f,out} = 4.0$  °C, which means that it varies between  $41.0 \div 48.6$  °C. The average HCF temperature variation between outflow and inflow is  $\Delta T_f = T_{f,in} - T_{f,out} = 5.9$  °C.

The flow rate imposed by the circulation pump sharply increases when  $T_{f,out}$  rises and then remains constant during the heating phase. The maximum variation of the flow rate is  $\Delta \dot{V}_f = 9$  l/min, varying between  $\dot{V}_f = 18 \div 27$  l/min, with an average value of  $\dot{V}_{f,avg} = 18$  l/min. Cold air is produced at the ventilator  $T_{ventilator} = 8.0$  °C. The technical room temperature is constant at  $T_{techroom} = 11.0$  °C.

The HP behavior in typical cycles is shown in Figure 8.6, in terms of temperature and flow rate values. The overall behavior of the heat pump during the total test duration is shown in Figure 8.7, including details of temperature, flow rate and thermal power. The evaluation of the thermal power is performed as follows:

$$Q_{th,f} = \dot{V}_f \rho_f C p_f (-\Delta T_f) \quad (8.1)$$

where  $\rho_f$  and  $C p_f$  are the HCF density and specific heat at constant pressure, respectively. During this test, the average thermal power is  $Q_{th,f} = -7$  kW, where the negative sign stands for heat injection.

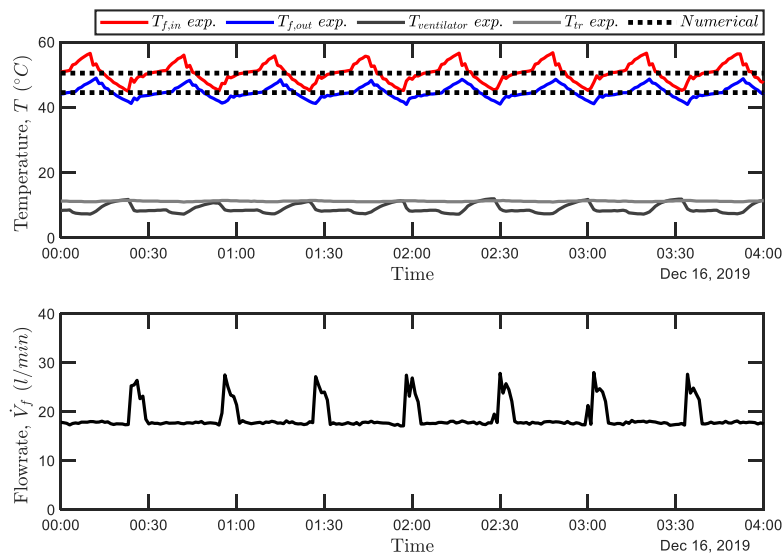


Figure 8.6 HP behavior zoomed during some cycle type (data related to the test performed in December 2019)

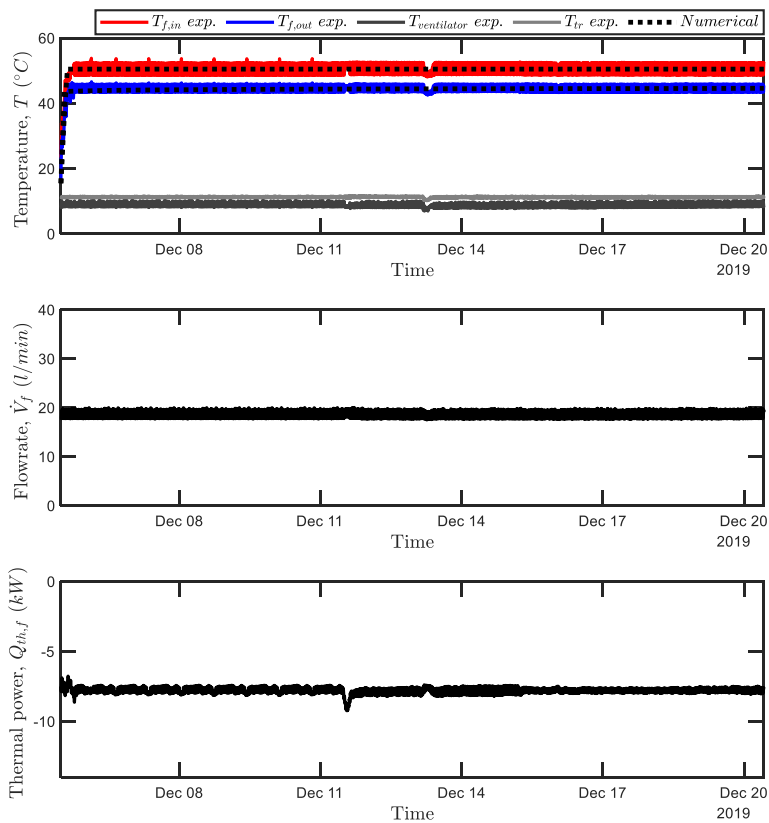


Figure 8.7 HP behavior during the test performed in December 2019

The second heating test was performed in February 2020. The imposed inflow temperature was set to  $T_{f,in} = 40.0$  °C. The HP behavior is shown in detail in Figure 8.8. It is very similar to the one shown

during the test performed in December 2019.  $T_{f,in}$  range between  $35.0 \div 44.7$  °C. Consequently,  $T_{f,out}$  ranges between  $31.8 \div 38.6$  °C. The average temperature difference between the inflow and the outlet is  $\Delta T_f = 4.9$  °C. The average flowrate is  $\dot{V}_{f,avg} = 17$  l/min, and the flowrate varies between  $15 \div 26$  l/min. Cold air is produced at the ventilator  $T_{ventilator} = 9.0$  °C. The technical room temperature is constant at  $T_{techroom} = 10.5$  °C. During this test, the average thermal power is  $Q_{th,f} = -6$  kW.

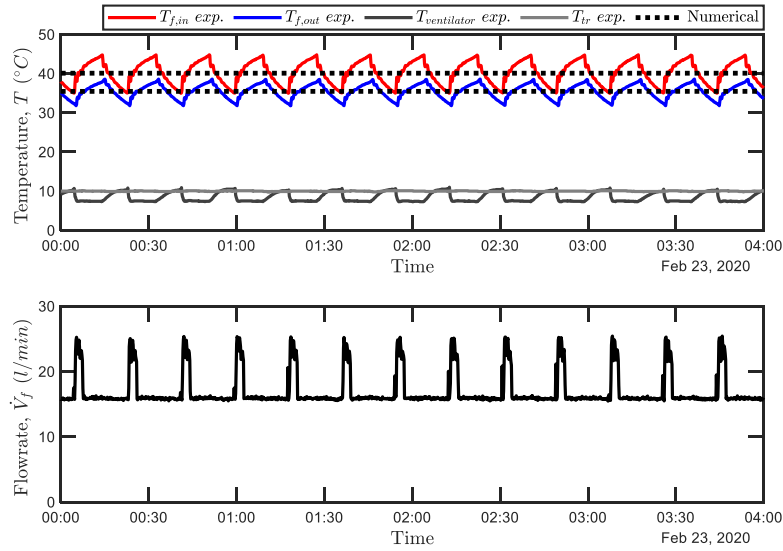


Figure 8.8 HP behavior zoomed during some cycle type (data related to the test performed in February 2020)

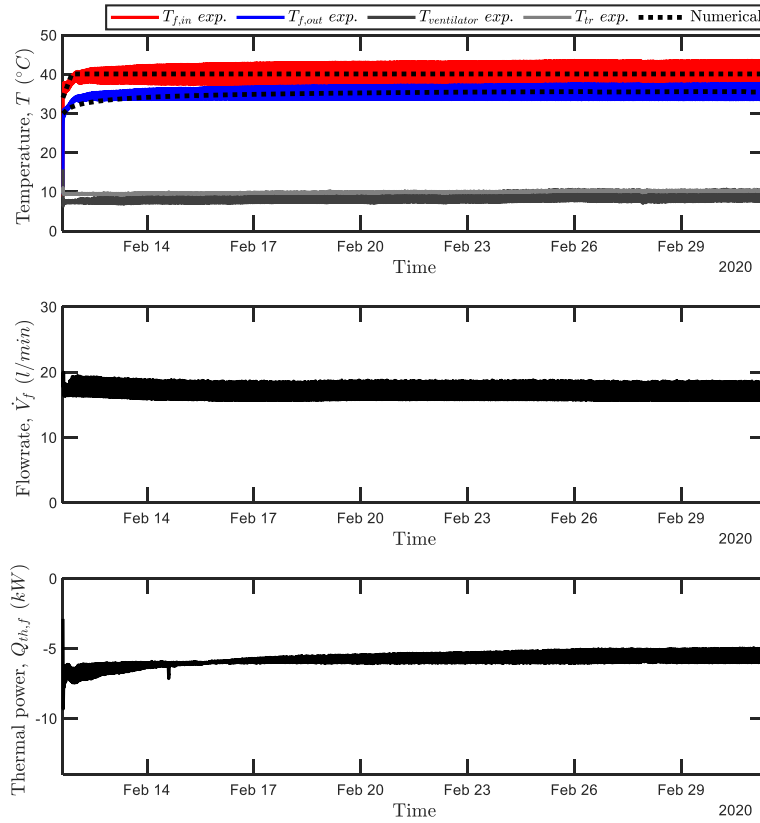


Figure 8.9 HP behavior during the test performed in February 2020

The overall HP behavior during the heating tests is very satisfactory, showing the good promising potential for thermal storage and air conditioning given by the underground energy infrastructure.

### 8.3.3.2 Cooling test

A cooling test was performed in March 2020. Cooling test represent the winter behavior of an UEI: a cold HCF is injected in the heat exchangers and, by extracting heat from the surroundings, the fluid is heated until the outlet point. It follows that the materials within the UEI (i.e., pipes, wall, soil and tunnel) are cooled as heat is extracted by the HCF. During such operation the HP produces hot air to be used for heating the superstructure. The cooling test performed here, aims at achieving the lowest values of HCF temperature allowable by the HP, simulating real winter operation.

The inflow temperature was set to  $T_{f,in} = 1.0$  °C. The heat pump response was highly discontinuous, on a cyclic basis (Figure 8.10 and Figure 8.11). HP switches on for a limited period (i.e., around 15 minutes every 30 minutes) and then switches off stopping the imposition of the inflow temperature but letting the fluid to circulate at ambient temperature. In this way, some thermal recharge of the materials surrounding the fluid was possible and the heat extraction could afterwards resume. Such strongly

intermittent, periodical behavior was due to the fact that the minimum allowable HCF temperature value was reached and the HP needed to stop to avoid freezing issues. This is considered to be one of the major limitations for this installation: thermal boundary conditions effects during winter in conjunction with limitations in the operative temperature range of the HCF strongly reduce the thermal potential of the UEI for winter operation. This observation will be recalled and expanded in the following.

The inflow temperature ranged between  $T_{f,in} = 0.5 \div 9.2$  °C. Outlet temperature varied between  $T_{f,out} = 2.3 \div 8.2$  °C. The average inflow-outlet fluid temperature difference was  $\Delta T_f = 2.5$  °C. The flowrate sharply increased when the HP switched on, ranging between  $\dot{V}_f = 12 \div 24$  l/min, and presenting an average value of  $\dot{V}_{f,avg} = 13$  l/min. Hot air is produced at the ventilator  $T_{ventilator} = 15.0 \div 24.0$  °C. The technical room temperature is constant at  $T_{techroom} = 10.5$  °C. The average thermal power is  $Q_{th,f} = 2$  kW, where the positive sign means heat extraction.

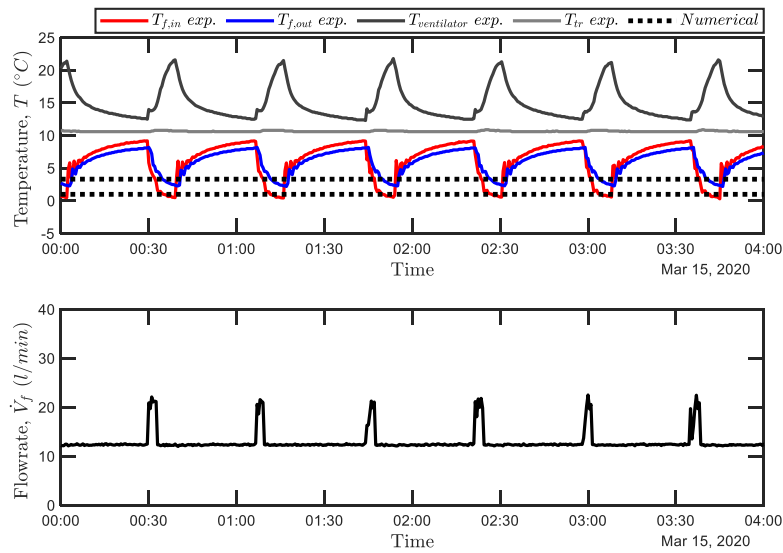


Figure 8.10 HP behavior zoomed during some cycle type (data related to the test performed in March 2020)

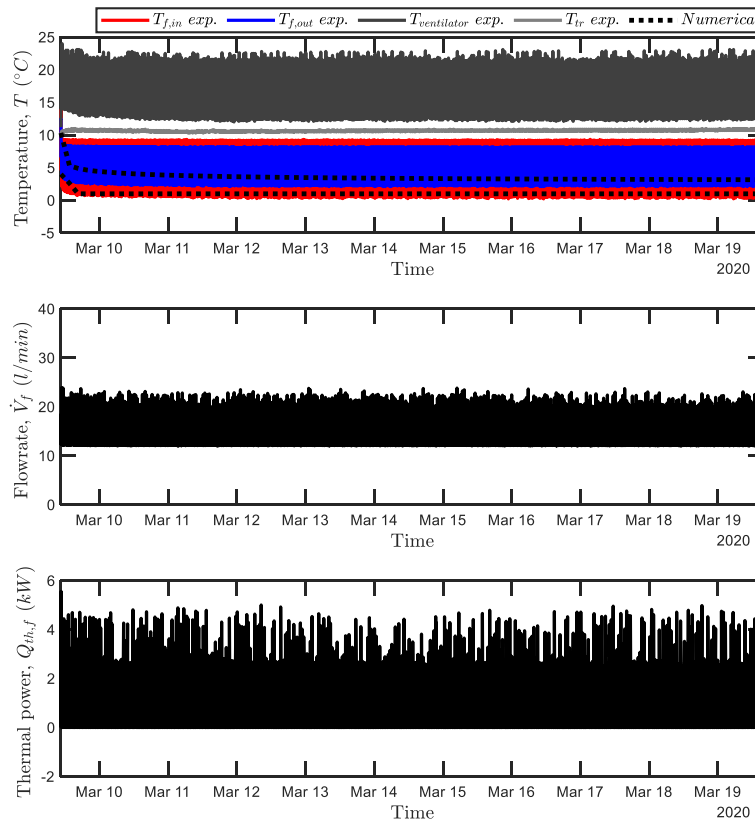


Figure 8.11 HP behavior during the test performed in March 2020

#### 8.3.4 Wall intrados temperature and wall-tunnel interactions

The wall intrados is affected by temperature variations induced by the thermal activation of the UEI. With the objective to analyze the impact of temperature diffusion within the wall thickness and to detect wall-tunnel hydrothermal interactions, thermal photos were taken at the end of each test. Results are presented in Figure 8.12, Figure 8.13 and Figure 8.14. Such results will also be further analyzed detailing the comparison with numerical results.

Some technical difficulties were found while taking the thermal photos. In fact, it was impossible to take the photos exactly perpendicularly to the wall because of the little space among the wall itself and the glass wall which prevents the correct focus of the device. For this reason, the thermal photos were taken at an angle of about 120 degrees from the perpendicular to the wall and showing a global view of the wall temperature. Because of these difficulties, thermal photos are only used as a qualitative comparison between experimental and numerical results.

During the heating tests (i.e., December 2019 and February 2020, Figure 8.12 and Figure 8.13) the wall intrados was heated. During the December 2019 test, the thermally affected portion was clearly visible (Figure 8.12a, following the yellowish vertical portion). The hottest portion was located at the top of

level -2B, as reported at Figure 8.12b. The longitudinal extent of the thermally affected region was of 1.5 m. The average temperature difference between the thermally affected portion and the undisturbed one was of 3.5 °C.

During the February 2020 test, the thermally affected portion is presented at Figure 8.13a,b. The longitudinal extent of the thermally affected portion was in the same order of magnitude of the one for the test carried out in December 2019. The average temperature difference between the thermally affected and the undisturbed region was of 2.0 °C.

During the March 2020 cooling test, the thermally affected portion is presented at Figure 8.14a,b. The cooling induced by the heat exchangers spreads in the surrounding materials. Consequently, the entire wall is cooled. The longitudinal extent of the thermally affected portion was of 1 m. The average temperature difference between the thermally affected and the undisturbed region was of −1.5 °C.

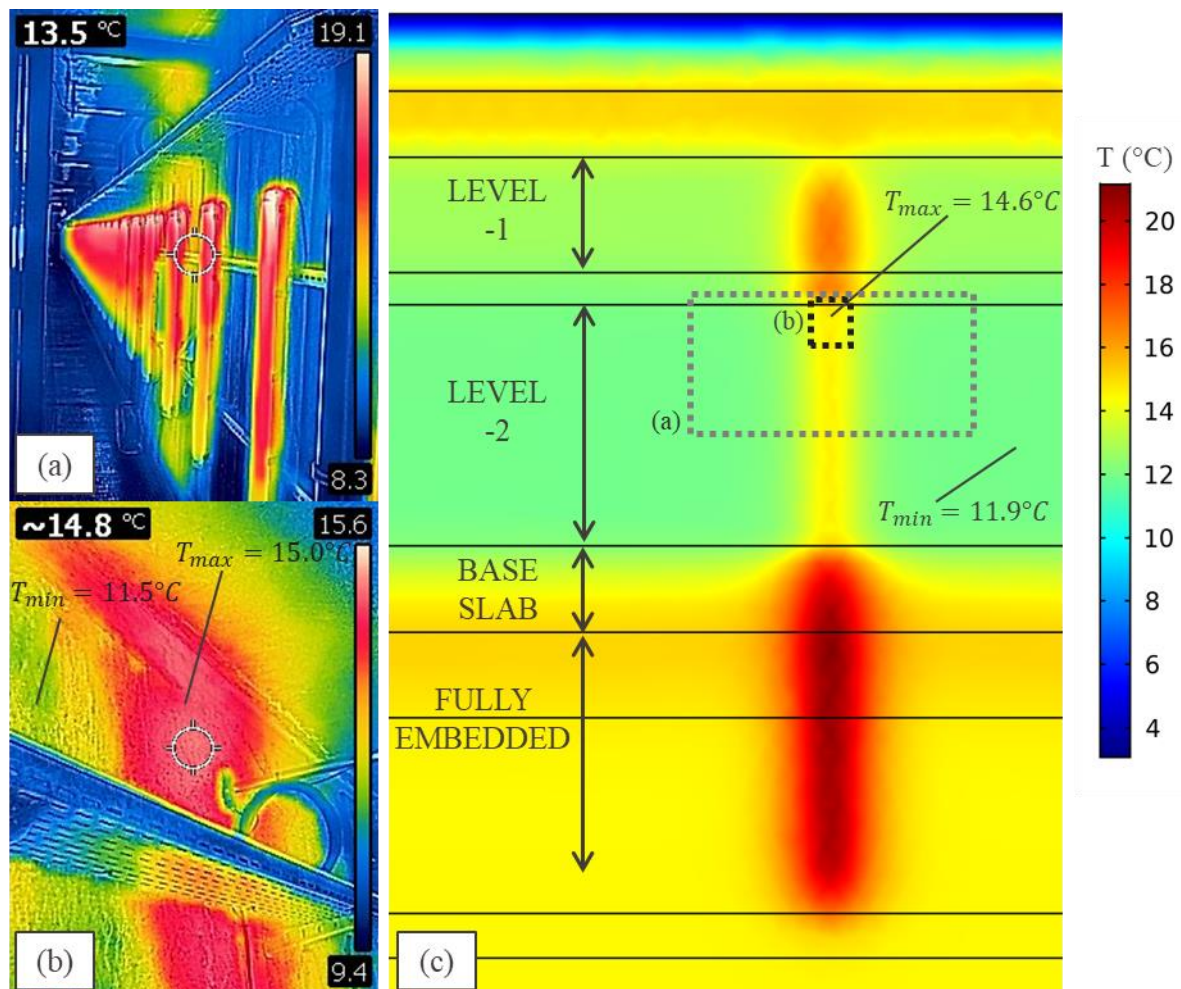


Figure 8.12 Analysis of the thermal camera photos taken at the end of the heating test performed in December 2019: (a) thermal camera photo taken at level -2B, (b) thermal camera photo taken at level -2B (zoomed image), (c) intrados temperature profile from numerical analysis. NOTE: the red coloured vertical bars at (a) are neon lights which are impossible to shut down, as they represent the only lighting system of the underground train station



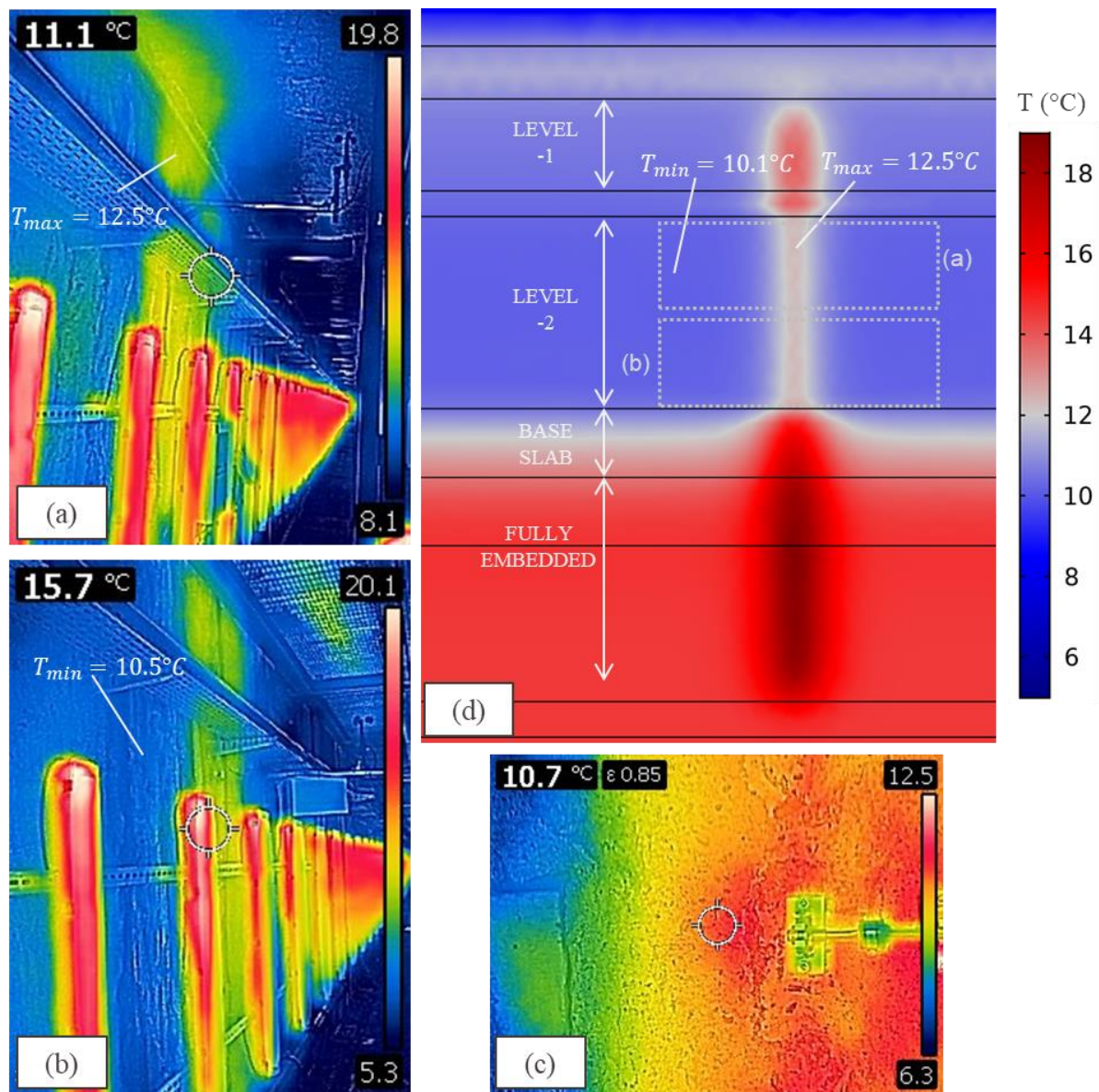


Figure 8.13 Analysis of the thermal camera photos taken at the end of the heating test performed in February 2020: (a) thermal camera photo taken at level -2B, (b) thermal camera photo taken at level -2A, (c) zoomed-in image taken at level -2B, (d) intrados temperature profile from numerical analysis. NOTE: the red coloured vertical bars at (a) and (b) are neon lights which are impossible to shut down, as they represent the only lighting system of the underground train station



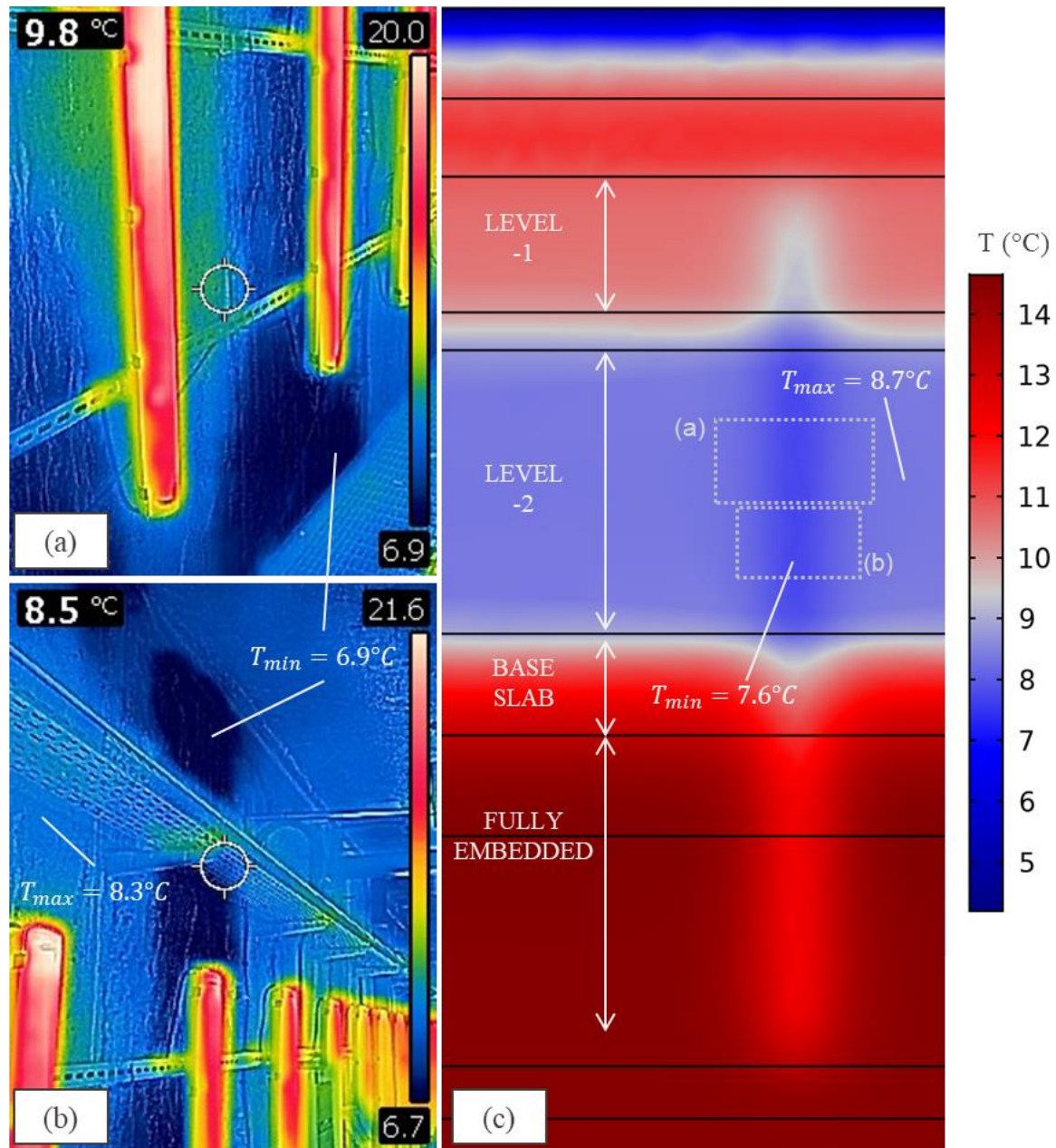


Figure 8.14 Analysis of the thermal camera photos taken at the end of the cooling test performed in March 2020: (a) thermal camera photo taken at the bottom part of level -2B, (b) thermal camera photo taken at the top part of level -2B, (c) intrados temperature profile from numerical analysis. NOTE: the red coloured vertical bars at (a) and (b) are neon lights which are impossible to shut down, as they represent the only lighting system of the underground train station

### 8.3.5 Numerical modelling: validation against experimental results and interpretation of the results

The numerical model presented in Chapter 7 is used here to simulate the HP tests. The same rationale applies: (i) the monitored data at the tunnel, technical room and outside (i.e., meteorological data) are used as boundary conditions (as summarized in Table 8.1); (ii)  $T_{f,in}$  is imposed at the heat

exchanger's inflow; (iii)  $T_{f,out}$  and the wall intrados temperatures are used as a comparison among the experimental and numerical data. Then, once it is established that the model simulates the experimental results satisfactorily, the numerical results are used to further interpret the hydrothermal behavior of the UEI.

The heating and cooling HP tests are hence simulated. Results in terms of the heat carrier fluid temperatures are reported, together with the experimental results in Figure 8.6 and Figure 8.7 for the heating test performed in December 2019, Figure 8.8 and Figure 8.9 for the heating test performed in February 2020, Figure 8.10 and Figure 8.11 for the cooling test performed in March 2020.

For the heating tests, the numerical results very satisfactorily simulate the average temperatures measured at the HP during its continuous, cyclic behavior.

For the cooling test, as mentioned above, the HP behavior is strongly intermittent. To reduce the computational cost, the numerical model simulates a continuous operation, hence the comparison among the experimental and the numerical results, should focus only to the times when the HP is in operation. With this regard, the numerical model is able to satisfactorily simulate the HP behavior: the heat carrier fluid temperature well represents the experimental data (Figure 8.10).

The comparison among experimental and numerical results in terms of the wall intrados temperature is reported at Figure 8.12, Figure 8.13 and Figure 8.14. For all tests, the temperature profiles evaluated through numerical analyses show a very good agreement with respect to the experimental results, with maximum local differences that reach  $0.5 \div 0.7$  °C. The lower bound applies for the heating tests, while the upper bound applies for the cooling test.

From the results presented in Chapter 7 and Chapter 8 of this thesis, we can conclude that the numerical model is able to satisfactorily simulate and reproduce the hydrothermal behavior of the UEI during winter and summer operations.

#### 8.3.5.1 Determination of wall-tunnel thermal interactions

Before analyzing the details of the wall-tunnel interactions during the thermal activation tests, it is worth to analyze the UEI-tunnel interactions induced by the applications of the boundary conditions only. As reported in Table 8.1, the temperature profiles at the boundaries presents a periodical behavior on a yearly basis, following a seasonal behavior. Such conditions have implications on the UEI operation as they modify the temperature profile of the UEI itself and its surroundings. It is particularly worth noting that, there is a portion of the wall and soil that undergo to a seasonal temperature variation of  $\Delta T \cong 6 \div 10$  °C (Figure 8.15). The concrete presents maximum/minimum temperatures of  $T_c = 19 \div 9$  °C during summer and winter, respectively. The soil (i.e., the portion within the grey, dashed line

reported at Figure 8.15) presents maximum/minimum temperatures of  $T_s = 17 \div 11$  °C during summer and winter, respectively.

It is key to consider such temperature variation when studying the UEI operation, because of two reasons. Firstly, temperature variations induced by natural effects of the order of magnitude of few degrees Celsius (or greater, as it is recorded here) may have repercussions on the validity of the hypothesis of “yearly constant soil temperature” that is often true for energy geostructures (Brandl, 2006; Laloui & Rotta Loria, 2019). Secondly, Figure 8.15 shows that the portion of materials that undergo to this temperature difference represent more than 50% of the volume of the most thermally affected materials during UEI operation. It follows that such environmental temperature variations will have an impact on the UEI operation, as the tunnel is heating the materials during summer and cooling them during winter, reducing the seasonal potential for heat injection and extraction, respectively. This is already partly visible from the HP results for the cooling test performed in March 2020 (Figure 8.10), as the heat pump is forced to periodically stop to allow for thermal recovery before resuming its operation. This effect is particularly detrimental for the winter operation, as a reduction of the average temperature of materials, reduces the potential of cooling the UEI, as the allowable temperature difference is already limited and freezing of the surrounding materials should be avoided as from most of operative prescriptions and available standards (CFMS-SYNTEC-SOFFONS-FNTP, 2017; GSHPA, 2012; SIA D0190, 2005).

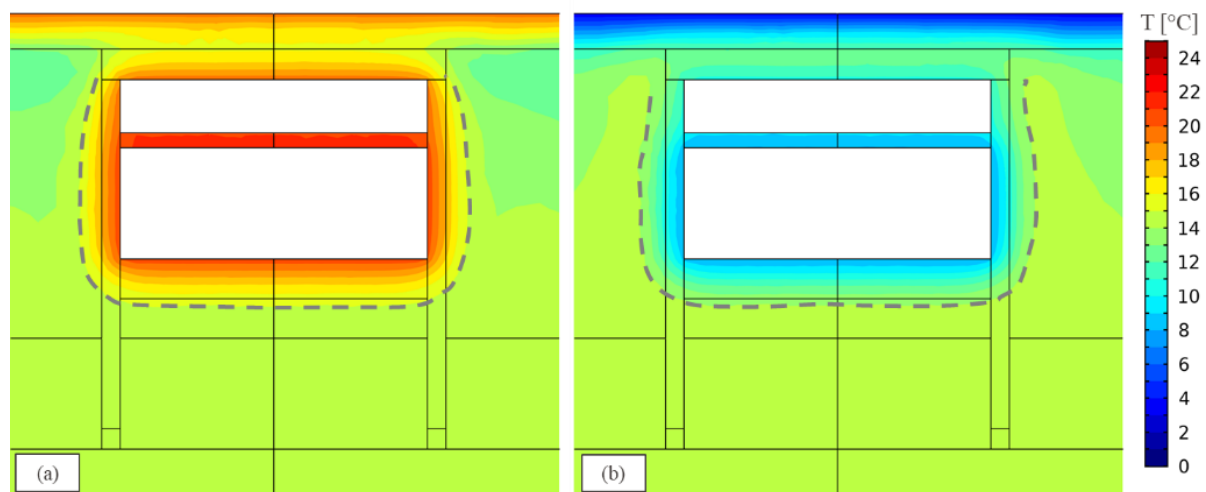


Figure 8.15 Temperature profile (from numerical analyses) within and around the UEI determined by the application of the tunnel, technical room and external boundary conditions: (a) summer; (b) winter

Moreover, wall-tunnel hydrothermal interactions include also the analysis of airflow conditions. Figure 8.2 and Figure 8.3 show how airflow conditions change because of the beginning of train circulation at the -2 level. Such variations suggest a re-evaluation of the convective heat transfer coefficient. After the start of train circulation, the anemometer recordings show that for 93.9% of the time, the wind velocity was below the lower limit of measurement of the instrument (i.e.,  $v_w < 0.5$  m/s). An upper limit of the average wind speed can be evaluated as if the wind speed during such time was exactly at

the lower limit of the reading of the instrument, which would lead to an average wind speed of 0.59 m/s in front of the glass wall and of 0.50 m/s behind the glass wall. A lower limit of the average wind speed can be evaluated by considering that wind speed goes exactly to zero during such time frame. This case would lead to a quantification of the average wind speed markedly below the minimum reading limit of the instrument (i.e., around 0.1 m/s). We can hence conclude that the average wind speed behind the glass wall was surely  $\leq 0.5$  m/s. These findings allow to estimate the convective heat transfer coefficient in the range named as the “quasi-zero” velocity as reported by Bourne-Webb et al. (2016). By using the chart reported by Peltier et al. (2019),  $h_c = 4$  W/m<sup>2</sup>/K.

The numerical analyses carried out to simulate the HP tests allow for detecting the temperature profile and the magnitude of the heat fluxes attained during UEI operation. Such results are reported at Figure 8.16, Figure 8.18 and Figure 8.20.

The results for the heating tests show that the portion of materials affected by thermal effects extends up to 2 m of soil (Figure 8.16d, Figure 8.18d), with the portion of soil affected by thermal effects that increases in volume as the heating continues. The maximum soil temperature recorded at the wall-soil interface is  $T_{s,max} = 31.0$  °C, recorded at the end of the December 2019 test. The maximum wall temperature is  $T_{w,max} = 38.0$  °C (Figure 8.16d). The magnitude of the heat fluxes at the intrados is transient. The wall and the tunnel act as conductors, with the heat flux magnitude that increases as the test continues (Figure 8.17 and Figure 8.19). The heat flux magnitude at the tunnel level is higher than at the fully embedded portion of the wall (Figure 8.16 to Figure 8.19). The heat flux at the extrados is maximum in intensity during the initial days of heating, taking advantage of the high temperature difference between the HCF and the soil. Then, the heat flux magnitude decreases consequently to the increase of the soil volume affected by thermal effects (Figure 8.17 and Figure 8.19). The heat flux at the extrados is slightly higher in the top portion of the wall (i.e., facing the tunnel level) with respect to the bottom one because the initial soil temperature is lower (e.g., this is clearly visible at Figure 8.18b,c,d). The magnitude of the heat flux at the extrados is considerably higher than at the intrados: three times higher for the December 2019 test, 2.5 times higher for the February 2020 test.

It is however worth noting that the heating tests were carried out in highly favorable conditions, since they were run during winter. The implications related to heating tests during summer are reported at section 7.4.

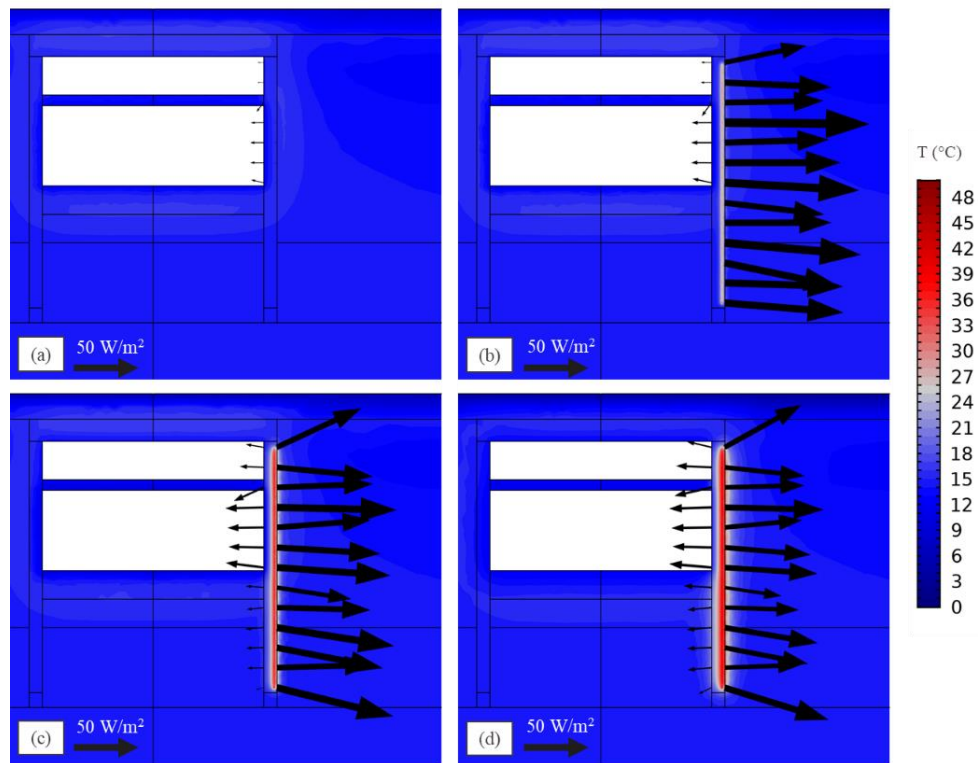


Figure 8.16 Contour plot of the temperature profile of the cross section in correspondence of the heat exchangers with indication (i.e., arrows) of the heat flux vectors at the intrados and extrados for the December 2019 heating test: (a) before the start of the test; (b) after 1 day of test; (c) after one week of test; (d) at the end of the test

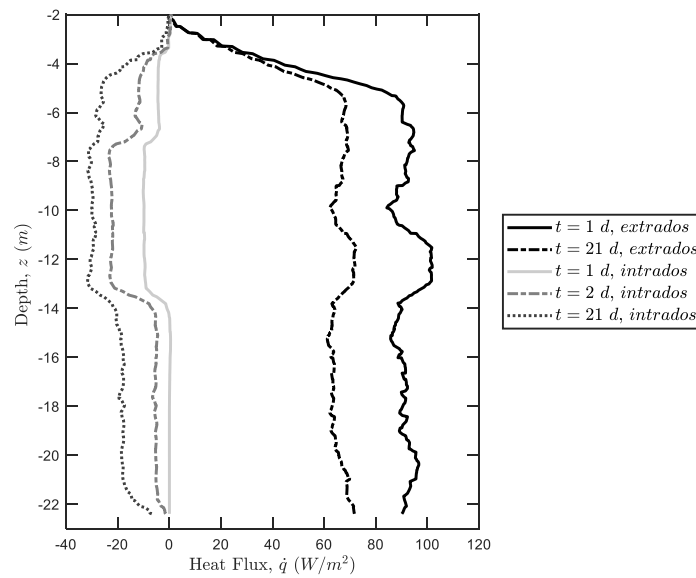


Figure 8.17 Magnitude of the heat flux at the intrados and extrados during the December 2019 heating test

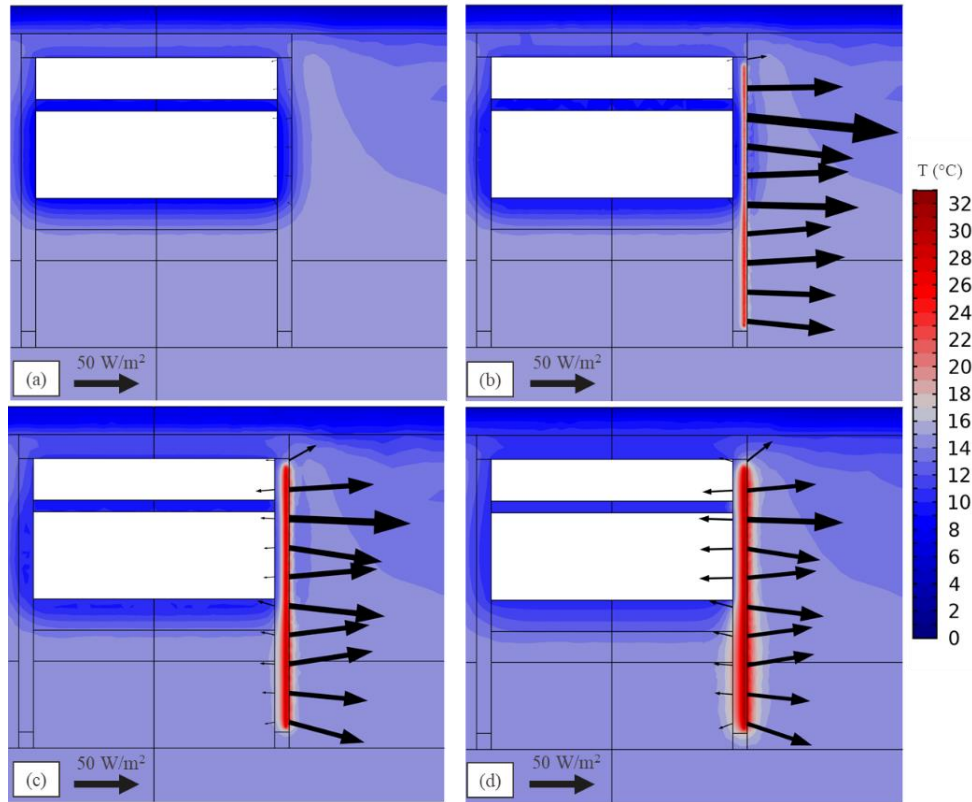


Figure 8.18 Contour plot of the temperature profile of the cross section in correspondence of the heat exchangers with indication (i.e., arrows) of the heat flux vectors at the intrados and extrados for the February 2020 heating test: (a) before the start of the test; (b) after 1 day of test; (c) after one week of test; (d) at the end of the test

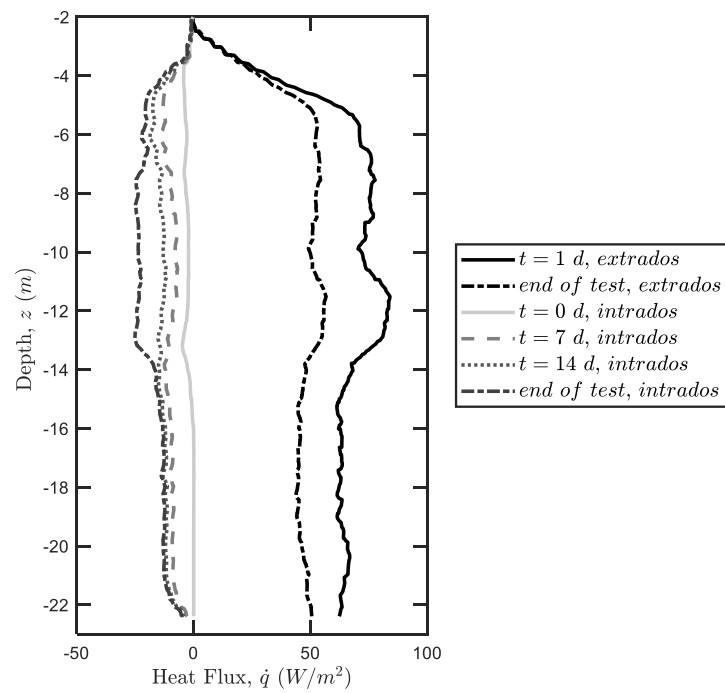


Figure 8.19 Magnitude of the heat flux at the intrados and extrados during the February 2020 heating test

The results for the cooling test show that the portion of materials affected by thermal effects extends up to  $1 \div 1.5$  m of soil (Figure 8.20), with the portion of soil affected by thermal effects that increases in volume as the cooling continues. The minimum soil temperature recorded at the wall-soil interface is  $T_{s,min} = 6.5$  °C, recorded at the end of the March 2020 test. The minimum wall temperature is  $T_{w,min} = 4.3$  °C (Figure 8.20c,f). The magnitude of the heat fluxes at the intrados is transient (Figure 8.21). The wall and the tunnel act as conductors, with the heat flux magnitude that increases as the test continues. The heat flux magnitude at the tunnel level is the same than that at the fully embedded portion of the wall. The heat flux at the extrados is maximum in intensity during the initial days of heating, taking advantage of the higher temperature difference between the soil and the HCF (Figure 8.20b). Then, the heat flux magnitude decreases consequently to the increase of the soil volume affected by thermal effects (Figure 8.20c, Figure 8.21). The heat flux at the extrados is higher in the fully embedded wall portion with respect to the top part, consequently to the higher temperature difference between the soil and the HCF (Figure 8.21). The magnitude of the heat flux at the extrados is five times higher than at the intrados.

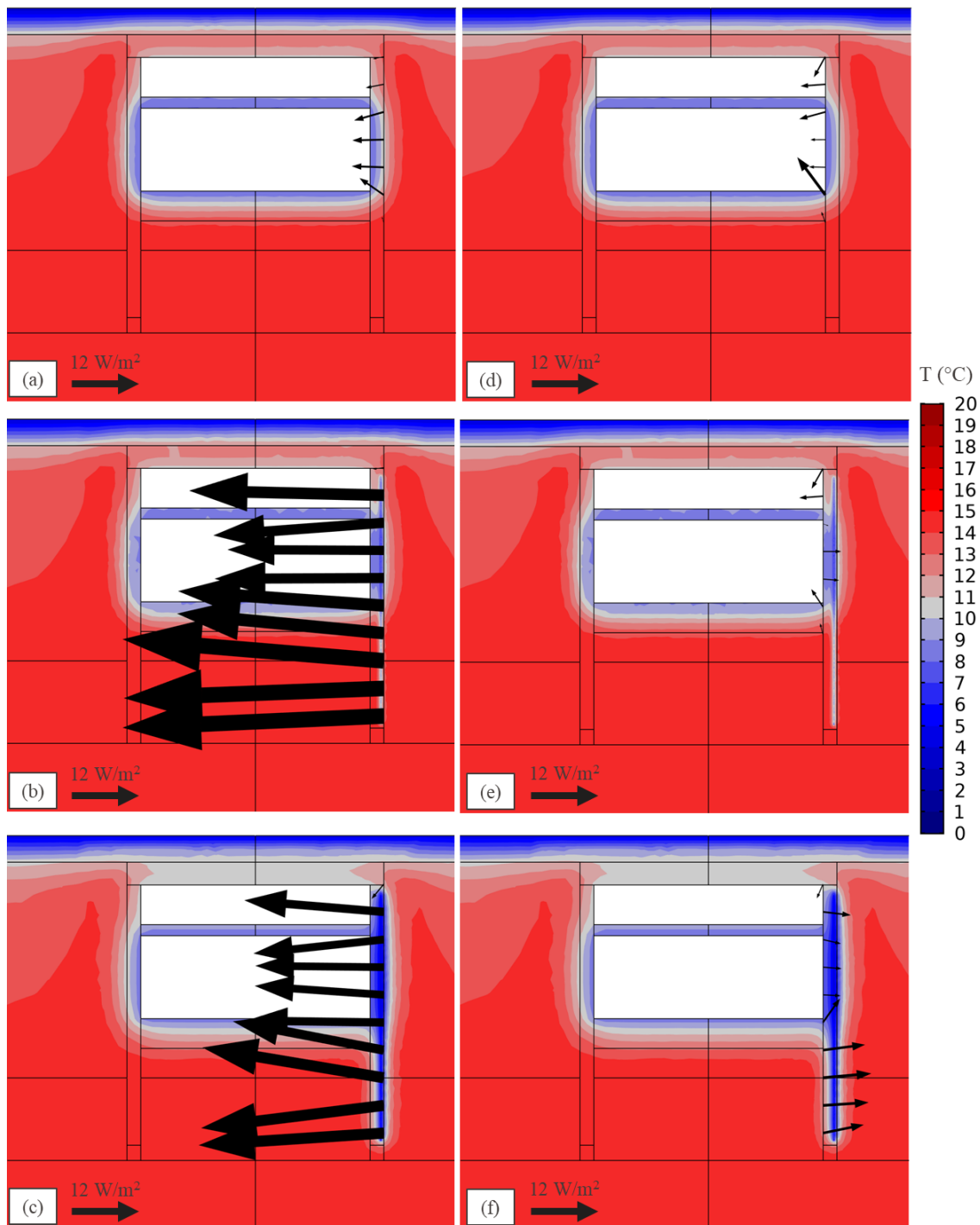


Figure 8.20 Contour plot of the temperature profile of the cross section in correspondence of the heat exchangers with indication (i.e., arrows) of the heat flux vectors at the intrados and extrados for the March 2020 cooling test: (a) at the extrados, before the start of the test; (b) at the extrados, after 1 day of test; (c) at the extrados, at the end of the test; (d) at the intrados, before the start of the test; (e) at the intrados, after one day of test; (f) at the intrados, at the end of the test



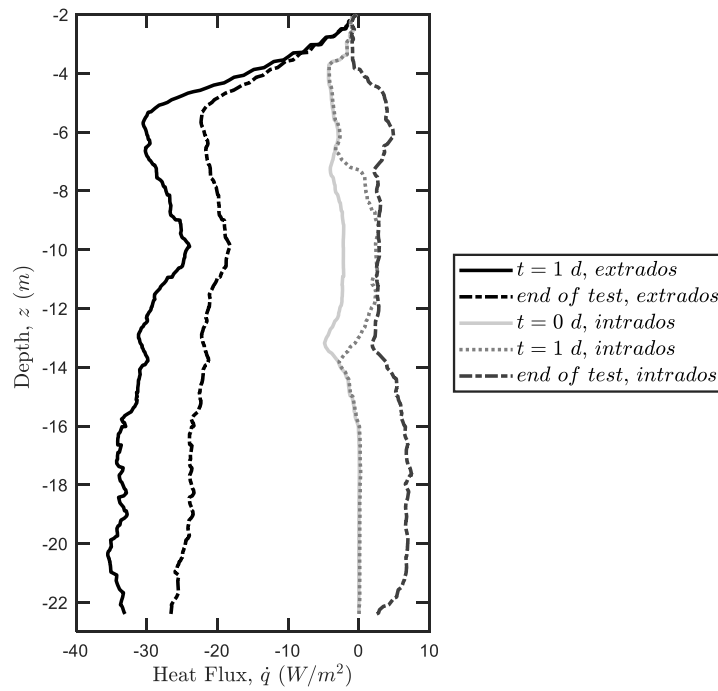


Figure 8.21 Magnitude of the heat flux at the intrados and extrados during the March 2020 cooling test

## 8.4 Thermomechanical behavior

Thermally induced effects in the wall are analyzed in this section with reference to the determination of the temperature profile in the UEI reached during the heating and cooling tests. A simple, 1D finite difference model, validated against the experimental results, that allows for the determination of the wall temperature distribution is proposed. Then, the thermomechanical behavior of the wall is analyzed with reference to the experimental results monitored at the tunnel intrados as well as with comparison with analytical and numerical modelling results.

### 8.4.1 Determination of the temperature distribution in the wall

During heating and cooling tests, the wall undergoes to temperature variations. Being the EW in contact with the soil on one side and in the fully embedded portion, in contact with a concrete structure (i.e., wall-slabs interactions) and with air (i.e., tunnel and technical room), different behaviors are envisaged at different locations. The contact with solid materials partly constrains thermally induced deformations (i.e., low  $DOF_a$  and  $DOF_c$ ), while at the air interface it has more freedom to deform (i.e., higher  $DOF_a$  and  $DOF_c$ ).

The experimental results as well as the numerical results presented at section 8.3 are here used to define the temperature profile of the EW before and at the end of each performed test. Two different temperature profiles are detected.

At the top, facing the excavation, the presence of the air helps to keep a low temperature variation at the intrados. The air “washes away” the temperature difference imposed by the heat exchangers. It follows that the EW temperature distribution is strongly non-uniform, with a maximum located at the wall-soil interface (i.e., in the vicinity of the heat exchangers) and a minimum at the intrados.

At the bottom, in the fully embedded portion, a less-pronounced non-uniform temperature profile is recorded by means of the numerical analyses. The temperature profile is not uniform between the intrados and the extrados consequently to the non-symmetrical heat exchangers location. The results for the three performed tests are presented in Figure 8.22.

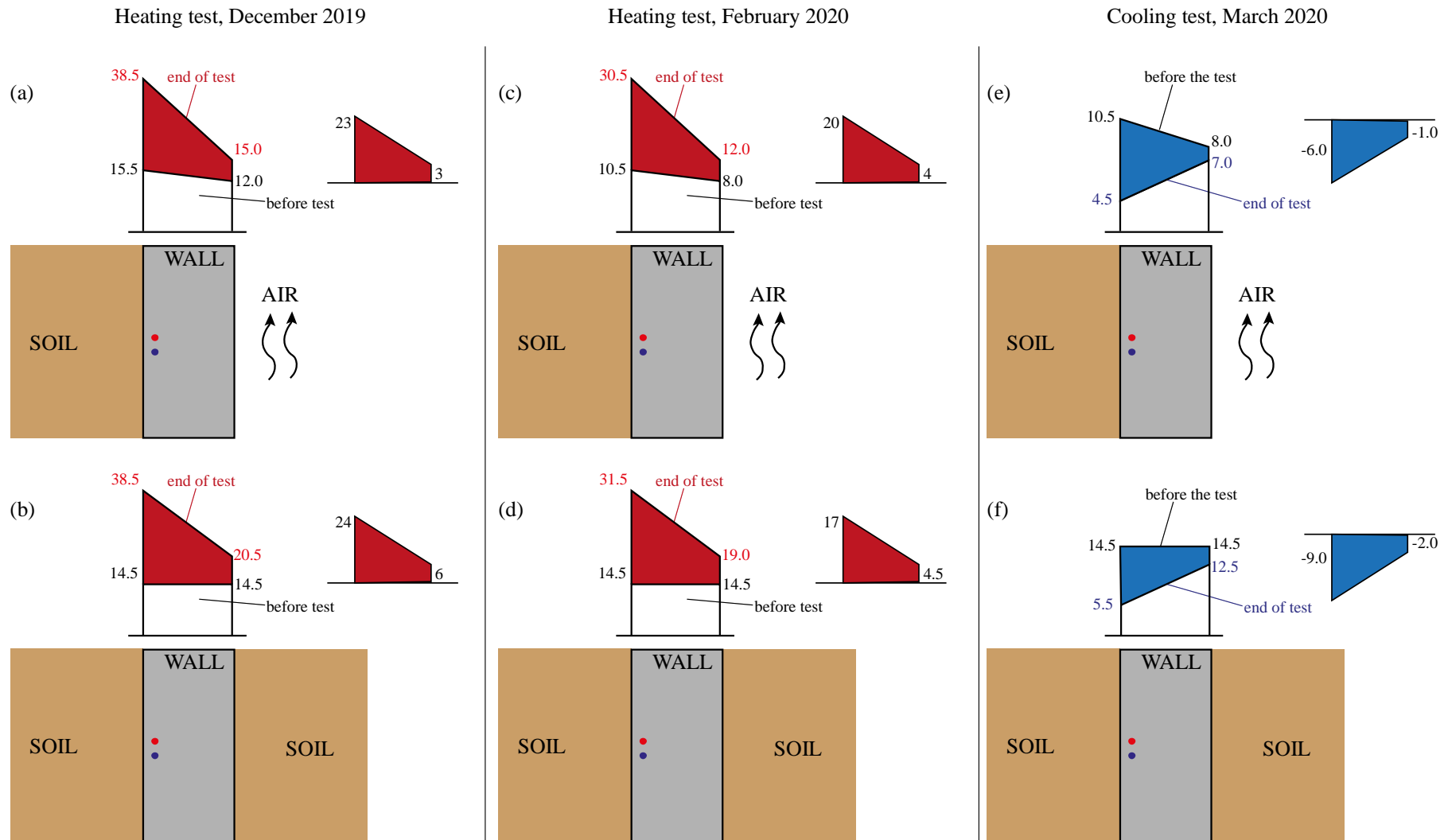


Figure 8.22 Determination of the temperature distribution (values in °C) in the EW. For the December 2019 heating test: (a) portion exposed to air; (b) fully embedded portion. For the February 2020 heating test: (c) portion exposed to air; (d) fully embedded portion. For the March 2020 cooling test: (e) portion exposed to air; (f) fully embedded portion. NOTE: figures are not scaled.

#### 8.4.1.1 Modelling of the temperature distribution in the wall facing the tunnel: a finite difference model

In this section, a 1D finite difference (FD) model based on thermal resistances is developed to determine the temperature distribution in the EW portion facing an air interface. The model is firstly described. Then, it is applied to simulate the in-situ tests carried out. The FD model results are compared with the numerical results showing closed agreement.

The objective of this FD model is to predict the temperature profile in a concrete cross section facing an air interface during thermal activation, and the location of the heat exchangers is nonsymmetrical with respect to the structural axis. The model results can then be employed to define the distribution of the thermal load (i.e., axial and bending components) to be used for thermomechanical analyses.

This model allows to analyze the 1D transient conduction case, using the concept of thermal resistances (Kürten et al., 2015a). The model is built following a FD scheme and discretizing the Fourier's heat equation through the so-called Explicit Method (Bergman et al., 2011).

The model is based on the following assumptions:

- A constant heat flux,  $q^*$ , is applied at the wall-soil interface. Positive heat flux denotes heat injection, while a negative heat flux denotes heat extraction.
- The wall-air interface is modelled through a convective boundary condition: the convective heat transfer coefficient,  $h_A$ , and the air temperature,  $T_A$ , remain constant.
- The initial temperature profile is known.

The problem, whose schematic view is presented in Figure 8.23, is firstly discretized in time and space using discrete nodal points (i.e., points from 0 to 10 in Figure 8.23). The computation of wall temperature is done for each point  $x = m \Delta x$ , with  $m$  being the space increment integer and  $\Delta x$  the increment in space, and at different time steps  $t = p \Delta t$ , with  $p$  being the time increment integer and  $\Delta t$  the time increment. The heat equation can hence be written in his FD form (Bergman et al., 2011):

$$\alpha_{th} \frac{T_{m+1}^p + T_{m-1}^p - 2T_m^p}{\Delta x^2} = \frac{T_m^{p+1} - T_m^p}{\Delta t} \quad (8.2)$$

with  $\alpha_{th}$  being the thermal diffusivity of the material and  $T$  the temperature.

By using the FD form of the Fourier number

$$Fo = \frac{\alpha_{th} \Delta t}{(\Delta x)^2} \quad (8.3)$$

The solution is expressed in its explicit form:

$$T_m^{p+1} = Fo \left( T_{m+1}^p + T_{m-1}^p + \frac{q^*(\Delta x)^2}{\lambda_c} \right) + (1 - 2Fo)T_m^p \quad (8.4)$$

with  $\lambda_c$  being the concrete thermal conductivity.

For the points at the heat exchangers location,  $T_0^p$ , and at the wall-air interface,  $T_{10}^p$ , respectively, the temperature is determined as:

$$T_0^{p+1} = Fo \left( 2T_1^p + \frac{q^*(\Delta x)^2}{\lambda_c} \right) + (1 - 2Fo)T_0^p \quad (8.5)$$

$$T_{10}^{p+1} = 2Fo \left( 2T_9^p + Bi T_A + \frac{q^*(\Delta x)^2}{2\lambda_c} \right) + (1 - 2Fo - 2FoBi)T_9^p \quad (8.6)$$

$$Bi = \frac{h_A \Delta x}{\lambda_c} \quad (8.7)$$

$Bi$  being the Biot number.

To avoid divergence of the solution,  $\Delta t$  (and  $\Delta x$ ) should remain within acceptable limits. For prescribed values of  $\Delta x$  and  $\alpha_{th}$  that depend on geometry and material characterization, a criterion should be defined to set an upper limit to  $\Delta t$ . The stability criterion for the FD explicit method, in 1D conditions, is (Bergman et al., 2011):

$$Fo(1 + Bi) \leq \frac{1}{2} \quad (8.8)$$

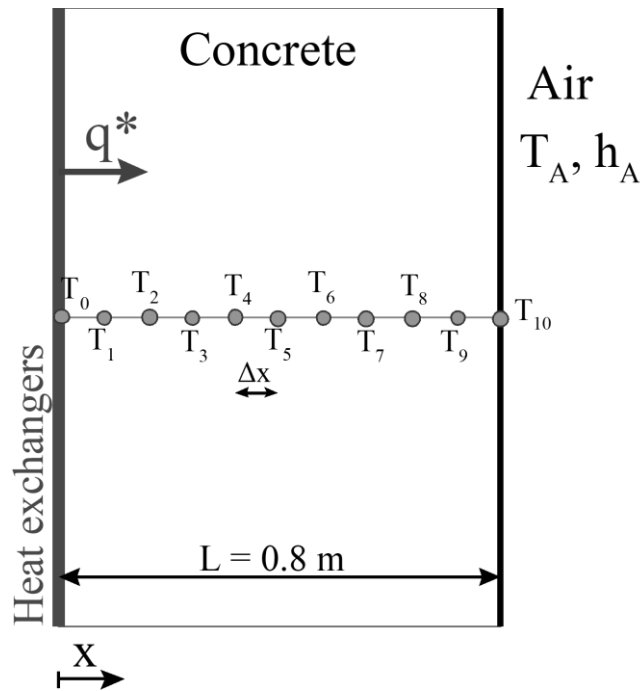


Figure 8.23 Schematic view of the model geometry

The model is then implemented in a spreadsheet and used to simulate the in-situ tests. The input parameters are reported in Table 8.2. The results are reported in terms of the temperature profile throughout the wall at different time steps. Intrados and extrados temperature values taken from numerical and experimental results are added to allow for a comparison among the different techniques. Results are reported at Figure 8.24, Figure 8.25 and Figure 8.26.

Table 8.2 Input parameters used for the FD model

Parameter	Value	Unit	Note
$\Delta x$	0.08	m	
$\Delta t$	1800	s	
$h_A$	8	W/m <sup>2</sup> /K	It considers train circulation (section 8.3.5.1)
$T_A$	10	°C	Taken equal for the three tests (Figure 8.2)
$q^*$	65, 50, -18	W/m <sup>2</sup>	Heat flux at the heat exchangers, from numerical analyses
$\lambda_c$	1.7	W/m/K	
$\rho_c C p_c$	2.3	MJ/kg/K	

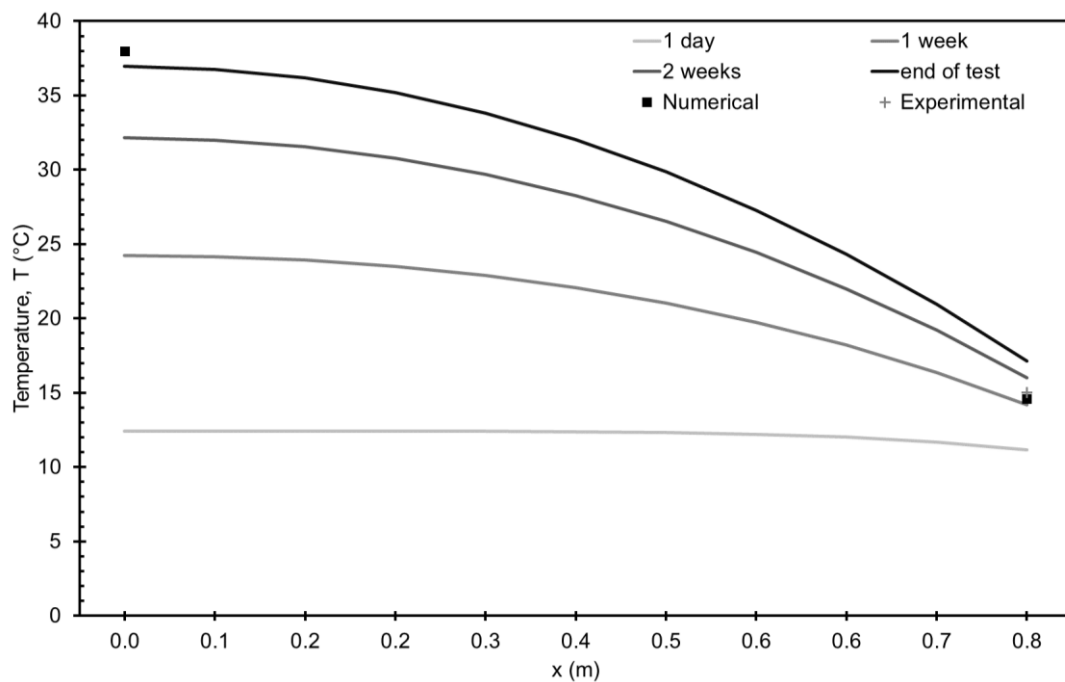


Figure 8.24 Results for the modelling of wall temperature through FD model, and comparison with numerical and experimental results: simulation of the December 2019 heating test

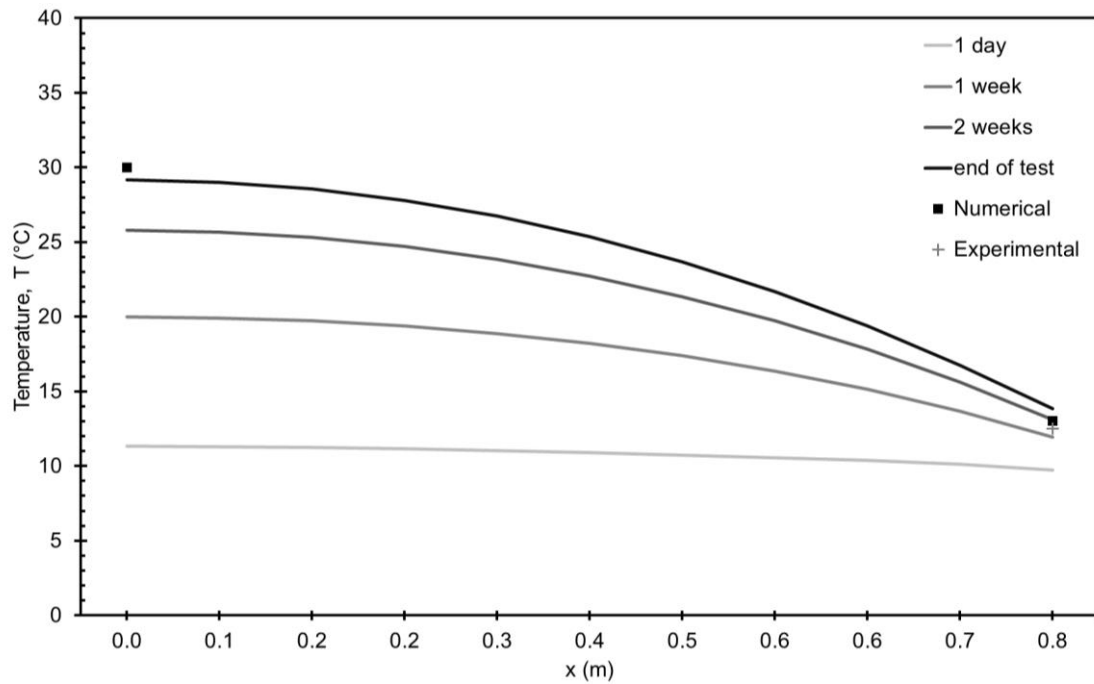


Figure 8.25 Results for the modelling of wall temperature through FD model, and comparison with numerical and experimental results: simulation of the February 2020 heating test

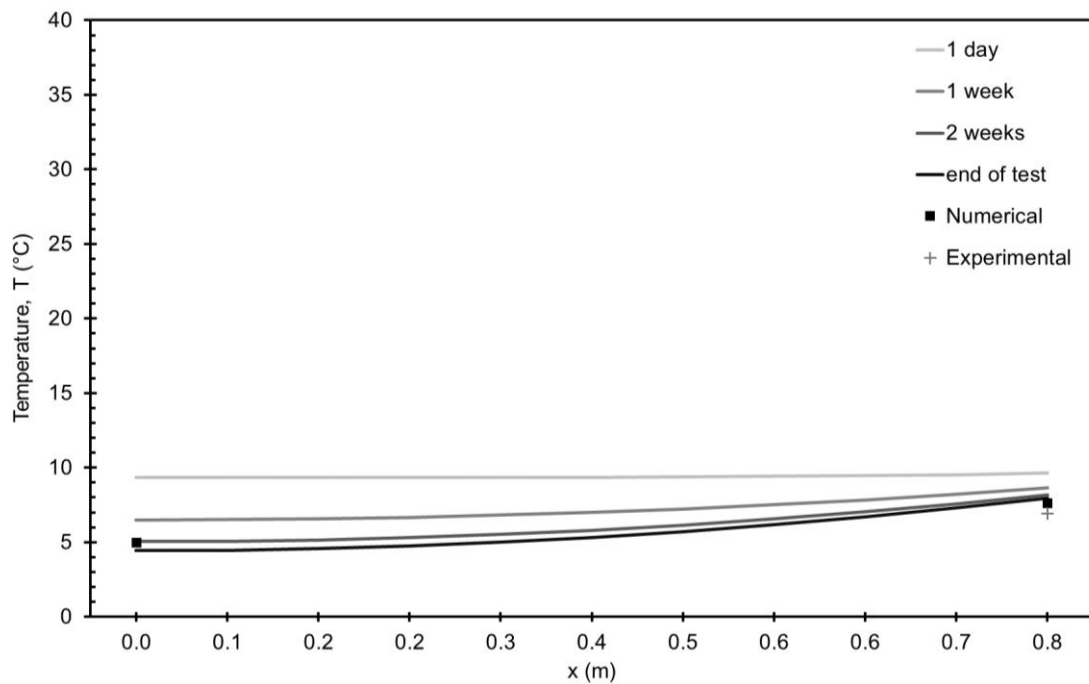


Figure 8.26 Results for the modelling of wall temperature through FD model, and comparison with numerical and experimental results: simulation of the March 2020 cooling test

The results show that this simple FD model is able to capture the EW temperature distribution when compared with experimental results and also with results obtained by running time-consuming, 3D, transient, FE analyses, showing closed agreement. The computational efforts needed to implement and

to run such model are minimal, consisting simply in implementing the Fourier equation in a spreadsheet, with results plotted in few seconds. This model, conversely, is not able at capturing the detailed three-dimensional, highly transient, nature of the ongoing hydrothermal phenomena, but it allows for a reliable representation of reality, useful for defining temperature profile and consequently quantify thermally induced actions.

#### 8.4.2 Thermomechanical behavior of the energy wall

The monitoring system detailed at section 7.3.1 is here used to evaluate the wall intrados mechanical behavior during the in-situ tests. Such monitoring system is capable of recording the axial deformation of the instruments, which are installed alternatively in vertical and longitudinal arrangements at the wall intrados of level -2 (Figure 7.3). Results are reported in figure Figure 8.27. The geo-structure deforms when subjected to temperature loads. Deformations are partly restrained by the presence of the soil and by the structural connections. The installed monitoring system is capable to record only the intrados deformations. The experimental results suggest that two distinct mechanisms can be identified: a vertical and a longitudinal one.

The temperature variation throughout the EW cross section is non uniform and it is the one shown at Figure 8.22. Longitudinally, temperature is diffusing (radially from the heat exchangers) in the wall from the vicinity of the heat exchangers towards the intrados and towards the soil. Upon heating, the EW extrados would tend to longitudinally dilate, but such dilation is partly blocked by the presence of the soil. Longitudinally, the only constraint to dilation is represented by the soil, no wall-slab connections are affecting the EW behavior at any longitudinal cross section at the level -2 (Figure 8.28). It follows that dilation at the extrados is partly blocked, but, following the intrados heating (Figure 8.22), intrados is free to dilate ( $DOF_{intrados} > DOF_{extrados}$ ). For this reason, positive (i.e., expansion) longitudinal deformation values are attained. The maximum longitudinal deformation is here recorded at the tunnel mid-height, where the wall presents the highest degree of freedom. The maximum recorded deformation value corresponds to  $\varepsilon_{h,max} = \Delta L/L_0 = 0.013\%$ . The deformation profile is not instantaneous, but it develops with time, in agreement with the time-dependent thermal diffusion inside the EW. The opposite was recorded upon cooling (Figure 8.27).

Upon heating, the EW extrados would tend to vertically dilate but such dilation is partly blocked by the presence of constraints (i.e., soil and structural connections). During heating tests, the extrados is hotter than the intrados (Figure 8.22). Treating the EW as a vertical beam and following the hypothesis that, for small deformations, the beam cross section maintain its planarity and remain orthogonal to the neutral axis (Euler-Bernoulli theory of beams (Truesdell, 1960)), the extrados would tend to vertically dilate and the intrados to contract (Figure 8.29). Additionally, structural constraints at the top and bottom of level -2 (i.e., wall-slab connection and additional stiffness offered by the embedded portion of the wall, wall-slab connection and self-weight of the superstructure at the top) are considerably restraining the



degree of freedom of the wall. It follows that vertical intrados deformations are quasi-null, with a tendency of being negative (i.e., contractive) following the extrados expansion towards the soil side. Contraction is maximum at the location of highest *DOF*: at mid-height of the wall facing the tunnel. During heating, the EW intrados vertically deforms exhibiting a contraction. The opposite is recorded upon cooling (Figure 8.27).

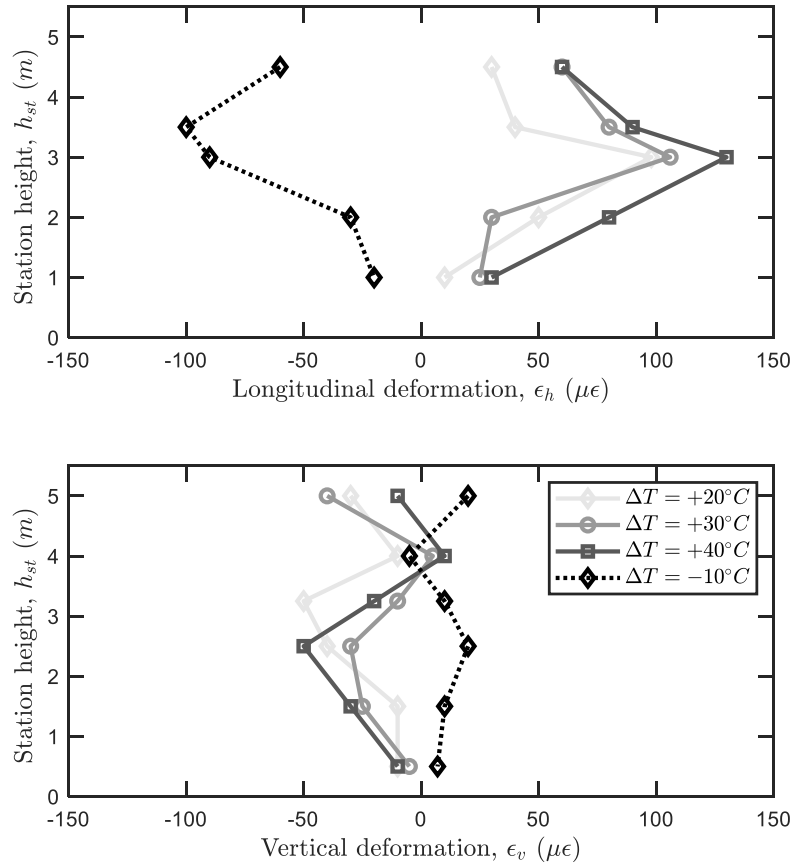


Figure 8.27 Mechanical behavior of the wall intrados facing the tunnel: experimental results. The figure includes results from the following in-situ tests: TRT (August 2019, details at section 7.4.1, indicated as  $\Delta T = +20^\circ\text{C}$ ), heating tests (December 2019, indicated as  $\Delta T = +40^\circ\text{C}$ , and February 2020, indicated as  $\Delta T = +30^\circ\text{C}$ ), cooling test (March 2020, indicated as  $\Delta T = -10^\circ\text{C}$ )

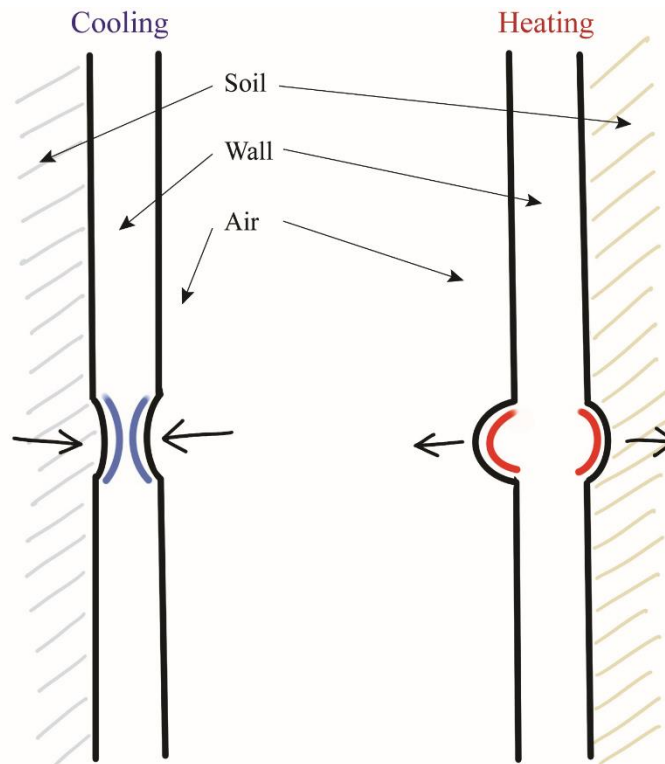


Figure 8.28 Sketch of the longitudinal deformed shape: plan view of the -2 level. NOTE: the figure is not scaled

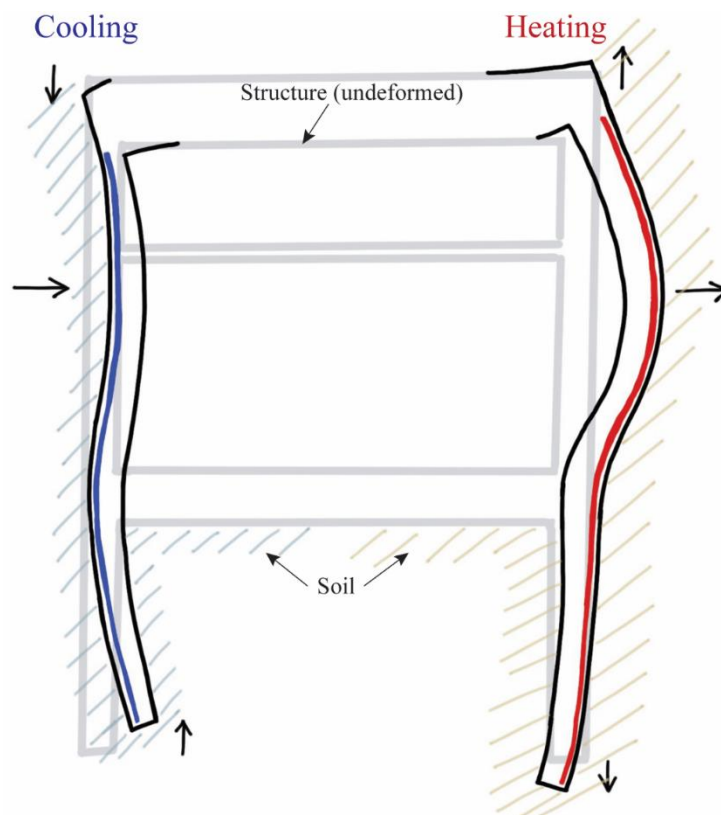


Figure 8.29 Sketch of the vertical deformed shape at a vertical cross section. NOTE: the figure is not scaled

Such results allow to have a qualitative representation of the thermomechanical behavior of the EW. The experimental setup used here, cannot capture a quantitative and exhaustive definition of the thermomechanical wall behavior, because of constraints for the sensor's installation (i.e., the EW was already constructed at the moment of our involvement in this project, and there was no possibility to install a monitoring system at the extrados). A comparison can be done with the only available in-situ results on an energy piled wall in Vienna (Brandl, 2016). The results reported in this thesis are consistent with the ones reported by Brandl (2016), which show maximum seasonal relative strains up to  $200 \mu\epsilon$ , located towards the mid-height of the underground tunnel. However, the strain measurement direction, as well as the magnitude of the temperature variation distribution in the wall are not mentioned by the author.

To estimate the intensity of internal actions developed consequently to the partial blocking of thermally induced deformations, the analytical model presented at section 6.2.3 is employed. Figure 8.30 shows the deflection, bending moment and shear force induced to the EW during heating (red curve) and cooling (blue curve) tests. The deflection ( $y$ ) shows very small transversal displacements with maximum up to  $y = 1.5 \text{ mm}$ . Bending moment exhibits a maximum at the bottom part of the excavated side, with maximum intensity of  $M_{max}^{th} = 480 \text{ kNm}$ . Shear force shows a maximum at the top wall-beam connection with intensity of  $V_{max}^{th} = 100 \text{ kN}$ .

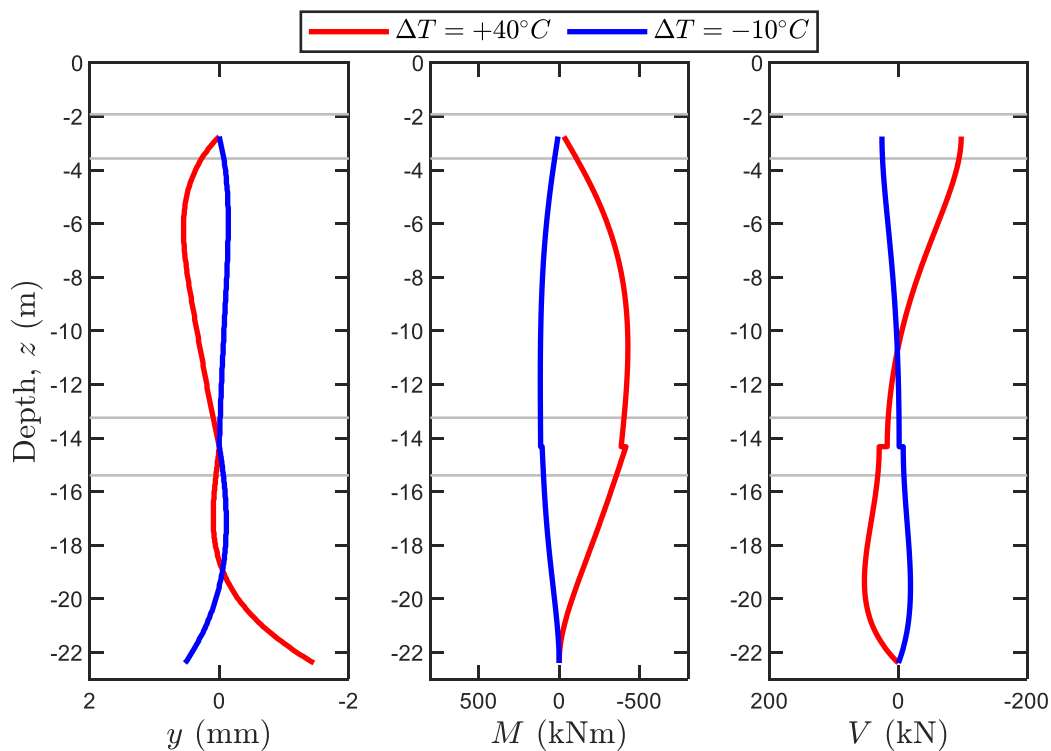


Figure 8.30 Evaluation of deflection and internal actions through the analytical model proposed at section 6.2.3 featuring for thermal loads only (positive signs of rotation and internal actions refer to Figure 6.16).

Deflection is very small when compared with the maximum allowable transversal displacement to avoid reaching serviceability limit state,  $d_{h,max} \cong 20$  mm.

A detailed comparison accounting for thermal and mechanical load combinations is performed through 3D finite element thermomechanical numerical analyses. The model formulation is detailed in the Appendix A, while the definition of material properties and analysis execution details are available in the Appendix E. A comparison among the experimental and the numerical results is firstly performed accounting only for thermal loads by simulating the December 2019 heating test and the March 2020 cooling test. The results of such comparison, referring to the tunnel intrados deformations, are reported in Figure 8.31 showing closed agreement.

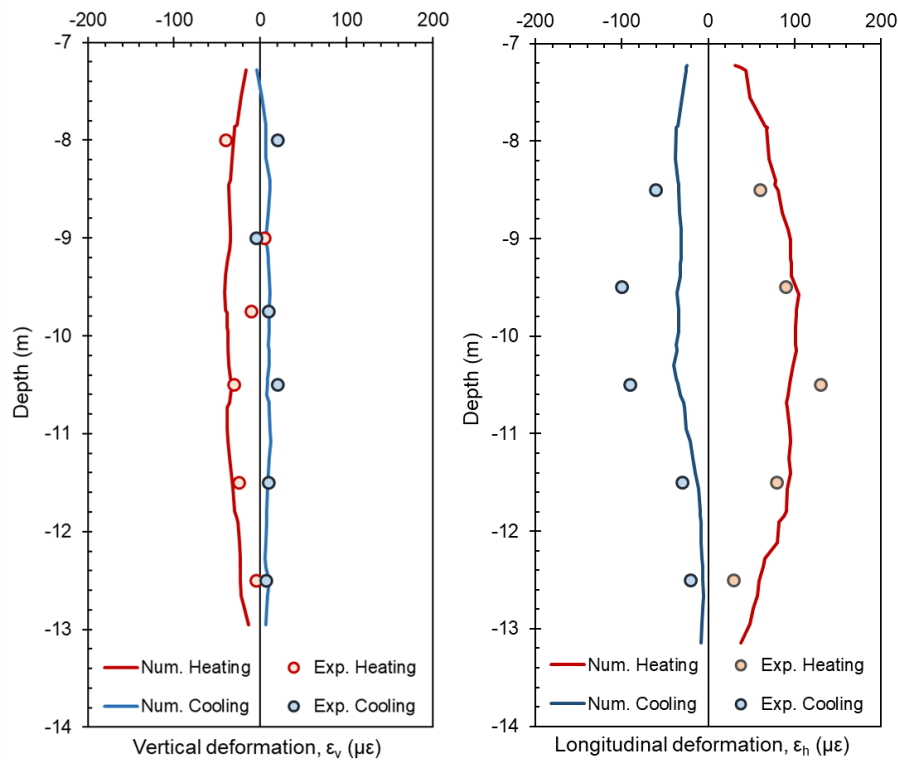


Figure 8.31 Comparison among the experimental and numerical results for the heating (December 2019) and cooling (March 2020) tests

Secondly, a series of numerical analyses is performed, focusing at analyzing all possible ultimate (ULS) and serviceability (SLS) limit states accounting for simultaneous thermal and mechanical actions in accordance to the Swiss Norm (SIA 197, 2004; SIA 197/1, 2004; SIA 260, 2003; SIA 261 and 261/1, 2003; SIA 262, 2003; SIA 267 and 267/1, 2003). In conjunction to geothermal operation, and following the design details of the UEI, additional mechanical loads are included, which are: train load, ballast load and structural surcharges at level -2, crowding load at level -1, road traffic, embankment and pedestrian surcharges at level 0 (Figure 8.32, Table 8.3). Following the Swiss Norm, the following load combinations for ULS (8.9) and SLS (8.10) are considered.

$$1.35 \sum_i G_i + 1.5 \left( \sum_i Q_i + q_T T \right) \quad (8.9)$$

$$\sum_i G_i + \sum_i Q_i + q_T T \quad (8.10)$$

$$\sum_i G_i + 0.6 \sum_i Q_i + T$$

Where  $G_i$  and  $Q_i$  are detailed in Table 8.3,  $T$  represents the yearly profile of heat carrier fluid temperature imposed at the inflow point.  $q_T = 0.6$  represents a non-dimensional multiplier, as from the Swiss Norm.

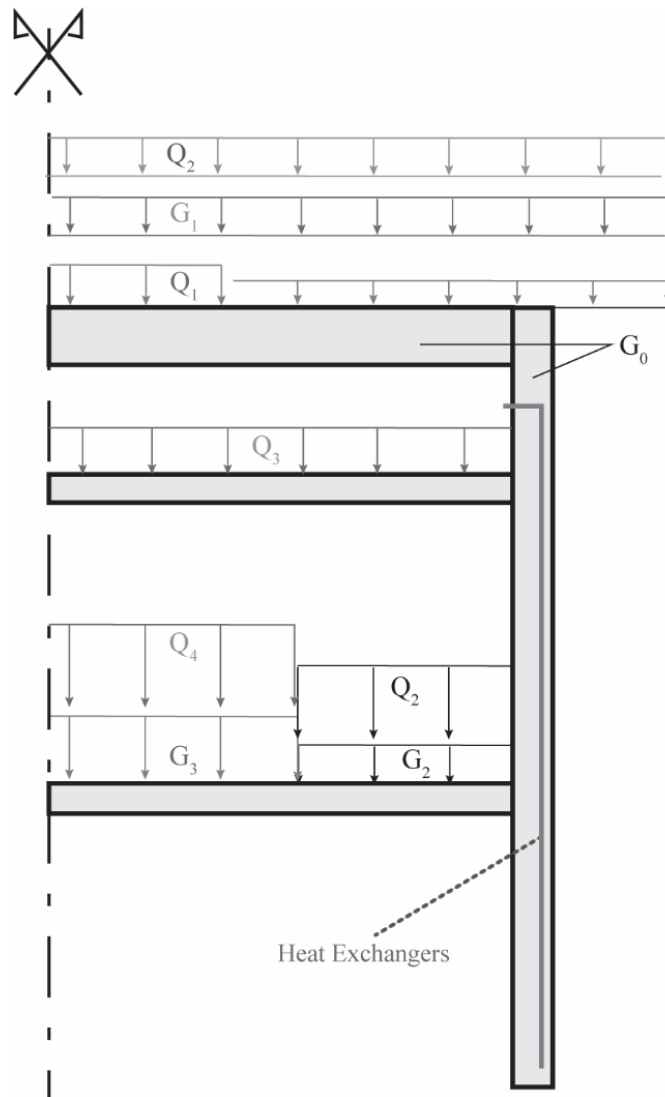


Figure 8.32 Sketch of the geostructural geometry over a vertical cross section in correspondence of the heat exchangers with indications of the mechanical loads detailed in Table 8.3

Table 8.3 Description of the mechanical loads considered for the thermomechanical analysis

Name	Description	Value	Unit
<i>Dead loads</i>			
$G_0$	Structure unit weight	25.0	kN/m <sup>3</sup>
$G_1$	Embankment surcharge	56.0	kN/m <sup>2</sup>
$G_2$	Structural surcharge	40.0	kN/m <sup>2</sup>
$G_3$	Rail ballast	22.0	kN/m <sup>2</sup>
<i>Live loads</i>			
$Q_1$	Road traffic (tramway)	26.6	kN/m <sup>2</sup>
		2.3	kN/m <sup>2</sup>
$Q_2$	Pedestrian load	4.0	kN/m <sup>2</sup>
$Q_3$	Crowding surcharge	10.0	kN/m <sup>2</sup>
$Q_4$	Train load	92.4	kN/m <sup>2</sup>

Figure 8.33 and Figure 8.34 show the results for the EW axial displacements and internal actions evaluated at the cross section in correspondence of the heat exchangers. It is worth noting that the deformed and internal actions shapes are different with respect to Figure 8.30 because what is shown at Figure 8.33 and Figure 8.34 are the results for the loading combination that maximizes each effect.

Vertical behavior of the EW is driven by the settlement (i.e., negative displacement) induced by the application of mechanical actions. During heating the EW partly expands, reducing the overall settlement. The null point is located at the fully embedded portion, in the vicinity of the EW toe. The opposite was recorded for cooling.

Thermal actions have a primary role in defining transversal (i.e., horizontal) displacements, consequently to the bending effects induced by the non-uniform temperature distribution. The recorded values are largely respecting the maximum acceptable limits defined by the Swiss Norm.

Internal actions follow the general behavior defined by the mechanical loads' application, with major variations located at the wall-slab interactions because of structural stress redistribution within the structure, particularly for axial force and shear force. Bending moment shows larger discrepancies among the isothermal and non-isothermal cases, with the maximum difference that is in closed agreement with Figure 8.30. Negative bending moment (Figure 8.34) upon heating means that traction develops at the intrados while contraction develops at the extrados due to the blocked portion of thermal expansion during heating (i.e., summer operation). The opposite was recorded during winter operation. The maximum internal actions capacities of the structure (i.e., resistant axial action, resistant bending moment, resistant shear force) are respected.

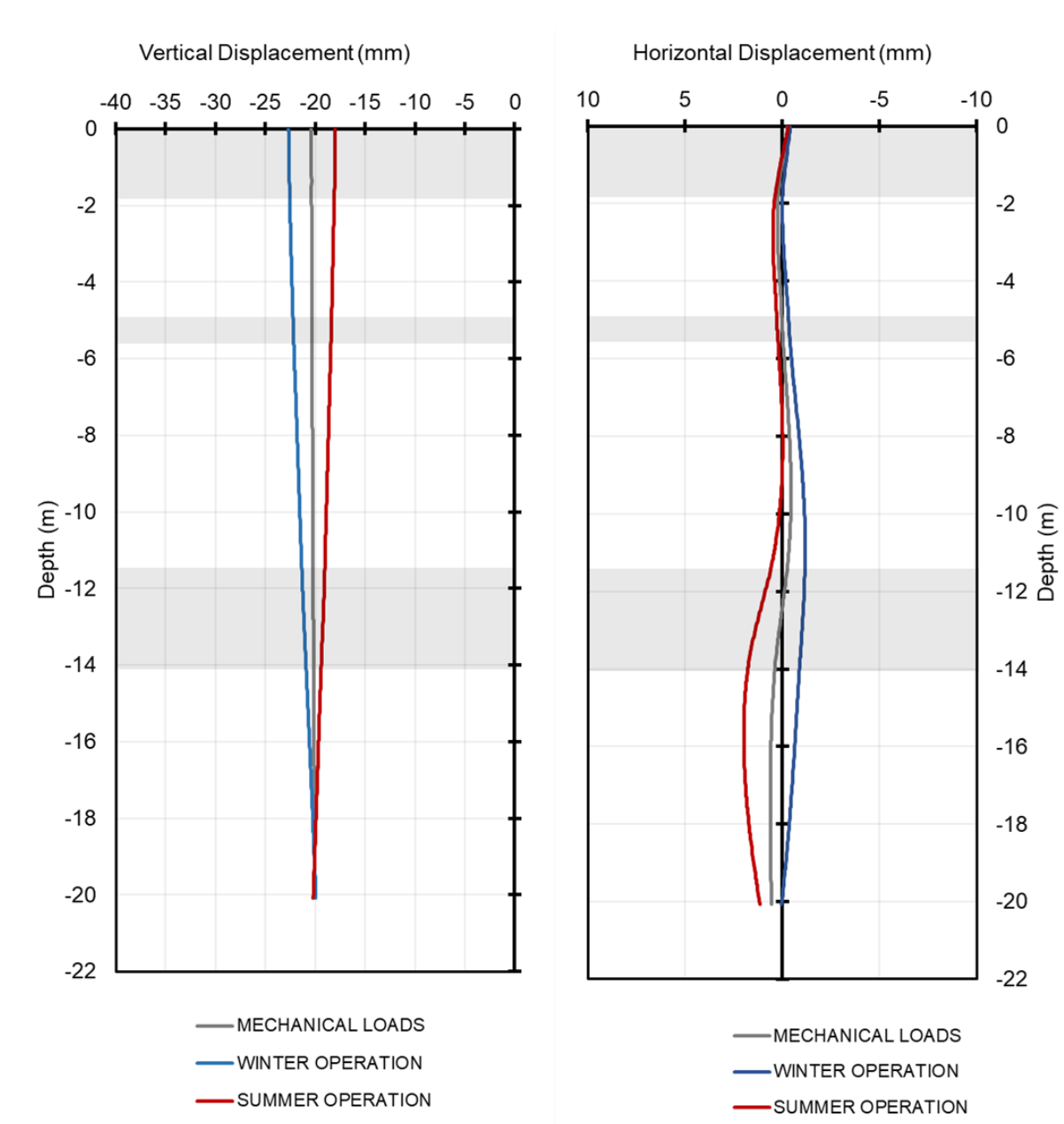


Figure 8.33 Wall axis vertical and horizontal displacement at SLS: results from 3D numerical thermomechanical model

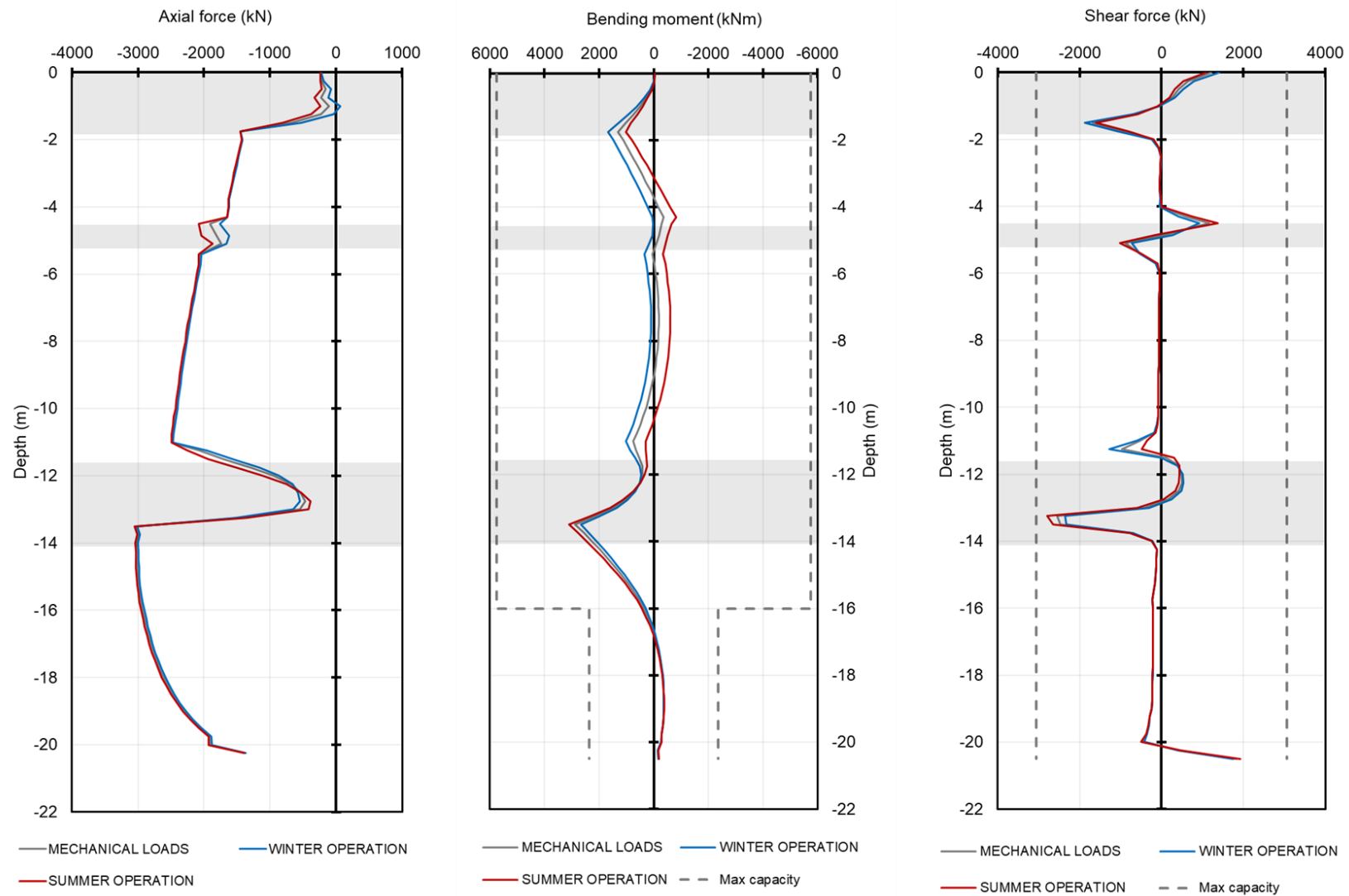


Figure 8.34 Internal actions in the wall at ULS: results from 3D numerical thermomechanical model



## 8.5 Main observations and outcomes from the in-situ activities

In conclusion to the analysis of the in-situ testing campaign and the related numerical modeling, the following main observations can be drawn:

- The wall-tunnel hydrothermal interactions show a strong correlation between the tunnel temperature and the external temperature, high seasonal temperature variations and a relatively low speed, scatter, wind velocity profile, if compared with respect to measurements on existing tunnels available in the literature (He et al., 2020; Jin et al., 2020; Pflitsch et al., 2012; Pflitsch & Kuesel, 2003; Steinemann et al., 2004; Woods & Pope, 1981; Zhao et al., 2020).
- Low-magnitude wind velocity induces low convective heat exchanges, hence low heat flux at the wall-tunnel interface. Additionally, the presence of the glass wall (Figure 8.5) in the tunnel dramatically reduces the wind speed profile, highlighting the boundary layer of the wind velocity at the wall-tunnel interface. It results that the tunnel, under certain circumstances, may act as a thermal resistance rather than as a conductor.
- High seasonal temperature variations at the boundary conditions induce non-negligible yearly temperature variations within the UEI.
- The UEI shows a very high heat storage potential (i.e., summer operation). The main key aspects that highlight the heat storage potential are: (i) the predominant heat exchange mechanism is conduction in the wall and in the soil, with absence of groundwater flow in the soil; (ii) the low heat flux magnitude at the wall intrados, minimizing heat losses towards the tunnel and acting as a natural insulator; (iii) the high capacity of storing heat developing high HCF temperature differences between the inflow and the outlet during heating tests.
- During winter operation, the UEI has a limited operative HCF temperature range. The employment of glycoled fluids to replace water is strongly suggested for future operations, as it would allow to reach HCF temperatures  $T_f < 0$  °C avoiding freezing issues within the HP and the surrounding, and consequently increasing the thermal potential.
- From a thermomechanical perspective, the UEI is very stiff. It is hence able to undergo high internal actions without mobilizing displacement (i.e., high mechanical capacity). The design limits are successfully respected.

These observations will be used in the following as a baseline to define the thermal potential of the entire UEI installation.

## 8.6 Determination of the thermal potential of the underground energy infrastructure

The objective of this section is to quantify the thermal potential of the whole installation. First of all, it is needed to upscale the behavior from the single tested energy wall to the behavior of the whole installation, which includes EW and energy slabs (ES). Then, the thermal potential of the whole station should be maximized by ensuring the respect of the design requirements.

In the following, the design requirements are firstly assessed. Secondly, an elementary unit is identified as a representative portion of the heat exchangers circuit installed onsite and its thermal behavior is studied. Finally, four different thermal exploitation scenarios are identified and modelled. For each scenario, the upscaling from the elementary unit to the whole station's thermal behavior is evaluated.

### 8.6.1 Definition of the design parameters and of the analysis tools

In this section, the design parameters are firstly defined. Secondly, the tool used in the following to perform the thermal and energy evaluations is described.

Design limits on energy geostructures operation are usually referred to limitations to the operational HCF temperature or to the temperature of materials surrounding the energy geostructure (EG) (e.g., soil and concrete) (e.g., CFMS-SYNTEC-SOFFONS-FNTP, 2017). HCF temperature limits usually refer to technological limits imposed by the chosen components. A typical example is to avoid freezing inside the HP. However, HP that are able to work at negative (Celsius) temperatures exist and, by engineering the chemical composition of the HCF, it is possible to inject fluids at negative temperatures. It follows that limitations of HCF temperatures are due to technological limitations: different designs may lead to different temperature limits.

Conversely, limitations of the temperature within the EG (i.e., soil and concrete) are based on physical aspects. Particularly, avoiding freezing of the saturating fluid in porous media is paramount because of the implications that it has during freezing-thawing processes (e.g., pore water pressure variations may induce important modifications of the effective stress state affecting the local mechanical stability).

For these reasons, the temperature limitations are related to defining maximum and minimum temperatures ( $T_{EG}$ ) evaluated at the portion of the EG that undergoes to the strongest temperature variations during thermal operation: the soil-wall interface and the structure temperature facing the excavated side. In the following, temperature will be evaluated at the six locations (i.e., A to F) as indicated in Figure 8.5. The temperature limits are, hence:

$$0\text{ °C} < T_{EG} < 50\text{ °C} \quad (8.11)$$

The lower limit is chosen to avoid freezing of materials, while the upper limit is chosen as an average value for heat storage applications (Gehlin, 2016) or for energy geostructures used for “cooling dominated” (Anis Akrouh et al., 2020) behavior. It follows that the HCF temperature is allowed to be  $T_f < 0\text{ °C}$  and/or  $T_f > 50\text{ °C}$  as long as the  $T_{EG}$  ranges within the limits.

The tool used in the following to investigate the thermal potential is 3D finite element hydrothermal numerical modelling employing the numerical model detailed at section 7.4.2. Two modifications of such model are performed.

Firstly, a little modification that allows to impose a thermal power to the heat exchangers instead of an inflow temperature is performed. The thermal power of the heat exchangers is known, and it is imposed through a time-dependent function. A new boundary condition at the HCF inflow point allows to impose at each time step the inlet temperature depending on the outlet temperature at the previous time step, to simulate the temperature difference at the heat pump evaporator due to the extraction/injection of a given thermal power.  $T_{f,in}$  is evaluated by reverting equation (8.1). The flowrate of the circulating HCF is set to  $\dot{V} = 20\text{ l/min}$ , taken as an average value from the experimental, in-situ, results.

Secondly, the material defining the HCF is modified. To allow for an operative temperature range that goes down to  $T_f = -10\text{ °C}$ , the water is replaced with a 20% in volume glycoled mixture (MEG20), whose thermo-hydraulic properties are retrieved from Batini et al. (2015) and VDI V. (2010).

### 8.6.2 Definition of the elementary unit and upscaling to the entire installation’s behavior

In this section, focus is given on how to model the whole UEI, given the existing design implemented in-situ. The UEI design follows a pattern which features heat exchangers installed in the walls and in the base slab (i.e., bottom slab of level -2). Following the number of loops and the piping circuit, the UEI is composed by  $n_{EU} = 20$  elementary units (i.e., subscript “EU” means elementary unit). Each elementary unit is composed by  $n_W = 8$  wall loops and  $n_S = 1$  slab loop. Heat exchangers loops are connected in parallel to the main pipe collectors, as sketched in Figure 8.35.

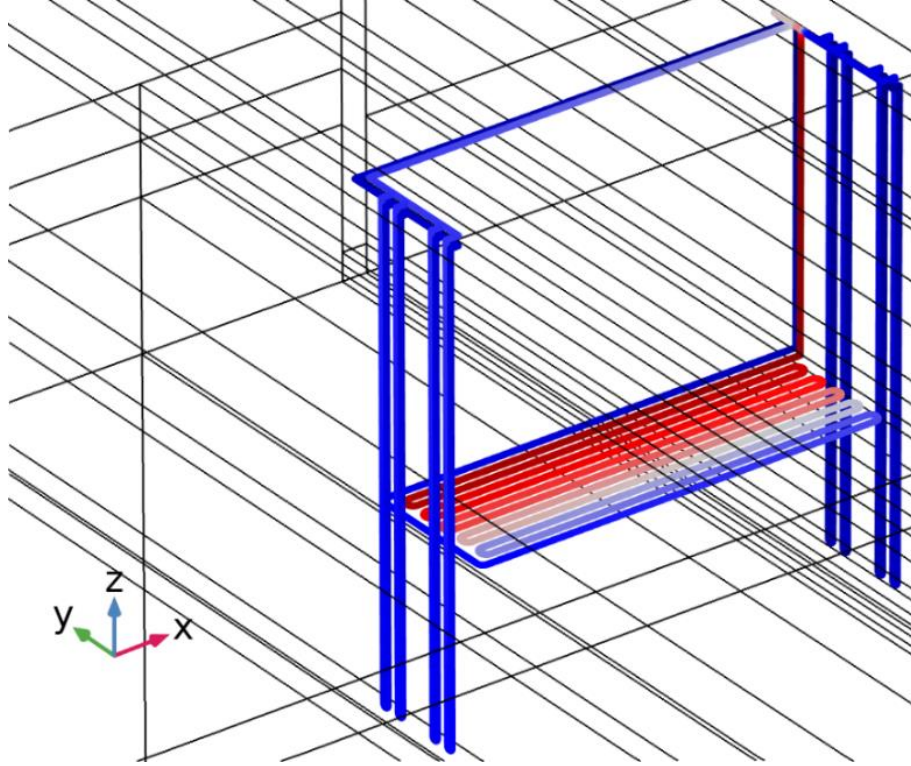


Figure 8.35 Sketch of one elementary unit featuring 8 wall U-loops and one slinky-shaped slab loop, connected in parallel

Following the heat exchangers' design, the thermal response of different shapes (i.e., wall and slab) is different, hence they have to be modelled to thoroughly represent realistic conditions. In this view, the elementary unit aims at standardizing the thermal response of a slice of the UEI. Then, the overall response is evaluated through the hypothesis that all the elementary units behave equally. Since they are all connected in parallel, from the conservation of energy and of mass, the thermal power of the entire installation from the primary circuit ( $P_{th,S}$ ) can be written as:

$$P_{th,S} = n_{EU} P_{th,EU} \quad (8.12)$$

where  $P_{th,EU}$  is the thermal power of an elementary unit.

The delivered thermal power is evaluated considering a constant coefficient of performance for the heat pump for both heating and cooling of  $COP = 4$  (Brandl, 2006). The thermal power delivered to the served structure ( $P_{th}$ ) and the energy ( $E_{th}$ ) can be evaluated as:

$$P_{th} = \frac{P_{th,S} COP}{COP - 1} \quad (8.13)$$

$$E_{th} = t P_{th} \quad (8.14)$$

Where  $t$  is the time. With the objective being to define the maximum thermal potential and to guarantee long term (i.e., over 20 years of operation) sustainability of the thermal exploitation, the model simulates

the continuous HP operation and cannot capture the thermal behavior upon very short thermal demands (e.g., daily or hourly operations).

In the following, two additional evaluations are performed. Per each month, the surface and number of units for apartments and offices to which the energy could be delivered is evaluated after a dedicated literature review (ENTRANZE, 2014; Sutman et al., 2020; Zangheri et al., 2014). As reference cases, apartments of 40 m<sup>2</sup> and offices of 20 m<sup>2</sup> are used.

### 8.6.3 Determination of the thermal potential

In this section, the thermal potential of the whole site is evaluated through the definition of four possible scenarios for thermal exploitation, representative of realistic thermal behaviors. To save computation time, the energy behaviour of the building is simulated as a continuous extracted power with a varying amplitude rather than a constant power extracted for varying durations. Those methodologies are equivalent as the energy is evaluated as the integral of the power curve in the function of time according to equation (8.14). Four typical behaviours in the form of yearly demand profiles are investigated in this section. The first case is represented by a sinusoidal demand, representative of recent buildings. The second case is represented by a thermal demand curve typical of existing buildings in the European climate, defined after a dedicated literature review. The third case is represented by a modification of the second case where summer operation is maximized. The fourth case represents the case where the UEI is the main thermal central for the neighbourhood.

For each case, the curve representing the yearly thermal demand profile is firstly defined in form of a dimensionless parameter,  $f_{th}$ . Such curve is then multiplied by a scalar factor (strictly positive),  $P_{max}^{th}$ , that defines the maximum amplitude of the thermal demand which is determined through numerical analyses to respect the design limits previously introduced. The dimensionless thermal demand curves for each of the four analyzed scenarios are shown in Figure 8.36. Positive values indicate winter operation (i.e., heat extraction from the ground) while negative values indicate summer operation (i.e., heat injection in the ground).

In the following, each scenario is firstly defined, followed by the results of the analyses. A comparison and discussion of the results for the four scenarios is eventually reported.

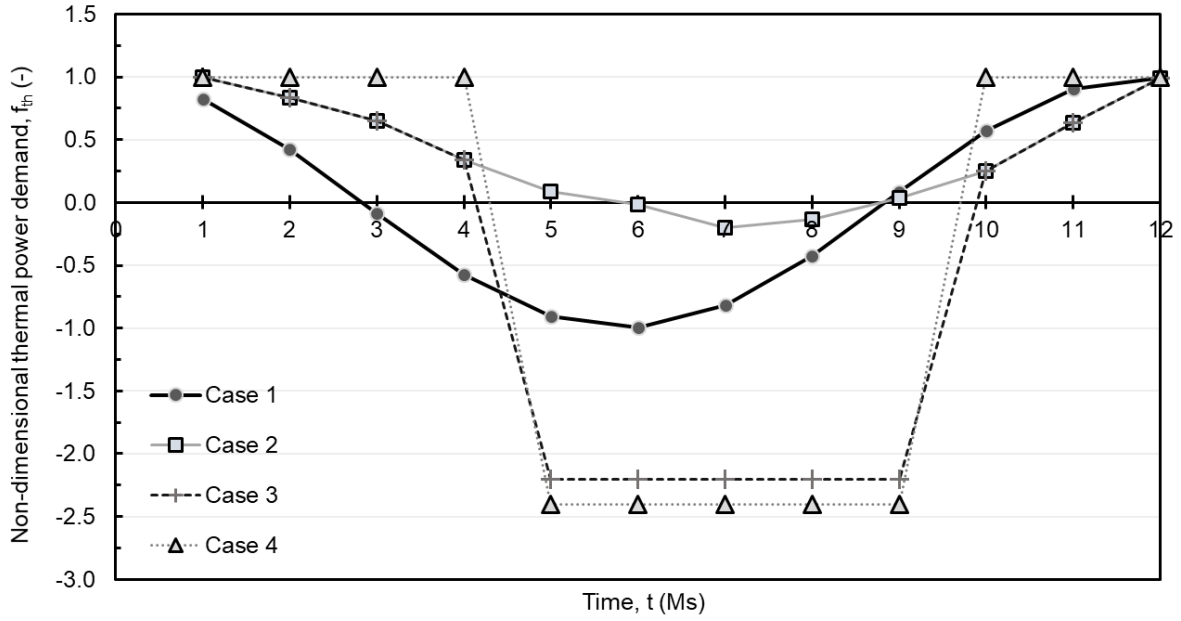


Figure 8.36 Yearly dimensionless thermal demand curves

#### 8.6.3.1 Case 1: sinusoidal thermal demand

The first scenario is defined by employing a sinusoidal thermal demand curve (Figure 8.36) which presents a maximum at the peak of the winter thermal demand and a minimum in correspondence to the peak for summer operation. A sinusoidal curve is representative of the energy demand of recent and new buildings in European climates built following demanding energy performance regulations so that the winter heating demand is similar to the summer cooling demand. Additionally, such definition allows for an easy determination of the peak value,  $P_{1,max}^{th}$ , and to consequently identify which of the design limits is reached first. Also, such a curve is balanced in terms of heating and cooling power, hence ensuring a constant, periodical behavior on a yearly basis. Such periodic behavior ensures the long-term sustainability of the UEI because the soil temperature remains within acceptable limits.

The thermal demand curve for Case 1,  $P_i^{th} = P_1^{th}$ , with  $i = 1, 2, 3, 4$  representing the numbering for each considered case in the following, is defined as:

$$P_1^{th} = P_{1,max}^{th} f_{th,1} = P_{1,max}^{th} \cos(2\pi t + p_s) \quad (8.15)$$

where  $P^{th}$  is the thermal power in W,  $P_{1,max}^{th}$  is the maximum thermal power,  $f_{th,1}$  represent a fraction of the thermal power as a function of time with  $f_{th,1} \leq +1$ , with the maximum value representing the maximum heating demand,  $t$  is the time in years and  $p_s = 1/12$  is a phase shift in years. The elapsed time starts from January, and  $p_s$  represent the shifting of the peak demand of one month with respect to the initial condition.

$P_{max}^{th}$  is increased until one of the absolute maximums of the design parameters is triggered. In this case, the lower limit of the soil temperature,  $T_{EG,min} = 0^\circ\text{C}$ , is triggered for a value  $P_{1,max}^{th} = 2 \text{ kW}$ .

To check the respect of the design limits, the temperature profile is evaluated at the locations shown in Figure 8.5 (points A to F). Since the thermal demand is balanced and the consequent thermal response is periodical, the thermal behavior is zoomed in the first 5 years. Figure 8.37 shows the temperature values at selected locations. The locations that undergo to the most severe temperature changes between winter and summer are those at the wall-soil interface (i.e., A, B and C).

Figure 8.37 clearly shows that with a sinusoidal thermal demand the design limit for winter operation,  $T_{EG} > 0$ , is triggered, but the thermal potential for summer operation is not well used. The maximum recorded temperature is  $T_{EG} \cong 30^\circ\text{C}$  which leaves room for further improvement of the thermal demand curve for summer operation. The heat carrier fluid temperature at the main inflow and outflow of each elementary unit ranges among  $-3^\circ\text{C} \div +33^\circ\text{C}$  (Figure 8.38).

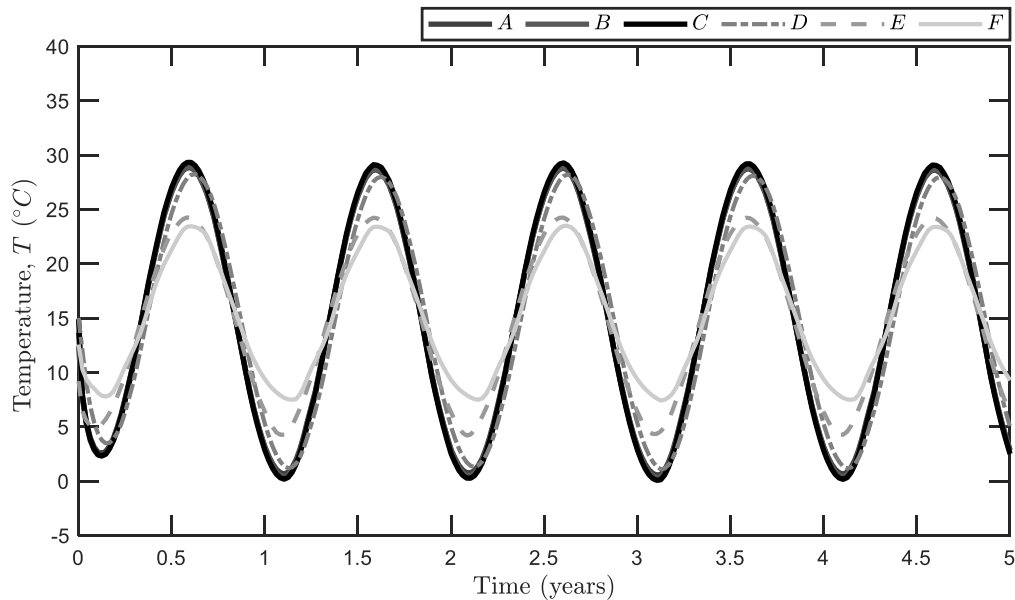


Figure 8.37 Temperature evaluated at the points A to F indicated in Figure 8.5 for case 1

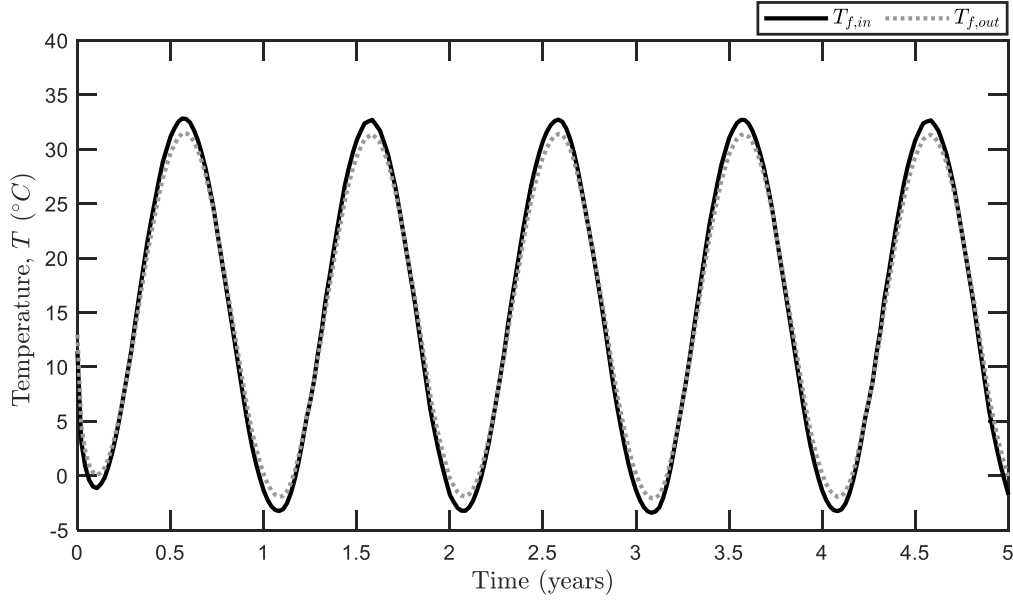


Figure 8.38 Heat carrier fluid temperature for case 1

Based on the procedure detailed at section 8.6.2, the annual energy delivered for heating amounts to  $E_{th,W} = 148$  MWh/y, the annual energy delivered for cooling amounts to  $E_{th,S} = -148$  MWh/y. The total annual energy delivered reaches  $E_{th} = 295$  MWh/y.

#### 8.6.3.2 Case 2: Typical thermal demand curve for apartment or office building

The second scenario employs the typical thermal demand curve for apartments or offices. This curve is representative of existing buildings. Such curve is defined from a dedicated literature review. Zangheri et al. (2014) reported thermal demand curves for ten different European cities and for different uses (i.e., single houses, apartment and office buildings) (ENTRANZE, 2014). The city of Geneva (Switzerland) was not included in that study, hence the evaluation was done on the basis of evaluating the average monthly needs from the data for Milan (Italy), Vienna (Austria) and Paris (France), being the three closest cities to Geneva. From such data, the non-dimensional monthly thermal demand curve for apartments and offices,  $f_{th,2}$ , was derived and it is reported in Figure 8.39. Being the two thermal demand curves very similar, the average between the apartments' and the offices' thermal demand curve for Case 2 is shown in Figure 8.36 and it is employed in the following.



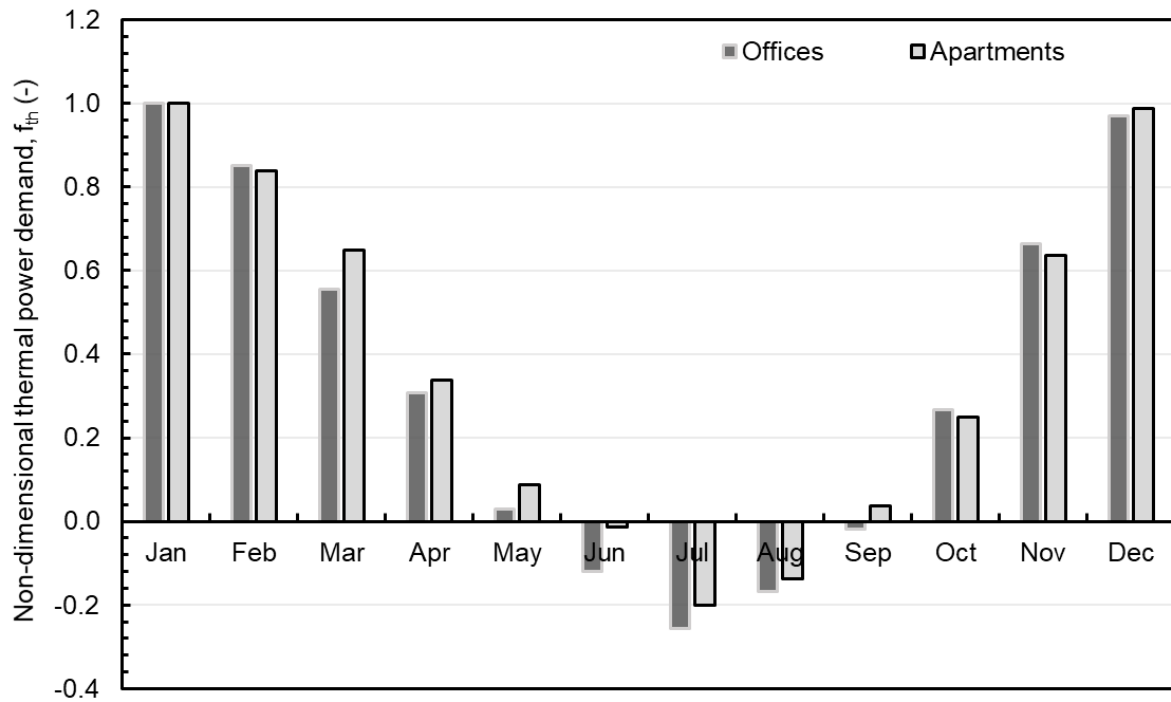


Figure 8.39 Details of the thermal demand curve for offices and apartments after a dedicated literature review

The thermal demand curve,  $P_2^{th}$ , is hence defined as:

$$P_2^{th} = P_{2,max}^{th} f_{th,2} \quad (8.16)$$

The main features of this case are: (i) high heating demand during winter; (ii) low cooling demand during summer; (iii) rest phase corresponding to May, June and September.

The amplitude,  $P_{2,max}^{th}$ , has to be determined so that to satisfy the prescribed design limits. In this case, the lower limit of the soil temperature,  $T_{EG,min} = 0^\circ\text{C}$ , is triggered for a value  $P_{2,max}^{th} = 1.6 \text{ kW}$ .

To check the respect of the design limits, the temperature profile is evaluated at the locations shown in Figure 8.5 (points A to F). Figure 8.40 shows the temperature values at selected locations. The locations that undergo to the most severe temperature changes between winter and summer are those at the wall-soil interface (i.e., A, B, C and D).

With this curve, the lower design limit,  $T_{EG} > 0^\circ\text{C}$  is triggered, but the thermal potential for summer operation remains considerably unexploited: the maximum temperature reached is  $T_{EG} \cong 30^\circ\text{C}$ . The heat carrier fluid temperature at the main inflow and outflow of each elementary unit ranges among  $-2^\circ\text{C} \div +20^\circ\text{C}$  (Figure 8.41).

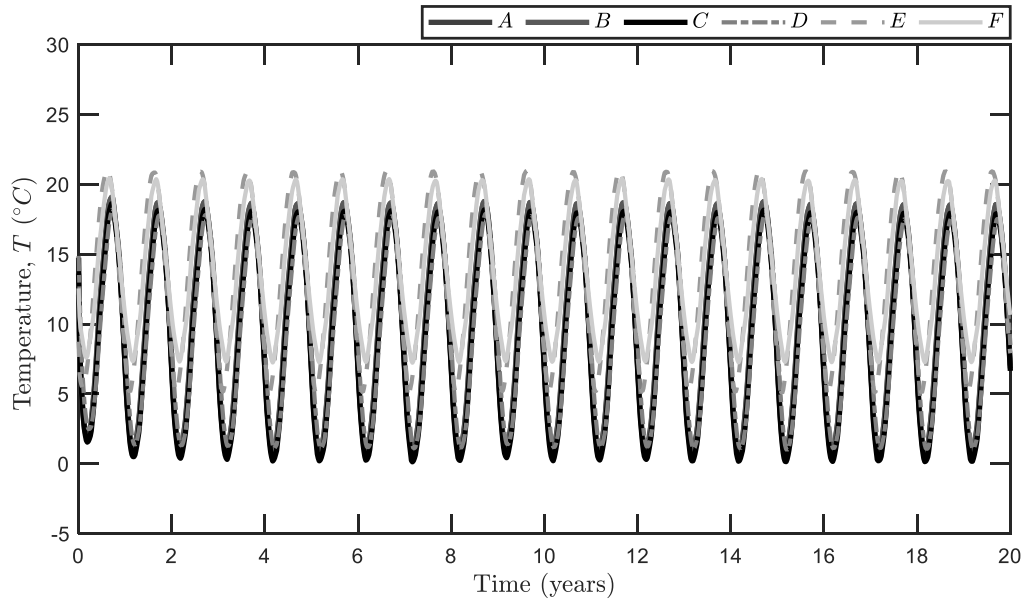


Figure 8.40 Temperature evaluated at the points A to F indicated in Figure 5 for case 2

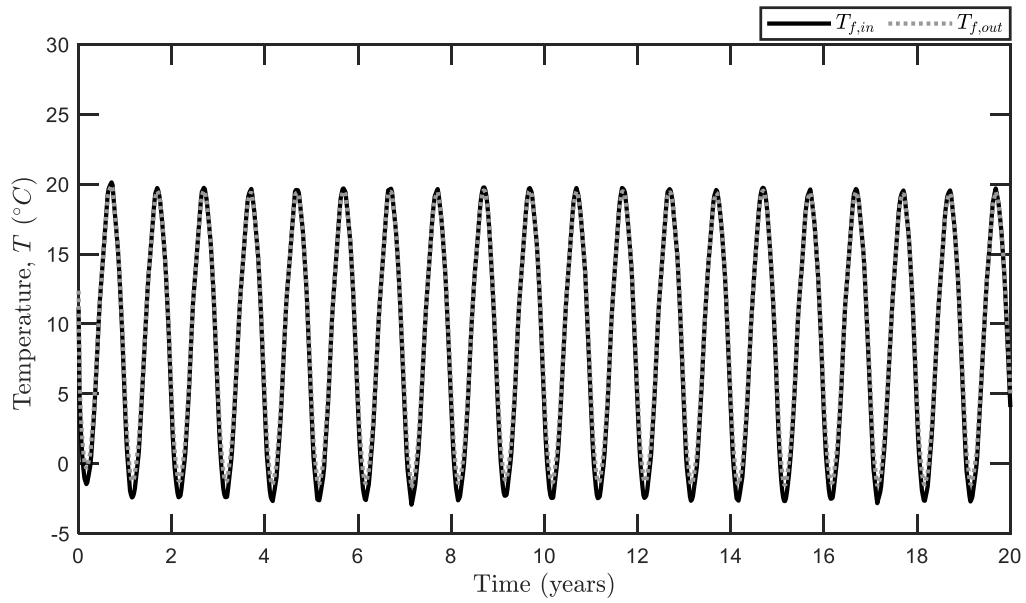


Figure 8.41 Heat carrier fluid temperature for case 2

Based on the procedure detailed at section 8.6.2, the annual energy delivered for heating amounts to  $E_{th,W} = 150$  MWh/y, the annual energy delivered for cooling amounts to  $E_{th,S} = -11$  MWh/y. The total annual energy delivered reaches  $E_{th} = 161$  MWh/y.

This scenario will be kept as a reference case in the following, as it represents the most realistic case for the application to existing residential and office buildings. Case 2 will be used as reference case for the evaluation of the surface to which the energy could be delivered.

### 8.6.3.3 Case 3: Modified curve for apartments and offices

The third scenario aims at maximizing the thermal potential for summer operation, by employing the curve presented at Case 2 for winter (that already reaches the lower temperature design limit) and modifying the summer behavior ( $f_{th,3}$  as from Figure 8.36). This optimised scenario with a modified summer operation could, for example, correspond to the injection of excessive solar thermal power production in the ground during summer. Rest periods and summer behavior are used to heat up the soil (i.e., heat injection) so that to consequently increase the thermal behavior during heat extraction. The result is an unbalanced curve with predominant summer operation.

The thermal demand curve,  $P_3^{th}$ , is hence defined as:

$$P_3^{th} = P_{3,max}^{th} f_{th,3} \quad (8.17)$$

The amplitude,  $P_{3,max}^{th}$ , has to be determined so that to satisfy the prescribed design limits. In this case, the upper limit of the soil temperature,  $T_{EG,max} = 50$  °C, is triggered for a value  $P_{3,max}^{th} = 2.0$  kW.

To check the respect of the design limits, the temperature profile is evaluated at the locations shown in Figure 8.5 (points A to F). Figure 8.42 shows the temperature values at selected locations. The locations that undergo to the most severe temperature changes between winter and summer are those at the wall-soil interface (i.e., A, B, C and D).

This curve allows to reach the upper temperature limit, and the lower limit is almost reached ( $T_{EG,min} \cong 1$  °C). The heat carrier fluid temperature at the main inflow and outflow of each elementary unit ranges among  $-2$  °C ÷  $+55$  °C (Figure 8.43).

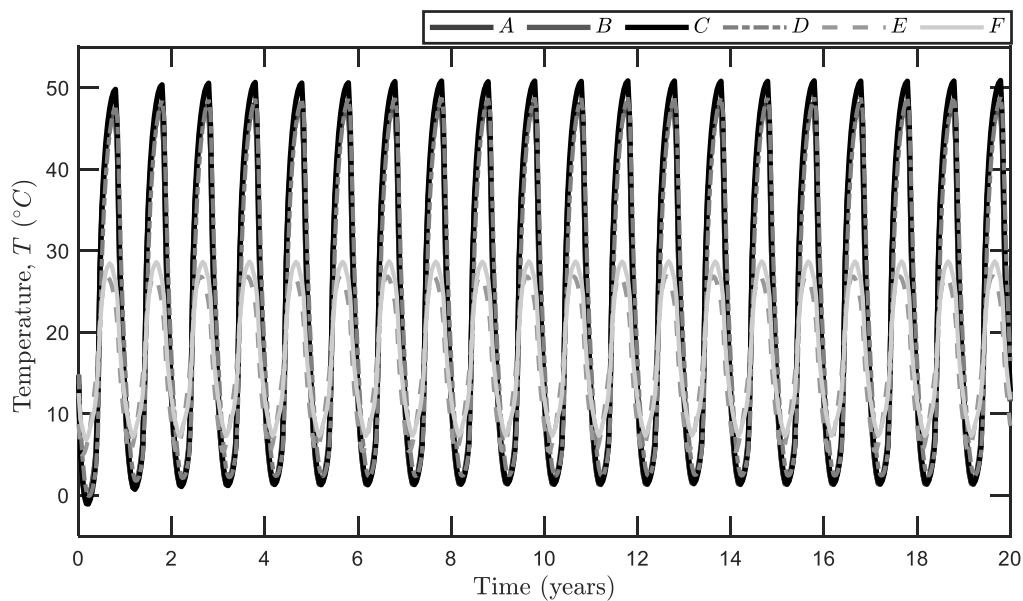


Figure 8.42 Temperature evaluated at the points A to F indicated in Figure 8.5 for case 3

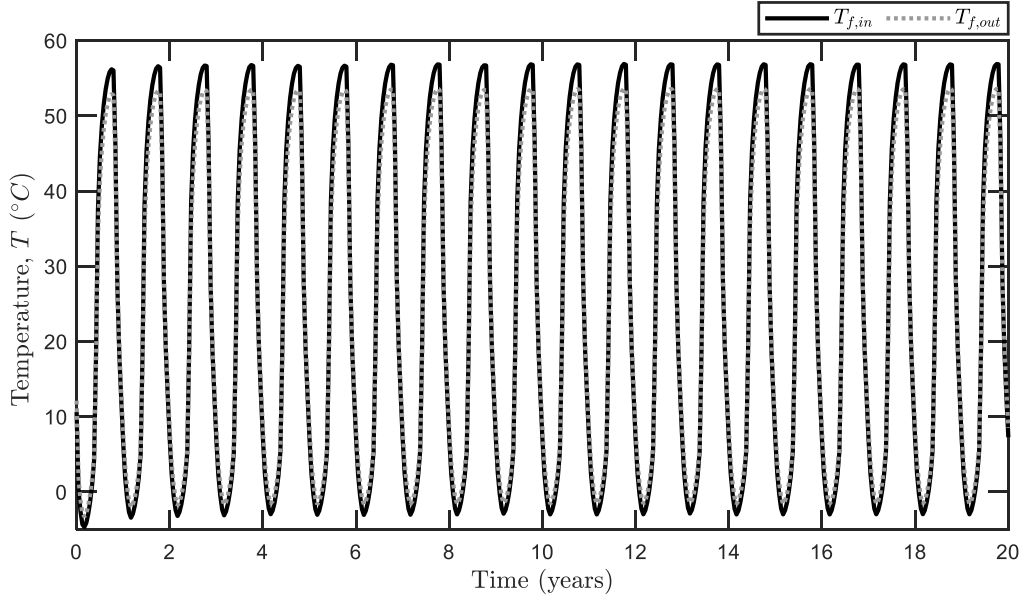


Figure 8.43 Heat carrier fluid temperature for case 3

Based on the procedure detailed at section 8.6.2, the annual energy delivered for heating amounts to  $E_{th,W} = 182$  MWh/y, the annual energy delivered for cooling amounts to  $E_{th,S} = -423$  MWh/y. The total annual energy delivered reaches  $E_{th} = 606$  MWh/y.

#### 8.6.3.4 Case 4: Maximization of thermal resources

The 4<sup>th</sup> scenario aims at simulating the case where the UEI installation acts as a thermal central for the neighbourhood equipped with a district heating network. Such network would thus act as a buffer system between the UEI installation and the buildings so that the UEI could be operated more independently from the specific demand profile of the buildings. The UEI operation is hence made to constantly maximize heating and cooling operations, as shown in Figure 8.36 reporting  $f_{th,4}$ . No rest periods are envisaged. The summer behavior allows to increase the soil temperature so that to maximize winter operation, too, by taking advantage of the high storage potential. The result is an unbalanced thermal operation, with predominant summer behavior.

The thermal demand curve,  $P_4^{th}$ , is hence defined as:

$$P_4^{th} = P_{4,max}^{th} f_{th,4} \quad (8.18)$$

The amplitude,  $P_{4,max}^{th}$ , has to be determined so that to satisfy the prescribed design limits. In this case, both design limits are triggered for a value  $P_{4,max}^{th} = 1.8$  kW.

To check the respect of the design limits, the temperature profile is evaluated at the locations shown in Figure 8.5 (points A to F). Figure 8.44 shows the temperature values at selected locations. The locations

that undergo to the most severe temperature changes between winter and summer are those at the wall-soil interface (i.e., A, B, C and D).

The heat carrier fluid temperature at the main inflow and outflow of each elementary unit ranges among  $-3\text{ }^{\circ}\text{C} \div +55\text{ }^{\circ}\text{C}$  (Figure 8.45).

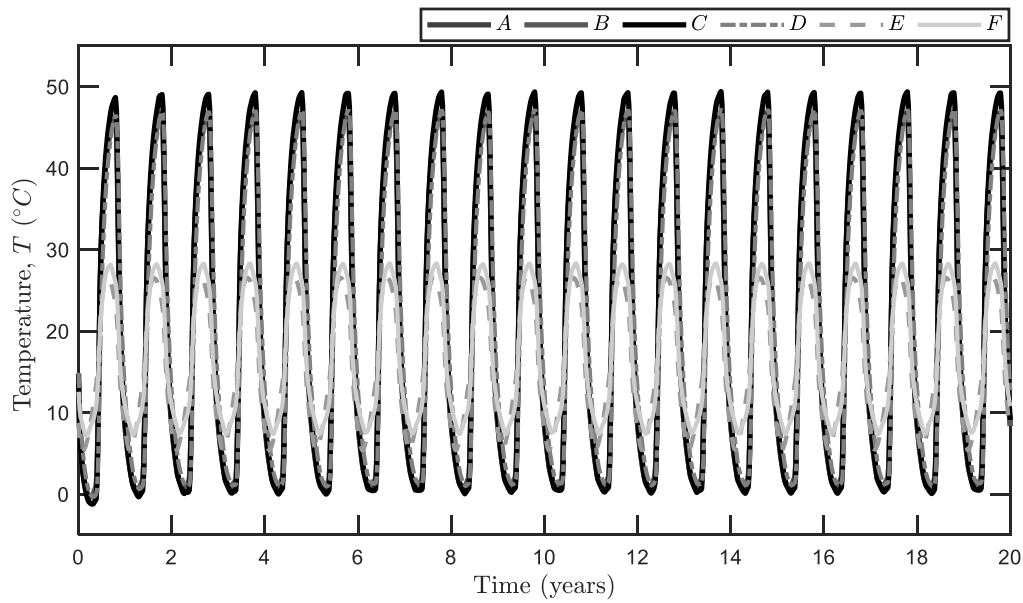


Figure 8.44 Temperature evaluated at the points A to F indicated in Figure 5 for case 4

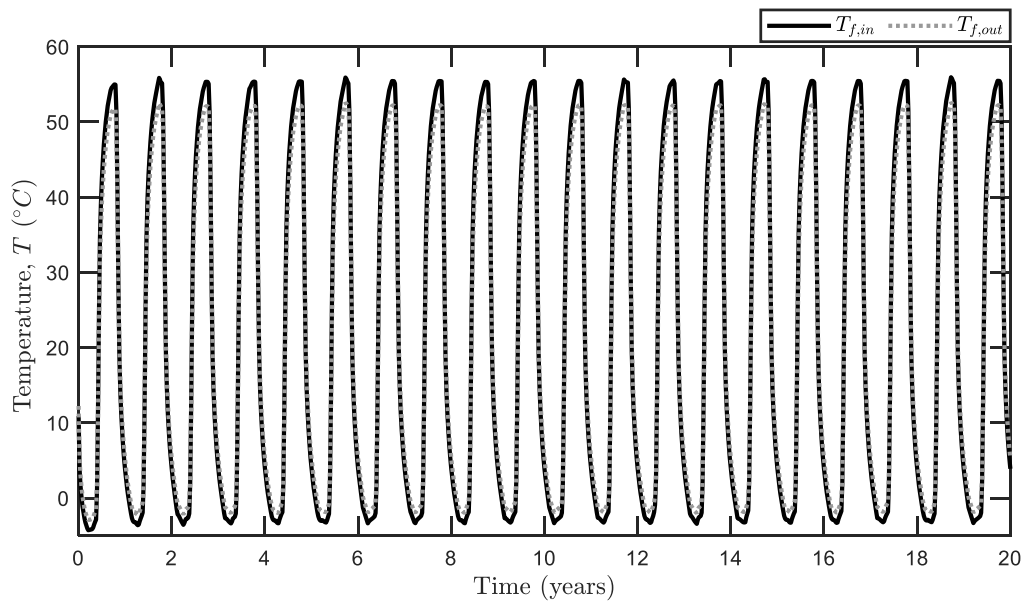


Figure 8.45 Heat carrier fluid temperature for case 4

Based on the procedure detailed at section 8.6.2, the annual energy delivered for heating amounts to  $E_{th,W} = 245\text{ MWh/y}$ , the annual energy delivered for cooling amounts to  $E_{th,S} = -415\text{ MWh/y}$ . The total annual energy delivered reaches  $E_{th} = 660\text{ MWh/y}$ .

#### 8.6.4 Comments on the thermal behavior for the four scenarios

Case 1 could seem unrealistic because it is not able to thoroughly capture the sign of the energy needs especially during shoulder seasons. However, the presence of new, modern buildings under construction in the vicinity of the UEI make it suitable for a future usage. The main advantages are that it allows for a balanced thermal load which can easily define the strong points and limitations of the UEI installation. The main strong point is the high storage potential, while the main limitation is the low potential for winter operation due to the concurrent occurring of boundary effects (i.e., low tunnel temperature, Figure 8.15) and low range of operative heat carrier fluid temperature. Case 1 may guarantee to satisfy the thermal energy needs of  $1000 \div 2000 \text{ m}^2$  of apartments or offices during winter operation and to a surface  $> 2000 \text{ m}^2$  during summer operation (Table 8.4).

Case 2 is strongly unbalanced, denoting the high thermal needs for winter operation and the low ones during summer. Because of the predominant winter operation, the risk of long-term lowering  $T_{EG}$  below the design limits is high. It follows that  $P_{2,max}^{th}$  must be evaluated to guarantee the long-term sustainability of the EG. This scenario does clearly not use the full thermal potential and there exists a large margin for improvement. It follows that the typical energy demand curve for residential and office buildings is not the most suitable for UEI in the European climate, as it requires very low cooling during summer. Case 2 may guarantee to satisfy the thermal energy needs of  $1165 \text{ m}^2$  of apartments and to  $700 \div 1100 \text{ m}^2$  offices during both winter and summer operations (Table 8.5).

Case 3 represents a first attempt to improve the weak points of Case 2. The maximization for summer operation allows for an increase of the winter thermal behavior consequently to the UEI heating during summer (i.e., heat storage). Case 3 reports an increase of 25% and of  $> 1000\%$  with respect to Case 2 for winter and summer operations, respectively. Case 3 may guarantee to satisfy the thermal energy needs of  $1400 \text{ m}^2$  of apartments or  $1100 \text{ m}^2$  of offices during winter operation and to a surface  $> 10000 \text{ m}^2$  during summer operation (Table 8.6).

Case 4 aims at maximizing the thermal behavior for summer and winter operation modes. It aims at representing the case when this UEI installation acts as a major thermal plant for the neighborhood. The thermal demand curve employed within Case 4 may lead to delivering the produced energy not only to residential and office needs but also to commerce and/or industries located in the vicinity. Case 4 reports an increase of the thermal behavior of  $12\% \div 35\%$  and of  $> 1000\%$  with respect to Case 2 for winter and summer operations, respectively. Case 4 may guarantee to satisfy the thermal energy needs of  $1300 \div 5000 \text{ m}^2$  of apartments or  $1000 \div 3000 \text{ m}^2$  of offices during winter operation and to a surface  $> 10000 \text{ m}^2$  during summer operation (Table 8.7).

Comparisons among the four scenarios in terms of monthly and annual energy production are shown in Figure 8.46 and Figure 8.47.

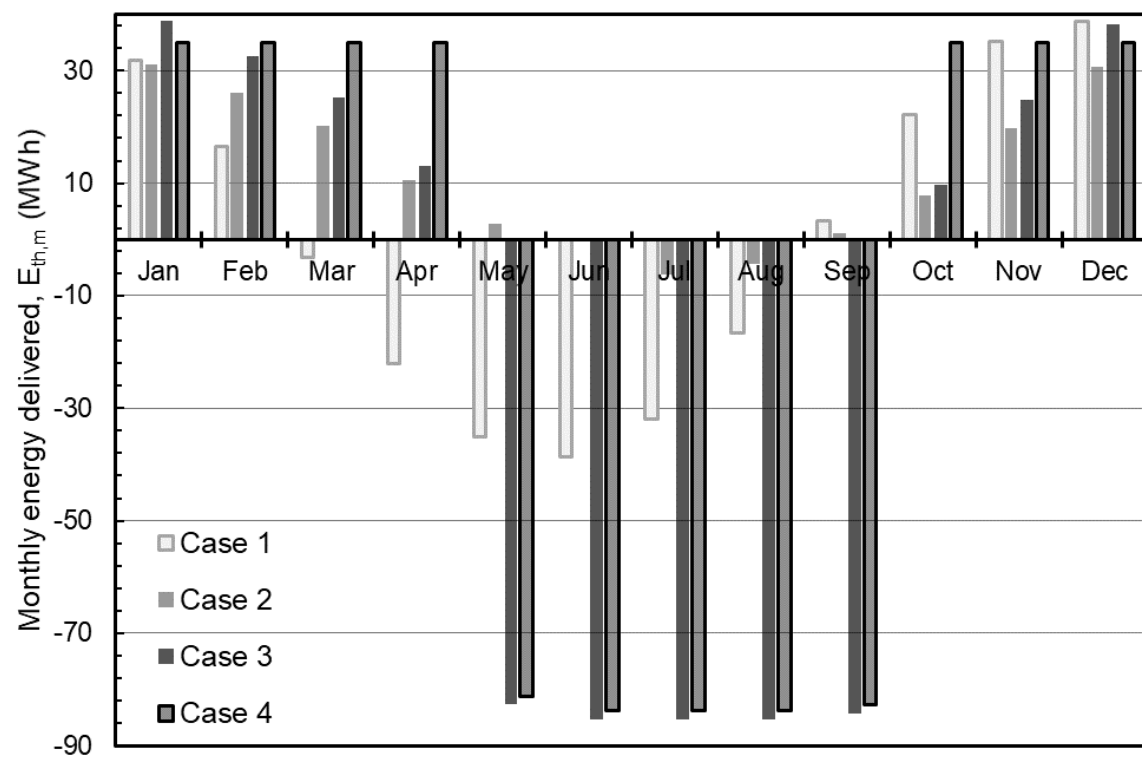


Figure 8.46 Comparison of the monthly energy delivered among the four scenarios

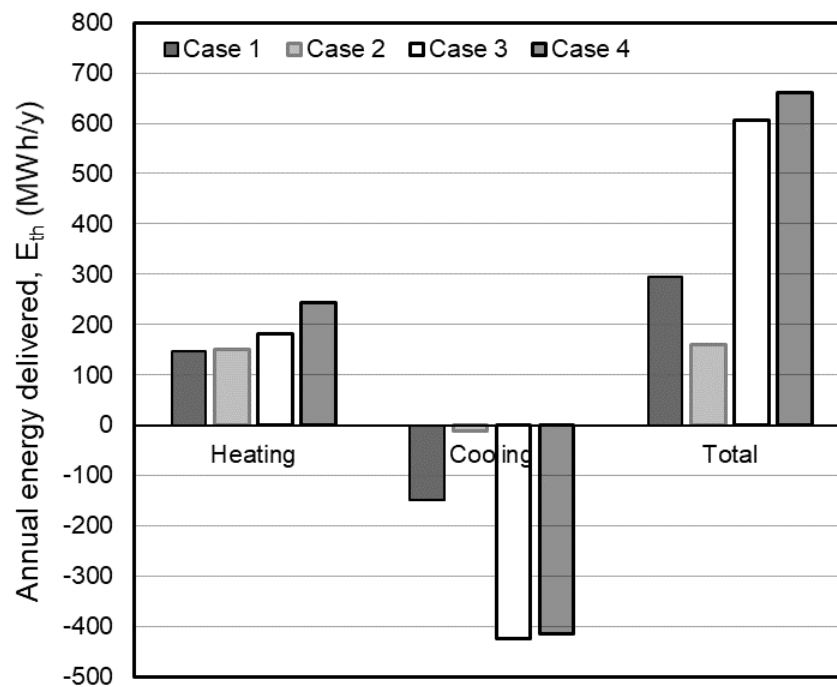


Figure 8.47 Summary of the annual energy delivered for the four scenarios

After this analysis, the following main conclusions on the definition of the most suitable thermal activation modes for this UEI can be summarized as follows:

- The potential for heat storage is strongly unused when dealing with apartments and/or offices thermal demand curves, hence the maximization of the storage potential could lead to two strong points:
  - i. To increase soil temperature during summer and to extract such heat during winter leading to an increase of around 25% of the winter operation potential because the soil is hotter at the beginning of the extraction operation.
  - ii. To use soil as a thermal battery. To do so, and to reduce the environmental impact during summer operation, a coupling of the EG technology with other renewable sources (e.g., solar) could be envisaged allowing to store heat in summer and use it during winter (Elghamry & Hassan, 2020; Olabi et al., 2020). An alternative solution could be to collect the waste heat produced in the built environment during summer and store it in the ground. In this context, UEIs may represent a great opportunity as they are already located, by definition, in the vicinity of the built environment.

With this concept in mind, a main potential future use of EGs, which seems to be particularly suitable for underground energy infrastructures, would be to act as a thermal plant for the built environment, allowing to collect the waste heat from the vicinity and to deliver heating and cooling to the whole neighborhoods. A technological gap between the actual situation and the future usage exist, and it relate to the lack of a suitable distribution network.



Table 8.4 Summary of the thermal behavior for the first scenario: Case 1

CASE 1			Unit	Jan	Feb	Mar	Apr	May	Jun	Jul	Aug	Sep	Oct	Nov	Dec
	Monthly energy delivered	$E_{th}$	MWh	32	17	-3	-22	-35	-39	-32	-17	3	22	35	39
APARTMENT	Monthly energy need		kWh/m <sup>2</sup>	27	22	17	9	2	0	-5	-4	1	7	17	26
	Surface		m <sup>2</sup>	1196	741	-186	-2461	-15053	116076	5980	4513	3232	3322	2066	1469
	Nr. of units		-	30	19	-5	-62	-376	2902	149	113	81	83	52	37
OFFICES	Monthly energy need		kWh/m <sup>2</sup>	34	29	19	10	1	-4	-9	-6	-1	9	22	33
	Surface		m <sup>2</sup>	947	577	-173	-2143	-35124	9673	3680	2920	-4848	2461	1573	1184
	Nr. of units		-	47	29	-9	-107	-1756	484	184	146	-242	123	79	59

Table 8.5 Summary of the thermal behavior for the first scenario: Case 2

CASE 2			Unit	Jan	Feb	Mar	Apr	May	Jun	Jul	Aug	Sep	Oct	Nov	Dec
	Monthly energy delivered	$E_{th}$	MWh	31	26	20	10	3	0	-6	-4	1	8	20	31
APARTMENT	Monthly energy need		kWh/m <sup>2</sup>	27	22	17	9	2	0	-5	-4	1	7	17	26
	Surface		m <sup>2</sup>	1165	1165	1165	1165	1165	1165	1165	1165	1165	1165	1165	1165
	Nr. of units		-	29	29	29	29	29	29	29	29	29	29	29	29
OFFICES	Monthly energy need		kWh/m <sup>2</sup>	34	29	19	10	1	-4	-9	-6	1	9	22	33
	Surface		m <sup>2</sup>	923	907	1082	1015	2718	97	717	754	1165	863	887	939
	Nr. of units		-	46	45	54	51	136	5	36	38	58	43	44	47

Table 8.6 Summary of the thermal behavior for the first scenario: Case 3

CASE 3			Unit	Jan	Feb	Mar	Apr	May	Jun	Jul	Aug	Sep	Oct	Nov	Dec
	Monthly energy delivered	$E_{th}$	MWh	39	33	25	13	-83	-85	-85	-85	-84	10	25	38
APARTMENT	Monthly energy need		kWh/m <sup>2</sup>	27	22	17	9	-1	0	-5	-4	-1	7	17	26
	Surface		m <sup>2</sup>	1456	1456	1456	1456	82701	256256	16016	23296	84254	1456	1456	1456
	Nr. of units		-	36	36	36	36	2068	6406	400	582	2106	36	36	36
OFFICES	Monthly energy need		kWh/m <sup>2</sup>	34	29	19	10	-1	-4	-9	-6	-1	9	22	33
	Surface		m <sup>2</sup>	1153	1134	1352	1268	82701	21355	9856	15074	126381	1079	1108	1174
	Nr. of units		-	58	57	68	63	4135	1068	493	754	6319	54	55	59

Table 8.7 Summary of the thermal behavior for the first scenario: Case 4

CASE 4			Unit	Jan	Feb	Mar	Apr	May	Jun	Jul	Aug	Sep	Oct	Nov	Dec
	Monthly energy delivered	$E_{th}$	MWh	35	35	35	35	-81	-84	-84	-84	-83	35	35	35
APARTMENT	Monthly energy need		kWh/m <sup>2</sup>	27	22	17	9	-1	0	-5	-4	-1	7	17	26
	Surface		m <sup>2</sup>	1310	1565	2016	3883	81148	251597	15725	22872	82701	5242	2056	1327
	Nr. of units		-	33	39	50	97	2029	6290	393	572	2068	131	51	33
OFFICES	Monthly energy need		kWh/m <sup>2</sup>	34	29	19	10	-1	-4	-9	-6	-1	9	22	33
	Surface		m <sup>2</sup>	1038	1219	1872	3382	81148	20966	9677	14800	124051	3883	1565	1070
	Nr. of units		-	52	61	94	169	4057	1048	484	740	6203	194	78	53



## 8.7 Concluding remarks

Firstly, hydrothermal aspects related to in-situ testing are firstly presented in this chapter. Insights on the wall-tunnel hydrothermal interactions are monitored in-situ and allow to define the magnitude of heat fluxes exchanged by the EW and the tunnel. Heating and cooling EW tests are carried out and successfully simulated through 3D numerical simulations, allowing to thoroughly understand all the hydrothermal aspects involving the thermal activation of underground infrastructures. A hydrothermal numerical model is developed and validated through the experimental results, showing closed agreement.

Secondly, thermomechanical aspects linked to the EW thermal activation are studied. The definition of the EW temperature distribution during thermal tests is studied with reference to the monitored experimental results. During both heating and cooling tests, the temperature distribution variations to which the EW is subjected to are strongly nonuniform. A 1D, FD model is developed to capture the wall temperature distribution at the excavated levels, showing closed agreement with the experimental results and needing for a very low computational cost. The definition of the thermomechanical behavior of the EW through experimental results shows low wall intrados deformations. Internal actions, developed consequently to the blocked portion of thermally induced deformations, are estimated through analytical modelling and 3D finite element modelling. Low magnitude thermally induced internal actions with respect to the concurrent mechanical actions seem to take place. The design limits are respected.

Finally, the determination of the thermal potential of the entire UEI installation at Lancy-Bachet (Geneva, Switzerland) is tackled. Four different thermal exploitation scenarios are studied to define the thermal potential. The UEI shows a very high potential for heat storage and a lower one for heat extraction. Thermal exploitation scenarios that aim at maximizing the thermal storage are also capable to maximize heat extraction. Annual heating and cooling production of around  $E_{th} = 600$  MWh/y may guarantee to satisfy the future annual energy needs of around  $1500 \div 5000$  m<sup>2</sup> of residential, office buildings or commerce located in the neighborhood.



## Chapter 9 Conclusions and perspectives

This doctoral thesis focused on the thermomechanical behavior of underground energy infrastructures (UEI), which are innovative and multifunctional technologies that aim to couple the structural roles of the geostructural elements composing underground infrastructures (e.g., retaining walls, slabs, etc...) with the heat exchangers' roles (i.e., energy geostructures, EG). This coupling affects thermal-hydraulic-mechanical aspects within the EG.

### 9.1 Main conclusions

The main challenges and objectives arisen prior to this study were related to three fundamental aspects, and are summarized as follows:

1. Limited knowledge was available on the determination of the heat exchange modes within and around the UEI. Particularly, *(i)* to detect all relevant heat exchange modes and *(ii)* their impacts on thermal exploitation was key to *(iii)* propose guidelines for the thermal performance design.
2. No detailed studies were available on detecting the impact of thermally induced mechanical actions on the geostructures composing UEIs. Moreover, no simplified models able to describe thermomechanical behavior of geostructures subjected to axial and bending thermomechanical actions were available.
3. No detailed studies on *(i)* in-situ testing procedures, related *(ii)* monitoring techniques and *(iii)* determination of the thermal potential of sites equipped with UEIs were available. The knowledge acquired from the monitoring of real installation will be a crucial aspect for future developments on this topic.

The methods adopted to investigate such challenges are: *(i)* numerical and *(ii)* analytical modelling, and *(iii)* in-situ, experimental testing. The main conclusions that allow to reply to each challenge are summarized in the following.

- The main heat exchange modes involved in underground energy infrastructures operation account for conduction and convection. Conduction is predominant in the solid parts of porous materials (e.g., soil, concrete), while convection plays an important role when solid-fluid interfaces are present (e.g., groundwater flow in soil, concrete/air interface in underground environments such as tunnels or basements). Thermal and hydraulic interactions within the different materials composing an UEI involve transient processes in the three-dimensional space, causing so-called hydraulically induced thermal interactions. A correct heat exchangers design ensures performance optimization. An optimization procedure based on the type of needed thermal operation is proposed. Additionally, a correct assessment of hydraulically induced thermal interactions within the heat exchangers design, could lead to doubling the heat exchangers' performance.

- To assess the impact of conductive and convective heat exchanges in porous materials, an analytical methodology based on heat transfer and fluid mechanics is employed. The so-called Péclet number,  $Pe$ , explains the magnitude of each heat transfer mode. Convection in soil becomes predominant when the groundwater velocity is  $v_{gw} \geq 0.5$  m/d. This value is valid not only for applications to underground energy infrastructures, but also to EGs in general, as the geometry of the problem remains nearly unchanged for applications such as, for example, energy piles, walls, slabs, tunnels.
- A methodology for early-stage thermal performance design of underground energy infrastructures is proposed. It is based on sound theoretical fundamentals from heat transfer and fluid dynamics and collects the results of an extensive campaign of parametric numerical results. The flowchart allows to assess the thermal potential of sites that can be equipped with underground energy infrastructures. Average thermal power rates range between  $10 \div 50$  W/m<sup>2</sup> for applications on underground energy infrastructures.
- Thermal activation of geostructures in contact with air interfaces show dual thermomechanical effects: axial and bending. This is due to the nonuniform temperature distribution within the geostructure due to geothermal activation. The presence of air in motion at the interface, washes away the heat coming from/to the heat exchangers maintaining a pronounced temperature difference between the intrados and the extrados of the concrete geostructure.
- Stresses and strains developed at the EG affect the neighboring materials and they redistribute in all connected portions of the underground energy infrastructure (e.g., wall-slab, wall-anchors, etc...). It follows that thermomechanical behavior of the entire geostructure is modified and thermomechanical interactions among adjoining elements must be correctly assessed. In particular, the connections itself are the elements which are the most severely affected by thermally induced mechanical effects.
- The degree of freedom ( $DOF$ ) concept, usually employed for axial thermal loads ( $DOF_a$ ), is extended to account for bending (i.e., flexural) thermal actions ( $DOF_c$ ), allowing for an extensive description of thermomechanical effects on energy geostructures.
- The first analytical model able to describe the thermomechanical response of a geostructure accounting for axial and bending thermal and mechanical actions is proposed. It relates to the extension of Winkler's model in non-isothermal conditions. Applications to simple (e.g., single beams) as well as complex (e.g., cut-and-cover tunnel) geometries are reported. The results are compared with numerical ones showing closed agreement. Analytical modelling is of paramount importance even though it is based on strong assumptions (i.e., it assumes elastic behavior of the involved materials only), narrowing its applicability only to small deformations (i.e., serviceability conditions), which seem to be the case of energy geostructures.
- Examples of applications of this analytical model to different energy geostructures (i.e., energy piles, partly embedded walls and horizontal footings) show the importance of bending actions on the thermomechanical response. Particularly, when axial deformation is blocked, axial thermal loads

contribute to the development of bending actions (i.e., transversal displacement and internal actions): for energy piles, the impact of thermal actions on the bending thermomechanical behavior, may reach up to 30% of internal actions magnitude variations. Additionally, the same model is here extended to analyze thermomechanical behavior of complex plane geometries such as multi-span beams and partly embedded geostructures. Results are presented and compared with more rigorous yet time consuming tools showing closed agreement, as well as in terms of dimensionless charts. Moreover, variations of the Winkler's extension to non-isothermal conditions with related applications are also proposed referring to: (i) the two-parameters soil model, and (ii) the linearly varying subgrade reaction model.

- Details, results, and procedural hints on the execution of a thermal response test (TRT) on energy walls (and, more generally, to any geostructure in contact with an air interface) are reported. The test execution should differ and be longer than the standard one (i.e., the one used for borehole heat exchangers or energy piles) allowing for reaching steady state conditions and ensuring precise knowledge on the hydrothermal interactions with air interfaces. Additionally, the duration of the initial phase of the test (i.e., fluid circulation phase) should last long enough to detect any influence of daily boundary condition variations on fluid temperature. If needed, the installation of hydrothermal monitoring system is strongly encouraged. The results from a TRT executed at an underground train station in Geneva showed the strong effects induced by the wall-tunnel air interfaces, having a strongly transient behavior and affecting geothermal operations.
- Long term hydrothermal monitoring of the tunnel environment and its interactions with geothermal operations, showed marked seasonal temperature variations and airflow circulation. This implies important temperature variations at the tunnel boundaries induced by the application of boundary conditions. The occurring of train traffic drives the tunnel airflow dynamics.
- Thermal activation of the UEI induce non-uniform temperature distribution in the concrete geostructure, inducing axial and flexural actions. Thermomechanical monitoring of the wall-tunnel intrados showed very limited deformations during geothermal operation. The structure is capable of absorbing strong internal actions while showing little deformations.
- When submitted to heating and cooling tests, the underground energy infrastructure showed very high heat storage potential (i.e., summer operation) thanks to the conductive heat exchange with the surrounding materials and the low-magnitude wall-tunnel heat fluxes. The potential for winter operation is affected by the cooling induced by the temperature drop at the tunnel (boundary conditions), having a detrimental effect on geothermal operation. Such detrimental effect could be mitigated by lowering the operational heat carrier fluid temperature to values lower than 0 °C and designing the system accordingly. The large storage potential, however, may act as a mitigation for the lower extraction potential because maximizing the storage may increase the heat extraction by 25% due to the higher initial temperature induced by storage operations. To maximize the storage potential, coupling with existing alternative technologies able to collect and store underground the waste heat produced on surface (e.g., solar) could lead to a major performance boost for UEIs.



- The determination of thermal potential for the entire underground energy infrastructure reveals that the thermal needs of a total surface of several thousands of square meters of residential or office buildings could be satisfied by the underground energy infrastructure installed at the Lancy-Bachet underground train station in Geneva (CH).

## 9.2 Perspectives

This doctoral thesis aimed at developing key topics characterizing multiphysical aspects linked to geothermal use of underground infrastructures. The employment of underground infrastructures as thermal energy sources is at its early days, hence several perspectives and opportunities for further developments remain. The strongly multiphysical nature of this shallow geothermal technology make the study of thermo-active geostructures far from being thoroughly assessed. Aspects linked to (i) long term thermomechanical behavior, (ii) resilience, and (iii) novel applications and couplings with existing technologies represent important research topics in the sustainable energy agenda.

When dealing with thermomechanical aspects, a detailed assessment of the real, nonlinear behavior of materials (e.g., concrete and soil) subjected to concurring thermomechanical loads is paramount. To close the gap between research and practice, there is a need for reliable and possibly simple analysis and design solutions. Aspects such as the inclusion of nonisothermal aspects in the calibration of simplified (e.g., analytical) models remain paramount for future developments. Additionally, the proposed analytical models could be employed and further extended to develop a software (e.g., ThermoPile) able to consider axial and flexural thermomechanical actions as well as to thoroughly model the mechanical behavior of materials (e.g., nonlinearities, creep, etc...).

Resilience is another key aspect and defines another challenge: it should be considered in its wider, multiphysical meaning. Not only mechanical resilience (e.g., extreme natural events, multi-hazard analysis, etc...), but also in terms of hydraulic and thermal resilience of the shallow geothermal system accounting for dedicated mitigation measures, remain to be assessed.

Novel applications and novel couplings may represent the most promising future for shallow geothermal technologies. The concurrent exploitation of different renewable energy sources (e.g., solar and geothermal) may have a tremendous impact on the built environment of the future. Challenges including the definition of measures and best practices for upscaling from the single building to the neighborhood (or city) scale of shallow geothermal installations (e.g., underground energy infrastructures), the coupling with existing alternative technologies, that do not have to be seen as enemies or as competitors, represent the main path for a future assessment and sustainable use of shallow geothermal resources allowing for satisfying growing energy needs of the built environment and contributing for a better, brighter, future for the society.

# References

- Adam, D. (2008). *Tunnels and foundations as energy sources—Practical applications in Austria*. Deep Foundations on Bored and Auger Piles - BAP V; CRC Press. <https://doi.org/10.1201/9780203882870-50>
- Adam, D., & Markiewicz, R. (2009). Energy from earth-coupled structures, foundations, tunnels and sewers. *Géotechnique*, 59(3), 229–236. <https://doi.org/10.1680/geot.2009.59.3.229>
- Amatya, B. I., Soga, K., Bourne-Webb, P. J., Amis, T., & Laloui, L. (2012). Thermo-mechanical behaviour of energy piles. *Géotechnique*, 62(6), 503–519. <https://doi.org/10.1680/geot.10.P.116>
- Amis, T., Robinson, C. A. W., & Wong, S. (2010). Integrating geothermal loops into the diaphragm walls of the Knightsbridge Palace Hotel project. In *Proc. 11th DFI/EFEC Int. Conf. Geotechnical Challenges in Urban Regeneration*.
- Anis Akrouch, G., Sánchez, M., & Briaud, J.-L. (2020). Thermal performance and economic study of an energy piles system under cooling dominated conditions. *Renewable Energy*, 147, 2736–2747. <https://doi.org/10.1016/j.renene.2018.11.101>
- Asadi, I., Shafigh, P., Abu Hassan, Z. F. B., & Mahyuddin, N. B. (2018). Thermal conductivity of concrete – A review. *Journal of Building Engineering*, 20, 81–93. <https://doi.org/10.1016/j.job.2018.07.002>
- Balay, J. (1984). *Recommandations pour le choix des paramètres de calcul des écrans de soutènement par la méthode aux modules de réaction*. Note d'Information Technique, Laboratoire Central des Ponts et Chaussées.
- Barbier, E. (2002). Geothermal energy technology and current status: An overview. *Renewable and Sustainable Energy Reviews*, 6(1), 3–65. [https://doi.org/10.1016/S1364-0321\(02\)00002-3](https://doi.org/10.1016/S1364-0321(02)00002-3)
- Barden, L. (1963b). *The Winkler model and its application to soil*. 9(41), 279–280.
- Barden, L. (1962). Distribution of Contact Pressure Under Foundations. *Géotechnique*, 12(3), 181–198. <https://doi.org/10.1680/geot.1962.12.3.181>
- Barla, M., Di Donna, A., & Insana, A. (2019). A novel real-scale experimental prototype of energy tunnel. *Tunnelling and Underground Space Technology*, 87, 1–14. <https://doi.org/10.1016/j.tust.2019.01.024>
- Barla, M., Di Donna, A., & Santi, A. (2020). Energy and mechanical aspects on the thermal activation of diaphragm walls for heating and cooling. *Renewable Energy*, 147, 2654–2663. <https://doi.org/10.1016/j.renene.2018.10.074>
- Barnard, A. C. L., Hunt, W. A., Timlake, W. P., & Varley, E. (1966). A Theory of Fluid Flow in Compliant Tubes. *Biophysical Journal*, 6(6), 717–724. [https://doi.org/10.1016/S0006-3495\(66\)86690-0](https://doi.org/10.1016/S0006-3495(66)86690-0)
- Batini, N., Rotta Loria, A. F., Conti, P., Testi, D., Grassi, W., & Laloui, L. (2015). Energy and geotechnical behaviour of energy piles for different design solutions. *Applied Thermal Engineering*, 86, 199–213. <https://doi.org/10.1016/j.applthermaleng.2015.04.050>
- Benazza, A., Blanco, E., Aichouba, M., Rio, J., & Laouedj, S. (2011). Numerical investigation of horizontal ground coupled heat exchanger. *Energy Procedia*, 6, 29–35. <https://doi.org/10.1016/j.egypro.2011.05.004>
- Bergman, T. L., Lavine, A. S., Incropera, F. P., & Dewitt, D. P. (2011). *Fundamentals of heat and mass transfer* (7th ed.). John Wiley & Sons.
- Bidarmaghz, A., & Narsilio, G. A. (2018). Heat exchange mechanisms in energy tunnel systems. *Geomechanics for Energy and the Environment*, 16, 83–95. <https://doi.org/10.1016/j.gete.2018.07.004>

- 
- Biot, M. (1937). *Bending of an Infinite Beam on an Elastic Substrate*. 4, A1–A7.
- Bolton, M. D., Powrie, W., & Symons, I. F. (1989). The design of stiff, in situ walls retaining overconsolidated clay, Part I & Part II. *Ground Engineering*, 22(8), 44–48; 22(9), 34–40; and 23(2), 22–28.
- Bond, A., & Harris, A. (2008). *Decoding Eurocode 7*. CRC Press.
- Borák, L., & Marcián, P. (2014). Beams on elastic foundation using modified Betti's theorem. *International Journal of Mechanical Sciences*, 88, 17–24. <https://doi.org/10.1016/j.ijmecsci.2014.06.014>
- Bourne-Webb, P., Burlon, S., Javed, S., Kürten, S., & Loveridge, F. (2016). Analysis and design methods for energy geostructures. *Renewable and Sustainable Energy Reviews*, 65, 402–419. <https://doi.org/10.1016/j.rser.2016.06.046>
- Bourne-Webb, P., & da Costa Goncalves, R. (2016). *On the Exploitation of Ground Heat Using Transportation Infrastructure*. 143, 1333–1340. <https://doi.org/doi:10.1016/j.proeng.2016.06.157>
- Bourne-Webb, P. J., Bodas Freitas, T. M., & da Costa Gonçalves, R. A. (2016). Thermal and mechanical aspects of the response of embedded retaining walls used as shallow geothermal heat exchangers. *Energy and Buildings*, 125, 130–141. <https://doi.org/10.1016/j.enbuild.2016.04.075>
- Bowles, J. E. (1974). *Analytical and computer methods in foundation engineering* (McGraw-Hill Companies).
- Bowles, J. E. (1988). *Foundation analysis and design, Fourth Edition* (McGraw-Hill Book Company).
- Brandl, H. (2006). Energy foundations and other thermo-active ground structures. *Géotechnique*, 56(2), 81–122. <https://doi.org/10.1680/geot.2006.56.2.81>
- Brandl, H. (2016). Geothermal Geotechnics for Urban Undergrounds. *Procedia Engineering*, 165, 747–764. <https://doi.org/10.1016/j.proeng.2016.11.773>
- Brandl, H. (1998). Energy piles and diaphragm walls for heat transfer from and into the ground. *Proc. of the Conference on Deep Foundations on Bored and Auger Piles BAP III*, 37–60. <http://pascal-francis.inist.fr/vibad/index.php?action=getRecordDetail&idt=6214556>
- Brandl, H., Adam, D., Markiewicz, R., Unterberger, W., & Hofinger, H. (2010a). Concrete absorber technology for earth-coupled concrete structures using geothermal energy for the Vienna Underground line U2 (in German). *Österr. Ingenieur- Und Architekten-Zeitschrift*, 155. Jg., Heft 7-9/2010 Und Heft 10-12/2010.
- Brandl, H., Adam, D., Markiewicz, R., Unterberger, W., & Hofinger, H. (2010b). *Massivarbsorbertechnologie zur Erdwärmennutzung bei der Wiener U-Bahnlinie U2* (Wien: Österr. Wien: Österr. Ingenieur-und Architekten-Zeitschrift). [https://publik.tuwien.ac.at/files/PubDat\\_188373.pdf](https://publik.tuwien.ac.at/files/PubDat_188373.pdf)
- Burland, J. B., Potts, D. M., & Walsh, N. M. (1981). The overall stability of free and propped embedded cantilever retaining walls. *Ground Engineering*, 14(5). <https://trid.trb.org/view/173474>
- Carella, R., & Sommaruga, C. (1999). Italian agricultural uses of geothermal energy. *Bulletin d'Hydrologie Centre d'Hydrologie, Université de Neuchâtel*, 19.
- Carslaw, H. S., & Jaeger, J. C. (1952). *Conduction of Heat in Solids*. Clarendon Press.
- CFMS-SYNTec-SOFFONS-FNTP. (2017). *Recommandations pour la conception, le dimensionnement et la mise en oeuvre des géostructures thermiques*, pp. 120.
- Childs, T., Maekawa, K., Obikawa, T., & Yamane, Y. (2000). *Metal machining: Theory and applications* (Butterworth-Heinemann.).
- Chong, C. S. A., Gan, G., Verhoef, A., Garcia, R. G., & Vidale, P. G. (2013). Simulation of thermal performance of horizontal slinky-loop heat exchangers for ground source heat pumps. *Applied Energy*, 104, 603–610. <https://doi.org/10.1016/j.apenergy.2012.11.069>
- Clastornik, J., Eisenberger, M., Yankelevsky, D. Z., & Adin, M. A. (1986). Beams on Variable Winkler Elastic Foundation. *Journal of Applied Mechanics*, 53(4), 925–928. <https://doi.org/10.1115/1.3171882>

- 
- Clayton, C. R. I., Woods, R. I., Bond, A. J., & Milititsky, J. (2014). *Earth Pressure and Earth-Retaining Structures*. CRC Press.
- Colebrook, C. F., Blench, T., Chatley, H., Essex, E. H., Finnicome, J. R., Lacey, G., Williamson, J., & Macdonald, G. (1939). Correspondence. Turbulent flow in pipes, with particular reference to the transition region between the smooth and rough pipe laws. (Includes plates). *Journal of the Institution of Civil Engineers*, 12(8), 393–422. <https://doi.org/10.1680/ijoti.1939.14509>
- COMSOL Inc. (2018). *COMSOL Multiphysics Reference Manual, version 5.3*. [www.comsol.com](http://www.comsol.com).
- Congedo, P. M., Colangelo, G., & Starace, G. (2012). CFD simulations of horizontal ground heat exchangers: A comparison among different configurations. *Applied Thermal Engineering*, 33–34, 24–32. <https://doi.org/10.1016/j.applthermaleng.2011.09.005>
- Connor, J., & Faraji, S. (2016). *Fundamentals of Structural Engineering*. Springer.
- Consulanten, I. (1994). *Temperaturen in U-Bahnstationen*. Wien.
- Cornelio, C., Di Donna, A., & Barla, M. (2016). Energy diaphragm walls for Turin metro. *European Geothermal Congress, Strasbourg, France*.
- Coulomb. (1776). *Essai sur une application des regles de maximis et minimis a quelques problemes de statique, relatifs a l'architecture* (Vol. 1). Paris: Memoires de Mathematique et de Physique présentés a l'Academic Royale des Sciences.
- Cousin, B., Rotta Loria, A. F., Bourget, A., Rognon, F., & Laloui, L. (2019). Energy performance and economic feasibility of energy segmental linings for subway tunnels. *Tunnelling and Underground Space Technology*, 91, 102997. <https://doi.org/10.1016/j.tust.2019.102997>
- Coyle, H. M., & Reese, L. C. (1966). Load Transfer for Axially Loaded Piles in Clay. *Journal of the Soil Mechanics and Foundations Division*, 92(2), 1–26.
- Dean, S., Montes, F., Valavala, S., & Haselbach, L. (2005). A New Test Method for Porosity Measurements of Portland Cement Pervious Concrete. *Journal of ASTM International*, 2(1), 12931. <https://doi.org/10.1520/JAI12931>
- Delattre, L. (2001). Un siecle de methodes de calcul d'ecrans de soutènement. I. L'approche par le calcul—Les methodes classiques et la methode au coefficient de reaction. *BULLETIN DES LABORATOIRES DES PONTS ET CHAUSSEES*, 234. <https://trid.trb.org/view/958165>
- Delattre, L., & Marten, S. (2003). Un siecle de methodes de calcul d'ecrans de soutènement: II - Les approches empiriques et semi-empiriques. *BULLETIN DES LABORATOIRES DES PONTS ET CHAUSSEES*, 244/245. <https://trid.trb.org/view/966243>
- Delerablée, Y., Rammal, D., Mroueh, H., Burlon, S., Habert, J., & Froitier, C. (2018). Integration of Thermoactive Metro Stations in a Smart Energy System: Feedbacks from the Grand Paris Project. *Infrastructures*, 3(4), 56. <https://doi.org/10.3390/infrastructures3040056>
- Di Donna, A. (2016). Energy walls for an underground car park. In *25th European Young Geotechnical Engineering Conference*, 21–24.
- Di Donna, A., Barla, M., & Amis, T. (2017). Energy geostructures: A collection of data from real applications. *Wuhan (China): 15th IACMAG*.
- Di Donna, A., Cecinato, F., Loveridge, F., & Barla, M. (2016). Energy performance of diaphragm walls used as heat exchangers. *Proceedings of the Institution of Civil Engineers - Geotechnical Engineering*, 170(3), 232–245. <https://doi.org/10.1680/jgeen.16.00092>
- Di Donna, A., Ferrari, A., & Laloui, L. (2015). Experimental investigations of the soil–concrete interface: Physical mechanisms, cyclic mobilization, and behaviour at different temperatures. *Canadian Geotechnical Journal*, 53(4), 659–672. <https://doi.org/10.1139/cgj-2015-0294>

- 
- Di Donna, Alice, Barla, M., & Amis, T. (2017, October). Energy Geostructures: Analysis from research and systems installed around the World. *DFI 42nd Annual Conference on Deep Foundations*. <https://hal.archives-ouvertes.fr/hal-02006604>
- Diamond, S. (1999). Aspects of concrete porosity revisited. *Cement and Concrete Research*, 29(8), 1181–1188. [https://doi.org/10.1016/S0008-8846\(99\)00122-2](https://doi.org/10.1016/S0008-8846(99)00122-2)
- Dong, S., Li, X., Tang, A. M., Pereira, J. M., Nguyen, V. T., Che, P., & Xiong, Z. (2019). Thermo-mechanical behavior of energy diaphragm wall: Physical and numerical modelling. *Applied Thermal Engineering*, 146, 243–251. <https://doi.org/10.1016/j.applthermaleng.2018.09.054>
- Dupray, F., Li, C., & Laloui, L. (2014). Heat-exchanger piles for the de-icing of bridges. *Acta Geotechnica*, 9(3), 413–423. <https://doi.org/10.1007/s11440-014-0307-2>
- Elghamry, R., & Hassan, H. (2020). Impact a combination of geothermal and solar energy systems on building ventilation, heating and output power: Experimental study. *Renewable Energy*, 152, 1403–1413. <https://doi.org/10.1016/j.renene.2020.01.107>
- EN 1997 Eurocode 7: Geotechnical design. (2004).
- ENTRANZE. (2014). *Entranze Policies to Enforce the Transition to Nearly Zero Energy Buildings in the EU-27*. <https://www.entranze.eu/>
- E.P.B.D.r., E. P. of B. D. (2010). Directive 2010/31/EU of the European Parliament and of the Council of 19 May 2010 on the energy performance of buildings (recast). *Official Journal of the European Union*, 153, 13–35.
- Eugster, W. J. (2007). Road and Bridge Heating Using Geothermal Energy. Overview and Examples. *Proceedings European Geothermal Congress, Unterhaching, Germany, 30 May-1 June 2007*.
- Fages, R., & Bouyat, C. (1971). Calcul de rideaux de parois moulées ou de palplanches. Modele mathématique integrante le comportement irréversible du sol en état elasto-plastique. *Travaux*, 439. <https://trid.trb.org/view/1080844>
- Filonenko-Borodich, M. M. (1940). *Some approximate theories of elastic foundation (in Russian)*. 3–18.
- Filonenko-Borodich, M. M. (1945). *A very simple model of an elastic foundation capable of spreading the load (in Russian)*.
- Finnish Meteorological Institute. (2019). *Finnish Meteorological Institute*. Retrieved 02 05, 2019, from <https://en.ilmateenlaitos.fi/statistics-from-1961-onwards>.
- Frank, R., & Zhao, S.-. (1982). Estimation par les paramètres pressiométriques de l'enfoncement sous charge axiale des pieux forés dans des sols fins. *Bull. Liaison Lab. Ponts. Chauss.*, 119. <https://trid.trb.org/view/1044395>
- Franklin, J. N., & Scott, R. F. (1979). Beam equation with variable foundation coefficient. *ASCE J Eng Mech Div*, 105(5), 811–827. Scopus.
- Froio, D., & Rizzi, E. (2016). Analytical solution for the elastic bending of beams lying on a variable Winkler support. *Acta Mechanica*, 227(4), 1157–1179. <https://doi.org/10.1007/s00707-015-1508-y>
- Froio, D., & Rizzi, E. (2017). Analytical solution for the elastic bending of beams lying on a linearly variable Winkler support. *International Journal of Mechanical Sciences*, 128–129, 680–694. <https://doi.org/10.1016/j.ijmecsci.2017.04.021>
- Froio, D., Rizzi, E., Simões, F. M. F., & Costa, A. P. D. (2018). Universal analytical solution of the steady-state response of an infinite beam on a Pasternak elastic foundation under moving load. *International Journal of Solids and Structures*, 132–133, 245–263. <https://doi.org/10.1016/j.ijsolstr.2017.10.005>
- Fromentin, A., Pahud, D., Laloui, L., & Moreni, M. (1999). Pieux échangeurs: Conception et règles de pré—dimensionnement. *Revue Française de Génie Civil*, 3(6), 387–421. <https://doi.org/10.1080/12795119.1999.9692263>
- Galin, L. (1943). *On the Winkler-Zimmermann hypothesis for beams (in Russian)*. 7(4), 293–300.

- 
- Gao, L., Zhao, J., & Tang, Z. (2015). A review on borehole seasonal solar thermal energy storage. *Energy Procedia*, 70, 209–218.
- Gehlin, S. (2016). 11—Borehole thermal energy storage. In S. J. Rees (Ed.), *Advances in Ground-Source Heat Pump Systems* (pp. 295–327). Woodhead Publishing. <https://doi.org/10.1016/B978-0-08-100311-4.00011-X>
- Gehlin, S., & Hellström, G. (2000). Recent status of in-situ thermal response tests for BTES applications in Sweden. *Proc. Terrastock 2000*, 159–164.
- Gehlin, Signhild. (2002). *Thermal response test: Method development and evaluation*. <http://urn.kb.se/resolve?urn=urn:nbn:se:ltu:diva-18433>
- Gnielinski, V. (1976). New equations for heat and mass transfer in turbulent pipe and channel flow. *Int. Chem. Eng.*, 16(2), 359–368.
- GSHPA, G. S. H. P. A. (2012). *Thermal piles standard*. [https://www.gshp.org.uk/pdf/GSHPA\\_Thermal\\_Pile\\_Standard.pdf](https://www.gshp.org.uk/pdf/GSHPA_Thermal_Pile_Standard.pdf)
- Guo, L., Guo, L., Zhong, L., & Zhu, Y. (2011). Thermal conductivity and heat transfer coefficient of concrete. *Journal of Wuhan University of Technology-Mater. Sci. Ed.*, 26(4), 791–796. <https://doi.org/10.1007/s11595-011-0312-3>
- Guo, Y.-J., & Weitsman, Y. J. (2002). Solution method for beams on nonuniform elastic foundations. *Journal of Engineering Mechanics*, 128(5), 592–594. Scopus. [https://doi.org/10.1061/\(ASCE\)0733-9399\(2002\)128:5\(592\)](https://doi.org/10.1061/(ASCE)0733-9399(2002)128:5(592))
- Haaland, S. E. (1983). Simple and Explicit Formulas for the Friction Factor in Turbulent Pipe Flow. *Journal of Fluids Engineering*, 105(1), 89–90. <https://doi.org/10.1115/1.3240948>
- Habert, J., & Burlon, S. (2015). Modelling Thermo-active Diaphragm Walls. *Second EAGE Workshop on Geomechanics and Energy*.
- He, X., Li, A., & Ning, Y. (2020). Optimization of outdoor design temperature for summer ventilation for undersea road tunnel using field measurement and statistics. *Building and Environment*, 167, 106457. <https://doi.org/10.1016/j.buildenv.2019.106457>
- Hétenyi, M. (1946). *Beams on elastic foundations Theory with applications in the fields of civil and mechanical engineering*. Ann Arbor: The University of Michigan Press.
- Hétenyi, M. (1950). A general solution for the bending of beams on an elastic foundation of arbitrary continuity. 1(21), 55–58. <https://doi.org/doi:https://doi.org/10.1063/1.1699420>
- IC Consulanten ZT GmbH. (2005). *Wirtschaftliche Optimierung von TunnelThermie-Absorberanlagen, Grundlagenuntersuchung und Planungsleitfaden*. Wien.
- Jin, S., Jin, J., & Gong, Y. (2020). A theoretical explanation of natural ventilation at roof openings in urban road tunnels. *Tunnelling and Underground Space Technology*, 98, 103345. <https://doi.org/10.1016/j.tust.2020.103345>
- Kavanaugh, S. P., & Rafferty, K. D. (2014). *Geothermal heating and cooling: Design of ground-source heat pump systems* (ASHRAE). ASHRAE.
- Kearsley, E. P., & Wainwright, P. J. (2001). Porosity and permeability of foamed concrete. *Cement and Concrete Research*, 31(5), 805–812. [https://doi.org/10.1016/S0008-8846\(01\)00490-2](https://doi.org/10.1016/S0008-8846(01)00490-2)
- Kearsley, E. P., & Wainwright, P. J. (2002). The effect of porosity on the strength of foamed concrete. *Cement and Concrete Research*, 32(2), 233–239. [https://doi.org/10.1016/S0008-8846\(01\)00665-2](https://doi.org/10.1016/S0008-8846(01)00665-2)
- Kerr, A. D. (1965). A study of a new foundation model. *Acta Mechanica*, 1(2), 135–147. <https://doi.org/10.1007/BF01174308>
- Kézdi, A., & Réthati, L. (1974). *Handbook of soil mechanics* (Vol. 1). Elsevier, Amsterdam.
- Kim, K.-H., Jeon, S.-E., Kim, J.-K., & Yang, S. (2003). An experimental study on thermal conductivity of concrete. *Cement and Concrete Research*, 33(3), 363–371. [https://doi.org/10.1016/S0008-8846\(02\)00965-1](https://doi.org/10.1016/S0008-8846(02)00965-1)

- 
- Knellwolf, C., Peron, H., & Laloui, L. (2011). Geotechnical Analysis of Heat Exchanger Piles. *Journal of Geotechnical and Geoenvironmental Engineering*, 137(10). [https://doi.org/10.1061/\(ASCE\)GT.1943-5606.0000513](https://doi.org/10.1061/(ASCE)GT.1943-5606.0000513)
- Kumar, R., & Bhattacharjee, B. (2003). Porosity, pore size distribution and in situ strength of concrete. *Cement and Concrete Research*, 33(1), 155–164. [https://doi.org/10.1016/S0008-8846\(02\)00942-0](https://doi.org/10.1016/S0008-8846(02)00942-0)
- Kupiec, K., Larwa, B., & Gwadera, M. (2015). Heat transfer in horizontal ground heat exchangers. *Applied Thermal Engineering*, 75, 270–276. <https://doi.org/10.1016/j.applthermaleng.2014.10.003>
- Kürten, S., Mottaghy, D., & Ziegler, M. (2015a). A new model for the description of the heat transfer for plane thermo-active geotechnical systems based on thermal resistances. *Acta Geotechnica*, 10(2), 219–229. <https://doi.org/10.1007/s11440-014-0311-6>
- Kürten, S., Mottaghy, D., & Ziegler, M. (2015b). Design of plane energy geostructures based on laboratory tests and numerical modelling. *Energy and Buildings*, 107, 434–444. <https://doi.org/10.1016/j.enbuild.2015.08.039>
- Laloui, L., & Di Donna, A. (2013). *Energy geostructures: Innovation in Underground Engineering* (ISTE and John Wiley&Sons).
- Laloui, L., Nuth, M., & Vulliet, L. (2006). Experimental and numerical investigations of the behaviour of a heat exchanger pile. *International Journal for Numerical and Analytical Methods in Geomechanics*, 30(8), 763–781. <https://doi.org/10.1002/nag.499>
- Laloui, L., & Rotta Loria, A. F. (2019). *Analysis and Design of Energy Geostructures—1st Edition*. Academic Press. <https://www.elsevier.com/books/analysis-and-design-of-energy-geostructures/laloui/978-0-12-816223-1>
- Laloui, L., Lyesse, Moreni, M., & Vulliet, L. (2003). Comportement d'un pieu bi-fonction, fondation et échangeur de chaleur. *Canadian Geotechnical Journal*, 40(2), 388–402. <https://doi.org/10.1139/t02-117>
- Lee, S., Speight, J. G., & Loyalka, S. K. (2007). *Handbook of alternative fuel technologies*. CRC Press.
- Lee, Y., Choi, M.-S., Yi, S.-T., & Kim, J.-K. (2009). Experimental study on the convective heat transfer coefficient of early-age concrete. *Cement and Concrete Composites*, 31(1), 60–71. <https://doi.org/10.1016/j.cemconcomp.2008.09.009>
- Li, M., & Lai, A. C. K. (2015). Review of analytical models for heat transfer by vertical ground heat exchangers (GHEs): A perspective of time and space scales. *Applied Energy*, 151, 178–191. <https://doi.org/10.1016/j.apenergy.2015.04.070>
- Loveridge, F., McCartney, J. S., Narsilio, G. A., & Sanchez, M. (2020). Energy geostructures: A review of analysis approaches, in situ testing and model scale experiments. *Geomechanics for Energy and the Environment*, 22, 100173. <https://doi.org/10.1016/j.gete.2019.100173>
- Lund, J. W., & Boyd, T. L. (2016). Direct utilization of geothermal energy 2015 worldwide review. *Geothermics*, 60, 66–93. <https://doi.org/10.1016/j.geothermics.2015.11.004>
- MacDonald, M. (2004). *Crossrail Line 1 Ventilation Requirements Review Study*. London.
- Madhav, M. R., Rao, N. S. V. K., & Madhavan, K. (1971). Laterally Loaded Pile in Elasto-Plastic Soil. *Soils and Foundations*, 11(2), 1–15. [https://doi.org/10.3208/sandf1960.11.2\\_1](https://doi.org/10.3208/sandf1960.11.2_1)
- Makasis, N., Narsilio, G. A., & Bidarmaghaz, A. (2018). A robust prediction model approach to energy geo-structure design. *Computers and Geotechnics*, 104, 140–151. <https://doi.org/10.1016/j.compgeo.2018.08.012>
- Makasis, N., Narsilio, G. A., Bidarmaghaz, A., & Johnston, I. W. (2019). The Application of Retaining Walls and Slabs as Energy Structures in Underground Train Stations. In A. Ferrari & L. Laloui (Eds.), *Energy Geotechnics* (pp. 43–50). Springer International Publishing. [https://doi.org/10.1007/978-3-319-99670-7\\_6](https://doi.org/10.1007/978-3-319-99670-7_6)
- Makasis, N., Narsilio, G. A., Bidarmaghaz, A., Johnston, I. W., & Zhong, Y. (2020). The importance of boundary conditions on the modelling of energy retaining walls. *Computers and Geotechnics*, 120, 103399. <https://doi.org/10.1016/j.compgeo.2019.103399>

- 
- Mattsson, N., Steinmann, G., & Laloui, L. (2008). Advanced compact device for the in situ determination of geothermal characteristics of soils. *Energy and Buildings*, 40(7), 1344–1352. <https://doi.org/10.1016/j.enbuild.2007.12.003>
- Ménard, L., & Bourdon, C. (1965). *Calcul des rideaux de soutènement. Méthode nouvelle prenant en compte les conditions réelles d'encastrement*. 12.
- Mimouni, T., Dupray, F., & Laloui, L. (2014). Estimating the geothermal potential of heat-exchanger anchors on a cut-and-cover tunnel. *Geothermics*, 51, 380–387. <https://doi.org/10.1016/j.geothermics.2014.02.007>
- Mimouni, T., & Laloui, L. (2015). Behaviour of a group of energy piles. *Canadian Geotechnical Journal*, 52(12), 1913–1929. <https://doi.org/10.1139/cgj-2014-0403>
- Mimouni, Thomas, & Laloui, L. (2014). Towards a secure basis for the design of geothermal piles. *Acta Geotechnica*, 9(3), 355–366. <https://doi.org/10.1007/s11440-013-0245-4>
- Monnet, A. (1994). Module de réaction, coefficient de décompression, au sujet des paramètres utilisés dans la méthode de calcul élasto-plastique des soutènements. *Revue Française de Géotechnique*, 66, 67–72.
- Moreni, M., Vulliet, L., & Laloui, L. (2003). Behavior of a dual-purpose pile as foundation and heat exchanger. *Canadian Geotechnical Journal*, 40, 388–402. <https://doi.org/DOI: 10.1139/T02-117>
- Nicholson, D. P., Chen, Q., de Silva, M., Winter, A., & Winterling, R. (2014). The design of thermal tunnel energy segments for Crossrail, UK. *Proceedings of the Institution of Civil Engineers - Engineering Sustainability*, 167(3), 118–134. <https://doi.org/10.1680/ensu.13.00014>
- Nicholson, D., Smith, P., Bowers, G. A., Cuceoglu, F., Olgun, C. G., McCartney, J. S., Henry, K., Meyer, L. L., & Loveridge, F. A. (2014). Environmental impact calculations, life cycle cost analysis. *DFI Journal - The Journal of the Deep Foundations Institute*, 8(2), 130–146. <https://doi.org/10.1179/1937525514Y.0000000009>
- Nield, D. A. (1998). Effects of local thermal non-equilibrium in steady convective processes in a saturated porous medium: Forced convection in a channel. *Journal of Porous Media* 1 (2).
- Nield, D. A., & Bejan, A. (2006). *Convection in porous media*. Third Edition. Springer.
- Nordell, B., Andersson, O., Rydell, L., & Scorpo, A. L. (2015). *Long-term Performance of the HT-BTES in Emmaboda, Sweden*. Greenstock 2015 : International Conference on Underground Thermal Energy Storage 19/05/2015 - 21/05/2015. <http://urn.kb.se/resolve?urn=urn:nbn:se:ltu:diva-32614>
- Olabi, A. G., Mahmoud, M., Soudan, B., Wilberforce, T., & Ramadan, M. (2020). Geothermal based hybrid energy systems, toward eco-friendly energy approaches. *Renewable Energy*, 147, 2003–2012. <https://doi.org/10.1016/j.renene.2019.09.140>
- Pahud, D., & Matthey, B. (2001). Comparison of the thermal performance of double U-pipe borehole heat exchangers measured in situ. *Energy and Buildings*, 33(5), 503–507. [https://doi.org/10.1016/S0378-7788\(00\)00106-7](https://doi.org/10.1016/S0378-7788(00)00106-7)
- Pasternak, P. (1954). *On a New Method of Analysis of an Elastic Foundation by Means of Two Foundation Constants*.
- Peltier, M., Rotta Loria, A. F., Lepage, L., Garin, E., & Laloui, L. (2019). Numerical investigation of the convection heat transfer driven by airflows in underground tunnels. *Applied Thermal Engineering*, 159, 113844. <https://doi.org/10.1016/j.applthermaleng.2019.113844>
- Pflitsch, A., Bruene, M., Steiling, B., Killing-Heinze, M., Agnew, B., Irving, M., & Lockhart, J. (2012). Air flow measurements in the underground section of a UK light rail system. *Applied Thermal Engineering*, 32, 22–30. <https://doi.org/10.1016/j.applthermaleng.2011.07.030>
- Pflitsch, A., & Kuesel, H. (2003). Subway-Climatology—New research Field for the Management of possible Catastrophes in subway systems. *Man and Climate in the 20th Century, Studia Geograficzne*, 75, 384–394.
- Potts, D. M., & Fourie, A. B. (1984). The behaviour of a propped retaining wall: Results of a numerical experiment. *Géotechnique*, 34(3), 383–404. <https://doi.org/10.1680/geot.1984.34.3.383>



- 
- Powrie, W. (1996). Limit equilibrium analysis of embedded retaining walls. *Géotechnique*, 46(4), 709–723.  
<https://doi.org/10.1680/geot.1996.46.4.709>
- Powrie, W. (2018). *Soil Mechanics: Concepts and Applications, Third Edition*. CRC Press.
- Prat, M., Bisch, P. H., Millard, A., Mestat, P., & Pijaudier-Calot, G. (1995). *La modélisation des ouvrages* (Editions Hermes).
- Randolph, M. F. (1981). The response of flexible piles to lateral loading. *Géotechnique*, 31(2), 247–259.  
<https://doi.org/10.1680/geot.1981.31.2.247>
- Ravera, E., Sutman, M., & Laloui, L. (2019). Analysis of the interaction factor method for energy pile groups with slab. *Computers and Geotechnics*, 103294. <https://doi.org/10.1016/j.compgeo.2019.103294>
- Rees, S. (2016). *Advances in Ground-Source Heat Pump Systems*. Woodhead Publishing.
- Reissner, E. (1958). A note on deflections of plates on a viscoelastic foundation. *J. Appl. Mech., ASME*, 25, 144–145.
- Reissner, M. E. (1937). On the Theory of Beams Resting on a Yielding Foundation. *Proceedings of the National Academy of Sciences of the United States of America*, 23(6), 328–333.
- Reuss, M. (2015). 6—The use of borehole thermal energy storage (BTES) systems. In L. F. Cabeza (Ed.), *Advances in Thermal Energy Storage Systems* (pp. 117–147). Woodhead Publishing.  
<https://doi.org/10.1533/9781782420965.1.117>
- Rotta Loria, A. F. (2018). Performance-based Design of Energy Pile Foundations. *DFI Journal - The Journal of the Deep Foundations Institute*, 12(2), 94–107. <https://doi.org/10.1080/19375247.2018.1562600>
- Rotta Loria, A. F., & Laloui, L. (2017a). Thermally induced group effects among energy piles. *Géotechnique*, 67(5), 374–393. <https://doi.org/10.1680/jgeot.16.P.039>
- Rotta Loria, A. F., & Laloui, L. (2017b). Group action effects caused by various operating energy piles. *Géotechnique*, 68(9), 834–841. <https://doi.org/10.1680/jgeot.17.P.213>
- Rotta Loria, A. F., Bocco, M., Garbellini, C., Muttoni, A., & Laloui, L. (2020). The role of thermal loads in the performance-based design of energy piles. *Geomechanics for Energy and the Environment*, 21, 100153.  
<https://doi.org/10.1016/j.gete.2019.100153>
- Rotta Loria, Alessandro F., & Laloui, L. (2016). The interaction factor method for energy pile groups. *Computers and Geotechnics*, 80, 121–137. <https://doi.org/10.1016/j.compgeo.2016.07.002>
- Rotta Loria, Alessandro F., & Laloui, L. (2017). Displacement interaction among energy piles bearing on stiff soil strata. *Computers and Geotechnics*, 90, 144–154. <https://doi.org/10.1016/j.compgeo.2017.06.008>
- Rotta Loria, Alessandro F., & Laloui, L. (2019). Thermo-mechanical Schemes for Energy Piles. In Alessio Ferrari & L. Laloui (Eds.), *Energy Geotechnics* (pp. 218–225). Springer International Publishing.  
[https://doi.org/10.1007/978-3-319-99670-7\\_28](https://doi.org/10.1007/978-3-319-99670-7_28)
- Rotta Loria, Alessandro F., Vadrot, A., & Laloui, L. (2018). Analysis of the vertical displacement of energy pile groups. *Geomechanics for Energy and the Environment*, 16, 1–14. <https://doi.org/10.1016/j.gete.2018.04.001>
- Rowe, P. W. (1952). Anchored sheet pile walls. *Proceedings of the Institution of Civil Engineers, Pt 1*, 1, 27–70.
- Rui, Y., & Yin, M. (2017). Thermo-hydro-mechanical coupling analysis of a thermo-active diaphragm wall. *Canadian Geotechnical Journal*, 55(5), 720–735. <https://doi.org/10.1139/cgj-2017-0158>
- Sailer, E., Taborda, D. M. G., Zdravković, L., & Potts, D. M. (2019). Fundamentals of the coupled thermo-hydro-mechanical behaviour of thermo-active retaining walls. *Computers and Geotechnics*, 109, 189–203.  
<https://doi.org/10.1016/j.compgeo.2019.01.017>
- Sailer, E., Taborda, D. M. G., Zdravkovic, L., & Potts, D. M. (2019). Numerical Modelling of Thermo-Active Shafts. In A. Ferrari & L. Laloui (Eds.), *Energy Geotechnics* (pp. 97–104). Springer International Publishing.  
[https://doi.org/10.1007/978-3-319-99670-7\\_13](https://doi.org/10.1007/978-3-319-99670-7_13)

- 
- Sanner, B., Hellström, G., Spitler, J., & Gehlin, S. (2005). Thermal response test—current status and world-wide application. *Proceedings World Geothermal Congress*, 24–29.
- Schlosser, S. (2007). *Potential der Tunnelbaustrecke des Bahnprojektes Stuttgart 21*.
- Schmitt, P. (1995). Méthode empirique d'évaluation du coefficient de réaction du sol vis-à-vis des ouvrages de soutènement souples. *Revue Française de Géotechnique*, 71, 3–10. <https://doi.org/10.1051/geotech/1995071003>
- Selvadurai, A. P. S. (1979). *Elastic analysis of soil-foundation interaction* (Vol. 17). Elsevier Scientific Publishing Company.
- Servizio Meteorologico dell'Aeronautica Militare. (2019). *Atlante Climatico d'Italia*. Retrieved 02 05, 2019, from [www.meteoam.it](http://www.meteoam.it).
- Shafagh, I., Rees, S., Urrea Mardaras, I., Curto Janó, M., & Polo Carbayo, M. (2020). A Model of a Diaphragm Wall Ground Heat Exchanger. *Energies*, 13(2), 300. <https://doi.org/10.3390/en13020300>
- SIA 197. (2004). *Projets de tunnels, bases générales*. Société suisse des ingénieurs et des architectes.
- SIA 197/1. (2004). *Projets de tunnels, tunnels ferroviaires*. Société suisse des ingénieurs et des architectes.
- SIA 260. (2003). *Bases pour l'élaboration des projets de structures porteuses*. Société suisse des ingénieurs et des architectes.
- SIA 261 and 261/1. (2003). 'Actions sur les structures porteuses' et "Actions sur les structures porteuses – spécifications complémentaires". Société suisse des ingénieurs et des architectes.
- SIA 262. (2003). *Construction en béton*. Société suisse des ingénieurs et des architectes.
- SIA 267 and 267/1. (2003). 'Géotechnique' et "Géotechnique –spécifications complémentaires". Société suisse des ingénieurs et des architectes.
- SIA D0190. (2005). *Utilisation de la Chaleur du Sol par des Ouvrages de Fondation et de Soutènement en Béton. Guide pour la Conception, la Realisation et la Maintenance*. Zurich, Switzerland.
- Simon, B. (1995). Commentaires sur le choix des coefficients de réaction pour le calcul des écrans de soutènement. *Revue Française de Géotechnique*, 71, 11–19. <https://doi.org/10.1051/geotech/1995071011>
- Soga, K., & Rui, Y. (2016). 7—Energy geostructures. In S. J. Rees (Ed.), *Advances in Ground-Source Heat Pump Systems* (pp. 185–221). Woodhead Publishing. <https://doi.org/10.1016/B978-0-08-100311-4.00007-8>
- Soga, K., Rui, Y., & Nicholson, D. (2015). Behaviour of a thermal wall installed in the Tottenham Court Road station box. *Proc. Crossrail Conference, Crossrail Ltd and Federation of Piling Specialists, City Hall, London*.
- Steinemann, U., Zumsteg, F., & Wildi, P. (2004). Measurements of air flow, temperature differences and pressure differences in road tunnels. In *International Conference Tunnel Safety and Ventilation, Graz, Austria*, 220–226.
- Sterpi, D., Angelotti, A., Habibzadeh-Bigdarvish, O., & Jalili, D. (2018). Assessment of thermal behaviour of thermo-active diaphragm walls based on monitoring data. *Journal of Rock Mechanics and Geotechnical Engineering*, 10(6), 1145–1153. <https://doi.org/10.1016/j.jrmge.2018.08.002>
- Sterpi, D., Coletto, A., & Mauri, L. (2017). Investigation on the behaviour of a thermo-active diaphragm wall by thermo-mechanical analyses. *Geomechanics for Energy and the Environment*, 9, 1–20. <https://doi.org/10.1016/j.gete.2016.10.001>
- Sterpi, D., Tomaselli, G., & Angelotti, A. (2020). Energy performance of ground heat exchangers embedded in diaphragm walls: Field observations and optimization by numerical modelling. *Renewable Energy*, 147, 2748–2760. <https://doi.org/10.1016/j.renene.2018.11.102>
- Sun, M., Xia, C., & Zhang, G. (2013). Heat transfer model and design method for geothermal heat exchange tubes in diaphragm walls. *Energy and Buildings*, 61, 250–259. <https://doi.org/10.1016/j.enbuild.2013.02.017>

- 
- Sutman, M., Speranza, G., Ferrari, A., Larrey-Lassalle, P., & Laloui, L. (2020). Long-term performance and life cycle assessment of energy piles in three different climatic conditions. *Renewable Energy*, 146, 1177–1191. <https://doi.org/10.1016/j.renene.2019.07.035>
- Sutman Melis, Olgun C. Guney, & Brettmann Tracy. (2015). Full-Scale Field Testing of Energy Piles. *IFCEE 2015*, 1638–1647. <https://doi.org/10.1061/9780784479087.148>
- Sutman Melis, Olgun C. Guney, & Laloui Lyesse. (2019). Cyclic Load–Transfer Approach for the Analysis of Energy Piles. *Journal of Geotechnical and Geoenvironmental Engineering*, 145(1), 04018101. [https://doi.org/10.1061/\(ASCE\)GT.1943-5606.0001992](https://doi.org/10.1061/(ASCE)GT.1943-5606.0001992)
- Sutman Melis, Olgun Guney, Laloui Lyesse, & Brettmann Tracy. (2017). Effect of End-Restraint Conditions on Energy Pile Behavior. *Geotechnical Frontiers 2017*, 165–174. <https://doi.org/10.1061/9780784480472.017>
- Terzaghi, K. (1955). *Evaluation of coefficients of subgrade reaction*. 4(5).
- Truesdell, C. (1960). *The rational mechanics of flexible or elastic bodies 1638–1788. Leonhardi Euleri Opera Omnia* (Turici : Venditioni exponunt Orell Füssli(IS)).
- Valore, R. (1980). Calculations of U-values of hollow concrete masonry. *Concrete International*, 2, 40–63.
- VDI V., V.-G. V. und C. (VDI-G. (2010). *VDI Heat Atlas* (2nd ed.). Springer-Verlag. <https://www.springer.com/gp/book/9783540778769>
- Vesic, A. (1961b). *Beams on elastic subgrade and Winkler's hypothesis*. 1, 845–850.
- Vesic, A. B. (1961a). *Bending of beams resting on isotropic elastic solid*. 87: EM2, 35–53.
- Vesic, A., & Johnson, W. (1963). *Model studies of beams resting on a silt subgrade*. 89: SM1, 1–31.
- Vlasov, V. Z. (1949a). General theory of shells and its applications in technology. *Gostekhizdat, Moscow-Leningrad*.
- Vlasov, V. Z. (1949b). Structural mechanics of thin-walled three-dimensional systems. *Stroizdat, Moscow*.
- Vulliet, L., Laloui, L., & Zhao, J. (2016). *Mécanique des sols et des roches (TGC volume 18): Avec écoulements souterrains et transferts de chaleur*. PPUR Presses polytechniques.
- Wang, C., Liu, H., Kong, G., Ng, C. W. W., & Wu, D. (2016). Model tests of energy piles with and without a vertical load. *Environmental Geotechnics*, 3(4), 203–213. <https://doi.org/10.1680/jenge.15.00020>
- Winkler, E. (1867). *Die Lehre von der elasticitaet und festigkeit*. Berlin: Prag Dominicus.
- Witte, H. J. L., & Van Gelder, A. J. (2007). Three years monitoring of a borehole thermal energy store of a UK office building. In H. Ö. Paksoy (Ed.), *Thermal Energy Storage for Sustainable Energy Consumption* (pp. 205–219). Springer Netherlands. [https://doi.org/10.1007/978-1-4020-5290-3\\_11](https://doi.org/10.1007/978-1-4020-5290-3_11)
- Wolfram Research. (2019). *Wolfram Language & System Documentation Center*. <https://reference.wolfram.com/language/>
- Wood, D. M. (2004). *Geotechnical modelling. Applied Geotechnics Vol. 1*. (Taylor&Francis).
- Woods, W. A., & Pope, C. W. (1981). A generalised flow prediction method for the unsteady flow generated by a train in a single-track tunnel. *Journal of Wind Engineering and Industrial Aerodynamics*, 7(3), 331–360. [https://doi.org/10.1016/0167-6105\(81\)90057-X](https://doi.org/10.1016/0167-6105(81)90057-X)
- Wu, Y., Gan, G., Verhoef, A., Vidale, P. L., & Gonzalez, R. G. (2010). Experimental measurement and numerical simulation of horizontal-coupled slinky ground source heat exchangers. *Applied Thermal Engineering*, 30(16), 2574–2583. <https://doi.org/10.1016/j.applthermaleng.2010.07.008>
- Xia, C., Sun, M., Zhang, G., Xiao, S., & Zou, Y. (2012). Experimental study on geothermal heat exchangers buried in diaphragm walls. *Energy and Buildings*, 52, 50–55. <https://doi.org/10.1016/j.enbuild.2012.03.054>
- Yankelevsky, D. Z., Eisenberger, M., & Adin, M. A. (1989). Analysis of beams on nonlinear winkler foundation. *Computers & Structures*, 31(2), 287–292. [https://doi.org/10.1016/0045-7949\(89\)90232-0](https://doi.org/10.1016/0045-7949(89)90232-0)

- 
- Zangheri, P., Armani, R., Pietrobon, M., Pagliano, L., Fernandez Boneta, M., & Muller, A. (2014). Heating and cooling energy demand and loads for building types in different countries of the EU. *D2.3. of WP2 of the Entranze Project; Intelligent Energy Europe Programme of the European Union*. [https://www.entranze.eu/files/downloads/D2\\_3/Heating\\_and\\_cooling\\_energy\\_demand\\_and\\_loads\\_for\\_building\\_types\\_in\\_different\\_countries\\_of\\_the\\_EU.pdf](https://www.entranze.eu/files/downloads/D2_3/Heating_and_cooling_energy_demand_and_loads_for_building_types_in_different_countries_of_the_EU.pdf)
- Zannin, J., Ferrari, A., Pousse, M., & Laloui, L. (2020). Hydrothermal interactions in energy walls. *Underground Space*. <https://doi.org/10.1016/j.undsp.2020.02.001>
- Zhang, W., Min, H., Gu, X., Xi, Y., & Xing, Y. (2015). Mesoscale model for thermal conductivity of concrete. *Construction and Building Materials*, 98, 8–16. <https://doi.org/10.1016/j.conbuildmat.2015.08.106>
- Zhao, P., Chen, J., Luo, Y., Li, Y., Chen, L., Wang, C., & Hu, T. T. (2020). Field measurement of air temperature in a cold region tunnel in northeast China. *Cold Regions Science and Technology*, 171, 102957. <https://doi.org/10.1016/j.coldregions.2019.102957>

---

# Appendix A Mathematical formulation of the numerical models

The mathematical formulation for the finite element models employed in Chapters 2,3,4,7,8 is reported here. Firstly, features for hydrothermal models are reported. The analyses reported at Chapter 2, Chapter 7 and Chapter 8 do not include any groundwater flow in the soil (i.e.,  $\mathbf{v}_{gw} = \mathbf{0}$ ), hence all related terms vanish. Then, the additional features employed for thermo-hydro-mechanical models are added (Chapter 2, Chapter 8).

The hydro-thermal behaviour is described by the following equations. The mass conservation equation of the fluid phase in the porous medium reads:

$$\frac{\partial}{\partial t}(n \rho_w) + \text{div}(\rho_w \mathbf{v}_{rw}) = 0 \quad (\text{A.1})$$

where  $n$  is the porosity of the porous medium,  $\rho_w$  the fluid density,  $t$  the time and  $\mathbf{v}_{rw}$  the fluid velocity as from Darcy's law.

$$\mathbf{v}_{rw} = -K \mathbf{grad} \left( z + \frac{p_w}{\gamma_w} \right) \quad (\text{A.2})$$

in which  $K$  is the hydraulic conductivity in the hypothesis of homogeneous porous medium,  $z$  is the vertical coordinate,  $p_w$  is the fluid pressure and  $\gamma_w = \rho_w g$ , with  $g$  being the gravity acceleration. The evaluation of the hydraulic conductivity,  $K$ , is done as a function of the geometric permeability,  $k^*$ ,  $\rho_w$ ,  $g$  and the fluid dynamic viscosity  $\mu_w$ .

$$K = k^* \frac{\rho_w g}{\mu_w} \quad (\text{A.3})$$

The energy conservation equation can be separated in two parts: one that relates to the conductive and convective heat transfer processes in the porous materials, and another to the hydro-thermal fluid flow inside the heat exchangers.

The former can be written as:

$$\text{div}(\lambda \mathbf{grad} T) = \rho C_p \frac{\partial T}{\partial t} + \rho_w C_{p,w} \mathbf{v}_{rw} \cdot \mathbf{grad} T \quad (\text{A.4})$$

in which  $\lambda$  is the effective materials' thermal conductivity:

$$\lambda = (1 - n)\lambda_s + n\lambda_w \quad (\text{A.5})$$

where the subscripts  $s$  and  $w$  relate to the solid and fluid phases, respectively.  $T$  is the temperature,  $\rho C_p$  is the effective volumetric heat capacity at constant pressure:

$$\rho C_p = (1 - n)\rho_s C_{p,s} + n\rho_w C_{p,w} \quad (\text{A.6})$$

The second part of the energy conservation equation relating to the non-isothermal fluid flow inside the heat exchangers accounts for the convective heat exchanges within the fluid and for conduction through the pipe wall:

$$\rho_f c_f A_p \frac{\partial T_{bulk,f}}{\partial t} + \rho_f c_f A_p \mathbf{u}_f \cdot \mathbf{grad}(T_{bulk,f}) = \text{div}[A_p \lambda_f \mathbf{grad}(T_{bulk,f})] + \dot{q}_p \quad (\text{A.7})$$

with  $\rho_f, c_f, T_{bulk,f}, \mathbf{u}_f, \lambda_f$  the bulk density, specific heat at constant pressure, bulk temperature, tangential velocity and thermal conductivity of the fluid, respectively. The cross section of the heat exchanger pipe is  $A_p$ ,  $\dot{q}_p$  expresses the heat flux per unit length through the pipe wall, which is defined as:

$$\dot{q}_p = U P_p (T_{ext} - T_{bulk,f}) \quad (\text{A.8})$$

where  $U$  relates to an effective value of the pipe heat transfer coefficient accounting for the thermal resistances of the internal film and the wall.  $U$  is expressed in function of the hydraulic radius, the pipe geometry and the thermal conductivity of the pipe material.  $P_p = 2\pi r_{int}$  is the wetted perimeter of the pipe cross section,  $T_{ext}$  is the external temperature of the pipe (Batini et al., 2015; COMSOL Inc., 2018; Gnielinski, 1976; Haaland, 1983; Zannin et al., 2020).

The features for considering the mechanical component are as follows. The equilibrium equation reads as:

$$\text{div } \boldsymbol{\sigma}_{ij} + \rho \mathbf{g}_i = 0 \quad (\text{A.9})$$

where  $\text{div}$  denotes the divergence operator and  $\boldsymbol{\sigma}_{ij}$  is the total stress tensor,  $\rho$  is the density of the porous material and  $\mathbf{g}_i$  is the gravity vector. In the framework of thermo-elasticity, when drained conditions are considered (*i.e.*, variations in total stress are equivalent to variations in effective stress), the constitutive law reads:

$$d\boldsymbol{\sigma}_{ij} = \mathbf{C}_{ijkl}(d\boldsymbol{\varepsilon}_{kl} + \boldsymbol{\beta}_{kl}dT) \quad (\text{A.10})$$

where  $\mathbf{C}_{ijkl}$  is the constitutive tensor,  $\boldsymbol{\varepsilon}_{kl}$  is the total strain tensor,  $\boldsymbol{\beta}_{kl}$  is a tensor that contains the thermal expansion coefficient ( $\alpha$ ) in the main diagonal, and  $T$  is the temperature.

## Appendix B Method of initial conditions

This appendix expands on critical features of the method of initial conditions, as remarked by Hétenyi (Hétenyi, 1946) and Selvadurai (Selvadurai, 1979). The method of initial conditions is powerful for solving the case of generally loaded beams. This method consists in replacing the integration constants with the four conditions at the origin of the beam ( $x = 0$ ):  $y_0$ ,  $\theta_0$ ,  $M_0$  and  $V_0$ . The general solution of the elastic line, in the case with axial load, is presented here. The fourth-order differential equation to be solved is:

$$EI \frac{d^4 y(x)}{dx^4} - N \frac{dy(x)}{dx} + k_s y(x) = 0 \quad (\text{B.1})$$

The general solution of the deflection is:

$$y(x) = (C_1 e^{\alpha x} + C_2 e^{-\alpha x}) \cos \beta x + (C_3 e^{\alpha x} + C_4 e^{-\alpha x}) \sin \beta x \quad (\text{B.2})$$

Where

$$\alpha = \sqrt{\sqrt{\frac{k}{EI} + \frac{N}{4EI}}} = \sqrt{\lambda^2 + \frac{N}{4EI}} \quad (\text{B.3})$$

$$\beta = \sqrt{\sqrt{\frac{k}{EI} - \frac{N}{4EI}}} = \sqrt{\lambda^2 - \frac{N}{4EI}} \quad (\text{B.4})$$

The values of  $y(x)$  and its derivatives at  $x = 0$  are:

$$y(0) = y_0 = C_1 + C_2 \quad (\text{B.5})$$

$$\frac{dy(0)}{dx} = \theta_0 = \alpha(C_1 - C_2) + \beta(C_3 + C_4) \quad (\text{B.6})$$

$$-EI \frac{d^2 y(0)}{dx^2} = M_0 = EI[\beta^2(C_1 + C_2) - \alpha^2(C_1 + C_2) - 2\alpha\beta(C_3 - C_4)] \quad (\text{B.7})$$

$$\begin{aligned} -EI \frac{d^3 y(0)}{dx^3} &= V_0 \\ &= -EI[-\beta^3(C_3 + C_4) + \alpha^3(C_1 - C_2) - 3\alpha\beta^2(C_1 - C_2) \\ &\quad + 3\alpha^2\beta(C_3 + C_4)] \end{aligned} \quad (\text{B.8})$$

The unknowns  $C_1$  to  $C_4$  become:

$$C_1 = \frac{1}{2}y_0 - \frac{\beta^2 - 3\alpha^2}{4\alpha(\beta^2 + \alpha^2)}\theta_0 + \frac{1}{4EI\alpha(\beta^2 + \alpha^2)}V_0 \quad (\text{B.9})$$



$$C_2 = \frac{1}{2}y_0 + \frac{\beta^2 - 3\alpha^2}{4\alpha(\beta^2 + \alpha^2)}\theta_0 - \frac{1}{4EI\alpha(\beta^2 + \alpha^2)}V_0 \quad (\text{B.10})$$

$$C_3 = \frac{\beta^2 - \alpha^2}{4\alpha\beta}y_0 + \frac{3\beta^2 - \alpha^2}{4\beta(\beta^2 + \alpha^2)}\theta_0 - \frac{1}{4EI\alpha\beta}M_0 - \frac{1}{4EI\beta(\beta^2 + \alpha^2)}V_0 \quad (\text{B.11})$$

$$C_4 = \frac{\alpha^2 - \beta^2}{4\alpha\beta}y_0 + \frac{3\beta^2 - \alpha^2}{4\beta(\beta^2 + \alpha^2)}\theta_0 + \frac{1}{4EI\alpha\beta}M_0 - \frac{1}{4EI\beta(\beta^2 + \alpha^2)}V_0 \quad (\text{B.12})$$

The general equation for the deflection, following the method of initial conditions (Hétenyi, 1946) becomes:

$$y(x) = y_0F_1(x) + \theta_0F_2(x) - \frac{1}{EI}M_0F_3(x) - \frac{1}{EI}V_0F_4(x) \quad (\text{B.13})$$

with:

$$F_1(x) = \cosh \alpha x \cos \beta x + \sinh \alpha x \sin \beta x \left( \frac{\beta^2 - \alpha^2}{2\alpha\beta} \right) \quad (\text{B.14})$$

$$F_2(x) = \frac{1}{2(\alpha^2 + \beta^2)} \left[ \cosh \alpha x \sin \beta x \left( \frac{3\beta^2 - \alpha^2}{\beta} \right) - \sinh \alpha x \cos \beta x \left( \frac{\beta^2 - 3\alpha^2}{\alpha} \right) \right] \quad (\text{B.15})$$

$$F_3(x) = \frac{1}{2\alpha\beta} [\sinh \alpha x \sin \beta x] \quad (\text{B.16})$$

$$F_4(x) = \frac{1}{2(\alpha^2 + \beta^2)} \left[ \frac{\cosh \alpha x \sin \beta x}{\beta} - \frac{\sinh \alpha x \cos \beta x}{\alpha} \right] \quad (\text{B.17})$$

# Appendix C Determination of the modulus of subgrade reaction for horizontal foundations

This appendix expands on key features of methods for determining the modulus of subgrade reaction. The evaluation of  $k_s$  is presented referring to a practical application for a horizontal geostructure made of reinforced concrete with Young's modulus of  $E = 25.0$  GPa, a cross-section height of  $h = 0.5$  m, breadth of  $B = 1.0$  m and length of  $L = 10.0$  m. Results are presented in Figure C.1. The geostructure is assumed to rest on a uniform soil with Poisson's ratio of  $\nu_s = 0.3$  and a varying Young's modulus between  $E_s = 10^6 \div 10^8$  N/m<sup>2</sup>. A sensitivity analysis on  $\nu_s$  indicates that this parameter induces minimal differences in the estimates of  $k_s$ .

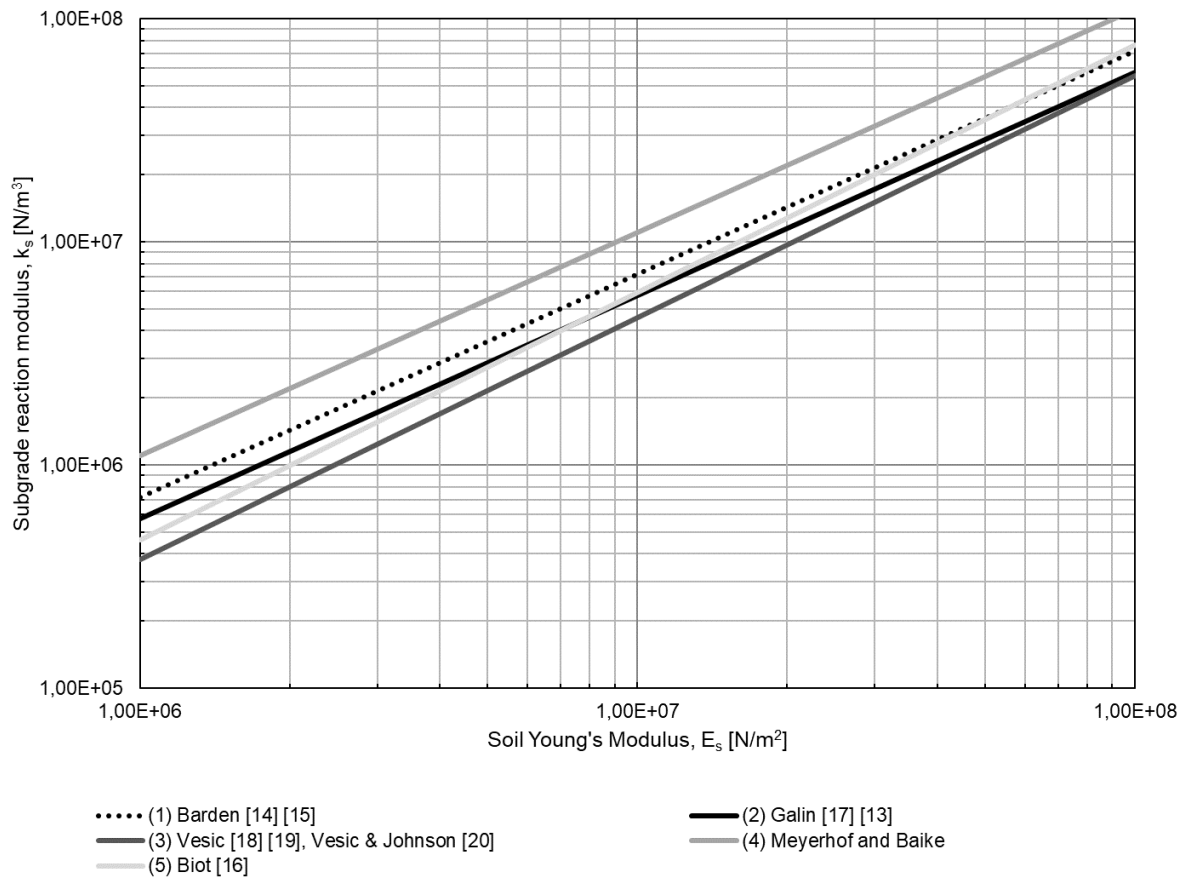


Figure C. 1 Evaluation of the subgrade reaction modulus based on empirical formulations

---

## Appendix D Description of the numerical model employed in Chapter 5

This appendix expands on key features of the numerical analyses and models employed in this paper to validate the proposed analytical models. The numerical models employing spring foundations are a numerical resolution of the analytical model presented here.

The numerical models employing a linear elastic soil mass are described here. Two-dimensional (2D) plane strain thermo-mechanical finite element models are built using Comsol Multiphysics (COMSOL Inc., 2018) for the considered purpose. In these models, the soil is modelled as a linear elastic medium. This approach involves considering the soil as an infinite heat reservoir that remains at a fixed constant temperature. While approximate, this assumption agrees with the hypotheses and features of the Winkler's solution extended in this work and finds due justification in the works of Rotta Loria et al. (Rotta Loria et al., 2018; Rotta Loria & Laloui, 2016, 2017). In this model, the geostructure is modelled with beam elements that follow Euler-Bernoulli theory while the soil mass follows continuum mechanics.

The behavior of beam elements is described through structural mechanics' theory, by employing the Euler-Bernoulli theory of beams. The beam is considered to be isotropic and homogeneous and the mechanical behavior is described through Navier formulation for bending of beams:

$$\sigma_n(y_n) = \frac{N}{A} + \frac{M}{I} y_n \quad (\text{D.1})$$

where  $\sigma_n(y_n)$  represents the bending stress and  $y_n$  the distance to the neutral axis.

Following linear elasticity, the axial, bending moment and shear force can be written as:

$$N(x) = EA \frac{du}{dx} \quad (\text{D.2})$$

$$M(x) = EI \frac{\partial^2 y}{\partial x^2} \quad (\text{D.3})$$

$$V(x) = EI \frac{\partial^3 y}{\partial x^3} \quad (\text{D.4})$$

where  $u$  represents the axial displacement.

A linear distribution of temperature variation can be applied by imposing a thermal curvature to the beam:

$$\chi^{th} = \frac{2\alpha\Delta T_c}{h} \quad (\text{D.5})$$

A mechanical load can be applied as a boundary load transversal to the beam's neutral axis.

---

The soil is modelled as a linear-elastic continuum, allowing for considering the portion of soil surrounding the beam. Winkler's solution (e.g., the analytical model proposed in this study) models the soil as unidirectional independent springs that present a linear elastic relation among load and displacement. Consequently, Winkler solution is not capable of capturing the behaviour of the materials surrounding the studied structural element. No heat transfer in the soil is considered in the numerical models. The mechanical behaviour of the continuum media is described by the following equations. The equilibrium equation reads:

$$\text{div } \boldsymbol{\sigma}_{ij} + \rho \mathbf{g}_i = 0 \quad (\text{D.6})$$

where  $\text{div}$  denotes the divergence operator,  $\boldsymbol{\sigma}_{ij}$  is the total stress tensor,  $\rho$  the bulk density of the material and  $\mathbf{g}_i$  is the gravity acceleration vector.

The constitutive law, in the incremental form reads:

$$d\boldsymbol{\sigma}_{ij} = \mathbf{C}_{ijkl} d\boldsymbol{\varepsilon}_{kl} \quad (\text{D.7})$$

in which  $\mathbf{C}_{ijkl}$  is the constitutive tensor and  $\boldsymbol{\varepsilon}_{kl}$  is the total strain tensor.

At the beam-soil interface, continuity of displacement is imposed:

$$u_{S,i} = u_{B,i} \quad \text{on } \Omega_S \cap \Omega_B \quad (\text{D.3})$$

where  $u_{S,i}$  and  $u_{B,i}$  represent the soil and beam displacement vector, respectively.  $\Omega_S$  and  $\Omega_B$  are the edges of soil and beam domains. The numerical models are detailed in Figure D.1.

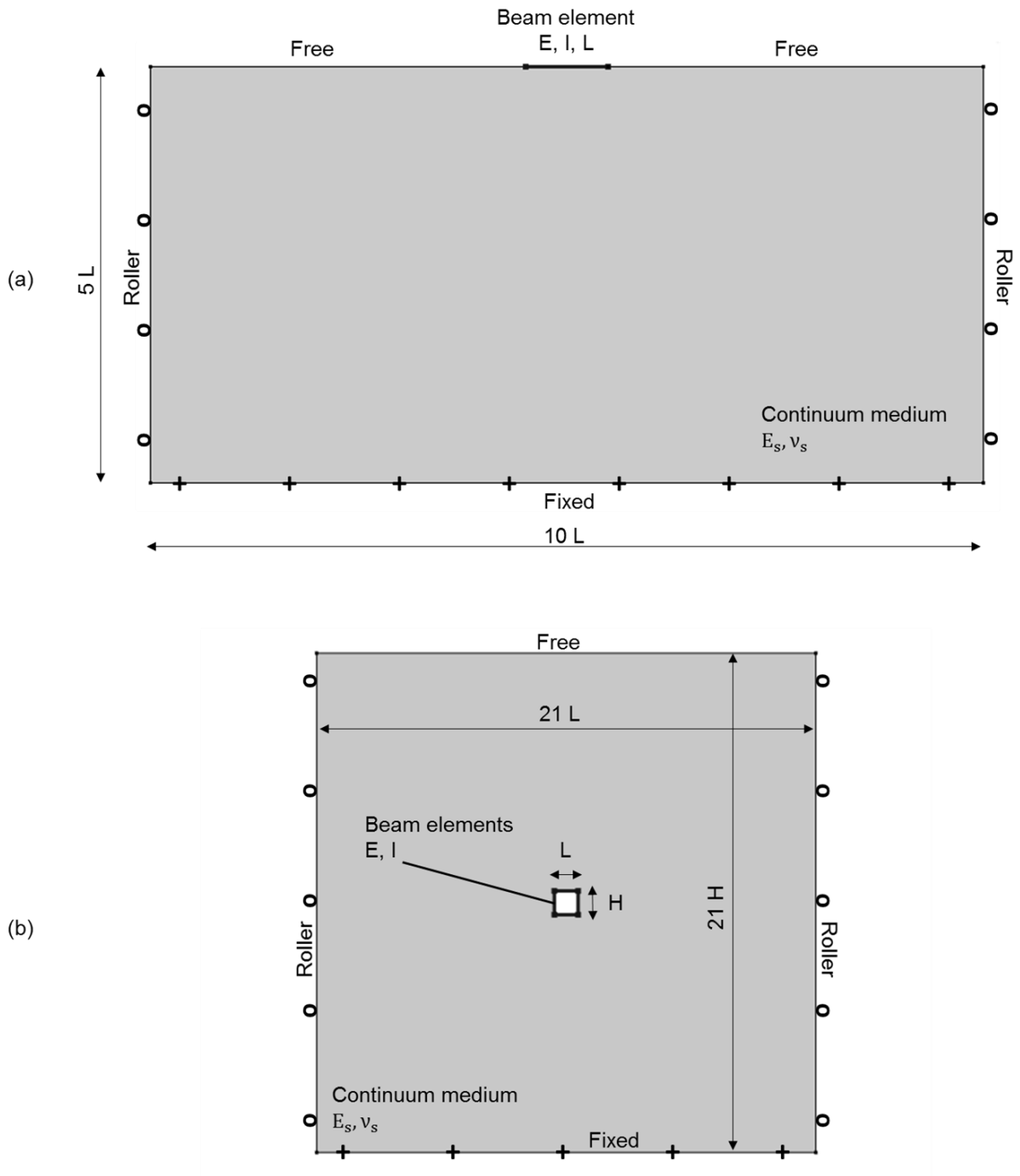


Figure D. 1 Features of the numerical models: (a) a beam on an elastic continuum material and (b) a cut-and-cover tunnel in an elastic continuum material

---

## Appendix E Additional features for the numerical model employed in Chapter 8

This appendix focuses on the geometrical and mechanical characterization of the materials, as well as on execution details of the thermo-hydro-mechanical analyses presented at Chapter 8.

With reference to the cross-section view of the site, as presented at Figure 8.5, the following Table E. 1 details the material properties for the soil layers and for the concrete. For layers B and C, the mechanical parameters are determined from the results of laboratory analyses on samples taken from the site and tested at the Laboratory for Soil Mechanics of EPFL in 2008. For layers A and D, the determination of mechanical parameters is done from a literature review (Bowles, 1988). Additionally, from these experimental results, the groundwater table is located in the gravel layer. Also, all the materials above the groundwater table are saturated.

With reference to the model geometry presented in Figure 7.4, the following mechanical boundaries are set: the bottom horizontal surface of the model is fixed, all the vertical sides of the model are rollers (i.e., allowing only for vertical displacement), the remaining boundaries are free. The external mechanical loads detailed in Table 8.3 and Figure 8.32 are applied as surface loads. The results from piezometric readings (dated to 2008) at a location around 150 m far from the considered cross section suggest that the groundwater table is located in the gravel layer. The following hydraulic boundaries are set: for SLS calculations, the groundwater table is considered at the top of layer D (Figure 8.5) and at hydrostatic conditions, hence negative pore water pressures develop above the groundwater table and the materials are considered to be saturated (saturated unit weight,  $\gamma_{sat}$ ); for ULS calculations an additional case is defined, aiming at defining a worst case scenario, which foresees the groundwater table located at the top of layer B (i.e., at the top of the geostructure) and at hydrostatic conditions. Under such conditions, layers B, C and D are below the groundwater table (i.e., characterized by their submerged unit weight,  $\gamma'$ ). Such two conditions are used in the definition of the combinations of actions together with the thermal and mechanical loads reported at Table 8.3.

Firstly, the model is hydromechanically initialized at rest ( $K_0$ ) conditions and at a uniform temperature  $T_s = 14.5$  °C. This is a simplification of the reality. No details and monitoring during the construction processes are available, making completely arbitrary, at this stage, any attempt of considering thermomechanical aspects during the construction process, which took place over 5 years before the execution of the first thermal tests (i.e., TRT test in August 2019). Additionally, the geostructural response following the hypothesis of elasticity on all materials (Figure 8.31) seems to give a satisfactory representation of the reality.

Secondly, a transient analysis is performed. In addition to the hydromechanical description reported at the first step, thermal boundary conditions (Table 8.1) are simulated for 10 years to ensure a periodical response independent to the initial conditions. Thirdly, thermomechanical loads are applied.

Table E. 1 Material properties

Material	Abbrevia- tion	Thickness (m)	$E$ (MPa)	$\nu$ (-)	$\gamma'$ (kN/m <sup>3</sup> )	$\gamma_{sat}$ (kN/m <sup>3</sup> )	$n$ (-)	$\alpha_{th}$ (K <sup>-1</sup> )
Backfill	A	1.92	30	0.3	9.8	19.6	0.35	10 <sup>-5</sup>
NC clay	B	15.60	19.9	0.3	9.9	19.7	0.35	10 <sup>-5</sup>
OC clay	C	5.98	41.6	0.3	10.4	20.2	0.37	10 <sup>-5</sup>
Gravel	D	37.91	150	0.25	16.7	26.5	0.30	10 <sup>-5</sup>
Concrete	Concrete	Structural geometry	28000	0.25	-	26.7	0.1	10 <sup>-5</sup>

$E$  is the Young Modulus,  $\nu$  the Poisson's ratio,  $\gamma'$  the submerged unit weight,  $\gamma_{sat}$  the saturated unit weight,  $n$  the porosity and  $\alpha_{th}$  the thermal expansion coefficient.

## Curriculum Vitae

### JACOPO ZANNIN

CIVIL ENGINEER, EARLY STAGE RESEARCHER

Pl. Crêt-Dessous, 6, 1098 Epesses (CH)

+41 78 646 0306

[jacopo.zannin@gmail.com](mailto:jacopo.zannin@gmail.com)

LinkedIn [Jacopo Zannin](#)

Skype live:jacopo.Zannin



### STRENGTHS

- **Multiphysical** analysis and design of coupled renewable energy systems
- **Sustainability**: development of design methodology for low-carbon engineering
- **Project management**: coordination, time management, international cooperation
- **Event organization**: international, scientific and cultural events, public speaking

### HIGHER EDUCATION

#### 2016 - 2020 Ph.D. - Swiss Federal Institute of Technology in Lausanne, EPFL

Thesis title: "Thermomechanical behavior of underground energy infrastructures"

Supervisors: Profs. Lyesse Laloui, Alessio Ferrari; Laboratory for Soil Mechanics, EPFL

Marie-Sklodowska Curie Project TERRE (low-carbon geotechnics, renewable energy)

Pilot project in shallow geothermal structures at CEVA, Geneva (industrial collaboration with BG Consulting Engineers and SIG Services Industriels Geneve)

#### 2013-2016 M.Sc in Civil Engineering - University of Trento (Italy)

Major in Infrastructures and Geotechnics

International exchange at Université Libre de Bruxelles (ULB)

#### 2010-2013 Bachelor Degree in Civil Engineering, University of Trento (Italy)

### EXPERIENCES

#### 2019 - 2020: Doctoral Assistant - EPFL

Contribution in achieving SDGs 7, 9, 11 and 13. Some of the main activities are described below.

- Pilot project in shallow geothermal energy at the Lancy-Bachet installation in Geneva (CH), in collaboration with BG Consulting Engineers and SIG Services Industriels de Genève. Project management, budget definition, execution timeline, development of testing methodologies, reporting, scientific writing in English and French, scientific publications, public speaking.
- Development of novel engineering design methods towards low-carbon geotechnical engineering. Proposition of novel models for engineering performance-based design of underground structures equipped with geothermal heat exchangers to satisfy thermal needs of the built environment in a renewable and sustainable way.
- Co-organization of international scientific events
- Participation to international conferences



- **2016 – 2019 Early-stage Researcher** – EU Marie-Sklodowska Curie project Terre
  - Technological development for shallow geothermal energy systems, determination of thermal potential of sites.
  - Collaboration between: Nobatek/INEF4 (France), Swiss Federal Institute of Technology in Lausanne, EPFL (Switzerland)
  - Co-organization of international scientific events
  - Participation to international conferences
- **2015 Visiting Scholar** – University of Colorado Boulder (USA)  
 Execution of experimental activity at the CREST Geotechnical Centrifuge Laboratory on the assessment and mitigation of catastrophic events induced by soil liquefaction during earthquakes.
- **2008-2009 Internship** – Idroesne Infrastrutture, Italy  
 Engineering design of road infrastructures and of retaining structures.

## LANGUAGES

- Italian: mother tongue
- English: currently C1 level (with B2 certificate from Cambridge Examinations, 2010)
- French: currently C1 level (with B1 certificate from Université Libre de Bruxelles, 2014)

## TECHNICAL SKILLS

- Modelling and design: Finite element analysis, Autocad, Allplan BIM, Comsol Multiphysics
- Management of information and data: Matlab, Microsoft Office, Adobe Illustrator, Grapher, Outlook
- Networking, Technical writing, Public speaking: English, French and Italian
- Research, teaching and training

## PROJECT MANAGEMENT SKILLS

- Leadership without hierarchical power, Supervision
- Budget management
- Innovation, Problem solving, Critical thinking

## ORGANIZATIONAL AND EXTRACURRICULAR SKILLS

- International experiences, Cross-cultural skills, Team working
- Multilingual
- Communication skills, Social media
- Event organization: yearly co-organization of international scientific events with 60+ participants;
- Co-organization of benefit comedy shows with 400+ yearly participants
- Music: guitar practice since 20 years, concerts, recordings, teaching

## PUBLICATIONS

### JOURNAL PAPERS

- Zannin, J., Ferrari, A., Larrey-Lassalle, P., Laloui, L. (accepted, 2020). Early-stage thermal performance design of thermo-active walls implemented in underground energy infrastructures. *Geomechanics for Energy and the Environment*.
- Zannin, J., Rotta Loria, A. F., Llabjani, Q., Laloui, L. (2020). Extension of Winkler's solution to non-isothermal conditions for capturing the behaviour of plane geostructures subjected to thermal and mechanical actions. *Computer and Geotechnics*.
- Zannin, J., Ferrari, A., Pousse, M., & Laloui, L. (2020). Hydrothermal interactions in energy walls. *Underground Space*. <https://doi.org/10.1016/j.undsp.2020.02.001>
- Olarte, J., Paramasivam, B., Dashti, S., Liel, A., & Zannin, J. (2017). Centrifuge modeling of mitigation-soil-foundation-structure interaction on liquefiable ground. *Soil Dynamics and Earthquake Engineering*, 97, 304-323. <https://doi.org/10.1016/j.soildyn.2017.03.014>
- Zannin, J., Ferrari, A., Laloui, L. (in preparation). Full-scale thermo-hydro-mechanical in-situ testing on an underground railway station equipped with energy geostructures.
- Zannin, J., Ferrari, A., Laloui, L. (in preparation). Analytical modelling of soil-structure interaction in non-isothermal conditions: new models and applications.
- Zannin, J., Rotta Loria, A.F., Llabiani, Q., Laloui, L. (in preparation). Estimation of the thermo-mechanical behavior of plane energy geostructures through design charts.

### CONFERENCE PAPERS AND EXTENDED ABSTRACTS

- Zannin, J., Ferrari, A., Pousse, M., & Laloui, L. (2019). Thermal design and full-scale thermal response test on Energy Walls. In *E3S Web of Conferences* (Vol. 92, p. 18011). EDP Sciences. "7th International Symposium on Deformation Characteristics of Geomaterials (IS-Glasgow 2019)" <https://doi.org/10.1051/e3sconf/20199218011>
- Zannin, J., Ferrari, A., Pousse, M., & Laloui, L. (2018). A flowchart for early-stage thermal design of Energy Walls. "International Symposium on Energy Geotechnics SEG2018"
- Zannin, J., Ferrari, A., Laloui, L. (abstract accepted 2020, conference postponed) In-situ testing of the energy behavior of a thermo-active underground train station. "Proceedings of the 3rd International Conference on Environmental Geotechnology, Recycled Waste Materials and Sustainability Engineering, Izmir-Turkey 2020"
- Rotta Loria, A. F., Zannin, J., Llabjani, Q., Laloui, L. (accepted 2020, conference postponed to 2021). Analytical solution for describing the thermo-mechanical behavior of plane energy geostructures. *ICEGT-2020, 2<sup>nd</sup> International Conference on Energy Geotechnics, La Jolla, California, USA, 28-31 March 2021*.
- Koliji, A., Rigaud, E., Kazerani, T., Zannin, J., Ferrari, A., Laloui, L. (submitted, 2020) Use of underground space as renewable energy sources for a sustainable society. "WTC2021 -World Tunnel Congress"